# Opto- and Electro-Mechanical coupling between the depletion and the piezoelectric region of a Gallium Arsenide (GaAs) Micro Torsional Resonator Photodiode

December 14, 2016

Opto- and Electro-Mechanical coupling between the depletion and the piezoelectric region of a Gallium Arsenide (GaAs) Micro Torsional Resonator Photodiode

By

ABHISHAIK RAMPAL, B.ENG., M.Sc

B.Eng.(McMaster University) 2004

M.Sc.(McMaster University) 2010

A Thesis

Submitted to the School of Graduate Studies in

Partial Fulfillment of the Requirements

for the Degree Doctor of Philosophy

McMaster University

©Copyright by Abhishaik Rampal, 2016.

DOCTOR OF PHILOSOPHY(2016) McMaster University
(Engineering Physics) Hamilton, Ontario

TITLE: Opto- and Electro-Mechanical coupling between the depletion and the piezoelectric region of a Gallium Arsenide (GaAs) Micro Torsional Resonator Photodiode
AUTHOR: Abhishaik Rampal
SUPERVISOR: Dr. R. N. Kleiman
NUMBER OF PAGES: xxvii, 202

# Abstract

In this work, the opto-piezo actuation and piezoelectric actuation in gallium arsenide ($GaAs$) is experimentally and theoretically verified. Experimentally the response of the respective actuations are measured using the current generated from the inverse piezoelectric effect. The mechanical structure used to generate this current is a micron size torsional resonator fabricated from a $GaAs$ photodiode heterostructure. The photodiode heterostructure is optically and electrically designed as a photovoltaic (PV) cell while mechanically the structure resembles a bimorph. The bimorph design is a result of the PV cell consisting of a $pn$ junction and a heterojunction where the depletion regions have the additional property of being piezoelectric. The opto-piezo actuation results from using the photogenerated voltage to piezoelectrically drive a mechanical structure. Using light modulated at the resonance frequency of the torsional resonator the measured current is shown to linearly increase with intensity. For the electrical actuation case, the torsional resonator is driven using the non-linear response of the $pn$ junction to an applied voltage. The non-linear response results in generation of voltage at the harmonic frequencies of the applied voltage. The voltage generated at twice the applied frequency is given the label $2f$ and is used to piezoelectrically drive the mechanical structure. The above results for the two methods of actuation are theoretically validated by deriving a model for the expected current. The model predicts the current as a function of the voltage. For the opto-piezo case this voltage is the photovoltage. The photovoltage is determined using the AC PV model. This model is derived using the DC PV model and predicts the AC operation of a photodiode in the 3rd and 4th quadrants to resistive and reactive loads. Using the opto-mechanical coupling coefficient the efficiency of the opto-piezo actuation is compared to opto-thermal actuation and radiation pressure actuation. It is shown that the opto-piezo effect, in general, is several orders of magnitude better than the other two in converting optical energy into mechanical energy. This is an important result because in situations where low optical powers are only available and power, in general, cannot be spared, for e.g. on a satellite, devices that make use of the opto-piezo effect could be used for either actuation or sensing. Generally however, using the opto-piezo effect can lead to either integration of existing photonic devices with mechanical resonators or new photonic devices all together. For e.g. using the opto-piezo effect an adaptable optical correlator can be made which could be used to make artificial intelligent machines.

# Acknowledgments

There are three people without whom this work would not have been possible. I would like to thank, first and foremost, Dr. Rafael N. Kleiman, my supervisor, who has not only provided the resources to make this research possible but has also provided helpful guidance and insightful ideas to further this work. I would also like to thank you for allowing me to explore my curiosities and funding them and always making the time, especially on weekends and holidays, to discuss physics. These years spent have been loads of fun. Second, I would like to thank Master Christopher Pope for choosing to join the MEMS group. Your fearlessness and technical abilities are an inspiration and the group has gained much with your time spent here. I hope we will have an opportunity to work together in the future. Third, I would like to thank Dr. Manuela Peter for the laughs and showing me different ways of tackling a problem.

I am very appreciative of the staff of Center for Emerging Device Technology (CEDT), Dr. Brad J. Robinson, Dr. Doug Bruce, Dr. Zhilin Peng, Master Doris V. Stevanovic and Dr. Shahram Tavakoli, for their patience while training me and for their thoughts and feedback on barriers which arose throughout this research. I would like to extend this appreciation to Master Sarah Selensnic.

Thank you to my summer students Paul Ciolek and Aaraon Trainor for all your help in the quartz tuning fork experiments and the radiation pressure experiments. I would also like to thank John Ramoul for continuing the work on the radiation pressure experiment.

Thank you to Linda Wilson, the secretary for CEDT, for taking care of all the administrative stuff.

Many thanks to Eng Phys technicians: Mr. Glen Leinweber and Mr. Peter Jonasson. Glen, I will miss our conversations about oscillators, circuits and life in general. Peter, thanks for allowing me to "borrow" all those electrical components, opening your lab to me and lending a ear to discuss problems with computers. My offer of cleaning your attic still stands. I would love to get access to those In Session betamax tapes that are stored there.

Thank you fellow MEMS grad student and now PhD Dr. Matthew Daniel Minnick for bringing laughter and your smarts to the office. Our conversations about physics have helped deepen my understanding about its principles. Thanks to fellow graduate student and now PhD Dr. Martin Gerber and Dr. Parsian Mohseni, Master Manuel Gil, Master Andrey Zdanovich and Kevin Boyd for your friendship, conversations and help.

Thank you Master Dannion Rigs 'Tusk' Smith and Master Shanon Nancekivell for your big hearts and keeping the door of your house open. The dinners, barbecues and excursions were fun. Thanks to Jaime 'Weaz' McMahon, Scott 'Bob' Schroeders, Master Scott 'Dr. Bones' Read, Sean 'Shack' Green and Iyer Gane for getting me outside of the lab.

Thank you Atwal brothers - Aman and Ajeet. You both still keep on kicking my butt and inspire me to strive for excellence. You two were the first kids I met when I came to this country and I am glad our friendship is still going strong 23 years later.

Adnan 'Ado' Bin Mahfooz and Mr. Steven Fabian; gentleman you were excellent house mates. We had a hell of a good time converting that house into a supposed alien ship.

Thank you to my committee members, Dr. Erik Sorensen and Dr. Dan Cassidy, for agreeing to be a part of my PhD committee.

Thank you to Dr. Sprung, Dr. Mascher and Dr. Preston for being excellent teachers.

Thank you dad, mom and my twin sister for your constant support, motivation and being the foundation on which I can be me.

Last but definitely not least I would like to thank Master Jack 'Duck' Kong. You, sir, are an infinite well of inspiration. I am glad our paths crossed.

# Contents


**1 Introduction** **1**
- 1.1 Development of *GaAs* technology . . . 2
  - 1.1.1 Substrate development . . . 2
  - 1.1.2 Epitaxy . . . 3
- 1.2 Piezoelectricity . . . 3
  - 1.2.1 Piezoelectricity in *GaAs* . . . 4
- 1.3 Motivation . . . 4
- 1.4 Thesis Overview . . . 6

**2 Background** **7**
- 2.1 Resonator . . . 7
  - 2.1.1 Forced Harmonic Motion: Resonance . . . 8
  - 2.1.2 Electrical Resonator . . . 11
- 2.2 Mechanical Structures . . . 11
  - 2.2.1 Flexural Bending . . . 12
    - 2.2.1.1 Cantilevers . . . 15
  - 2.2.2 Quality Factor, Q, of Mechanical Structures . . . 18
- 2.3 Piezoelectricity . . . 19
  - 2.3.1 Mathematical Description . . . 19
  - 2.3.2 Monomorph . . . 22
  - 2.3.3 Bimorph . . . 22
  - 2.3.4 Electrical Model of a Piezoelectric Resonator . . . 23
    - 2.3.4.0.1 BVD Model . . . 23
    - 2.3.4.0.2 Effect of $C_p$ . . . 23
- 2.4 Semiconductor . . . 27
  - 2.4.1 *pn* Junction . . . 31
    - 2.4.1.1 Electrical Circuit . . . 35
  - 2.4.2 Heterojunction Diode . . . 35
  - 2.4.3 Photodiode . . . 36
    - 2.4.3.1 Single Diode DC PV Model . . . 37
    - 2.4.3.2 Single Diode AC PV Model . . . 41
      - 2.4.3.2.1 Nomenclature . . . 41
      - 2.4.3.2.2 Literature Review . . . 41
      - 2.4.3.2.3 AC PV Model . . . 42
      - 2.4.3.2.4 AC Power . . . 45

2.4.3.2.5 Analytical Predictions . . . 46
2.4.3.2.5.1 Diode IV Curves . . . 46
2.4.3.2.5.2 Resistive Regime . . . 46
2.4.3.2.5.3 Reactive Regime: . . . 58
2.4.3.2.5.4 Mixture case: Resistive and Reactive . . . 59
2.5 Conclusion . . . 60

**3 AC PV Model** **63**
3.1 Introduction . . . 63
3.2 Experiment . . . 63
3.2.1 Resistive Load: . . . 64
3.2.1.1 IV Curves . . . 64
3.2.1.2 DC Case . . . 67
3.2.1.2.1 DC Power . . . 69
3.2.1.3 AC Case . . . 69
3.2.1.3.1 Experimental Setup . . . 73
3.2.1.3.2 AC Analysis . . . 73
3.2.1.3.3 $C$ Parameter . . . 74
3.2.1.3.4 AC Power . . . 74
3.2.1.3.5 Noise . . . 77
3.2.2 Capacitive Loads: . . . 78
3.2.2.1 Experimental Setup . . . 78
3.2.2.2 AC Results and Analysis . . . 80
3.2.2.3 Noise . . . 80
3.2.3 QTF Load: . . . 82
3.2.3.1 QTF Circuit Parameters . . . 83
3.2.3.2 Experimental Setup . . . 83
3.2.3.3 AC Results and Analysis . . . 86
3.2.3.3.1 $i_{d,3}$ Measurement and Analysis . . . 86
3.2.3.3.2 $p_{d,3}$ Analysis . . . 87
3.2.3.4 Noise . . . 89
3.3 Conclusion . . . 89

**4 Driving and Detecting of Torsional modes using Flexural Deformation of tines** **91**
4.1 Introduction . . . 91
4.1.1 Literature Review . . . 91
4.1.1.1 GaAs heterostructure resonator . . . 91
4.1.1.2 Torsional Resonators . . . 92
4.1.2 Motivation . . . 92
4.1.3 Outline . . . 93
4.2 Design . . . 93
4.2.1 Structural Design . . . 93
4.2.2 Piezoelectric properties . . . 94
4.2.3 MBE growth . . . 96

4.2.4 Depletion/Piezoelectric Regions . . . 99
4.2.5 Dimensional constraints . . . 99
4.3 Electrical Prediction . . . 103
4.4 Fabrication . . . 111
4.5 Experimental Setup and Results . . . 112
4.5.1 Experimental Setup . . . 121
4.5.2 Electrical Circuit . . . 123
4.5.3 Experimental Results . . . 123
4.6 Comparison to other Piezoelectric materials . . . 127
4.7 Conclusion . . . 128

**5 Electro-mechanical coupling in a GaAs Torsional Resonator 129**
5.1 Introduction . . . 129
5.1.1 Literature Review . . . 129
5.1.1.1 Electro-mechanical coupling . . . 129
5.1.1.2 Harmonic Drive . . . 130
5.1.1.3 Harmonic signals from diodes . . . 130
5.1.2 Motivation . . . 130
5.1.3 Outline . . . 131
5.2 Analytical Model . . . 131
5.2.1 $f$ Case . . . 131
5.2.1.1 $C_{m,x}(V)$ . . . 131
5.2.1.2 $C_{J,x}$ . . . 132
5.2.1.3 $C_J$ and $C_m$ . . . 132
5.2.2 $2f$ Case . . . 133
5.2.3 Analytical Predictions . . . 135
5.2.3.1 Electrical Response . . . 135
5.2.3.1.1 $C_J^f$ and $C_m^f$ . . . 135
5.2.3.1.2 $C_J^{2f}$ and $C_m^{2f}$ . . . 136
5.2.3.2 $V^{2f}$ . . . 136
5.2.3.3 Electro-Mechanical Response . . . 136
5.3 Experimental Setup and Results . . . 141
5.3.1 Equivalent Electrical Circuit . . . 143
5.3.2 Experimental Results . . . 143
5.3.2.1 AC Noise . . . 143
5.3.2.2 Electro-Mechanical Response . . . 146
5.3.2.3 Analysis at $f$ . . . 146
5.3.2.3.1 $C_J^f$ . . . 148
5.3.2.3.2 $C_m^f$ . . . 148
5.3.2.4 Analysis at $2f$ . . . 148
5.3.2.4.1 $C_J^{2f}$ . . . 148
5.3.2.4.2 $C_m^{2f}$ . . . 148
5.3.2.4.3 Comment about $C_m^f$ and $C_m^{2f}$ . . . 148
5.4 Conclusion . . . 151

**6 Opto-Electro-Mechanical Coupling** **152**
6.1 Introduction . . . 152
6.1.1 Literature Review . . . 152
6.1.1.1 Radiation Pressure . . . 152
6.1.1.2 Photothermal . . . 153
6.1.1.3 Photostrictive . . . 153
6.1.1.4 Opto-piezo effect in GaAs . . . 154
6.1.2 Motivation . . . 155
6.1.3 Outline . . . 155
6.2 Design . . . 155
6.2.1 Heterostructure Design . . . 155
6.2.1.1 Absorption Properties of $GaAs$ and $In_{0.485}Ga_{0.515}P$ . . . 155
6.2.1.2 Opto-Electrical Design . . . 156
6.2.1.3 Electrical Circuit . . . 157
6.2.2 Resonator Design . . . 159
6.3 Analytical Predictions . . . 160
6.3.1 Opto-Piezo Actuation . . . 160
6.3.1.1 Ideal Case . . . 160
6.3.1.2 Non-Ideal Case . . . 161
6.3.2 Opto-Electro-Mechanical Coupling . . . 163
6.3.2.1 Ideal Case . . . 163
6.3.2.2 Non-Ideal Case . . . 163
6.4 Experimental Setup and Results . . . 163
6.4.1 Experimental Setup . . . 167
6.4.2 Electrical Circuit . . . 168
6.4.3 IR LED Power . . . 168
6.4.4 Photodiode DC response . . . 170
6.4.5 AC Noise . . . 171
6.4.6 Resonance Measurements . . . 171
6.4.7 Impedance Matching . . . 171
6.4.8 Linear Response . . . 172
6.4.9 Opto-Electro-Mechanical Coupling . . . 172
6.5 Opto-Mechanical Coupling Coefficient . . . 175
6.5.1 Photothermal . . . 177
6.5.2 Radiation Pressure . . . 178
6.5.2.1 Opto-Piezo Effect . . . 179
6.5.3 Comparison of the three opto-mechanical coefficients . . . 180
6.5.4 Opto-Piezo Devices . . . 184
6.5.4.1 PIC . . . 184
6.5.4.2 Optical Correlator (OC) . . . 185
6.5.4.3 Optical Clock Signal Generator (OCSG) . . . 186
6.5.4.4 Mechanical Resonance Enhanced Photodetector (MREP) . . . 188
6.6 Conclusion . . . 189

**7 Conclusion and Future Work** **191**
7.1 Conclusion . . . 191
7.2 Future Work . . . 194
7.2.1 Heterostructure redesign . . . 194
7.2.2 Mechanical structures . . . 194

# List of Figures


2.1 Mass-Spring System $M$ is the mass, $k$ is the spring constant and $c$ is the damping term . . . . . 8

2.2 Graph of normalized displacement vs time for underdamped $\gamma = 0$ and $0.1$, critically damped, $\gamma = 1.0$ and overdamped,$\gamma = 2.0$ cases . . . . . 9

2.3 Graph of amplitude and normalized phase response of a driven harmonic oscillator: (a) Amplitude and (b) Normalized phase response are plotted for varying $\gamma$. The x-axis is $\frac{w}{w_0}$, i.e. applied frequency divided by resonance frequency. For $\frac{w}{w_0} < 1$ $A = \frac{F_0}{k}$ and $\phi = 0$. The amplitude is inversely dependent on the spring constant and force is in phase with the displacement. For $\frac{w}{w_0} = 1$, i.e. at resonance $A = \frac{F_0}{2\gamma m\sqrt{w_0^2-\gamma^2}}$ and $\frac{\phi}{\pi} = 0.5$. The amplitude is inversely dependent on $\gamma$ and the force is $\pm\frac{\pi}{2}$ out of phase with the displacement. For $\frac{w}{w_0} > 1$ $A = \frac{F_0}{mw^2}$ and $\phi \to \pi$. The amplitude is inversely dependent on both mass and applied frequency and the force is $\pm\pi$ out of phase with the displacement . . . . . 10

2.4 Types of Deformation: (a) Longitudinal, (b) Flexural, (c) Thickness Shear, (d) Face Shear and (e) Torsion[1] . . . . . 12

2.5 Member subjected to equal and opposite couples: (a)internal force at a cross-section, (b)equal and opposite couples[2] . . . . . 13

2.6 Normal and shearing stress in a prismatic member due to a couple[2] . . . . . 13

2.7 Cantilever's first three modes. The number of nodes increase with mode number. The first mode (red) has 0 nodes, the second mode (green) has 1 node and the third mode (yellow) has 2 nodes . . . . . 17

2.8 Piezoelectric Drive and Detect. (a) Piezoelectric Effect: An applied voltage results in a strain/stress, $\epsilon_p/\sigma_p$, due to the piezoelectric coefficient, $d_{pk}$, leading to a deflection - $\Delta\xi\ \alpha\ d_{pk}E_k$, (b) Inverse Piezoelectric Effect: The stress/strain as a result of the deflection produces a charge due to the inverse piezoelectric effect - $Q\ \alpha\ e_{iq}\epsilon_p$ where $e_{iq}$ is the piezoelectric coefficient. Here $\propto$ is a symbol for proportionality . . . . . 22

2.9 Layer sequence of a monomorph[3] . . . . . 22

2.10 Flexural deformation of monomorph due to an applied field **(E)**. The horizontal arrows indicate the direction of the piezoelectric strain and the vertical arrows indicate the direction of polarization, **P**, and the applied field. The strain is parallel to the $x - direction$. An applied field causes a longitudinal extension or compression of this layer while the elastic layer restricts the motion. As a result an internal piezoelectric moment arises causing a flexural deformation of the monomorph. The opposite direction of **E** and **P** indicates that for a field directed in the negative $z-$direction an extension occurs along the $x-$direction. [3] . . . . . 23
2.11 Deflection of bimorph subjected to a field - (a) parallel bimorph, (b) serial bimorph. Parallel bimorph is defined as a structure having two piezoelectric layers with the same polarization direction and fields applied in opposite directions. Serial bimorph is defined as a structure having two piezoelectric layers with opposite polarization direction and a field applied in a single direction [3] 24
2.12 Piezoelectric resonator circuit. $R_m$, $L_m$ and $C_m$ are the motional components at resonance and $C_p$ is the package or dielectric capacitance[4]. $C_m$ and $C_p$ are derived using equation (2.31) where the first term in this equation is the charge resulting from the deformation of the piezoelectric structure. Knowing $C_m$ $L_m$ is derived using equation (2.37) and $R_m$ is proportional to the inverse $Q$ 24
2.13 $Z\,vs$ Frequency The figure is generated using equation (2.34) where $C_p = 1.4178\,pF$, $C_m = 3.0666\,fF$, $L_m = 7.6943\,kH$ and $R_m = 15.953\,k\Omega$. The lowest impedance is at resonance $Z_R = R_m$ and highest impedance is at anti-resonance $Z_m = 734.06\,M\Omega$. The impedance off resonance is dominated by $\frac{1}{wC_p}$ . . . . . 26
2.14 Graph of $Z_{real}/Z_{imag}$ vs $Frequency$ of the BVD circuit. $Z_{real}$ and $Z_{imag}$ are generated using equations (2.35) and (2.36). The values used for $R_m$, $C_m$, $L_m$ and $C_p$ are $15.953\,k\Omega$, $3.0666\,fF$, $L_m = 7.6943\,kH$ and $C_p = 1.4178\,pF$ respectively. The impedance is dominated by $Z_{imag}$ except at resonance and anti-resonance. At these points, indicated by open blue circles, $Z_{real}$ dominates because $Z_{imag}$ decreases relative to $Z_{real}$ by over an order of magnitude 27
2.15 Graph of Phase ($\phi$) vs $Frequency$. Phase is generated using equation (2.41). The values used for $R_m$, $C_m$, $L_m$ and $C_p$ are $15.953\,k\Omega$, $3.0666\,fF$, $L_m = 7.6943\,kH$ and $C_p = 1.4178\,pF$ respectively. The open blue circles indicate the resonance and anti-resonance points. At these points the phase is $0^0$ while above and below these points the phase is $-90^0$ and between these points the phase is $90^0$. These correspond to the resistive, capacitive and inductive regimes of the resonator . . . . . 28

2.16 Energy Band arrangement for Insulators, Semiconductor and Metals. The y-axis is electron energy and increases from bottom to top. The gradient follows the Fermi-Dirac distribution. Red indicates 0 free states, blue indicates 0 filled states and the gradient indicates partially filled states. For electrical conduction to occur empty states are required. In metals the valence and conduction bands overlap resulting in the availability of low energy partially filled states. This allows for valence electrons to freely move through the material. For insulators and semiconductors the valence and conduction bands are separated by a band gap having energy $E_g$. Thus an electron has to transit from the valence to the conduction band. Insulators have large $E_g$ and hence lower conductivity while semiconductors have lower $E_g$ hence higher conductivity than insulators but lower than metal. . . . . 30
2.17 Band Diagram of p and n doped semiconductor. The colors and patterns used in this figure are carried over from figure (2.16). For the p doped material the fermi level is closer to the valence band indicating an increased conductivity due to an excess of holes while for the n doped material the fermi level is closer to the conduction band indicating increased conductivity due to an excess of electrons. The movement of the fermi-level is a result of introducing dopants or impurities in the semiconductor . . . . . 31
2.18 Non-Linear Current Response of a Diode. Current vs Voltage, IV Curve, of a diode. The curve is generated using equation (2.44). The current increases exponentially as the applied voltage approaches the built-in potential . . . . . 32
2.19 Capacitance Response of a Diode. (a)$C_J \, vs \, V$, (b)$\frac{1}{C_J^2} \, vs \, V$ (a) and (b) are generated using equation(2.45). As the applied voltage increases the capacitance increases or $\frac{1}{C_J^2}$ decreases . . . . . 33
2.20 Isolated p and n type materials. $E_c$ and $E_v$ are the energy of the conduction and valence band. $E_{Fn}$ is the Fermi-Energy of the n-type material and $E_{Fp}$ is the fermi energy level of the p-type material. The rectangles on top of the respective bands are a cartoon indicating the doped semiconductor . . . . . 34
2.21 *pn* junction. The cartoon at the top of the figure shows the space charge or depletion region forms at the interface between the two doped semiconductors. This region has a width $W$, and a field, $\vec{E}$, across this region. At the bottom of the figure the energy bands of the *pn* junction away from the interface and at the interface are shown. The bands at the interface bend such that $E_{Fn}$ and $E_{Fp}$ align. This bending results in a contact potential $V_0$ and its associated $\overrightarrow{E}$ . . . . . 34
2.22 Diode equivalent circuit. $C_J$ is the junction capacitance . . . . . 35
2.23 Heterojunction Band Discontinuity in the conduction band. A heterojunction between $N^+$-AlGaAs and lightly doped $GaAs$. A pile-up of electrons occur in the conduction band. This pile-up results in a potential well. If the potential well is thin then discrete states $E_1$ and $E_2$ are formed[5] . . . . . 36

2.24 Current vs Voltage for an illuminated junction. Quadrant III and IV are called the photoconductance and photovoltage quadrants. The photoconductance quadrant is used for information transfer while the photovoltage quadrant is used to deliver power by converting optical power to electrical power . . . . . 38
2.25 DC Bias Points. Illuminated Diode IV curve is plotted and three cases are indicated by open circles. The open circles indicate the DC bias points of interest, $V_D$, the value of load resistance, $R_L$ required and the resulting current, $I_{D,1}$ and power $P_{D,1}$ . . . . . 39
2.26 Single Diode DC PV Model: (a) Ideal circuit and (b) Real/Non-Ideal circuit. $I_{isc}$ is the photogenerated current. In the real circuit $R_{sh}$ and $R_s$ account for current losses due to manufacturing defects and poor contacts. $R_L$ is the load resistance. $I_{D,1}R_L$ or $I_{D,3}R_L$ biases the respective diode model at an operating point, $V_D$, on the illuminated IV curve given in figure (2.25) [6] . . 40
2.27 AC Single Diode Model. (a) Real/Non Ideal AC PV circuit (b) Ideal AC PV circuit. (a) and (b) are the extensions of the DC PV models, given in figures (2.26)(a) and (b), with the addition of junction capacitance, $C_J$, AC short circuit current, $i_{isc_1}$, and load impedance, $Z_L$. (a) is reduced to (b) by combining $R_{sh}$, $C_J$, $R_s$ and $Z_L$ into a total resistance $Z_t$. . . . . 43
2.28 Theoretical IV Curves. The curves are generated using equation (2.51) for the following $I_{isc}$ values 1.00 ,5.0 and 10.0 $A$. The associated $V_{oc}$ values are 1.00, 1.04 and 1.06 $V$. The increase in $V_{oc}$ is logarithmic with $I_{isc}$ as expected from equation (2.48) . . . . . 46
2.29 IV Curves with load lines. The load lines are for $R_L$ of 0.1, 0.2 and 1.0 $\Omega$ . . . 48
2.30 $I_{D,1}R_L \, vs \, I_{isc}R_L$ for $I_{isc} = 1$, 5 and 10 $A$. Two linear regions exist separated by a knee. The voltage to the left of the knee increases linearly with $I_{isc}$ ,or optical power, while the voltage to the right of the knee increases logarithmically with $I_{isc}$. As $I_{isc}$ increases the knee shifts to the right and $V_D$ increases . . . . 48
2.31 $\frac{I_{D,1}}{I_{isc}} \, vs \, I_{isc}R_L$ for $I_{isc} = 1$, 5 and 10 $A$. (a) Two distinct regions exist separated by a knee. To the left of the knee $\frac{I_{D,1}}{I_{isc}} = 1$ and to the right of the knee $\frac{I_{D,1}}{I_{isc}}$ decreases. The former corresponds to the flat or horizontal part of the IV curve, figure (2.28), while the latter corresponds to the vertical part of the IV curve. The lack of overlap in $\frac{I_{D,1}}{I_{isc}}$ past the knee is due to differences in $V_{oc}$. As $I_{isc}$ increases the knee shifts to the right. This is emphasized in (b) which is the exploded section of (a) around the knee . . . . . 50
2.32 $P_{D,1} \, vs \, I_{isc}R_L$ As $I_{isc}$ or optical power increases the extracted DC power, $P_{D,1}$, also increases. The maximum power point is indicated on the plots and is determined using equation (2.71). Using this equation maximum power point is extracted for $R_L = 0.88$, 0.18 and 0.09 $\Omega$ for $I_{isc} = 1$, 5 and 10 $A$ . . . 51
2.33 $IV$, $I_{D,1}R_L$, $\frac{I_{D,1}}{I_{isc}}$ and $P_{D,1}$ are plotted for $I = 1.0\,A$ and $V_{oc} = 1.0\,V$. The knee indicates the maximum power that can be extracted. The dotted line indicates the maximum power point on the IV curve . . . . . 51

2.34 $\frac{i_{d,1}}{I_{isc_1}}$ *vs* $I_{isc}R_L$ This plot is similar to DC plot in figure (2.31)(a). Similar to the DC case two distinct regions are separated by a knee. The lack of overlap right of the knee is due to the differences in $V_{oc}$. This is emphasized in (b) which is the exploded section of (a) in the vicinity of the knee . . . . . 52
2.35 $\frac{I_{D,1}}{I_{isc}}$ *vs* $I_{isc}R$ and $\frac{i_{d,1}}{i_{isc_1}}$ *vs* $I_{isc}R$ for the IV curve having $I_{isc} = 1.0\,A$. The knee for $\frac{i_{d,1}}{i_{isc_1}}$ is shifted towards lower $I_{isc}R_L$ and $\frac{i_{d,1}}{i_{isc_1}}$ reduces faster than $\frac{I_{D,1}}{I_{isc}}$ . . . 54
2.36 $p_{d,1}$ *vs* $I_{isc}R_L$ The plot is generated using equation (2.76) where $i_{isc_1}$ is 10% of $I_{isc}$. 10% is chosen in keeping with the small signal approximation used to derive equation (2.65). The plot shows that $p_{d,1}$ increases as $i_{isc_1}$ increases . . 55
2.37 $\frac{P_{D,1}}{max(P_{D,1})}$ *vs* $I_{isc}R_L$ and $\frac{p_{d,1}}{max(p_{d,1})}$ *vs* $I_{isc}R_L$. The maximum power point for the AC power does not coincide with the DC maximum power point. For the AC case the power point is shifted to the left by roughly 8.83% which indicates a reduction in $R_L$ or $I_{isc}$ if $I_{isc}$ or $R_L$ is kept fixed . . . . . 56
2.38 $\frac{i_{d,1}}{i_{isc_1}}$ *vs* $I_{isc}Z_L$ The shape of the curve is similar to the resistive curve. $\frac{i_{d,1}}{i_{isc_1}}$ is generated using equation (2.78) and the parameters: $I_{isc} = 1.0\,A$ and $V_{oc} = 1.0\,V$. Here $Z_L$ is swept by varying the frequency . . . . . 59
2.39 $\frac{i_{d,1}}{i_{isc_1}}$ *vs* $I_{isc}Z_L$. The plot is generated for a load comprising of a resistor $R$ in parallel with a reactive element $X = Rtan\phi$ and for the IV curves having $I_{isc} = 1.0\,A$ and $V_{oc} = 1.0\,V$. For $\phi = 0$ the circuit is purely resistive and for $\phi = \frac{\pi}{2}$ the circuit is purely capacitive. The knee shifts to the left as $\phi$ increases indicating a shift towards larger $R_L$and therefore towards $V_{oc}$ . 60
2.40 $p_{d,1}$ *vs* $I_{isc}Z_L$ Power dissipation decreases as the phase increases and the maximum power shifts to the left. The plot is generated for a load comprising of a resistor $R$ in parallel with a reactive element $X = Rtan\phi$ and for the IV curves having $I_{isc} = 1.0\,A$ and $V_{oc} = 1.0\,V$. For $\phi = 0$ the circuit is purely resistive and hence maximum power is dissipated. For $\phi = \frac{\pi}{2}$ the circuit is purely capacitive and zero power is dissipated . . . . . 61

3.1 LED Drive Circuit . . . . . 63
3.2 818-SL $I_{D,3}$ *vs* $V$ for optical power between $66 - 981\,\mu W$. The non-linear current response follows equation (2.49). As $I_{isc}$ or the optical power incident on the photodiode increases $V_{oc}$ increases logarithmically. The logarithmic increase in $V_{oc}$ explains the decrease in separation at $I_{D,3} = 0$. This logarithmic relationship is captured in equation (2.48). Lines are drawn as a guide to the eye . . . . . 65
3.3 818-SL IV Curves with Load Lines for $R_L = 1$, 2.2, 5 and $10\,k\Omega$ from bottom to top. Lines are drawn as a guide to the eye . . . . . 68
3.4 $I_{D,1}R_t$ *vs* $I_{isc}R_t$ for $R_L = 1$, 2.2, 5. and $10\,k\Omega$ (a) Two linear regions separated by a knee are seen. The voltage to the left of the knee increases linearly with optical power while the voltage to the right of the knee increases logarithmically with optical power (b) Exploded section of (a) in the vicinity of the knee. This is done to emphasize the point that the knee shifts to the right as $R_L$ decreases. The shifting to the right is indicative of increasing $I_{isc}$ or an increasing incident optical power. The dotted line is drawn as an aid to the eye 70

3.5 $\frac{I_{D,1}}{I_{isc}}$ *vs* $I_{isc}R_t$ for $R_L = 1,\ 2.2,\ 5.$ and $10\,k\Omega$: (a) Two distinct regions are seen separated by a knee. To the left of the knee $\frac{I_{D,1}}{I_{isc}} = 1$ and to the right $\frac{I_{D,1}}{I_{isc}}$ decreases. The former corresponds to the flat or horizontal part of the IV curve, (3.3), while latter corresponds to the vertical part of the same curve. The lack of overlap past the knee is due to differences in $V_{oc}$. The knee shifts to the right as $R_L$ decreases. This is emphasized in (b) and is indicative of increasing $I_{isc}$ or an increasing incident optical power. The dotted line is drawn as an aid to the eye . . . . . 71

3.6 $P_{D,1}$ *vs* $I_{isc}$ The solid line is generated from equation (2.71) using the measured $V_{oc}$ and $I_{isc}$ values. Symbol 'x' is the maximum power that can be extracted for each $I_{isc}$. The solid circle are the dissipated power due to $R_L$. Good agreement is seen amongst the three . . . . . 72

3.7 Block Diagram of experimental setup used for measuring the AC response of 818-SL biased by a resistive load, $R_L$. The HP-3425A and 33120A supply the DC and AC voltage required bias and modulate the LED. The light modulated light from the LED is incident on the $R_L$ biased 818-SL photodetector. The current, $i_{D,3}$, generated by the biased photodetector is amplified by the SR-570 low current noise pre-amp. The output of the amplifier is fed into the SR-830 lock-in. The lock-in is synchronized to the HP-33120A. The data from the lock-in is collected on a computer. The arrows in the diagram indicate light being emitted from the LED onto the 818-SL . . . . . 73

3.8 $\frac{I_1}{I_{sc_1}}$ *vs* $I_{sc}R_t$ for $R_L = 1,\ 2.2,\ 5.$ and $10\,k\Omega$. Good agreement is seen between experimental data and theoretical predictions. Similar to the DC case two distinct regions are separated by the knee. The region to the left of the knee corresponds to the horizontal section of the IV curves while to the right of the knee corresponds to the vertical section of the IV curves. The lack of overlap past the knee is due to differences in $V_{oc}$. The knee shifts to the right as $R_L$ decreases. . . . . 74

3.9 $C$ parameter for $1\,k\Omega$. The solid dots are the experimental $C$ generated by dividing $\frac{i_{d,1}}{i_{isc_1}}$ and $\frac{I_{D,1}}{I_{isc}}$. The solid line is determined from equation (2.75) using the experimentally determined $V_{oc}$, $\eta$ and $V_D$ DC parameters. . . . . 75

3.10 $C$ parameter for $2.2\,k\Omega$. The solid dots are the experimental $C$ generated by dividing $\frac{i_{d,1}}{i_{isc_1}}$ and $\frac{I_{D,1}}{I_{isc}}$. The solid line is determined from equation (2.75) using the experimentally determined $V_{oc}$, $\eta$ and $V_D$ DC parameters. . . . . 75

3.11 $C$ parameter for $5\,k\Omega$. The solid dots are the experimental $C$ generated by dividing $\frac{i_{d,1}}{i_{isc_1}}$ and $\frac{I_{D,1}}{I_{isc}}$. The solid line is determined from equation (2.75) using the experimentally determined $V_{oc}$, $\eta$ and $V_D$ DC parameters. . . . . 76

3.12 $C$ parameter for $10\,k\Omega$. The solid dots are the experimental $C$ generated by dividing $\frac{i_{d,1}}{i_{isc_1}}$ and $\frac{I_{D,1}}{I_{isc}}$. The solid line is determined from equation (2.75) using the experimentally determined $V_{oc}$, $\eta$ and $V_D$ DC parameters. . . . . 76

3.13 Normalized DC and AC Power for $1\,k\Omega$. The maximum power point for AC is shifted to the left by approximately 33% indicating that for the $1\,k\Omega\,R_L$ an $I_{isc}$ of approximately $250\,\mu A$ is required. For the same $R_L$ an $I_{isc}$ of approximately $370\mu A$ is required for the DC maximum power point . . . . . 77

3.14 Normalized DC and AC Power for $2.2\,k\Omega$. The maximum power point for AC is shifted to the left by approximately 43% indicating that for the $2.2\,k\Omega$ $R_L$ an $I_{isc}$ of approximately $89\,\mu A$ is required. For the same $R_L$ an $I_{isc}$ of approximately $160\,\mu A$ is required for the DC maximum power point . . . . . 78
3.15 Voltage Noise vs Frequency. Plotted are the individual contributions from the noise sources: shot noise of 818-SL, Johnson noise of $R_{sh}$ and $R_3$ and the noise floor of SR-570. Also plotted is the total noise, $V_{tot,noise}$. As is seen the SR-570 is the major contribution to the noise floor. $V_{tot,noise}$ is the quadrature sum of the four noise sources . . . . . 79
3.16 Block Diagram of experimental setup used for measuring the AC response of 818-BB-20 biased by a capacitive load, $Z_L$. The HP-3425A and 33120A supply the DC and AC voltage required to bias and modulate the LED. This light is incident on the $Z_L$ biased 818-BB-20 photodetector. The current, $i_{d,3}$, generated by the biased photodetector is fed into the current input of the SR-830 lock-in amplifier. The lock-in is synchronized to the HP-33120A. The data from the lock-in is collected on a computer. The arrows in the diagram indicate light being emitted from the LED onto the 818-BB-20 . . . . . 80
3.17 $\frac{i_{d,1}}{i_{isc_1}}\,vs\,\alpha I_{sc} Z_t$ for $C_L = 105.62\,pF$ The solid line matches the experimental data. This line is generated using equation (2.66) along with the following measured and fitted values of $2.15 \times 10^{-7}\,A \pm 0.97\%$, $49.5\,M\Omega \pm 2.56\%$, $0.443\,\Omega \pm 2.23\%$, $0.36\,V$, $228.25\,pF$ and $105.62\,pF$ for $I_{isc}$, $R_{sh}$, $R_s$, $V_{oc}$, $C_J$ and $C_L$ . . . . . 81
3.18 Current Noise vs Frequency. Plotted are the individual contributions from the noise sources: shot noise of 818-BB-20, Johnson noise of $R_{sh}$ and $R_s$ and the noise floor of SR-830. Also plotted is the total noise, $I_{tot,noise}$. As is seen the SR-830 is the major contribution to the noise floor. $I_{tot,noise}$ is the quadrature sum of the four noise sources . . . . . 82
3.19 AC Single Diode PV Model with QTF Load . . . . . 83
3.20 Electrically Driven QTF (a) Measured current and fit, (b) Measured phase. The resonance frequency of $f_r = 32764\,Hz$, an anti-resonance frequency of $f_a = 32800\,Hz$, and a quality factor of $Q = 100,000$. The circuit parameters determined from the fit to the BVD model are:$L_m = 7.69430 \times 10^3\,H \pm 2.92 \times 10^{-1}\%$, $C_m = 3.06662 \times 10^3\,F \pm 2.91 \times 10^{-1}\%$ and $R_m = 1.59533e4\,\Omega \pm 4.12\%$. $C_p = 1.41783e-12\,F$ is measured using AH-2500A capacitance bridge . . . . . 84
3.21 Block Diagram of experimental setup used for measuring the AC response of 818-BB-20 biased by the Quartz Tuning Fork (QTF) which is a capacitive load. The HP-3425A and 33120A supply the DC and AC voltage required to bias and modulate the LED. This light is incident on the 818-BB-20 photodetector which is biased by the QTF at $V_{oc}$. The current, $i_{d,3}$, generated by the biased photodetector is amplified by the Amptek A-250. The output of the A-250 is connected to the SR-830 lock-in amplifier. The lock-in is synchronized to the HP-33120A. The data from the lock-in is collected on a computer. The arrows in the diagram indicate light being emitted from the LED onto the 818-BB-20 . . . . . 85

3.22 Optically Driven QTF for $P_{opt} = 3.13\,\mu W$ and $p_{opt} = 341\,nW$. (a) $i_{d,3}$ *vs Frequency* The theoretical prediction is made using equation (3.3 (b) $\vartheta$ *vs Frequency* The theoretical prediction is made using equation (2.41). In general for both good agreement is seen between the theoretical prediction and the measured response . . . . . 88
3.23 Power dissipated at resonance, $p_{d,3}\,vs\,i_{isc_1}$. The $I_{isc}$ and $i_{isc_1}$ used in the experiment are given in table(3.4). The theoretical lines are generated using equation (3.4) for $i_{isc_1}$ values ranging from approximately $2 \times 10^{-9}$ - $2 \times 10^{-8}$ $A$ for an $I_{isc} = 4.074 \times 10^{-8}\,A$ and $i_{isc_1}$ values ranging from approximately $4.5 \times 10^{-9}$ - $5.2 \times 10^{-8}$ $A$ for an $I_{isc} = 4.074 \times 10^{-9}\,A$. The ranges of $i_{isc_1}$ are chosen to be lower than the respective $I_{isc}$ . . . . . 89
3.24 Current Noise vs Frequency in the vicinity or resonance. Plotted are the individual contributions from the noise sources: shot noise of 818-BB-20 and A-250, Johnson noise of $R_{sh}$, $R_m$ and $R_s$. Also plotted is the total noise, $I_{tot,noise}$. As is seen the dominant source of noise is the Johnson noise of $R_{sh}$ . . . . . 90

4.1 Y Structure. The structure is comprised of three sections: Pad, Spine and Tines. The Spine is parallel to [100] while the tines are parallel to $[\bar{1}\bar{1}0]$ and $[1\bar{1}0]$ 94
4.2 First three torsional Y-Structure Mode Shapes: (a) Symmetric Fundamental, (b) Anti-Symmetric Fundamental and (c) Anti-Symmetric 1st Harmonic. The shape of the tines for the first two torsional modes resemble the first two mode shapes of a cantilever having 0 and 1 node; respectively. The shape of the tine for the 3rd torsional mode is similar to a cantilever's 3rd mode shape only in the number of nodes, i.e. 2. . . . . 95
4.3 Cartoon of the orientation of GaAs Torsional Resonator with respect to the [100] wafer. Beside the cartoon is the coordinate system pertaining to the [100] wafer orientation. The flat lines are the primary and secondary flats on the wafer. They are parallel to $[\bar{1}\bar{1}0]$ and $[\bar{1}10]$. The spine in parallel to [100] while the tines of the resonator are parallel to $[\bar{1}\bar{1}0]$ and $[\bar{1}10]$ or the $x$ and $y$ axis. The spine of the resonator is clamped at the anchor. The corners of the anchor are parallel to [100] and $[\bar{1}00]$ . . . . . 96
4.4 Cross-Sectional view of the MBE grown structure parallel to [100]. The arrow is drawn parallel to [100]. $Al_{0.8}Ga_{0.4}As$ is the sacrificial layer. The bottom and top contacts are the $200\,nm\,p^+$ and $n^+$ layers. The $In_{0.485}Ga_{0.515}P$ layers are grown for surface passivation and to create a back surface field (BSF). The $p^-n^-$ $GaAs$ layers comprises the $pn$ junction . . . . . 98
4.5 Cross-section of a released tine. (a) Location of the depletion width/piezoelectric and passive layers, (b) $t_1$, $t_2$, $t_3\,t_4$ and $t_5$ are the thickness of passive and piezoelectric layers and (c) The applied potential appears across the depletion widths. The red arrows are the direction of the field going from positive (+) to negative (-) potential . . . . . 98
4.6 wxAmps simulated Energy Band Diagram. The pn and heterojunction depleted regions are indicated . . . . . 100

4.7 Modified Butterworth-Van Dyke (BVD) Electrical Circuit. $R_m$, $L_m$, $C_m$ are the motional terms and $C_J$ is the junction capacitance and $R_{sh}$ is the shunt resistance accounting for the finite resistance in the material . . . . . 103
4.8 Overview of $C_{m,j}$ derivation. An applied voltage results in an z-directed field which produces a $x$ or $y$ directed strain, depending on the orientation of the tine, due to the piezoelectric effect. The resulting strain produces a $x$ or $y$ directed stress. This stress due to the bimorph structure results in a bending moment in the $y$ or $x$ direction which then results in a deflection in the $z$-direction. The x or y directed strain also results in a dipole producing an electric displacement, $D_{m,j}$, in the $z$-direction which can then be integrated to determine the piezoelectric charge, $Q_m$. Using $Q_m$ $C_{m,j}$ is determined . . . 104
4.9 GaAs tine geometry coordinate system. The x-axis is the width, y-axis is the length and the z-axis is the thickness . . . . . 104
4.10 Segmentation of the tine's Y-Torsional Resonator tine. The tine is split into two segments. Segment#1 is the standard cantilever geometry and segment#2 is the extra piece of the tine whose length and width are the same, i.e. $W = L = 30\,\mu m$. For the calculations segment#2 is assumed to be clamped . . . . 107
4.11 Steps for fabrication of Y Torsional Resonator. (a) Optical Micrograph of a fabricated Y-Torsional Resonator where cross-sections A and B are the tine and the top and bottom contacts, (b) is the cross-section view of the heterostructure at sections A-A and B-B and (c) is a legend of the MBE heterostructure layers and additional layers used for fabrication . . . . . 113
4.12 Mask to fabricate torsional resonators. This is a 3' mask on a 4' plate. Each tile is a $14\,mm$ square. There are 21 tiles. To fabricate the resonator discussed in this chapter four tiles are used . . . . . 114
4.13 A small section of a single tile. In this image there are a bunch of resonators. The large cross pattern is an alignment marker . . . . . 115
4.14 Single device belonging to the above tile . . . . . 116
4.15 Mask#1: (a) Chemical vapor deposition (CVD) of $100.0\,nm$ $SiO_2$. $SiO_2$ is represented by the color red. Using mask #1 (d) the patterns for torsional resonators and their respective anchors are transferred to a positive photo-resist (PR). After development of PR exposed $SiO_2$ is etched using BHF exposing $n^+GaAs$. PR is removed and the heterostructure layers, $n^+GaAs$, $n^-In_{0.485}Ga_{0.515}P$, $n^-GaAs$, $p^-GaAs$ and $p^-In_{0.485}Ga_{0.515}P$ are wet-chemically etched using $C_6H_8O_7 : H_2O_2$ (7 : 1), (100%)$HCl$, $C_6H_8O_7 : H_2O_2$ (7 : 1) and (100%) $HCl$. (c) The top view of the structure . . . . . 117
4.16 Mask#2: Preparation for release: $Al_{0.8}Ga_{0.2}As$ layer between the devices and the regions required for releasing the torsional resonators is exposed. First; the remaining $SiO_2$ layer from the previous step is etched using BHF. A new $100.0\,nm\,CVD\,SiO_2$ layer is deposited. Using mask#2 the pattern is transferred to a positive PR. Following the development of PR the exposed $SiO_2$ is etched using BHF and the PR is removed. The exposed $p^+GaAs$ is wet chemically etched using $C_6H_8O_7 : H_2O_2$ (7 : 1). (b) The top view of the structure. Here the red line indicates the outline of the $p^+$ contacts. The region surrounding the $p^+$contacts have been etched . . . . . 118

4.17 Mask#3: Using mask#3 the patterns for the $p^+$ metal contact is transferred to a positive PR. Following the development of PR the exposed $SiO_2$ is wet-chemically etched using BHF exposing the underlying $p^+GaAs$. 25/50/200 nm of Ti/Pt/Au is deposited using a metal evaporator in UHV. The sample is then removed and placed in an Acetone bath for 24 hrs for lift-off. (b) the top view of the structure . . . . . 119
4.18 Mask#4: Using mask#4 the patterns for the $n^+$ metal contact is transferred to a positive PR. The same procedure follows as above with the exception of the metals used. They are 25/50/200 nm of Ni/Ge/Au. (b) the top view of the structure. The bottom and top contacts are indicated. . . . . 120
4.19 Back contact: A metal contact to the substrate is made by depositing 25/50/200 nm of Ti/Pt/Au using the evaporator . . . . . 121
4.20 Release of resonator: In the final fabrication step the torsional resonators are released by etching the exposed $Al_{0.8}Ga_{0.2}As$ layer from step 3. The chip is placed in a bath of (49%) $HF : H_20$ (1 : 9) for 5 minutes and 30 seconds. This timed etch removes $Al_{0.8}Ga_{0.2}As$ from underneath the tines, spine and the pad of the resonator. The etch is followed by a 10 minute $DI\,H_2O$ rinse. The chip is immersed in HLPC grade propanol and transferred to a critical point dryer (CPD) for successful release of the torsional resonators. A critical point dryer is used to avoid stiction. Stiction is the adhesion of the mechanical structure to the substrate. This occurs during the drying step after the sample has been removed from the $DI$ rinse process. During drying capillary forces pull the mechanical structure towards the substrate. The mechanical structure due to the van-der waals forces stick to the substrate. To avoid this the sample is placed in a CPD which displaces the propanol with liquid $CO_2$. By raising the temperature and pressure of the chamber to the critical point liquid $CO_2$ becomes gaseous $CO_2$. . . . . 122
4.21 SEM image of Y Torsional Resonator. The large square is the anchor. The spine, tines and pad are on top of the anchor . . . . . 122
4.22 Experimental setup used for frequency sweeping experiments. The function generator drives the torsional oscillator and supplies the synchronization signal to the SR-844 Lock-in Amplifier. The experiment is controlled by the computer using labview. The data from the lock-in is stored for later processing. The blue dash line indicates the components placed in the vacuum chamber. A vacuum pressure of $\sim 2\,mTorr$ is achieved . . . . . 123

4.23 Electrical Circuit of the two terminal device and the the A-250 amplifier (a) Diode circuit (b) Diode equivalent circuit around resonance. In (b) the diode is replaced by the modified BVD model. In this model $R_m$, $C_m$, $L_m$, $C_J$ and $R_{sh}$ are the motional resistances, capacitances, inductances, the junction capacitance and the shunt resistance. The shunt resistance accounts for the leakage current across the depletion regions. $R_s$ is the series resistance accounting for the finite resistance of the semiconductor metal contacts. The $10\,nF$ capacitor is placed to block the DC bias the output of the amplifier. The amplifier is a charge sensitive amplifier consisting of a JFET at the input stage and a feedback resistance and capacitance $R_f$ and $C_f$ respectively. Their values are $300\,M\Omega$ and $1.5\,pF$ . . . . . 124

4.24 Harmonic response of the device at the fundamental, 1st and 2nd harmonic torsional modes. The x-axis is frequency and y-axis is impedance. The solid line is a fit to the modified BVD model and the dotted circles are the experimental results. The y-axis is determined by first converting the measured voltage to a current using the transfer function of the amplifier and then converting the current to impedance using the drive voltage . . . . . 126

5.1 $C_J^f$ and $C_m^f$ as a function of $V_{DC}$: (a) and (b) are the plot of equations (5.5) and (5.6). In general, the capacitances increases as $V_{DC}$ increases . . . . . 137

5.2 Comparison of $\frac{C_J^f(V_{DC})}{C_J^f(0)}$ and $\frac{C_m^f(V_{DC})}{C_m^f(0)}$ vs $V_{DC}$. The motional capacitance is lower than the junction capacitance for $V_{DC}$ below $0\,V$. Above $0\,V$ the motional capacitance is greater . . . . . 138

5.3 Comparison of $\left(\frac{C_J^f(0)}{C_J^f(V_{DC})}\right)^2$ and $\left(\frac{C_m^f(0)}{C_m^f(V_{DC})}\right)^2$. The two are linear lines indicating that both $C_J^f$ and $C_m^f$ varies as $\frac{1}{\sqrt{1-\left(\frac{V_{DC}}{V_{bi}}\right)}}$. This is the familiar diode capacitance relationship, equation(2.45), with respect to $V_{DC}$. The slope of the normalized $C_J^f$ is lower than $C_m^f$ . . . . . 138

5.4 $C_J^{2f}$ and $C_m^{2f}$ as a function of $V_{DC}$: (a) and (b) are the plot of equations (5.14) and (5.15). In general, the capacitances increases as $V_{DC}$ increases . . . . . 139

5.5 Comparison of $\frac{C_J^{2f}(V_{DC})}{C_J^{2f}(0)}$ and $\frac{C_m^{2f}(V_{DC})}{C_m^{2f}(0)}$ vs $V_{DC}$. The capacitance follow the similar trend, i.e the nomalized capacitance increases with $V_{DC}$ . . . . . 140

5.6 Comparison of $\left(\frac{C_J^{2f}(0)}{C_J^{2f}(V_{DC})}\right)^{\frac{2}{3}}$ and $\left(\frac{C_m^{2f}(0)}{C_m^{2f}(V_{DC})}\right)^{\frac{2}{3}}$. The two are linear lines indicating that both $C_J^f$ and $C_m^f$ varies as $\frac{1}{\sqrt{\left(1-\frac{V_{DC}}{V_{bi}}\right)^3}}$ . . . . . 140

5.7 $V_{AC}^{2f}\,vs\,V_{AC}^{f}$ Generated AC voltage at $2f$ as a result of an AC drive voltage at $f$. The $\frac{V_{AC,Drv}}{2.66}$ line is plotted for reference . . . . . 141

5.8 $I^f$ and $I^{2f}$. The motional current for the $f$ and $2f$ case. Generally, in both these plots the motional current increases as $V_{DC}$ increases. For the $2f$ this increase is larger. . . . . 142

5.9 Experimental setup used for frequency sweeping experiments both at $f$ and $2f$. The function generator drives the torsional oscillator and supplies the synchronization signal to the SR-830 Lock-in Amplifier. The experiment is controlled by the computer using labview. The data from the lock-in is saved for later processing . . . . . 143
5.10 Electrical Circuit of the two terminal device and amplifier Equivalent circuit with drive voltage, $V_{AC}$. The $1.0\,M\Omega$ to ground provides a DC path to ground and $R_{sh}$ is the shunt resistance . . . . . 144
5.11 Torsional Resonator IV curve measured using the semiconductor parameter analyzer - HP4145-B . . . . . 144
5.12 Resonance curve at$f$ and $2f$. (a) and (b) Current and Phase vs Frequency at $f$ (c) and (d) Current and Phase frequency at $2f$. The resonance and the anti-resonance peaks are switched between $f$ and $2f$ and a $\frac{\pi}{2}$ phase shift exists between the phase of $f$ and $2f$ . . . . . 145
5.13 Measured Noise. The solid line is drawn as a guide to the eye . . . . . 146
5.14 Motional current at $f$ and $2f$. These curves are acquired by subtracting the current contribution due to background impedances. (a) $f$ case: as $V_{DC}$ increases the motional current decreases. This is the opposite trend as seen in figure (5.8)(a), (b) $2f$ case: the motional current increases as $V_{DC}$ increases. This is exactly as predicted. The prediction is plotted in figure (5.8)(b) . . . . 147
5.15 Comparison of experimental and theoretical trends for $C_J^f$ and $C_m^f$ (a) $C_J^f$: trends of the experimental results agrees well with the theoretical predictions. For $V_{DC} > 0.4\,V$ a deviation is seen between the two. This deviation occurs because the turn-on voltage for the diode is approximately $0.45\,V$ and not the equivalent $1.6\,V$ used for the theoretical predictions (b)$C_m^f$: the trend of the experimental results is opposite from the theoretical predictions. This is also seen in figure (5.14) (a) . . . . . 149
5.16 Comparison of experimental and theoretical trends for $C_J^{2f}$ and $C_m^{2f}$ (a) $C_J^{2f}$: trends of the experimental results agrees well with the theoretical predictions. For $V_{DC} > 0.2\,V$ a deviation is seen between the two. The reason for the deviation is the same as discussed for the $C_J^f$ case. The early occurrence of the deviation however is due to the $\frac{1}{\sqrt{\left(1-\frac{V_{DC}}{V_{bi}}\right)^3}}$ term in the $2f$ case. The denominator becomes larger for smaller $V_{DC}$ (b)$C_m^{2f}$: the trends of the experimental results agrees well with the theoretical predictions . . . . . 150

6.1 Hale-Bopp Comet. The primary tail of the comet is in white and the secondary is in blue. This picture was taken in 1997 . . . . . 153
6.2 Photon Energy vs Absorption Coefficient. $GaAs$ data has been recreated from[7] and $In_{0.485}Ga_{0.515}P$[8] . . . . . 156

6.3 Heterostructure Band Diagram: The x-axis in this figure is thickness of the heterostructure and the y-axis is energy. The fermi-level, conduction and valence bands are indicated by the blue, black and red lines respectively. In the x-axis 0 thickness refers to the top of the $n+$ $GaAs$ layer in figure (4.4). The vertical lines in figure(6.3) roughly indicate the pn junction depleted region. As is seen from the figure at the $n^-$GaAs and $n^-In_{0.485}Ga_{0.515}P$ interface a barrier height is created for holes but not for electrons. At the $p^-In_{0.485}Ga_{0.515}P$ and $p^-$GaAs interface a barrier height is created for electrons and holes . . . . . 158
6.4 Equivalent circuit of Opto-Piezo Resonator. Here $i_{isc_1}$ and $I_{isc}$ are the AC photocurrent and DC short circuit photocurrent, $R_{sh,4}$ is the shunt resistance of the pn junction and $Z_{j,4}$ is the respective BVD circuit, figure (2.12), $R_{sh,2}$ and $R_{j,2}$ are the shunt and hole-pile up resistances associated with the depleted $p^-In_{0.485}Ga_{0.515}P$ layer, $Z_{j,2}$ is the BVD circuit related to the depleted $p^-In_{0.485}Ga_{0.515}P$-$GaAs$ heterojunction, $R_s$ is the series resistance and $i_{D,3} = I_{D,3} + i_{d,3}$ is the total current comprised of the superposition of DC and AC current, respectively. This is the current measured at the load branch of the AC PV circuit . . . . . 159
6.5 Ideal Opto-Piezo circuit. In this circuit the shunt and series resistances are ignored and the effects due to hole pile-up are also ignored . . . . . 161
6.6 $i_{d,3}$ for the ideal circuit given in figure 6.5. The x-axis is frequency. $i_{d,3}$ is determined using equation (2.67) for the range of capacitive loads gives in the legend. The resonance and anti-resonance peaks are switched. The lowest current is at the resonance frequency while the highest current is at the anti-resonance frequency. This is expected because at resonance the impedance of the $Z_{j,4}$ branch is the lowest and hence most of the current flows through that branch. In anti-resonance the impedance of the $Z_{j,4}$ branch is the highest and hence most of the current flows through the load branch . . . . . 162
6.7 Background subtracted $i_{d,3}$. The current contributions to $i_{d,3}$ from the junction and load capacitances are subtracted from $i_{d,3}$. The remaining current is the motional current. This plot elucidates the idea of impedance matching. The largest current in the load branch occurs when $C_L = C_J = 55\,pF$ . . . . . 162
6.8 $i_{d,3}$ for the non-ideal case. $i_{d,3}$ is determined using equation (2.67) and the circuit in figure (6.4). In these plots the x-axis is frequency. (a), (b) and (c) are generated for $R_{j,2}$ having values of 1, 10 and $100\,k\Omega$ respectively. The following can be observed: as $R_{j,,2}$ is increased from (a) to (c) the contribution of $Z_{j,2}$ to $i_{d,3}$ increases. In (a) the contribution of $Z_{j,2}$ to $i_{d,3}$ can be ignored.In figures (b) and (c) as $C_{m,2}$ increases $i_{d,3}$ initially decreases till a cross-over point is reached where the contribution due to $Z_{j,2}$ becomes prevalent. In this case the current at resonance is larger than at anti-resonance. This is similar to what is observed for the optical driven QTF, figure(3.22)(a). In (c) as $C_{m,2}$ increases a splitting is observed between the two resonances resulting in a symmetric and anti-symmetric modes . . . . . 164

6.9 $\theta$ for the non-ideal case. In these plots the x-axis is frequency. (a), (b) and (c) are generated for $R_{j,2}$ having values of 1, 10 and 100 $k\Omega$ respectively. The following can be observed: as $R_{j,,2}$ is increased from (a) to (c) the contribution of $Z_{j,2}$ to $\theta$ increases. In (a) the contribution of $Z_{j,2}$ to $\theta$ can be ignored. In figures (b) and (c) as $C_{m,2}$ increases a cross-over point is reached where the contribution due to $Z_{j,2}$ becomes prevalent. In this case a second peak in (b) and (c) is seen . . . . . 165
6.10 $\frac{i_{d,3}}{i_{isc_1}}$ vs $V_{DC}$. $i_{isc_1}$is defined as the current at $V_{DC} = -0.5\,V$. This plot was generated using equation (6.1). As $V_{DC}$ increases the normalized current, $\frac{i_{d,3}}{i_{isc_1}}$ decreases . . . . . 166
6.11 $\frac{i_{d,3}}{i_{isc_1}}$ vs $V_{DC}$. $i_{isc_1}$is defined as the current at $V_{DC} = -0.5\,V$. This plot was generated using equation (6.1). As $V_{DC}$ increases the normalized current, $\frac{i_{d,3}}{i_{isc_1}}$ decreases. Finite $R_{j,2}$ is considered such that the voltage drop across $Z_{j,4}$ decreases. In these plots a voltage drop of 75% and 50% is considered. For a 50% voltage drop the normalized current is higher than for a 75% voltage drop 166
6.12 Block diagram of the experimental setup used to measure opto-piezo actuation. The HP-3352B supplies the DC and AC voltage required to bias and modulate the LED. This light is incident on the torsional resonator. The DC bias for the torsional resonator is supplied by the HP-3245A. $C_L$ is the load capacitor serving the purpose of a DC block and an AC load for the torsional resonator. The current, $i_{d,3}$, generated is amplified by the Amptek A-250. The output of the A-250 is connected to the SR-830 lock-in amplifier. The lock-in is synchronized to the HP-3352B. The data from the lock-in is collected on a computer. The arrows in the diagram indicate light is being emitted from the LED onto the torsional resonator. The dotted blue lines indicate the components held in vacuum. A vacuum pressure of $\sim 2\,mTorr$ is achieved . . . . . 167
6.13 Opto-Piezo resonator circuit used for measuring $i_{d,3}$. The opto-piezo resonator is represented by the photo-diode and the amplifier circuit is represented by the box labeled A-250. The amplifier circuit was discussed in chapter 4. The bias voltage to photodiode is supplied via $R_L$ . . . . . 168
6.14 LED Power: (a) LED illuminated power measured using 818-BB-20, (b) LED illuminated power incident on the opto-piezo device. The values in this plot are determined mathematically, i.e. taking the ratio of the absorption area of the opto-piezo resonator to the area of the 818-BB-20. The illuminated area of the 818-BB-20 is approximately $1.3 \times 10^{-7}\,m^2$ while the illuminated area of the opto-piezo resonator is approximately $2.1 \times 10^{-8}\,m^2$. The 818-BB-20 and opto-piezo device are placed 0.5 cm away from the LED . . . . . 169
6.15 Diode IV Curves for an incident powers of 0.3, 1.61 and 4.84 $\mu W$. As the optical power increases the optically generated current also increases . . . . . 170
6.16 $i_{d,3}$ measured noise. The solid line is drawn as a guide to the eye . . . . . 172

6.17 Optically driven torsional resonator for $P_{opt} = 304\,nW$ and $p_{opt} = 21\,nW$(a) $i_{d,3}\,vs\,Frequency$ The theoretical prediction is made using equation (2.67) and the circuit in figure (6.4) (b) $\vartheta\,vs\,frequency$ The theoretical prediction is made determined by calculating the arctan of the ratio of the imaginary and real part of $i_{d,3}$. In general for both good agreement is seen between the theoretical predictions and the measured response . . . . . 173
6.18 Optimal $C_L$ for impedance matching. The measured motional current is plotted for a $C_L$ of 222, 140 and $38\,pF$. As is seen from the figure the maximum resonance or motional current occurs for a load of $222\,pF$ . The motional current is determined by subtracting the background $i_{d,3}$ current from the total $i_{d,3}$. The total $i_{d,3}$ is a superposition of motional and background currents. The variation in the motional current at resonance is attributed to thermal drifts. The dotted line is drawn as a guide to the eye. . . . . 174
6.19 Normalized $i_{d,3}$ vs $p_{opt}$. Here $i_{d,3}$ is normalized to the value of $i_{d,3}$ at $2\,nW$. According to equation (2.67) $i_{d,3}$ should increase linearly with an increase in $i_{isc_1}$. $i_{isc_1}$ increases linearly with $p_{opt}$ therefore $i_{d,3}$ increases linearly with $p_{opt}$. This linear increase with $p_{opt}$ is seen. The theoretical predicted line is generated using equation (2.67) . . . . . 174
6.20 $\frac{i_{d,3}(V_{DC})}{i_{d,3}(-0.5)}$ vs $V_{DC}$ for $C_L = 222\,pF$. The measurement is made for an incident $P_{opt}$ and $p_{opt}$ of $304\,nW$ and $21\,nW$. $i_{d,3}$ is normalized to the value of $i_{d,3}$ for a $V_{DC} = -0.5\,V$. The theoretical line is also plotted. The prediction of $i_{d,3}$ using equation (2.67) is also normalized to the value of $i_{d,3}$ for a $V_{DC} = -0.5\,V$. Good agreement is seen between the experimental data and the predicted results. The variation in the data is attributed to thermal drifts. Each of the dots are an average of 5 measurement and the error bars are a result of this average. . . . . 175
6.21 Background subtracted $i_{d,3}$ for a $V_{DC}$ of $-0.5$, 0.0 and $0.5\,V$. As is seen from the plot and figure (6.20) as $V_{DC}$ increases from reverse to forward bias the normalized current decreases. The dotted line is drawn as a guide to the eye . 176
6.22 $\frac{i_{d,3}(V_{DC})}{i_{d,3}(-0.5)}$ vs $V_{DC}$ for $C_L = 144\,pF$. The measurement is made for an incident $P_{opt}$ and $p_{opt}$ of $304\,nW$ and $21\,nW$. $i_{d,3}$ is normalized to the value of $i_{d,3}$ for a $V_{DC} = -0.5\,V$. The theoretical line is also plotted. The prediction of $i_{d,3}$ using equation (2.67) is also normalized to the value of $i_{d,3}$ for a $V_{DC} = -0.5\,V$. Good agreement is seen between the experimental data and the predicted results. The variation in the data is attributed to thermal drifts. Each of the dots are an average of 5 measurement and the error bars are a result of this average. . . . . 176
6.23 Circular disk with an radius $r$ and a thickness $d$. This resonator vibrates contracts and expands parallel to the thickness direction . . . . . 177

6.24 $\kappa_x^2 \, vs \, P_0$ at $f = 10\,Hz$ for a disk having the same area and thickness of (a) $d = 400\,\mu m$ and (b) $d = 400\,nm$. The subscript $x$ in $\kappa_x^2$ represents the three cases - photothermal, radiation pressure and opto-piezo. Equations (6.3), (6.4) and (6.5) are used for generating the three cases. In general, $\kappa_{opz}^2$ is several orders of magnitude larger than $\kappa_{pt}^2$ and $\kappa_{rp}^2$. The power required for $\kappa_{pt}^2$ to become equivalent to $\kappa_{opz}^2$ is approximately $3\,MW$ for a disk having a thickness of $400\,nm$, figure (6.24)(b), while for a disk having a thickness of $400\,\mu m$, figure (6.24)(a), the power required is approximately $3\,KW$. This reduction in power with an increase in thickness is expected because thicker materials have a larger thermal gradient and hence a larger force. $\kappa_{rp}^2$ does not become equivalent to $\kappa_{opz}^2$. At most $\kappa_{rp}^2$ can be equivalent to $\frac{v}{c}$. This is because because physically the upper limit to the motion of the resonator is its sound velocity. The powers required for $\kappa_{rp}^2$ to reach the $\frac{v}{c}$ condition are approximately $1 \times 10^{21}\,W$ and $1.0 \times 10^{24}\,W$ for the disk having thicknesses of $400\,\mu m$ and $400\,nm$ respectively . . . . . 182

6.25 Plot of frequency roll-off, $\kappa_x^2 \, vs \, f$, for $P_0 = 1\,mW$ and $Q = 1$ for a disk having the same area but with thicknesses, $d$, of (a) $400\,\mu m$ and (b) $400\,nm$ respectively. Equations (6.3), (6.4) and (6.5) are used for generating the three cases. As $d$ decreases the roll off frequency increases. This is expected because as the thickness decreases $w_r$ increases. Both $\kappa_{rd}^2$ and $\kappa_{opz}^2$ have similar frequency roll off while $\kappa_{pt}^2$ frequency roll off is approximately thousand times lower. This earlier roll-off is due to the thermal time constant and is approximated as $\tau = \frac{\rho V c_p}{k}$ where $V$ and $k$ are the volume and thermal conductivity of the material. Therefore as seen from this approximation and the plots the roll off frequency increases approximately linearly as the volume decreases . . . . . 183

6.26 Illustration of the architecture of a deformable Optical Correlator (OC) on a PIC. The individual devices in this circuit are connected by waveguides. The circle in the figure is a bi-directional coupler. The structure containing the Bragg grating is released during fabrication thereby allowing for the gratings to deform. The opto-piezo effect is used to deform the gratings. Gratings are used because of their wavelength selectivity. Deforming the gratings away from the designed wavelength results in a "0" signal corresponding to no reflection while the "1" signal corresponds to reflection resulting from the undeformed grating. The electronic processing compares the output of the photodetector to a set threshold hence determining the existence of a pattern. An illustration of this is shown in figure (6.27). . . . . 187

6.27 Operation of the deformable Optical Correlator (OC). The input signal, for example, consists of the 1101 pattern. To create this pattern on the Bragg gratings only the third grating from the left is deformed via the opto-piezo effect . . . . . 188

6.28 Illustration of an Optical Clock Signal Generator (OCSG). The gain medium is the source of light and the bridge structure is free to deform. The gain and the bridge structure are connected by a waveguide. The materials used for both are $GaAs$. The waveguide is the depletion region of the PN junction. The inspiration for this design is taken form the electrical Colpitt oscillator circuit which is used to generate clock pulses in an IC[9] . . . . . 189

7.1 Arrow structure. This structure, called arrow, is similar to the Y-structure presented in chapter(4). In the arrow structure the tines are in the opposite direction to the Y tines . . . . . 195

7.2 Square resonator. (a) Mode shape of the resonator. Adjacent sides of the resonator flexurally deform in the opposite direction. The middle of the resonator does not deform. (b) Three terminal setup for the square resonator. The green sections is $p$ doped and runs across the midpoint of the resonator. This separates the two $n^+$ regions. Hence one of the $n^+$ regions can be used to drive the device while the other can be used to detect. This results in lowering the package capacitance . . . . . 196

# List of Tables


2.1 Mechanical-Electrical Analogy . . . . . 11
2.2 Roots of equation(2.23) . . . . . 16
2.3 Classification of $Q$ . . . . . 18
2.4 AC and DC comparison of voltage at the maximum power point. The values are determined graphically. The subscript $mp$ stands for maximum power point. $\Delta V_{mp} = V_{mp}^{DC} - V_{mp}^{AC}$ . . . . . 55
2.5 DC and AC maximum power point.$V_{mp}^{DC}$is approximated to $V_{oc}$. The same definition as used in table 2.4 is carried over . . . . . 58
2.6 Physics used and the objectives for the respective chapters . . . . . 62

3.1 HP-4145B Current Error recreated from HP-4145B Operation Manual . . . . 64
3.2 Measured $I_{isc}$ and $V_{oc}$ for the respective measured incident optical power. $\Delta P_{opt}$ and $\Delta I_{isc}$ are the measured uncertainties in $P_{opt}$ and $I_{isc}$. $\Delta V_{oc}$ is assumed to be small and hence ignored. . . . . 66
3.3 Values for $R_{sh}$, $R_s$ and $\eta$ for the respective incident optical power. These values are determined by fitting equation (2.49) to measured $I_{D,3}$. $\Delta R_{sh}$, $\Delta R_s$ and $\Delta\eta$ are the error in the fits . . . . . 67
3.4 818-BB-20 measured $I_{isc}$, $V_{oc}$ and $i_{isc_1}$ for the incident DC and AC optical powers - $P_{opt}$ and $p_{opt}$. $\Delta P_{opt}$, $\Delta I_{isc}$ and $\Delta p_{opt}$ are the measured uncertainties in $P_{opt}$, $I_{isc}$ and $p_{opt}$. Both $\Delta V_{oc}$ and $\Delta i_{isc_1}$ are assumed to be small and hence ignored. The justification for ignoring $\Delta i_{isc_1}$ is given below. Notice the DC and AC optical powers used vary by an order of magnitude . . . . . 86
3.5 818-BB-20 values for $R_{sh}$, $R_s$, $\eta$ are determined from fitting the IV curves to equation (2.49).$C_J$ is measured using AH. $\Delta R_{sh}$, $\Delta R_s$ and $\Delta\eta$ are the errors in the fitting to the mentioned equation. $\Delta C_J$ is small and hence ignored . . 86

4.1 Layers comprising the heterostructure, doping type, concentration, thickness and purpose . . . . . 97
4.2 Y resonator dimensions, mode number, resonant frequency and Q. The increasing mode numbers corresponds to the fundamental symmetric and the fundamental anti-symmetric and 1st harmonic anti-symmetric modes. In general, increasing the pad length results in decreasing the frequencies of the torsional modes and increasing the spine length results in decreasing the frequency of all the modes . . . . . 102
4.3 Table of constant for $GaAs$ and $In_{0.485}Ga_{0.515}P$ . . . . . 110

4.4 Comparison of Experimental Results and Theoretical predictions for the three Torsional modes for a resonator with a tine length of $80.0\mu m$: (a) Symmetric Torsional Mode, (b) 1st Anti-Symmetric Torsional Mode, (c) 2nd Anti-Symmetric Torsional Mode . . . . . 125
4.5 Piezoelectric matrix for $LiNbO_3$ [10], $SiO_2$ [11] and $PZT$ [12] . . . . . 127

6.1 Comparison of photostrictive properties of different compounds . . . . . 154
6.2 Measured $I_{isc}$ and $V_{oc}$ for the respective incident powers. $\Delta P_{opt}$ and $\Delta I_{isc}$ are the measured uncertainties in $P_{opt}$ and $I_{isc}$. $\Delta V_{oc}$ is assumed to be small and hence ignored . . . . . 171
6.3 Values for $R_{sh}$, $R_s$ and $\eta$ for the respective incident optical powers. These values are determined by fitting equation (2.49) to measured $I_{D,3}$. $\Delta R_{sh}$, $\Delta R_s$ and $\Delta\eta$ are the errors in the fit . . . . . 171
6.4 Opto-Mechanical coupling coefficient for the photothermal, radiation pressure and the opto-piezo cases . . . . . 181
6.5 Table of constants used for the calculations. The material parameters chosen are for $GaAs$ . . . . . 184

# Chapter 1

# Introduction

In this thesis, the opto-electro-mechanical and electro-mechanical coupling in a $GaAs$ photodiode hetreostructure is experimentally and theoretically verified. The results of these couplings are:

1. Optical and electrical actuation of a mechanical structure
2. Electrical measurements of the deformation of the structure
3. Ability to tune or vary the amount of mechanical deformation by varying the capacitance of the photodiode heterostructure

These couplings occur because $GaAs$, and in general III-V materials, are semiconductor materials that also have piezoelectric properties. Silicon and germanium are examples of semiconductor materials that do not have piezoelectric properties and hence do not exhibit this coupling.

To demonstrate the aforementioned couplings a micromechanical torsional resonator is fabricated from the heterostructure which is epitaxially grown on a $GaAs$ substrate. This is made possible because of:

1. knowledge of $GaAs$ and in general III-V materials electrical, optical, mechanical and piezoelectric properties
2. development of $GaAs$ and in general III-V materials processing technology

First a brief historical overview is given on the development of $GaAs$ technology. $GaAs$ is discussed because it is the substrate used in this work and heterostructures are epitaxially grown on the substrate. The aim of the historical overview is to indicate the key technological developments in $GaAs$ that made this work possible. For an extensive review please see[13, 14, 15]. This overview is then followed by a brief history on the discovery of piezoelectricity in general and then specifically in $GaAs$. Following this, the motivation for the work presented in the thesis is discussed and finally the chapter concludes with the layout of the chapters comprising the thesis. An in depth literature review will be provided in each of the subsequent chapters.

## 1.1 Development of $GaAs$ technology

Historically the motivation for developing semiconductor devices made from $GaAs$ and its compounds were to utilize their high electron mobilities and their high efficient light emitting properties; two material characteristics that do not exist in silicon. The electron mobility in $GaAs$ is an order of magnitude larger than in silicon and unlike silicon $GaAs$ is a direct band gap material. The high electron mobility is a requirement for making electronic devices, like radio frequency diodes, high electron mobility transistors (HEMT) etc that are used in high frequency applications. The direct band gap property is a requirement for making high efficiency solid state light sources like light emitting diodes (LED) and laser diodes (LD).

By 1953 the material properties of $GaAs$ and III-V compounds were reported by Welker[16] . Shortly after this, various transistors and diode device designs were proposed. Parallel to the development of electronic devices, from 1958 - 1961[17, 18, 19, 20] several photonic device designs using semiconductors as visible light sources were also proposed and developed.

The initial success for $GaAs$ electronic devices occurred in 1961 with the demonstration of a $GaAs$ bipolar transistor with performance superior to silicon[21]. By 1962 a visible LED made from $GaAs$ substrate was also demonstrated[22]. These were laboratory successes and many more continued. However commercial success was delayed by over a decade. The reasons for this are:

1. lack of knowledge on growing low defect density $GaAs$ substrates. The poor quality of substrates made it difficult to make devices having homogeneous electronic or photonic characteristics

2. invention of epitaxial growth technologies like molecular beam epitaxy (MBE), molecular organic chemical vapor deposition (MOCVD) etc. Such growth technologies are required for making electronic and optical devices through various heterostructure designs

Each of these are briefly discussed next.

### 1.1.1 Substrate development

In 1956 Gremmelmeier[23] used the Czochralski technique to grow single crystal $GaAs$. The technique was successful for growing single crystals but the yield was poor. This technique could not be used to make large substrates and the grown wafers were not circular. In 1965, Mullin et al.[24] applied the liquid-encapsulated Czochralski (LEC) technique to grow $GaAs$ crystals. This approach allows the growth of very low defect density crystals. To this day LEC is used to grow 2- and 3-in circular $GaAs$ wafers that are routinely processed by companies for making LEDs, HEMT, LDs etc. Prior to 1981, substrates of these diameters were not commercially available. In contrast, low defect density single crystalline silicon wafers were available in 1950. This was possible because it is easier to grow and purify a single element material. The early availability of high quality single crystal wafers is one of the many reasons for the dominance of silicon.

### 1.1.2 Epitaxy

By late 1960s MBE was developed by Arthur and Cho[25, 26]. This allowed for growing epitaxial layers with lower defect densities than the substrate. Additionally, using MBE thicknesses of the grown layers could also be controlled with atomic resolution. The MBE technique allowed for the implementation of device designs from the 1950s requiring heterostructure designs having numerous epitaxial layers and tight control on thickness of the grown layers. Using the MBE by 1974, Cho and Casey[27] fabricated $GaAs$-$AlGaAs$ double heterostructure lasers and in 1976 Cho and Ch'en[27] reported the fabrication of a $GaAs$ power FET.

## 1.2 Piezoelectricity

Piezoelectricity was discovered by brothers Pierre and Jacques Curie in 1880[28]. However, this did not happen randomly. In India and Ceylon the mysterious behavior of tourmalins was well-known. It was noticed if tourmalins were put into hot ash, at one side they attracted ash particles while at the opposite side they were rejected. After some time the effect of attraction and rejection inverted. At the beginning of the 18th century traders brought the tourmalin crystals to Europe. In 1747, Linne called the tourmalin crystals lapis electricus[3]. In the following century, researchers attempted to find a connection between the mechanical pressure effect and the electricity. Becquerel was aware of the fact, that such an effect could be expected with crystals. In 1877, Lord Kelvin established the correlation between pyroelectricity and piezoelectricity[3]. It was verified that the pyroelectric charge of the tourmalin is ascribed to the formation of piezoelectric surface charge caused by the elastic crystal deformation under temperature changes. The brothers Pierre and Jacques Curie discovered the direct piezoelectric effect in tourmalin crystals. They recognized that a mechanical deformation in certain directions causes opposite electrical surface charges at opposite crystal faces being proportional to the mechanical deformation. This effect, also found in quartz and other crystals without symmetry center, has been called piezoelectric effect (Greek: piezein = press)[3]. The inverse piezoelectric effect predicted by Lippmann[11] based on thermodynamic considerations was confirmed experimentally by the Curie brothers.

Common naturally occurring piezoelectric materials are $\alpha$-quartz, bone, silk, dentin etc. Man-made piezoelectric materials include Gallium Orthophosphate, Langasite, ceramics such as: Barrium Titanate ($BaTiO_3$), Lead Titanate ($PbTiO_3$), Lead Ziconate Titanate (PZT) etc. A common property of these materials, other than piezoelectricity, is their high resistivities; ranging from $1.0 \times 10^9 - 1.0 \times 10^{16}\Omega - cm$. In fact, having high resistivity is almost a requirement for detectable piezoelectric charge.

One of the common uses of piezoelectric materials is as a mechanical resonator for time keeping. The common choice of material used is quartz because it has high Q[1] and AT-cut quartz leads to frequency stability from $-65^0C$ to $100^0C$[29]. In addition for time keeping applications resonators are also found in:

1. computers and measuring equipment such as oscilloscopes, lock-in amplifiers, spectrum analyzers, vector network analyzers etc. In these equipment, the resonator provides a

[1] Q is a metric indicating the loss in a resonator. A low loss resonator, high Q, rings for a longer time when struck than a high loss resonator, low Q.

clock signal required to synchronize the operations from different parts of the integrated circuit and to provide clock pulses required to perform logical operations

2. telecommunication equipment such as modulators. The role of the resonator is to provide a clock pulse at a certain frequency which can then be multiplied with the desired signal converting the signal from DC to AC or vice-versa and for shifting frequencies of an AC signal

### 1.2.1 Piezoelectricity in $GaAs$

In 1946 Cady[30] published a paper in which theoretical predictions for the non-zero piezoelectric coefficient for all the 32 crystal classes were given. This work showed that materials having the zinc-blende crystal structure, such as $GaAs$, have non-zero longitudinal piezoelectric coefficient.

In 1961 White[31] qualitatively demonstrated the piezoelectric effect in $GaAs$. The motivation for this work was to develop high frequency transducers for ultrasonic applications. White was able to generate and detect longitudinal plane waves having frequencies of 500 MHz - 1.0 GHz. In 1968 Arlt et al[32] measured the piezoelectric constant in $GaAs$ and derived a model to explain their results.

It wasn't until 1993 that Hjort et al[1] demonstrated the use of $GaAs$ as a piezoelectric mechanical resonator. They made a tuning fork from a $GaAs$ semi-insulating substrate. This substrate was used to ensure that the semiconducting nature of $GaAs$ does not affect the performance of the fabricated resonator. In 1994 Hjort[33] published a paper titled $GaAs$ as a mechanical material. This paper reviewed the structural, piezoelectric and piezooptic properties of $GaAs$. The conclusions from this paper are:

1. Micromechanical structures that are possible to machine in silicon are also possible to machine in $GaAs$

2. $GaAs$ fracture toughness in one half that of silicon - this is because of the increased number of defect densities. The average fracture strength is 2.7 GPa which is still three times higher than that of construction steel

3. Piezoelectric effect in $GaAs$ is comparable to Quartz but lacks the temperature stability of Quartz

4. Given the high cost of $GaAs$ wafers the author suggests that $GaAs$ resonators should be used in applications that are unique to $GaAs$ material properties

## 1.3 Motivation

As discussed in the above sections $GaAs$, and III-V materials in general, have mechanical, electrical and optical degrees of freedom. Using these degrees of freedom and $GaAs$'s established growth and fabrication technologies, in this thesis, optical and electrical actuation of a torsional resonator is demonstrated. The motivations for this are:

1. to exploit the couplings in: (1) the optical and mechanical degrees of freedom and (2) the optical, electrical and mechanical degrees of freedom for the purpose of designing and building devices. In order to exploit these couplings they first have to be explored. This is because the couplings, although predicted from theory, have not been verified. Therefore this is done here. The couplings result in optical actuation, called opto-piezo actuation, arising from the photovoltaic and piezoelectric effect, and the ability to tune the amount of deflection from an incident light

2. to exploit the non-linear coupling between the electrical and mechanical degrees of freedom for the purpose of designing and building devices. Similar to the above couplings the non-linear coupling between the electrical and mechanical degrees of freedom have not been explored. Thus this is done here. The non-linear coupling results in electrical actuation of the torsional resonator using harmonics of the applied AC potential. The linear part of this coupling has been verified in other works[34]

These are important because:

1. a semiconductor material having piezoelectric properties can lead to the integration of ICs and mechanical resonators. The problem here is these discrete components are made from materials that have incompatible fabrication processes. ICs, found in computers, smart devices etc, are made form silicon while mechanical resonators, also found in computers, smart devices etc, are made from quartz. These ICs perform logic operations while the resonators are used to supply clock pulses which synchronizes the logic operations. The advantages of integrating the two are cost and performance. Cost becomes low because in discrete devices material is wasted while performance is higher because the components switch quickly and consume less power as a result of small size and close proximity. This integration issue can be alleviated using III-V materials because both logic circuits and clock sources can be integrated on a single IC. In fact; logic circuits have previously been demonstrated in $GaAs$[14, 35]. A demonstration of this is the Cray-3 supercomputer which used ICs made from $GaAs$. The technology did not flourish because the company went bankrupt. The primary reason for bankruptcy was not technological but political[36]

2. using the opto-piezo actuation photonic devices having mechanical degrees of freedom can be made. An example of such a device is an adaptable optical correlator which can be the main information processing element in a photonic processor. The function of such a processor is to process data, at the hardware level, by correlating the data set to known patterns. In addition to correlating to known patterns an adaptable processor will allow, again at the hardware level, to also correlate the data set to unknown patterns. This adaptability allows one to make an artificial intelligent machine based on the idea of a Perceptron[37]. In the optical correlator device the opto-piezo effect is used for deforming the components making up the optical correlator. For such types of applications processing with light is preferred because light offers larger bandwidth leading to higher data capacities and the speed of light is the ultimate speed for transferring and processing of information. $GaAs$, and III-V materials in general, are the preferred choice of materials for making these optical processors because of the

maturity in technology for making optical sources, detectors and monolithic microwave integrated circuit (MMIC) and they exhibit the opto-piezo effect.

## 1.4 Thesis Overview

Chapters 2 and 3 are the background chapters. In chapter 2 the theoretical foundations required to understand the work are discussed. In chapter 3 the experimental validation of a theoretical model describing the AC response of a photovoltaic cell derived in chapter 2 is presented. This chapter is considered part of the background because it presents the experimental validation of the derived model in all the domains of operation. In a later chapter the AC response model is used only in a single domain to verify experimental results. In chapter 4 the design of a heterostructure used for the fabrication of a torsional resonator is presented. Using the design of the heterostructure an analytical model is derived predicting the expected piezoelectric charge for three torsional modes. The predicted charge is compared to experimental results. In chapter 5 the analytical model developed in chapter 4 is extended to include the electro-mechanical coupling in the linear and non-linear regimes. The predictions are compared to experimental results. In chapter 6 the opto-electro-mechanical coupling is experimentally demonstrated and verified using the analytical model derived in chapter 2 and experimentally verified in chapter 3. Chapter 7 concludes the thesis and presents some ideas that could be explored in the future.

# Chapter 2

# Background

In this chapter a brief discussion on the physics of resonators, flexural deformations, piezoelectricity and semiconductor junctions is given. Using these as the ingredients, electro-opto-mechanical devices are designed and the measured response resulting from electrical and optical excitation are validated. This is presented in chapters(4)-(6). In addition to discussing the physics of the aforementioned topics, a theoretical model is derived in the semiconductor section describing the operation of a solar cell to modulated light. This model is given the name AC PV.

## 2.1 Resonator

A resonator is defined as a mechanical, electrical, optical etc system having natural modes of vibration. The mathematical analysis of a resonator is done using the concept of free oscillation. In free oscillation the response of the resonator is studied as a result of an applied initial impulse. The result of this response is the resonator's natural modes of vibration or its resonance frequencies. An example of such a system in the mechanical domain is mass on a spring, figure (2.1). The equation of motion describing the system is[38]:

$$\ddot{x} + 2\gamma\dot{x} + w_0^2 x = 0$$

where $x$ is the displacement, $\gamma = \frac{c}{2m}$ is the damping factor, $w_0 = \sqrt{\frac{k}{m}}$ is the frequency of oscillation for the system, $c$ is the damping term, $k$ is the spring constant and $m$ is the mass of the system. The solution to this equation is:

$$x(t) = A_1 exp(-(\gamma - q)t) + A_2 exp(-(\gamma + q)t) \tag{2.1}$$

where $q = \sqrt{(\gamma^2 - w_0^2)}$

The solution yields three possible scenarios:

1. Underdamped: $q = imaginary$, i.e. the resonance frequency is greater than the damping factor. A mass given some initial displacement will move in an oscillatory motion. The number of oscillations depend on $\gamma$. The mathematical function describing the resulting motion is: $x(t) = Aexp(-\gamma t)cos(wt + \phi)$. This motion is depicted in figure (2.2) for $\gamma = 0$ and 0.1. The figure is a plot of the normalized motion of the

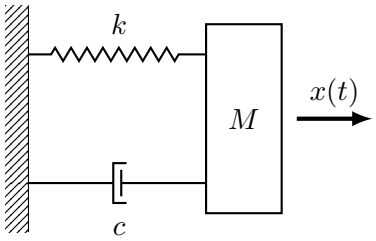


Figure 2.1: Mass-Spring System $M$ is the mass, $k$ is the spring constant and $c$ is the damping term

resonator with respect to time. The $\gamma = 0$ case is a case of zero damping and results in constant oscillations with respect to time. The $\gamma = 0.1$ case is a case of some damping and results in loss of oscillation amplitude with respect to time given by $exp\,(-\gamma t)$. Another method for characterizing this loss is using the quality factor $Q$. Mathematically $Q$ is defined as the ratio of the energy stored in the oscillator to the energy lost in a single period of oscillation. Using this definition $Q$ is: $Q = \frac{w_0}{2\gamma}$[38].

2. Critical Damping: $q = 0$, i.e. the resonance frequency is equivalent to the damping factor. A mass given some initial displacement does not oscillate and returns to equilibrium asymptotically. The mathematical function describing the resulting motion is: $x\,(t) = Atexp\,(-\gamma t) + Bexp\,(-\gamma t)$. This motion is depicted in figure (2.2) for $\gamma = 1.0$

3. Overdamped: $q > 0$, i.e. the resonance frequency is smaller than the damping factor. Similar to the critical damping case a mass released from rest returns to equilibrium but unlike that case takes a longer time to reach equilibrium. The mathematical function describing the resulting motion is equation (2.1) with two different decay constants $(\gamma - q)$ and $(\gamma + q)$. This motion is depicted in figure (2.2) for the $\gamma = 2.0$ curve

### 2.1.1 Forced Harmonic Motion: Resonance

A resonator driven by a force is called an oscillator[38]. The equation of motion for an oscillator is[38]:

$$\ddot{x} + 2\gamma\dot{x} + w_0^2 x = F_0 cos\,(wt) \tag{2.2}$$

Here $F_0$ is the applied force at frequency $w$. The amplitude and phase of oscillation are[38]:

$$A\,(w) = \frac{F_0}{m\sqrt{\left(w_0^2 - w^2\right)^2 + 4\gamma^2 w^2}} \tag{2.3}$$

$$tan\,(\phi) = \frac{2\gamma w}{w_0^2 - w^2} \tag{2.4}$$

The above equations are solutions to (2.2). The amplitude of oscillation at resonance is: $A_{max} = \frac{F_0}{2\gamma m\sqrt{w_0^2 - \gamma^2}}$. In the case of weak damping: $A_{max} = \frac{F_0}{2\gamma m w_0}$. Equations (2.3) and

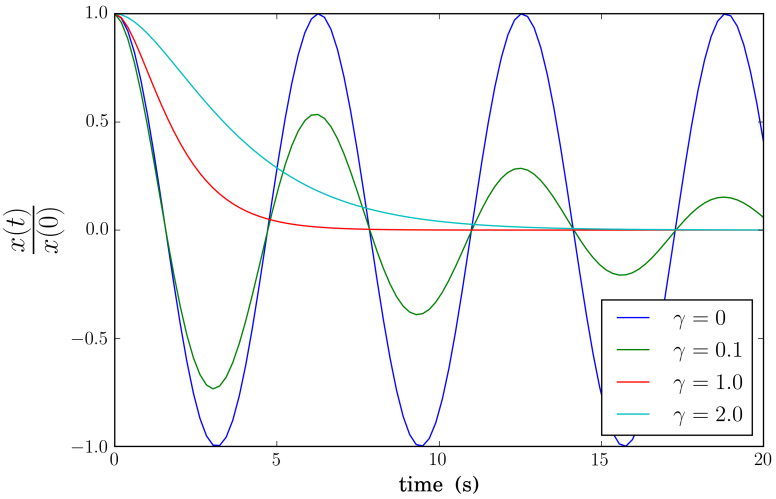


Figure 2.2: Graph of normalized displacement vs time for underdamped $\gamma = 0$ and 0.1, critically damped, $\gamma = 1.0$ and overdamped,$\gamma = 2.0$ cases

(2.4) are plotted in figures(2.3) (a) and (b). The x-axis in both figures is $\frac{w}{w_0}$, i.e. applied frequency divided by resonance frequency, while the y-axis in (a) is the amplitude response of the system and in (b) is the normalized phase response of the system. The solution yields three possible scenarios with respect to the driving frequency:

1. Low frequencies $w << w_0$, $\phi = 0$. The displacement of the resonator is in phase with the driving force, i.e. $\phi = 0$. This can be seen from figure (2.3)(b) for $\frac{w}{w_0} < 1$. The amplitude of the displacement results from the spring constant of the oscillator, i.e $A\,(w \to 0) = \frac{F_0}{k}$. Physically; the motion results from a mass slowly pushed back and forth by a force acting against the retarding force of the spring

2. Resonance, $w = w_0$, $\phi = \pm\frac{\pi}{2}$. The displacement of the resonator is $\pm\frac{\pi}{2}$ out of phase with the driving force. This can be seen from (2.3)(b) at $\frac{w}{w_0} = 1$. At resonance the applied force is in phase with the velocity which results in large amplitudes. The amplitude is dependent on $\gamma$ as shown in figure (2.3)(a)

3. Large frequencies: $w >> w_0$, $\phi \to \pi$. The displacement of the resonator is $\pm\pi$ out of phase with the driving force. This can be seen from figure (2.3)(b) for $\frac{w}{w_0} > 1$. The amplitude of the displacement is $A\,(w >> w_0) = \frac{F_0}{mw^2}$ and results from the mass and the applied frequency. The amplitude falls off as $\frac{1}{w^2}$. Physically; the mass responds essentially like a free object, being rapidly shaken back and forth by the applied force. The main effect of the spring is to cause the displacement to lag behind the driving force by $\pm\pi$

   Using figure (2.3)(a) the $Q$ can be determined using[38]:

$$Q = \frac{f_r}{\Delta f} \tag{2.5}$$

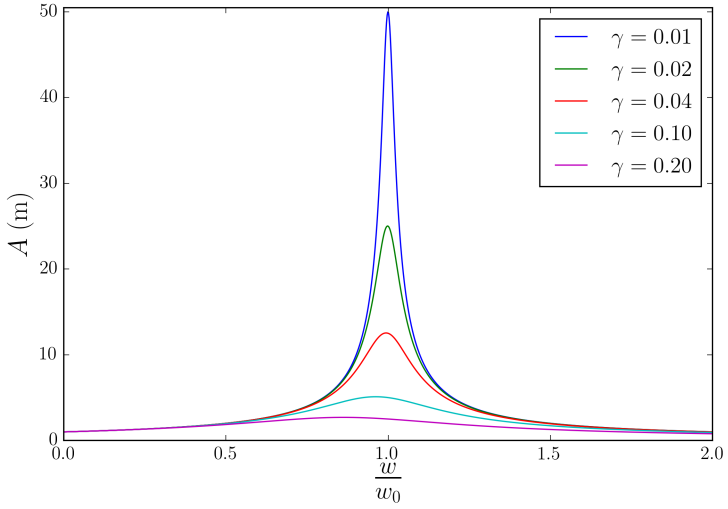


(a)

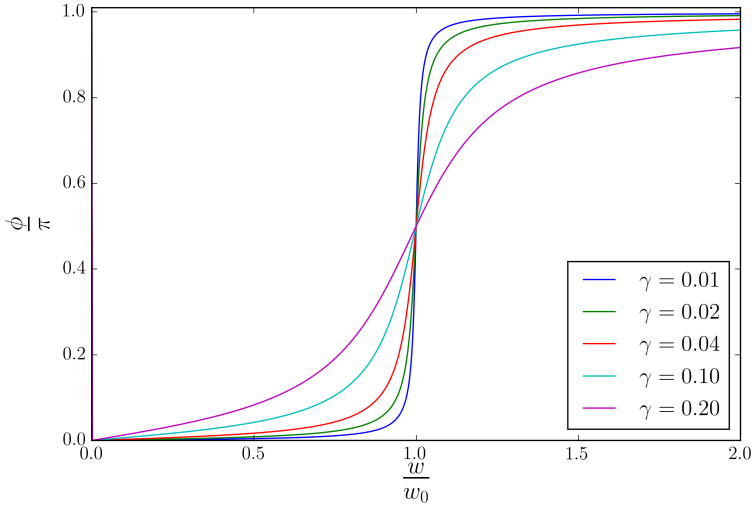


(b)

Figure 2.3: Graph of amplitude and normalized phase response of a driven harmonic oscillator: (a) Amplitude and (b) Normalized phase response are plotted for varying $\gamma$. The x-axis is $\frac{w}{w_0}$, i.e. applied frequency divided by resonance frequency. For $\frac{w}{w_0} < 1$ $A = \frac{F_0}{k}$ and $\phi = 0$. The amplitude is inversely dependent on the spring constant and force is in phase with the displacement. For $\frac{w}{w_0} = 1$, i.e. at resonance $A = \frac{F_0}{2\gamma m\sqrt{w_0^2 - \gamma^2}}$ and $\frac{\phi}{\pi} = 0.5$. The amplitude is inversely dependent on $\gamma$ and the force is $\pm\frac{\pi}{2}$ out of phase with the displacement. For $\frac{w}{w_0} > 1$ $A = \frac{F_0}{mw^2}$ and $\phi \to \pi$. The amplitude is inversely dependent on both mass and applied frequency and the force is $\pm\pi$ out of phase with the displacement

| | Mechanical | | Electrical |
|---|---|---|---|
| $x$ | Displacement | $q$ | Charge |
| $\dot{x}$ | Velocity | $i = \dot{q}$ | Current |
| $m$ | Mass | $L$ | Inductance |
| $k$ | Stiffness | $C^{-1}$ | Reciprocal of capacitance |
| $c$ | Damping Resistance | $R$ | Resistance |
| $F$ | Force | $V$ | Potential Difference |

Table 2.1: Mechanical-Electrical Analogy

where $f_r$ is the resonance frequency and $\Delta f = f_2 - f_1$. $f_2$ and $f_1$ are the frequencies corresponding to the amplitude at $3dB$ or $\frac{A_{max}}{\sqrt{2}}$.

### 2.1.2 Electrical Resonator

The electrical equivalent of an oscillating system is a resistor, inductor and capacitor (RLC) placed in a series or parallel circuit configuration. This circuit is the electrical analog of mass on a spring with a damper. The RLC circuit is the electrical analog of a mechanical resonator and a driven RLC circuit is the electrical analog of a mechanical oscillator. The equation of motion for a RLC oscillator is:

$$L\ddot{q} + R\dot{q} + \frac{q}{C} = V sin\,(wt + \phi)$$

yielding the same response as described above. In this equation inductance, $L$ and charge, $q$, are analogous to mass and displacement, resistance, $R$, is analogous to the dissipation factor and $\frac{1}{C}$, the inverse capacitance, is analogous to the spring constant. These analogies and additional ones are shown in table(2.1).

## 2.2 Mechanical Structures

The mass spring system discussed above is an example of a system having a single resonance frequency. A mechanical structure, however, is a continuous system having numerous modes of vibrations with distinct resonance frequencies. The modes of vibration common to mechanical resonators, as depicted in figure (2.4), are: longitudinal, flexural, thickness shear, face shear and torsion.

Most micromechanical structures use flexural modes of vibration because:

1. these structures follow the planar fabrication scheme and hence are easy to fabricate
2. flexural modes are easy to drive and detect

However, structures using flexural modes suffer from low Q[39] and low frequencies. Mechanical structures using torsion, thickness face and shear modes naturally have high Q and high frequencies but do not follow the planar fabrication scheme and are difficult to drive and detect. In this research work flexural deformation of tines or cantilevers are used to cause torsional motion. Hence; a detailed derivation of the flexural mechanical modes is presented below.

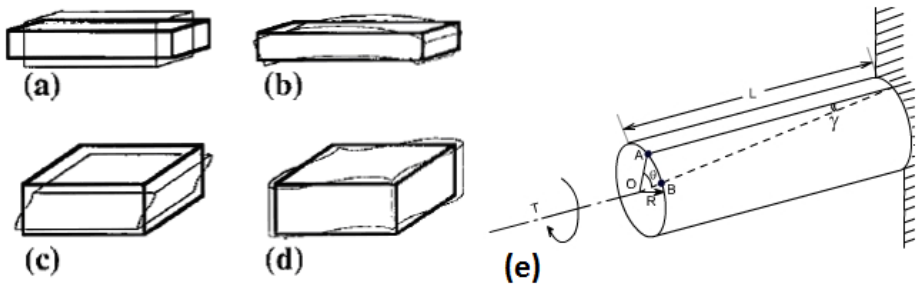


Figure 2.4: Types of Deformation: (a) Longitudinal, (b) Flexural, (c) Thickness Shear, (d) Face Shear and (e) Torsion[1]

### 2.2.1 Flexural Bending

For the simplistic case of a member in pure bending subjected to equal and opposite bending moments the internal forces in any cross section of a member is equivalent to the applied moment as illustrated in figure 2.5. In order to calculate the deformation of the beam the strain, or equivalently the stress, due to a couple must be determined. Using the methods of statics relations are derived which satisfy the stresses exerted on any cross-section of a prismatic member in pure bending. Denoting $\sigma_x$ the normal stress due to a normal force, at a given point of the cross section, $\tau_{xy}$ and $\tau_{xz}$ the components of the shearing stress, an expression is derived showing the system of the elementary internal forces exerted on the section is equivalent to the couple $M$, figure 2.6. From statics a couple, $M$, consists of two equal and opposite forces. The sum of the components of these forces in any direction is therefore equal to zero. Additionally, the moment of the couple is the same about any axis perpendicular to its plane, and is zero about any axis contained in that plane. Selecting arbitrarily the *z-axis*, figure 2.6 equations (2.6)-(2.8) expressing the equivalence of the elementary internal forces and of the couple $M$ by writing that the sums of the components and of the moments of the elementary forces are equal to the corresponding components and moment of the couple $M$ (ignoring the shearing stress):

$$x - components : \int \sigma_x dA = 0 \tag{2.6}$$

$$moment\, about\, y\, axis : \int z\sigma_x dA = 0 \tag{2.7}$$

$$moment\, about\, z\, axis : \int -y\sigma_x dA = M \tag{2.8}$$

The minus sign in equation (2.8) is due to the fact that a tensile stress leads to a negative moment of the normal forces $\sigma_x dA$ about the *z axis*. Equation (2.7) is trivial if the prismatic member is symmetric with respect to the plane containing the couple $M$, and if the y-axis is chosen in that plane. The distribution of the normal forces on the section will be symmetric about the y-axis.

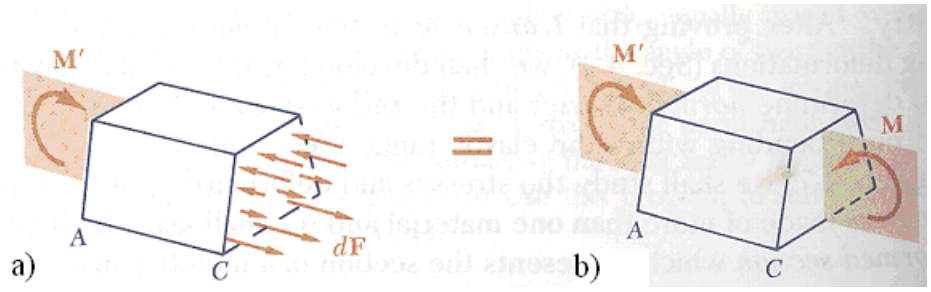


Figure 2.5: Member subjected to equal and opposite couples: (a)internal force at a cross-section, (b)equal and opposite couples[2]

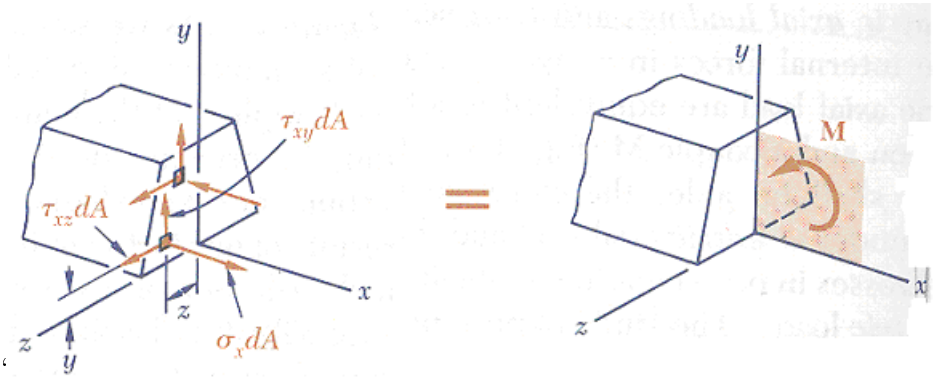


Figure 2.6: Normal and shearing stress in a prismatic member due to a couple[2]

To determine the deflection of a beam the following is required: (a) relationship between the deflection of the beam and moment, (b) the mode shapes of the beam and (c) the principle of virtual work equated to the strain energy.

Equation (2.9)[2] is a $2^{\text{nd}}$ order differential equation where $\xi(x)$ is the deflection along x-axis and $I$, $Y$ is the inertia and Young's modulus of the beam.

$$\frac{d^2\xi(x)}{dx^2} = \frac{M(x)}{YI} \tag{2.9}$$

Equation (2.10)[40] is the general equation for the modes of a prismatic member. The constants $C_1$, $C_2$, $C_3$ and $C_4$ are solved for various boundary conditions for the cantilever case.

$$\begin{aligned} X_i &= C_1(cos(k_i y) + cosh(k_i y)) + C_2(cos(k_i y) - cosh(k_i y)) \\ &\quad + C_3(sin(k_i y) + sinh(k_i y)) + C_4(sin(k_i y) - sinh(k_i y)) \end{aligned} \tag{2.10}$$

The virtual work, equation (2.11)[40], is defined in terms of internal moment, $M$, and virtual slope, $\delta\phi$. Using the definition of virtual displacement, $\delta\xi(x)$, and virtual slope the

relationship between the two is $\delta\phi = \frac{\partial(\delta\xi(x))}{\partial x}$. Therefore, virtual work in terms of deflection is equation (2.12).

$$\delta W = M\delta\phi \tag{2.11}$$

$$\delta W = M\frac{\partial\left(\delta\xi\left(x\right)\right)}{\partial x} \tag{2.12}$$

Strain Energy of a beam, equation (2.13)[40], is expressed in terms of an initial deflection, $v_o$, where the initial deflection is a combination of the mode shapes of a prismatic member, equation (2.14)[40]. Here $X_i$ are the normal functions pertaining to the mode shapes equation (2.10) and $b_i$ is the constant scale factor, i.e. contribution from each mode, to be determined. Combining the two, the strain energy within a prismatic member in the deflected position is equation (2.15).

$$U_o = \frac{YI}{2}\int\left(v_o^{''}\right)^2 dx \tag{2.13}$$

$$v_o = \xi\left(x\right) = b_1X_1 + b_2X_2 + b_3X_3 + ... = \sum b_iX_i \tag{2.14}$$

$$U_o = \frac{YI}{2}\sum b_i^2\int\left(X_i^{''}\right)^2 dx$$

$$U_o = \frac{YI}{2}\sum b_i^2k_i^4\int\left(X_i\right)^2 dx \tag{2.15}$$

Similarly virtual work can be expressed in terms of equation (2.14) yielding equation (2.16). Setting virtual work equation (2.16) equal to the incremental strain energy equation (2.15) yields equation (2.17) for deflection. This equation consists of two terms: constant which is proportional to the moment and summation which is the product of the mode shape and its derivative or curvature evaluated at some $x = x_1$ independent of the evaluation of $\xi\left(x\right)$. The prismatic member considered here is a cantilever because the tines of the resonator used in this work are cantilevers.

$$\frac{\partial\left(\delta\xi\left(x\right)\right)}{\partial x} = \frac{\partial\left(v_o\right)}{\partial x} = \frac{\partial\left(\delta b_iX_i\right)}{\partial x} = \frac{\delta b_i\partial X_i}{\partial x}$$

$$W = M\frac{\delta b_i\partial X_i}{\partial x} \tag{2.16}$$

$$M\delta b_i \frac{\partial X_i}{\partial x} = \frac{\partial U_o \delta b_i}{\partial b_i}$$

$$M\delta b_i \frac{\partial X_i}{\partial x} = \frac{\partial U_o \delta b_i}{\partial b_i} = \frac{\partial \left( \frac{YI}{2} \sum b_i^2 k_i^4 \int (X_i)^2 \, dx \right) \delta b_i}{\partial b_i}$$

$$M\frac{\partial X_i}{\partial x} = YI \sum b_i k_i^4 \int (X_i)^2 \, dx$$

$$b_i = \frac{M}{YI \sum k_i^4 \int (X_i)^2 \, dx} \left( \frac{\partial X_i}{\partial x} \right)$$

$$\xi(x) = \sum b_i X_i = \frac{M}{YI} \sum \frac{X_i}{k_i^4 \int (X_i)^2 \, dx} \left( \frac{\partial X_i}{\partial x} \right)$$

$$\xi(x) = \frac{M}{YI} \sum \frac{X_i}{k_i^4 L} \left( \frac{\partial X_i}{\partial x} \right)$$

$$\xi(x) = \frac{ML^3}{YI} \sum \frac{X_i}{(k_i L)^4} \left( \frac{\partial X_i}{\partial x} \right)_{x=x_1} \tag{2.17}$$

#### 2.2.1.1 Cantilevers

The mode shapes of a cantilever are determined using equation (2.10) for the following boundary conditions equation (2.18)-(2.21)[40]. These boundary conditions describe the deformation and strain at $x = 0$ is zero, curvature and shear force at $x = L$ are also zero. The first two conditions yield, $C_1 = 0$ and $C_3 = 0$, reducing equation (2.10) to equation (2.22).

$$X_{x=0} = 0 \tag{2.18}$$

$$\left( \frac{dX}{dy} \right)_{x=0} = 0 \tag{2.19}$$

$$\left( \frac{d^2X}{dy^2} \right)_{x=L} = 0 \tag{2.20}$$

$$\left( \frac{d^3X}{dy^3} \right)_{x=L} = 0 \tag{2.21}$$

| $i$ | $k_iL$ |
|---|---|
| 1 | 1.875104069 |
| 2 | 4.69409133 |
| 3 | 7.85475748 |
| 4 | 10.99554073 |
| 5 | 14.13716839 |
| 6 | 17.27875953 |
| 7 | 20.42035225 |
| 8 | 23.56194490 |
| 9 | 26.70353756 |
| 10 | 29.84513021 |

Table 2.2: Roots of equation(2.23)

$$X_i = C_2 \left(cos\left(k_i x\right) - cosh\left(k_i x\right)\right) + C_4 \left(sin\left(k_i x\right) - sinh\left(k_i x\right)\right) \tag{2.22}$$

Applying the third and fourth condition yields:

$$C_2 \left(cos\left(k_i L\right) + cosh\left(k_i L\right)\right) + C_4 \left(sin\left(k_i L\right) + sinh\left(k_i L\right)\right) = 0$$

$$C_2 \left(sin\left(k_i L\right) - sinh\left(k_i L\right)\right) - C_4 \left(cos\left(k_i L\right) + cosh\left(k_i L\right)\right) = 0$$

The resonance frequencies, equation (2.24)[40], are determined by taking the determinant of the above equations yielding a transcendental equation, equation (2.23). The first ten roots of this equation are given in table (2.2). Additionally, solving for the constants $C_2$ and $C_4$ results in the general equation describing the mode shapes of a cantilever, equation (2.25). The mode shapes associated with first three roots are given in figure (2.7).

$$cosh\left(k_i L\right) cos\left(k_i L\right) = -1 \tag{2.23}$$

$$f_r = \frac{1}{2\pi} \left(k_i L\right)^2 \frac{t}{L^2} \sqrt{\frac{Y}{12\rho}} \tag{2.24}$$

$$X_i = \left(cos\left(k_i x\right) - cosh\left(k_i x\right) - \alpha_i \left(sin\left(k_i x\right) - sinh\left(k_i x\right)\right)\right) \tag{2.25}$$

where

$$\alpha_i = \frac{cosh\left(k_i L\right) + cos\left(k_i L\right)}{sinh\left(k_i L\right) + sin\left(k_i L\right)}$$

Using equations (2.25) and (2.17) equation (2.26) is the general expression for the deflection of a cantilever beam. The maximum deflection for the fundamental mode occurs at $x = L$. This is solved using equations (2.17) and (2.25) yielding equation (2.27) as shown below:

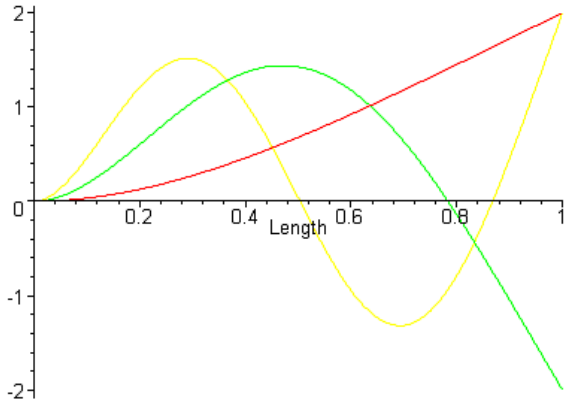


Figure 2.7: Cantilever's first three modes. The number of nodes increase with mode number. The first mode (red) has 0 nodes, the second mode (green) has 1 node and the third mode (yellow) has 2 nodes

$$\xi(x) = \frac{ML^3}{YI} \sum \frac{X_i}{(k_i L)^4} \left( \frac{\partial X_i}{\partial x} \right)_{x=x_1}$$

$$\frac{\partial X_i}{\partial x} = \frac{\partial \left( cos\left(k_i x\right) - cosh\left(k_i x\right) - \alpha_i \left( sin\left(k_i x\right) - sinh\left(k_i x\right) \right) \right)}{\partial x}$$

$$\frac{\partial X_i}{\partial x} = k_i \left( -sin\left(k_i x\right) - sinh\left(k_i x\right) - \alpha_i \left( cos\left(k_i x\right) - cosh\left(k_i x\right) \right) \right)$$

$$\xi(x) = \frac{ML^3}{YI} \sum \frac{X_i}{(k_i L)^4} k_i \left( -sin\left(k_i x_1\right) - sinh\left(k_i x_1\right) - \alpha_i \left( cos\left(k_i x_1\right) - cosh\left(k_i x_1\right) \right) \right)$$

$$\xi(x) = \frac{ML^2}{YI} \sum \frac{X_i}{(k_i L)^4} \left(k_i L\right) \left( -sin\left(k_i x_1\right) - sinh\left(k_i x_1\right) - \alpha_i \left( cos\left(k_i x_1\right) - cosh\left(k_i x_1\right) \right) \right)$$

$$\xi(x) = \frac{ML^2}{YI} \sum \frac{X_i}{(k_i L)^3} \left( -sin\left(k_i x_1\right) - sinh\left(k_i x_1\right) - \alpha_i \left( cos\left(k_i x_1\right) - cosh\left(k_i x_1\right) \right) \right)$$

$$\begin{aligned} \xi(x) \quad = \quad & \frac{ML^2}{YI} \sum_{i=1}^{\infty} \left[ \frac{\left( cos\left(k_i x\right) - cosh\left(k_i x\right) - \alpha_i \left( sin\left(k_i x\right) - sinh\left(k_i x\right) \right) \right)}{\left(k_i L\right)^3} \right. \\ & \left. \frac{\left( -sin\left(k_i x_1\right) - sinh\left(k_i x_1\right) - \alpha_i \left( cos\left(k_i x_1\right) - cosh\left(k_i x_1\right) \right) \right)}{\left(k_i L\right)^3} \right] \end{aligned} \tag{2.26}$$

| $Q$ | Value |
|---|---|
| Low | $0 - 10^3$ |
| Medium | $10^3 - 10^5$ |
| High | $> 10^5$ |

Table 2.3: Classification of $Q$

$$\xi(L) = \frac{ML^2}{YI} \sum_{i=1}^{\infty} \frac{4}{(k_i L)^3} \left( \frac{sin(k_i L)\, sinh(k_i L)}{(sinh(k_i L) + sin(k_i L))^2} \left[ sin(k_i L)\, cosh(k_i L) - sinh(k_i L)\, cos(k_i L) \right] \right) \tag{2.27}$$

### 2.2.2 Quality Factor, Q, of Mechanical Structures

As discussed in the introduction section mechanical resonators are used for generating timing pulses. They are also used as sensors, filters etc. For these applications dissipation matters. Dissipation within the resonator results in:

1. limiting the sensitivity to external applied forces
2. broadening of the natural linewidth
3. determining the minimum intrinsic power at which the device must operate

Generally; medium $Qs$ are desired for most applications. Table (2.3) is the classification of $Qs$ and their associated values. High $Qs$ are desired in applications where the $Q$ is the performance limiting aspect. Examples of such applications are: low phase noise oscillators such as those required in time keeping [41][42], highly selective filters [43] for signal processing, resonant sensors where resonance frequency shifts are tracked due to external perturbations [44][45] etc.

The mechanisms that limit the Q-value of mechanical resonators are characterized as intrinsic and extrinsic. Intrinsic means processes that are fundamental to the material. These occur because deformations in mechanical vibrations are accompanied by processes that are not thermodynamically reversible. These processes are responsible for dissipation of the oscillation energy[46]. Extrinsic mechanisms are energy losses resulting from technological and design factors. Intrinsic mechanisms include:

1. Thermoelastic Dissipation: caused by vibratory volume changes producing spatially inhomogeneous temperature changes. These resulting temperature gradients induce heat flow, which is accompanied by an entropy increase and a conversion of vibration energy into thermal energy
2. Dissipation due to phonon-phonon interactions: caused by interactions between acoustic waves, as a result of resonant vibrations, and thermal phonons. If the acoustic wavelength is considerably larger than the mean free path of the phonons, one can consider the acoustic waves as locally changing the phonon frequencies thereby perturbing the phonon distribution function away from its equilibrium Planck form. This

process of the phonon gas restoring to thermal equilibrium is accompanied by dissipation of the acoustic-wave energy

3. Dissipation due to lattice defects: are characterized as internal friction mechanisms. These internal friction mechanisms produce a phase lag between the stress and strain relaxation times causing dissipation of energy. Lattice defects include: point defects, dislocations, interfaces etc

Extrinsic mechanisms include:

1. Losses due to gas damping: Mechanical resonator oscillating in a gaseous medium creates sound waves that carry its power away. For high $Qs$ low pressures are required

2. Clamping losses: cause dissipation of energy from an oscillating resonator to the clamp. This energy dissipation occurs due to acoustic coupling to the clamps. Therefore, to achieve high-$Qs$ resonators must be designed to minimize this energy loss

## 2.3 Piezoelectricity

The piezoelectric effect is found with crystal structures lacking a symmetry center regarding the positive and negative ions of the crystal lattice. Thus, the condition for occurrence of the piezoelectric effect is the existence of polar axes within the crystal structure. Polar means, that there is an electrical dipole moment in the axis directions caused by the distribution of the electrical charge in the chemical bond. From the outer point of view, the crystal is electrically neutral. A deformation along the polar axis, by applying an electric field or a mechanical force, causes an additional electrical polarization to form along this axis. The electrical polarization is caused by the displacement of the positive and negative ions of the crystal lattice against each other resulting in an electrical charge on the appropriate crystal surfaces either along or perpendicular to the polar axis and thus in an outside electrical polarization voltage. An important property of materials exhibiting a measurable piezoelectric effect is their high resistivity. Usually this is to be expected because the piezoelectric charge is small.

### 2.3.1 Mathematical Description

Mathematically piezoelectricity can be described by the strain matrix formulation equation (2.28) or stress matrix formulation equation (2.29); where $\sigma_p/\sigma_q$ are the stress terms, $\epsilon_p/\epsilon_q$ are the strain terms, $d_{iq}/d_{pk}$ is the piezoelectric coefficient, $e_{iq}/e_{pk}$ is the piezoelectric modulus, $D_i$ is the electric displacement, $\epsilon^{\epsilon}_{ik}$ is the permittivity at constant strain, $\epsilon^{\sigma}_{ik}$ is the permittivity at constant stress, $Y^E_{pq}$ is the modulus of elasticity and $s^E_{pq}$ is the elastic compliance coefficient. The elastic compliance coefficient is the inverse of the modulus of elasticity. The piezoelectric coefficient and elastic compliance have the following relationship: $d_{iq} = \sum_p e_{ip} S^E_{pq}$ and stress and strain have the following relationship: $\sigma_p = \sum_p Y^E_{pq} \epsilon_q$

$$\begin{bmatrix} \epsilon_p \\ D_i \end{bmatrix} = \begin{bmatrix} S^E_{pq} & d_{pk} \\ d_{iq} & \epsilon^{\sigma}_{ik} \end{bmatrix} \begin{bmatrix} \sigma_q \\ E_k \end{bmatrix} \tag{2.28}$$

$$\begin{bmatrix} \sigma_p \\ D_i \end{bmatrix} = \begin{bmatrix} Y_{pq}^E & e_{pk} \\ e_{iq} & \epsilon_{ik}^{\epsilon} \end{bmatrix} \begin{bmatrix} \epsilon_q \\ E_k \end{bmatrix} \tag{2.29}$$

The terms above, for brevity, are given in tensor notation where $p$ and $q$ are between 1 and 6 and $i$ and $k$ are between 1 and 3. The associated axial relation to: (a)$p$ and $q$ numbers are: 1, 2, 3, 4, 5, 6 related to x, y, z, yz, xz and xy and (b)$i$ and $k$ numbers are: 1, 2, 3 related to x, y and z. This yields the following matrix for each of the components:

Strain Matrix:

$$\epsilon_p = \begin{bmatrix} \epsilon_1 \\ \epsilon_2 \\ \epsilon_3 \\ \epsilon_4 \\ \epsilon_5 \\ \epsilon_6 \end{bmatrix} = \begin{bmatrix} \epsilon_x \\ \epsilon_y \\ \epsilon_z \\ \epsilon_{yz} \\ \epsilon_{xz} \\ \epsilon_{xy} \end{bmatrix}$$

Stress Matrix:

$$\sigma_p = \begin{bmatrix} \sigma_1 \\ \sigma_2 \\ \sigma_3 \\ \sigma_4 \\ \sigma_5 \\ \sigma_6 \end{bmatrix} = \begin{bmatrix} \sigma_x \\ \sigma_y \\ \sigma_z \\ \sigma_{yz} \\ \sigma_{xz} \\ \sigma_{xy} \end{bmatrix} \frac{N}{m^2}$$

Elastic Compliance Matrix:

$$s_{pq}^E = \begin{bmatrix} s_{11} & s_{12} & s_{13} & s_{14} & s_{15} & s_{16} \\ s_{21} & s_{22} & s_{23} & s_{24} & s_{25} & s_{26} \\ s_{31} & s_{32} & s_{33} & s_{34} & s_{35} & s_{36} \\ s_{41} & s_{42} & s_{43} & s_{44} & s_{45} & s_{46} \\ s_{51} & s_{52} & s_{53} & s_{54} & s_{55} & s_{56} \\ s_{61} & s_{62} & s_{63} & s_{64} & s_{65} & s_{66} \end{bmatrix} \frac{m^2}{N}$$

Modulus of Elasticity:

$$Y_{pq}^E = \begin{bmatrix} Y_{11} & Y_{12} & Y_{13} & Y_{14} & Y_{15} & Y_{16} \\ Y_{21} & Y_{22} & Y_{23} & Y_{24} & Y_{25} & Y_{26} \\ Y_{31} & Y_{32} & Y_{33} & Y_{34} & Y_{35} & Y_{36} \\ Y_{41} & Y_{42} & Y_{43} & Y_{44} & Y_{45} & Y_{46} \\ Y_{51} & Y_{52} & Y_{53} & Y_{54} & Y_{55} & Y_{56} \\ Y_{61} & Y_{62} & Y_{63} & Y_{64} & Y_{65} & Y_{66} \end{bmatrix} \frac{N}{m^2}$$

Piezoelectric Coefficient Matrix:

$$d_{iq} = \begin{bmatrix} d_{11} & d_{12} & d_{13} \\ d_{21} & d_{22} & d_{23} \\ d_{31} & d_{32} & d_{33} \\ d_{41} & d_{42} & d_{43} \\ d_{51} & d_{52} & d_{53} \\ d_{61} & d_{62} & d_{63} \end{bmatrix} \frac{C}{N}$$

Piezoelectric Constant Matrix:

$$e_{iq} = \begin{bmatrix} e_{11} & e_{12} & e_{13} \\ e_{21} & e_{22} & e_{23} \\ e_{31} & e_{32} & e_{33} \\ e_{41} & e_{42} & e_{43} \\ e_{51} & e_{52} & e_{53} \\ e_{61} & e_{62} & e_{63} \end{bmatrix} \frac{C}{m^2}$$

Permittivity Matrix:

$$\epsilon_{iq}^{E} = \begin{bmatrix} \epsilon_{11} & \epsilon_{12} & \epsilon_{13} \\ \epsilon_{21} & \epsilon_{22} & \epsilon_{23} \\ \epsilon_{31} & \epsilon_{32} & \epsilon_{33} \end{bmatrix}$$

The matrices above are properties of material. The possible vibration modes and suitable electrode configuration for piezoelectric activation are determined by either piezoelectric coefficient matrix or piezoelectric constant matrix. An applied field will cause a strain/stress in a particular direction resulting in a charge proportional to the amount of deflection. Mathematically, for an applied electric field the matrix in equation (2.28) and (2.29) reduces to equations (2.30) and (2.31). The former is the strain produced due to the applied electric field and the latter is the electric displacement due to the piezoelectric strain produced from the applied field, or the inverse piezoelectric effect, and the dielectric. These strains/stress produce moments, calculated using equation (2.8), which can be used to determine the deflection of the cantilever using equation (2.26). Additionally the piezoelectric charge, equation (2.32), can be derived using the electric displacement. Therefore, an applied field drives the device while the resulting charge from the deflection is detected.

$$\epsilon_p = d_{pk} E_k \tag{2.30}$$

$$D_i = d_{ip}\sigma_p + \epsilon_{ik} E_k$$

$$D_i = d_{ip} Y_{pq}^{E} e_q + \epsilon_{ik} E_k = e_{iq}\epsilon_p + \epsilon_{ik} E_k \tag{2.31}$$

$$Q = \iint D_i didj \tag{2.32}$$

These equations are captured as a block diagram in figure (2.8).

Using the longitudinal piezoelectric coefficients flexural vibrations/deflection can be achieved by creating either a monomorph or a bimorph structure. This is discussed next.

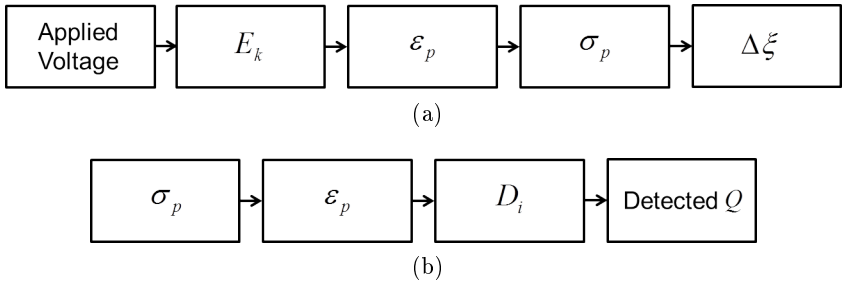


Figure 2.8: Piezoelectric Drive and Detect. (a) Piezoelectric Effect: An applied voltage results in a strain/stress, $\epsilon_p/\sigma_p$, due to the piezoelectric coefficient, $d_{pk}$, leading to a deflection - $\Delta\xi \ \alpha \ d_{pk}E_k$, (b) Inverse Piezoelectric Effect: The stress/strain as a result of the deflection produces a charge due to the inverse piezoelectric effect - $Q \ \alpha \ e_{iq}\epsilon_p$ where $e_{iq}$ is the piezoelectric coefficient. Here $\propto$ is a symbol for proportionality

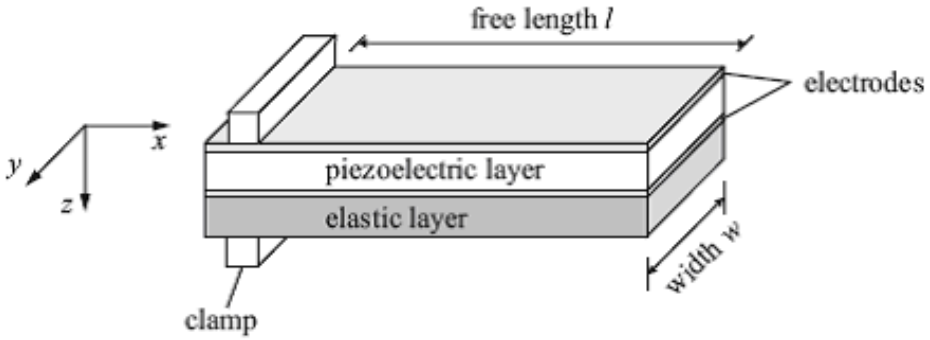


Figure 2.9: Layer sequence of a monomorph[3]

### 2.3.2 Monomorph

A monomorph consists of an active piezoelectric layer and a passive elastic layer, figure (2.9). In this figure the piezoelectric strain component is along the $x-$direction. The movement of the piezoelectric component resulting from its expansion or compression is restricted by the passive elastic component. As a result an internal piezoelectric moment arises deforming the monomorph as shown in figure (2.10). As is seen in the figure, the total deflection in the $z-direction$ is much larger than the deformation of the piezoelectric component in the $x-direction$ and the applied electric field is opposite in direction to the polarization.

The resulting deflection hence the detected piezoelectric charge is dependent on the thickness of the piezoelectric and elastic layer. In order to increase deflection, the passive elastic component can be replaced by a second active piezoelectric component. This structure is called a bimorph.

### 2.3.3 Bimorph

A bimorph consists of two active piezoelectric layers. These layers can either be polarized in the same or opposite directions. If the polarization of both layers are identical the field applied must be in the opposite direction in order to induce an extension in one component

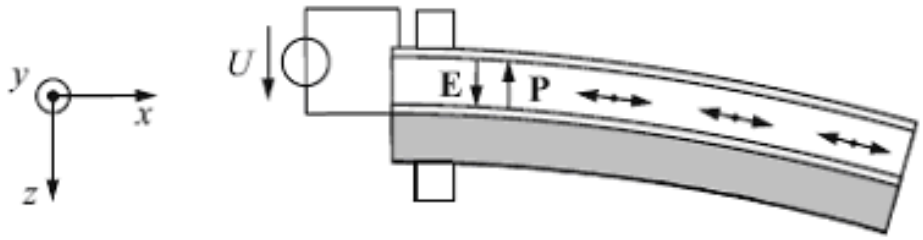


Figure 2.10: Flexural deformation of monomorph due to an applied field **(E)**. The horizontal arrows indicate the direction of the piezoelectric strain and the vertical arrows indicate the direction of polarization, **P**, and the applied field. The strain is parallel to the $x-$ *direction*. An applied field causes a longitudinal extension or compression of this layer while the elastic layer restricts the motion. As a result an internal piezoelectric moment arises causing a flexural deformation of the monomorph. The opposite direction of **E** and **P** indicates that for a field directed in the negative $z-$direction an extension occurs along the $x-$direction. [3]

and compression in the other, thereby creating a bending moment. This type of electrical configuration is called parallel connection, figure (2.11)(a). However, if the polarization is in the opposite direction the applied field can be in the same direction, figure (2.11)(b). This type of configuration is called series connection. The advantage of series connection is a contact between the layers is not required. However, within one single layer the value of the electric field is almost half as large as with the parallel bimorph.

### 2.3.4 Electrical Model of a Piezoelectric Resonator

The equivalent circuit of an electrical resonator is the familiar RLC circuit discussed in section (2.1.2). For a piezoelectric resonator the electrical circuit is the RLC circuit with an additional parallel or package capacitance. This circuit is given in figure (2.12) and is called the Butterworth Van Dyke (BVD) model. The parallel capacitance has the effect of introducing another resonant frequency called the anti-resonant frequency. In this section the motivation for the BVD model is first discussed and then the consequence of parallel capacitance is discussed via circuit analysis.

**2.3.4.0.1 BVD Model** From equation (2.31) there are two components to the total detected charge: piezoelectric and dielectric. These charges, $Q_x$, are related to their respective capacitances, $C_x$, via the relationship $C_x = \frac{Q_x}{V}$; where $V$ is the applied voltage. The equivalent circuit for such a system is two capacitors in parallel - piezoelectric or motional capacitance, $C_m$ and dielectric or package capacitance, $C_p$. At resonance the motional branch consists of the RLC circuit, i.e. $R_m$, $L_m$ and $C_m$ while the package or dielectric branch is the same as before.

**2.3.4.0.2 Effect of $C_p$** The equivalent impedance and magnitude for the BVD circuit is given in equations (2.33) and (2.34). The derivation of the impedance using circuit analysis is as follows:

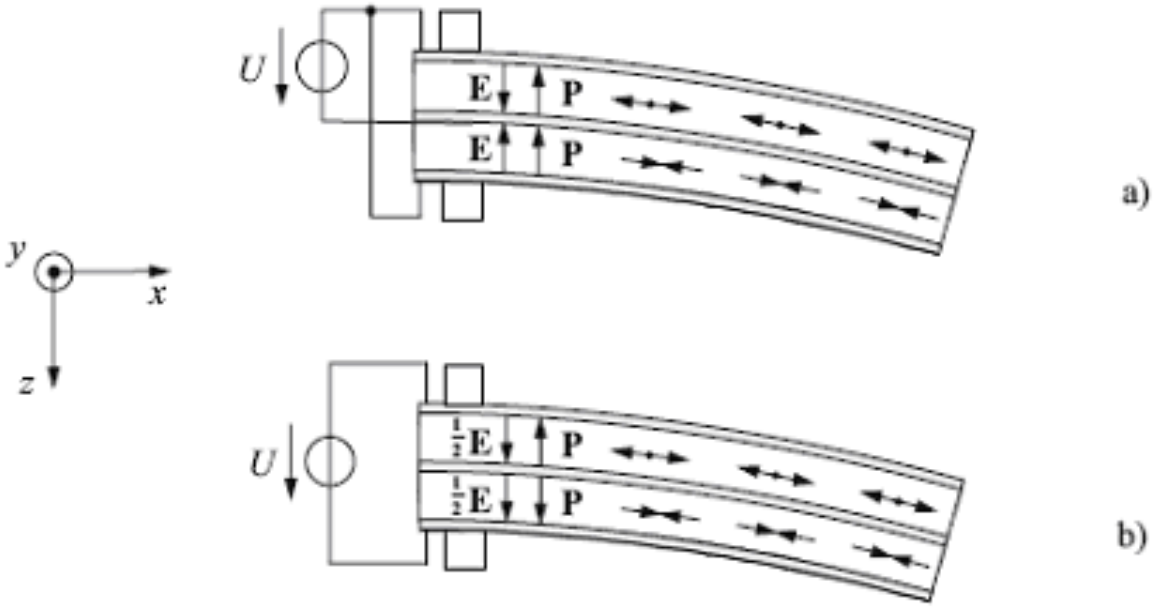


Figure 2.11: Deflection of bimorph subjected to a field - (a) parallel bimorph, (b) serial bimorph. Parallel bimorph is defined as a structure having two piezoelectric layers with the same polarization direction and fields applied in opposite directions. Serial bimorph is defined as a structure having two piezoelectric layers with opposite polarization direction and a field applied in a single direction [3]

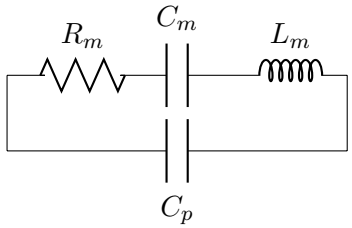


Figure 2.12: Piezoelectric resonator circuit. $R_m$, $L_m$ and $C_m$ are the motional components at resonance and $C_p$ is the package or dielectric capacitance[4]. $C_m$ and $C_p$ are derived using equation (2.31) where the first term in this equation is the charge resulting from the deformation of the piezoelectric structure. Knowing $C_m$ $L_m$ is derived using equation (2.37) and $R_m$ is proportional to the inverse $Q$

$$Z = \left( \frac{1}{R_m + j\left(wL_m - {}^{1}/_{wC_m}\right)} + jwC_p \right)^{-1}$$

$$Z = \left( \frac{1 + jwC_pR - w^2LC_p + {}^{C_p}/_{C_m}}{R_m + j\left(wL_m - {}^{1}/_{wC_m}\right)} \right)^{-1}$$

$$Z = \left( \frac{R_m + j\left(wL_m - {}^{1}/_{wC_m}\right)}{1 + jwC_pR_m - w^2L_mC_p + {}^{C_p}/_{C_m}} \right) \tag{2.33}$$

$$Z = \frac{1}{(wC_p)} \sqrt{\frac{R_m^2 + \left(wL_m - \frac{1}{wC_m}\right)^2}{R_m^2 + \left(wL_m - \frac{1}{wC_m} - \frac{1}{wC_p}\right)^2}} \tag{2.34}$$

The resonant and anti-resonant frequencies are derived from equation (2.33) by finding equivalent real and imaginary impedances and setting the imaginary part to zero. The real and imaginary impedances are:

$$Z_{real} = \frac{R_m}{1 - 2w^2L_mC_p + {}^{(2C_p)}/_{C_m} + w^4L_m^2C_p^2 - 2w^2L_mC_p^2/C_m + C_p^2/C_m + (wR_mC_p)^2} \tag{2.35}$$

$$Z_{imag} = \frac{-wR_m^2C_p + wL_m - w^3L_m^2C_p + {}^{(2wL_mC_p)}/_{C_m} - {}^{1}/_{wC_m} - {}^{C_p}/_{(wC_m)^2}}{1 - 2w^2L_mC_p + {}^{(2C_p)}/_{C_m} + w^4L_m^2C_p^2 - 2w^2L_mC_p^2/C_m + C_p^2/C_m + (wR_mC_p)^2} \tag{2.36}$$

Setting the imaginary impedance to zero yields:

$$w^2L_mC_m^2 - C_m - w^4L_m^2C_pC_m^2 + 2w^2L_mC_mC_p - C_p - w^2R_m^2C_pC_m^2 = 0$$

The last term in this equation is assumed to be negligible as compared to other terms in the equation. This assumption is only valid in the regime where $R_m$ is small. Omitting this term and calculating the roots of the equation gives the resonant and anti-resonant frequencies – equations (2.37) and (2.38). Substituting these equations into equation (2.33), the resonance and anti-resonance impedance are given in equations (2.39) and (2.40). The impedance at resonance is assumed to be approximately equal to $R_m$, in the regime where $R_m$ is much lower than the impedance of the package capacitance.

$$w_r = \sqrt{\frac{1}{L_mC_m}} \tag{2.37}$$

$$w_A = \sqrt{\frac{1}{L_mC_m} + \frac{1}{L_mC_p}} \tag{2.38}$$

$$Z_R = \frac{R_m}{1 - (w_rC_pR_m)^2} \sim R_m \tag{2.39}$$

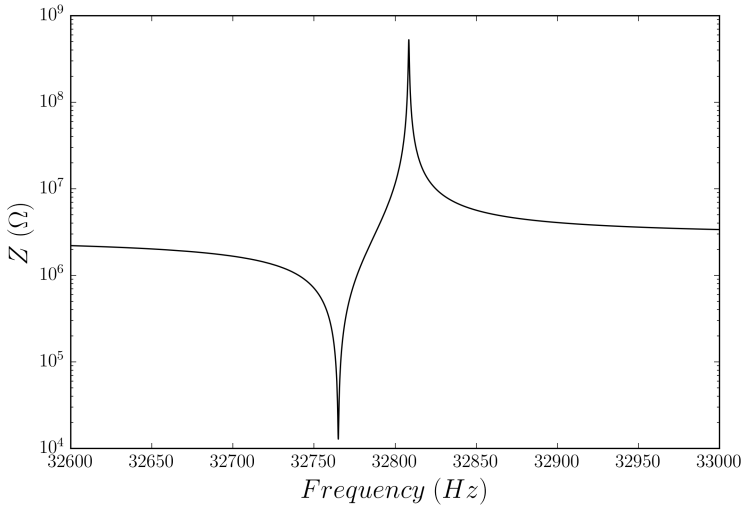


Figure 2.13: $Z\,vs$ Frequency The figure is generated using equation (2.34) where $C_p = 1.4178\,pF$, $C_m = 3.0666\,fF$, $L_m = 7.6943\,kH$ and $R_m = 15.953\,k\Omega$. The lowest impedance is at resonance $Z_R = R_m$ and highest impedance is at anti-resonance $Z_m = 734.06\,M\Omega$. The impedance off resonance is dominated by $\frac{1}{wC_p}$

$$Z_A = \frac{1}{w_A^2 C_p^2 R_m} \tag{2.40}$$

Figure (2.13) is a plot of the total impedance of the circuit as a function of frequency as given by equation (2.34). This curve is generated using the following values for $R_m$, $C_m$, $L_m$ and $C_p$: $15.953\,k\Omega$, $3.0666\,fF$, $7.6943\,kH$ and $1.4178\,pF$, respectively. The lowest and highest impedances are the resonant and anti-resonant points. The frequency at these points are $f_r = 32768\,Hz$ and $f_A = 32800\,Hz$. The tails in this figure is the impedance of the dielectric or package capacitance, i.e. at frequencies other than the resonance/anti-resonance regime the impedance of the package capacitance dominates.

Figure (2.14) is a plot of the real and imaginary impedance of the BVD circuit, i.e. equations (2.35) and (2.36). Here the x-axis is frequency. The real and imaginary impedances are generated using the same values for $R_m$, $C_m$, $L_m$ and $C_p$ as stated above. As is seen from the plot the dominant impedance is $Z_{imag}$ except at resonance and anti-resonance. At these points, indicated by open blue circles on the figure, $Z_{real}$ dominates because $Z_{imag}$ decreases relative to $Z_{real}$ by over an order of magnitude. This is attributed to the fact that the magnitude of positive and negative components comprising the numerator of $Z_{imag}$ become approximately comparable. Thus adding to decrease $Z_{imag}$. This is also seen by looking at the phase of the circuit. The phase is plotted in figure (2.15) using equation (2.41). The numerator of equation (2.41) which is the numerator of equation (2.36) changes with frequency. At resonance and antiresonance the numerator of equation (2.41) is lower than the denominator hence the phase is $0^0$ and the circuit is purely resistive. These points are indicated by open blue circles. Below and above these points the phase is $-90^{\,0}$, i.e. the

circuit is purely capacitive while between these points the phase is $90^0$ indicating that the circuit is purely inductive.

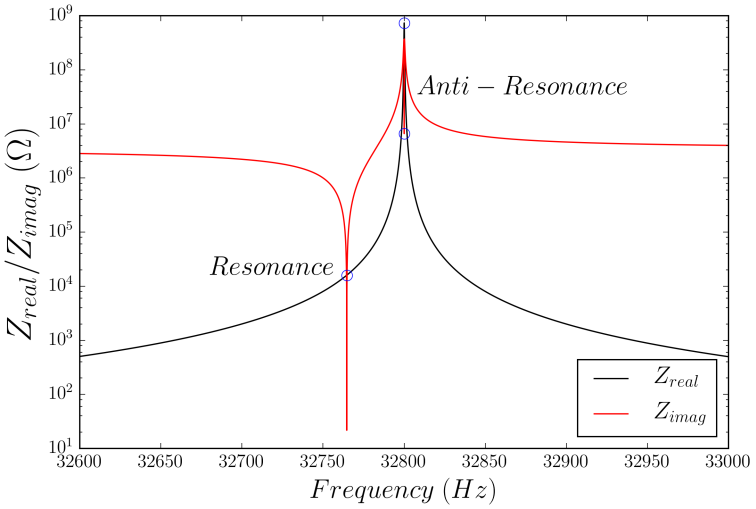


Figure 2.14: Graph of $Z_{real}/Z_{imag}$ vs $Frequency$ of the BVD circuit. $Z_{real}$ and $Z_{imag}$ are generated using equations (2.35) and (2.36). The values used for $R_m$, $C_m$, $L_m$ and $C_p$ are $15.953\,k\Omega$, $3.0666\,fF$, $L_m = 7.6943\,kH$ and $C_p = 1.4178\,pF$ respectively. The impedance is dominated by $Z_{imag}$ except at resonance and anti-resonance. At these points, indicated by open blue circles, $Z_{real}$ dominates because $Z_{imag}$ decreases relative to $Z_{real}$ by over an order of magnitude

$$\theta = tan^{-1}\left(\frac{Z_{imag}}{Z_{real}}\right)$$

$$\theta = tan^{-1}\left(\frac{-wR_m^2C_p + wL_m - w^3L_m^2C_p + {}^{(2wL_mC_p)}/_{C_m} - {}^{1}/_{wC_m} - {}^{C_p}/_{(wC_m)^2}}{R_m}\right) \tag{2.41}$$

## 2.4 Semiconductor

Semiconductor materials, for e.g. Silicon, GaAs, InP etc, have conductivity that are between an insulator and a metal. Conductivity is the ability for charge carriers to move when a potential is applied. Charge carriers are able to move because empty states are available for the charge carriers to propagate into. For metals abundant of empty states are available however for insulator and semiconductors these empty states are only available at some higher energy. This is best understood in terms of an illustrated energy band diagram, figure (2.16). In this figure x-axis is the type of materials and the y-axis is electron energy. The materials from left to right are insulators, semiconductors and metals. Two bands are shown, valence

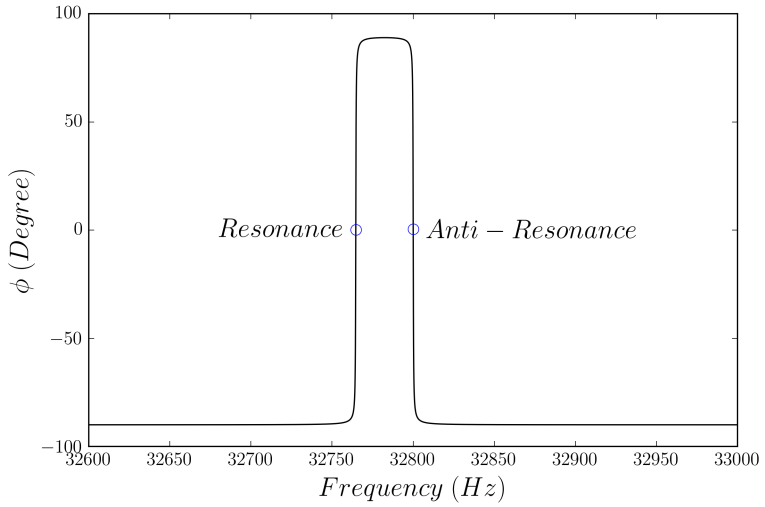


Figure 2.15: Graph of Phase ($\phi$) vs *Frequency*. Phase is generated using equation (2.41). The values used for $R_m$, $C_m$, $L_m$ and $C_p$ are $15.953\,k\Omega$, $3.0666\,fF$, $L_m = 7.6943\,kH$ and $C_p = 1.4178\,pF$ respectively. The open blue circles indicate the resonance and anti-resonance points. At these points the phase is $0^0$ while above and below these points the phase is $-90^0$ and between these points the phase is $90^0$. These correspond to the resistive, capacitive and inductive regimes of the resonator

and conduction bands, and the separation between these bands is characterized by the band gap energy $E_g$. The valence band has lower energy states while the conduction band has higher energy states. The gradient in this figure follows the Fermi-Dirac distribution. This distribution gives the probability for an electron to occupy an energy level relative to the fermi energy $E_F$. The following is illustrated in the figure:

1. Red indicates filled states, i.e. the probability of occupancy is 1
2. Blue indicates empty states, i.e. the probability of occupancy is 0
3. The gradient indicates partially filled states, i.e. a probability of occupancy is between 0 and 1

Using $E_g$ and $E_F$ with the aid of figure (2.16) the conductivity of metals, insulators and semiconductors can be explained as follows:

1. In metals the valence and conduction bands overlap, i.e. $E_g = 0$ and $E_F$ lies inside the bands. As a result of the former and the latter an abundance of low energy partially filled states are available with a probability of occupancy much greater than 0. This allows for valence electrons to freely move through the material resulting in large conductivity
2. In semiconductors $E_g$ is larger than for metals and $E_F$ is inside the band gap. Therefore for conduction an electron has to transit from the filled valence band to the empty conduction band. $E_F$ and $E_g$ are close enough in energies that the probability of occupancy, due to thermal energy, for electrons in the conduction band is not 0. As a result of this finite probability and accessibility to empty states in the conduction band semiconductors conduct electricity. The conductivity is lower than for metals
3. Insulators are similar to semiconductors with the difference being that $E_g$ is much larger than $E_F$ such that the probability for the conduction band to be thermally populated with electrons is negligible. Hence the conductivity is negligible

The relatively low band gap of semiconductors allows for doping. Doping is the process of introducing impurities into a material in order to change its conductivity. These impurities introduce excess of charge carriers holes[1] or electrons. These are called p and n, i.e. positive and negative. The role of the impurities is to introduce extra empty or filled energy states with in the band gap allowing for greater number of thermally generated charge carriers, i.e. holes or electrons, with in the valence or conduction bands. These extra states shift the fermi level towards the valence or conduction band for p or n type dopants. This is illustrated in figure (2.17). The colors and patterns used in this figure are carried over from figure (2.16).

Using the ingredients of dopants and band gaps various electrical, optical and electro-optical devices are made from semiconductors. These devices are metal oxide field effect transistors (MOSFETS), bipolar junction transistors (BJT), light amplifier by stimulated emission or radiation (LASERS), photodiodes etc. A diode is at the heart of all these devices. There are various types of diodes: *pn*, heterojunction, metal insulator semiconductor

[1] Hole is defined as the absence of an electron in a particular place in an atom

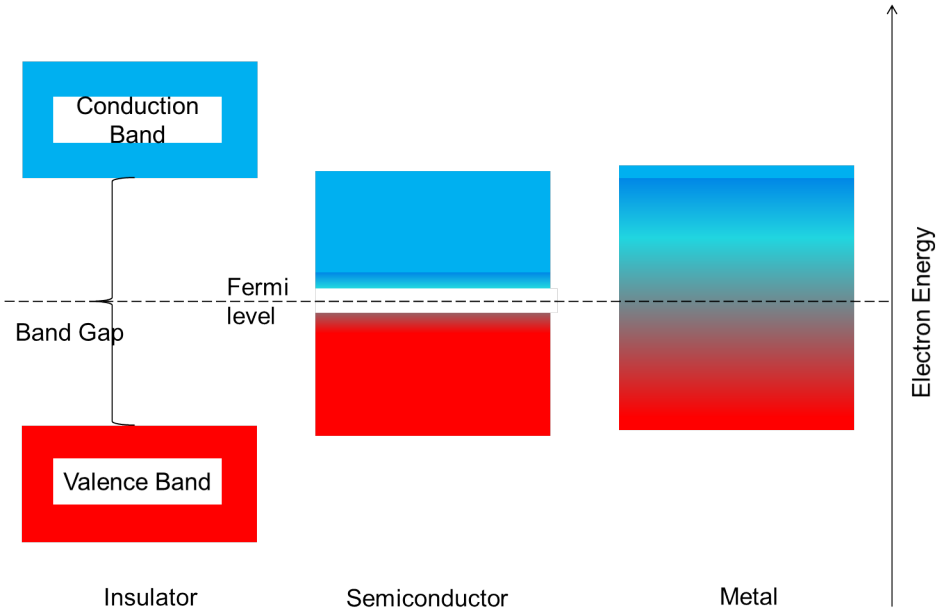


Figure 2.16: Energy Band arrangement for Insulators, Semiconductor and Metals. The y-axis is electron energy and increases from bottom to top. The gradient follows the Fermi-Dirac distribution. Red indicates 0 free states, blue indicates 0 filled states and the gradient indicates partially filled states. For electrical conduction to occur empty states are required. In metals the valence and conduction bands overlap resulting in the availability of low energy partially filled states. This allows for valence electrons to freely move through the material. For insulators and semiconductors the valence and conduction bands are separated by a band gap having energy $E_g$. Thus an electron has to transit from the valence to the conduction band. Insulators have large $E_g$ and hence lower conductivity while semiconductors have lower $E_g$ hence higher conductivity than insulators but lower than metal.

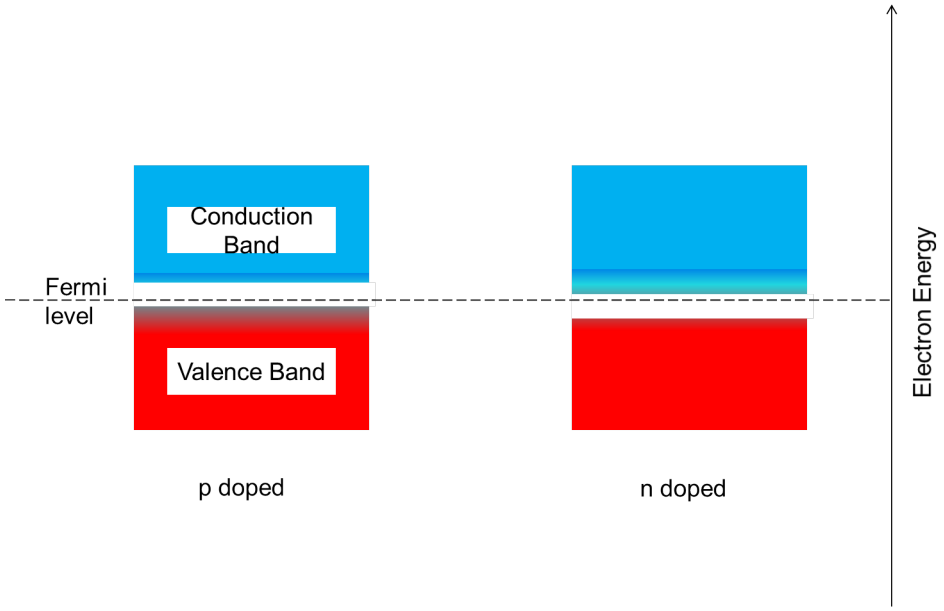


Figure 2.17: Band Diagram of p and n doped semiconductor. The colors and patterns used in this figure are carried over from figure (2.16). For the p doped material the fermi level is closer to the valence band indicating an increased conductivity due to an excess of holes while for the n doped material the fermi level is closer to the conduction band indicating increased conductivity due to an excess of electrons. The movement of the fermi-level is a result of introducing dopants or impurities in the semiconductor

(MIS) etc. A brief discussion of *pn* junction diode is given below. Using this description heterojunctions are then discussed. The torsional oscillator discussed in this thesis is comprised of both *pn* and heterojunctions.

### 2.4.1 *pn* Junction

Bringing a p material in contact with an n material results in a junction. This junction has non-linear current-voltage (IV) and capacitance-voltage (CV) response. Figure (2.18) is the IV curve and figure (2.19)(a) is the CV curve of a diode as a function of an applied bias. The non-linear response can be understood qualitatively via band diagrams. Figure (2.20) is the band diagram of an isolated p and n doped material. In this figure the x-axis is the type of doped semiconductor and the y-axis is energy. Unlike the diagrams above the top of the valence band and the bottom of the conduction band are only shown and the energy of the two bands are labeled, i.e. $E_v$ and $E_c$ respectively. As discussed above for the n-type material $E_F$ is closer to the conduction band while for p-type material $E_F$ is closer to the valence band. In this figure the fermi levels for the n and p material are labeled as $E_{Fn}$ and $E_{Fp}$.

Figure (2.21) is an illustration of the result of contacting the two doped materials. When the two doped materials are brought in contact with each other their respective fermi-levels align, green line in the bottom of figure (2.21), causing band bending at the interface

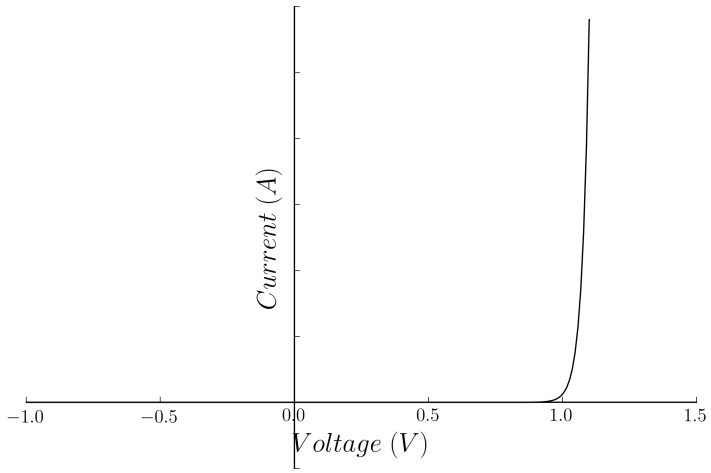


Figure 2.18: Non-Linear Current Response of a Diode. Current vs Voltage, IV Curve, of a diode. The curve is generated using equation (2.44). The current increases exponentially as the applied voltage approaches the built-in potential

of the two junction. The fermi levels align because of diffusion of holes from the p side to the n side and the diffusion of electrons from the n to p side. The flow of charges is called diffusion current. With the build up of the diffused charges on either side of the junction a field develops in the direction opposite the diffusion current. The direction of the field, $\overrightarrow{E}$, is indicated in the top of figure (2.21). This field creates a drift current from n to p, opposing the diffusing current. The field appears across a region of a certain width about the junction and there is an equilibrium potential difference across the region. This region is called the depletion region or space charge region and the potential difference is called built-in potential, $V_0$. The width of the depletion region is indicated as $W$ in the top of figure (2.21). The built-in potential, $V_0$, is shown in the bottom of figure (2.21) and is equivalent to the energy of the band bending at the interface of the two junctions. The depletion region, as the name suggests, is depleted of carriers or is insulating. At equilibrium no net current flows across the junction and there can be no net build-up of electrons or holes on either side of the junction as a function of time. The drift and diffusion currents must exactly cancel for each type of carrier. Equations (2.42) and (2.43)[5] are the expressions for $V_0$ and $W$. In these expressions $N_a$, $N_d$ and $n_i$ are the p, n doping concentration and the intrinsic carrier concentration. $k$, $T$ and $q$ are the Boltzmann constant, temperature and charge.

$$V_0 = \frac{kT}{q} ln\left(\frac{N_a N_d}{n_i^2}\right) \tag{2.42}$$

$$W = \sqrt{\frac{2\epsilon_r \epsilon_0 \left(V_0 - V\right)}{q}\left(\frac{1}{N_a} + \frac{1}{N_d}\right)} \tag{2.43}$$

The above description is for a zero applied potential across the junction. Applying

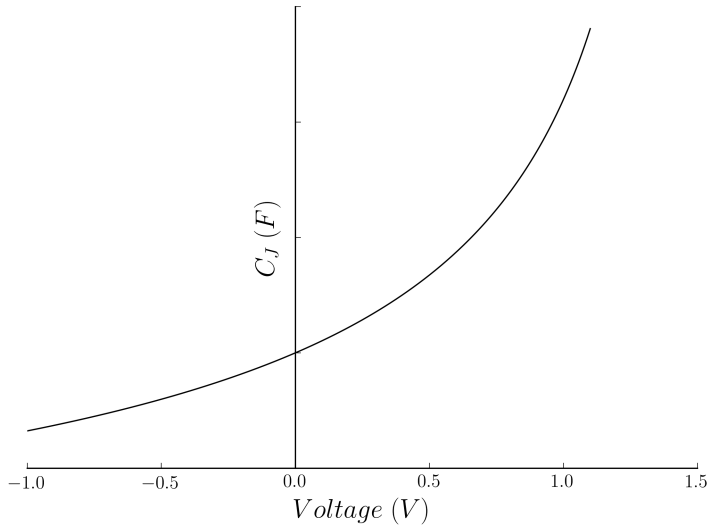


(a)

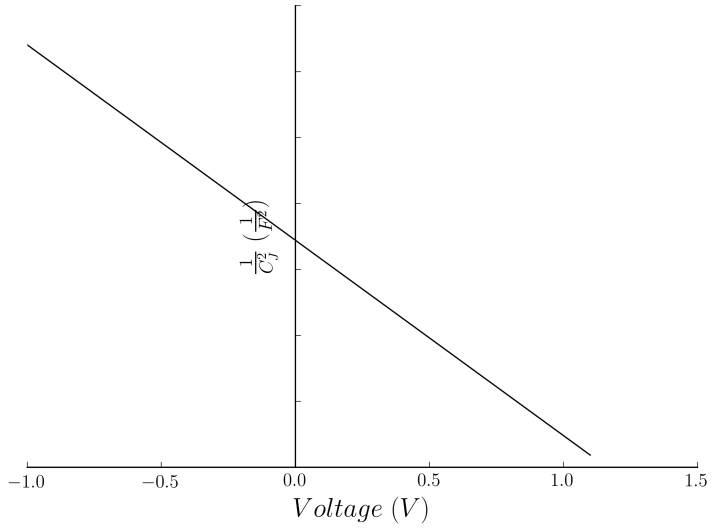


(b)

Figure 2.19: Capacitance Response of a Diode. (a)$C_J\,vs\,V$, (b)$\frac{1}{C_J^2}\,vs\,V$ (a) and (b) are generated using equation(2.45). As the applied voltage increases the capacitance increases or $\frac{1}{C_J^2}$ decreases

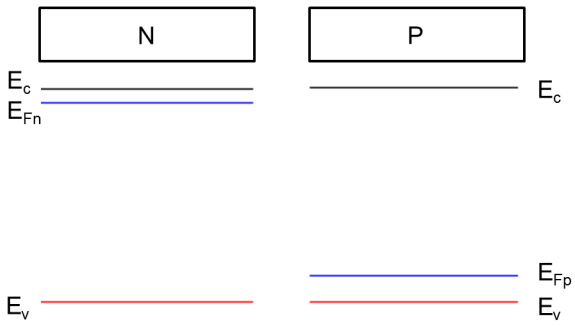


Figure 2.20: Isolated p and n type materials. $E_c$ and $E_v$ are the energy of the conduction and valence band. $E_{Fn}$ is the Fermi-Energy of the n-type material and $E_{Fp}$ is the fermi energy level of the p-type material. The rectangles on top of the respective bands are a cartoon indicating the doped semiconductor

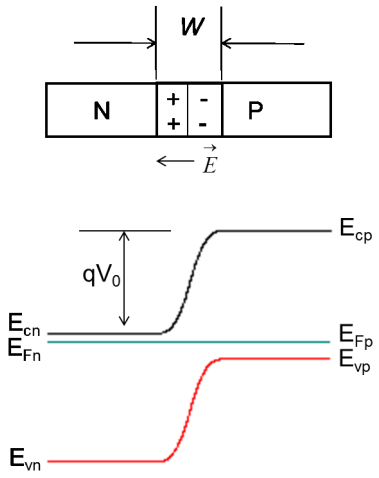


Figure 2.21: *pn* junction. The cartoon at the top of the figure shows the space charge or depletion region forms at the interface between the two doped semiconductors. This region has a width $W$, and a field, $\vec{E}$, across this region. At the bottom of the figure the energy bands of the *pn* junction away from the interface and at the interface are shown. The bands at the interface bend such that $E_{Fn}$ and $E_{Fp}$ align. This bending results in a contact potential $V_0$ and its associated $\overrightarrow{E}$

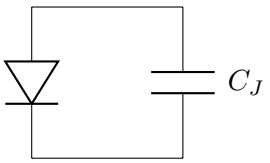


Figure 2.22: Diode equivalent circuit. $C_J$ is the junction capacitance

a potential across the junction either enhances or reduces the built-in potential. Enhancing the built-in potential increases the depletion width resulting in drift being the major contribution to current while reducing the potential barrier reduces the depletion width resulting in diffusion being the major contribution to the current. The reduction of the potential barrier causes an exponential rise of current for a small change in voltage; as illustrated in figure (2.18). Mathematically the current response is given in equation (2.44) where $I_{th}$ is the thermal current. Reduction in the built-in potential barrier is called forward bias while enhancement of the built-in potential is called reverse bias. It is worth noting that the drift current is independent of the applied potential and dependent on the amount of minority carriers in the junction. Hence the flat line in the reverse and the low forward bias regions. For an illuminated junction the drift current is dominant. This will be discussed in the section on photodiodes (2.4.3).

$$I = I_{th}\left(exp\left(\frac{qV}{kT}\right) - 1\right) \tag{2.44}$$

The capacitance of the junction, formally called junction capacitance, is a result of the depleted or the insulated region encapsulated on either side by a conducting region. This is the configuration of a parallel plate capacitor and for this configuration the capacitance is given as:

$$C_J = \frac{\epsilon_r \epsilon_0 A}{W(V)} = \frac{C_0}{\sqrt{1 - \frac{V}{V_0}}} \tag{2.45}$$

Reducing the thickness of the depletion region results in an increase of capacitance. Since the depletion width has a non-linear response with respect to the applied potential so does the junction capacitance. The capacitance increases as the inverse square root of the applied potential. This is illustrated in figure (2.19)(a). In figure (2.19)(b) $\frac{1}{(C_J)^2}$ is plotted showing that as the applied potential increases $\frac{1}{(C_J)^2}$ decreases linearly.

#### 2.4.1.1 Electrical Circuit

Figure (2.22) is the the equivalent circuit of a diode. The diode is related to the IV curve while $C_J$ is the junction or diode capacitance. The diode and its capacitance are in a parallel circuit configuration. A detailed explanation of this model is given in [5].

### 2.4.2 Heterojunction Diode

The discussion above is for a homojunction, i.e. the doped material is the same. A junction also forms when at least two doped or undoped semiconductors having two different bandgaps

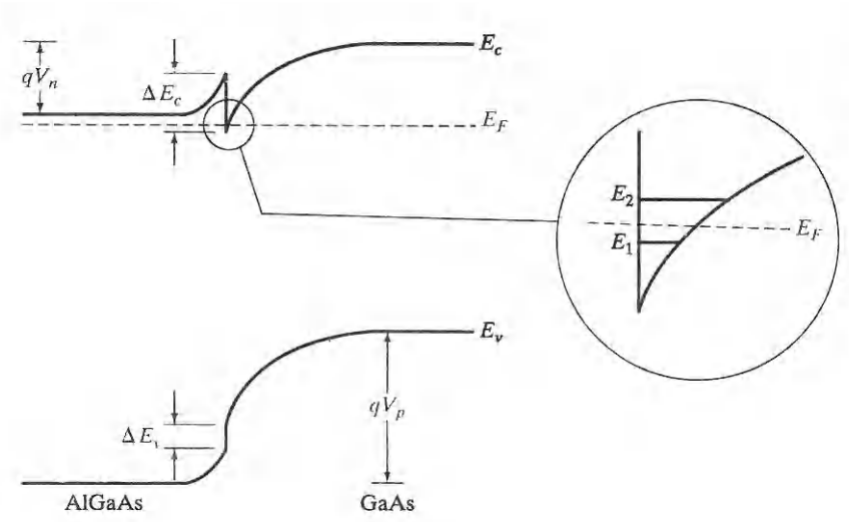


Figure 2.23: Heterojunction Band Discontinuity in the conduction band. A heterojunction between $N^+$-AlGaAs and lightly doped $GaAs$. A pile-up of electrons occur in the conduction band. This pile-up results in a potential well. If the potential well is thin then discrete states $E_1$ and $E_2$ are formed[5]

come in contact with each other. Such junctions are called heterojunctions. Similar to the homojunction $pn$ junction heterojunctions are also characterized by a built-in voltage $V_0$ and the charge transport equations resulting in drift and diffusion currents are also valid. However, unlike homo $pn$ junctions band discontinuities in heterojunctions occur leading to trapping or piling up of charge, figure (2.23). Charge carriers having energies greater than the barrier cross this barrier and contribute to the current. This current is called thermionic emission. The current density is: $J_n = AT^2 exp\left(\frac{-q\phi_B}{V_T}\right) exp\left(\frac{qV}{kT} - 1\right)$[5] where $A = \frac{4\pi q m^* k^2}{h^3}$ is known as the Richardson constant and $\phi_B$ is the barrier height. Thermionic emissions are prevalent in $n - n^+$ or $p - p^+$ heterojunctions.

In the event that the barrier height or the built-in potential is not large carriers can tunnel across the barrier instead of overcoming the potential. This type of current is called the tunneling current. The expression for the tunneling current density is: $J_n = qv_R n exp\left(-\frac{4}{3}\frac{\sqrt{2qm^*\phi_B}}{\hbar}L\right)$[5]

### 2.4.3 Photodiode

A photodiode responds to incident light by generating current. This current is called photogenerated current and is only generated if the energy of light is greater than the band-gap energy of the diode material, i.e. $hv \geq E_g$. Here $h$ and $\nu$ are planck's constant and frequency of light. The illumination results in the creation of electron-hold pairs (EHPs). If the EHPs are created in the depletion region or with in a diffusion length of the depletion region the electrons and holes are swept by the built-in field to the n and p regions adding to the existing thermally generated drift current. This optical generation current is given in equation (2.46) and is a function of the generation rate, $g_{op}$, and the geometry of the semiconductor. Equa-

tion (2.47) is the modified diode equation accounting for the photogenerated current, $I_{isc}$. The IV curve resulting from this equation is illustrated in figure (2.24). The nomenclature used in equation (2.46)is discussed in section (2.4.3.2.1). As indicated in the figure the curve can be separated into four quadrants. Depending on the intended application a photodiode is operated in either the third or the fourth quadrant. For applications where the intended use is for information transfer a photodiode is operated in the third quadrant because $C_J$ is small resulting in a low RC time constant or large bandwidth. The third quadrant is called the photoconductance quadrant. For applications requiring power delivery a photodiode is operated in the fourth quadrant. In this quadrant the junction voltage is positive while the current through the diode is negative. The product of the two results in negative power or power from the diode can be delivered to an external circuit. This quadrant is called the photovoltaic (PV) quadrant and is used for solar cells.

$$I_{isc} = qAg_{op}\left(L_p + L_n + W\right) \tag{2.46}$$

$$I_{D,1} = I_{th}\left[exp\left(\alpha V_D\right) - 1\right] - I_{isc} \tag{2.47}$$

where

$$\alpha = \frac{q}{kT}$$

The PV response of a diode to DC light is well developed[6] however a theoretical model for the photovoltaic response to modulated light has not been developed. Here this is developed and the model experimentally verified. The model, called AC-PV, is derived using the following:

1. The AC electrical circuit resulting from the structure of the diode, figure (2.22)
2. The single diode DC model of a PV cell

The single diode DC model is reviewed next. The objective is to highlight the details required for deriving the AC-PV model. A detailed explanation of this models is given elsewhere[6].

#### 2.4.3.1 Single Diode DC PV Model

As mentioned above a PV cell is operated in the 4th quadrant. Figure (2.26)(a) is the circuit representation of this shift while equation (2.47)[6] is the mathematical description of the circuit. In the circuit $R_L$ is the load resistance placed across the photodiode and $I_{D,1}$ is the current measured through $R_L$. $I_{D,1}$ is therefore affected by the value of, $R_L$. $R_L$ in conjunction with $I_{D,1}$ biases the diode with a value of $V_D = -I_{D,1}R_L$. This is termed the DC-bias point and will be used often in the derivation and experimental validation of the AC model. There are three DC-bias points of interest. These points are indicated in figure (2.25) and are achieved as follows:

1. Short-Circuit condition; $I_{D,1} = -I_{isc}$. This occurs when $R_L = 0$ leading to a measurement of the short-circuit current. Here $V_D = 0$

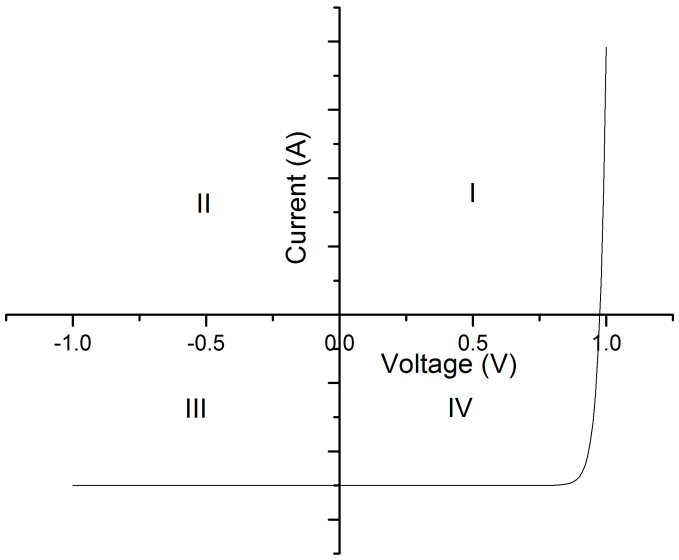


Figure 2.24: Current vs Voltage for an illuminated junction. Quadrant III and IV are called the photoconductance and photovoltage quadrants. The photoconductance quadrant is used for information transfer while the photovoltage quadrant is used to deliver power by converting optical power to electrical power

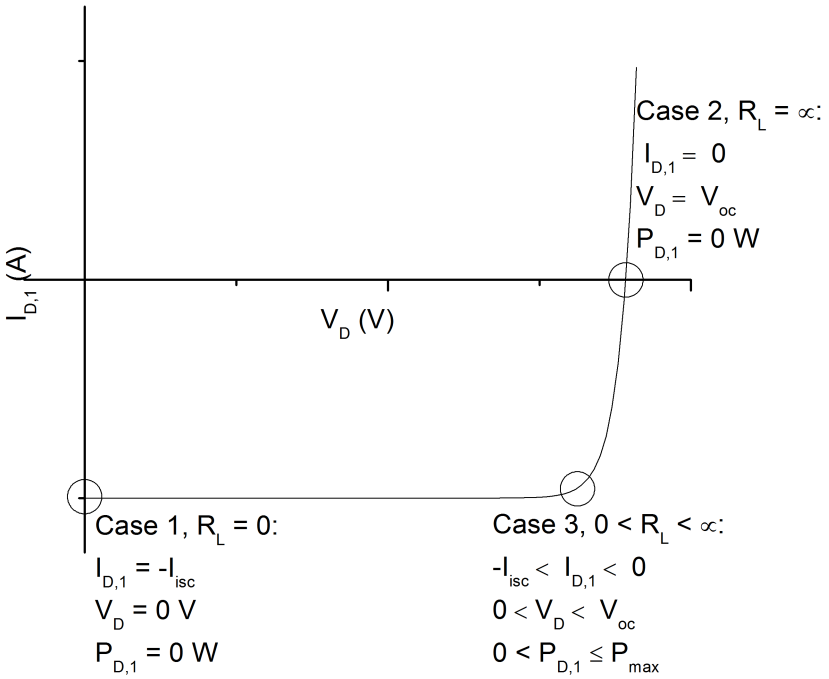


Figure 2.25: DC Bias Points. Illuminated Diode IV curve is plotted and three cases are indicated by open circles. The open circles indicate the DC bias points of interest, $V_D$, the value of load resistance, $R_L$ required and the resulting current, $I_{D,1}$ and power $P_{D,1}$

2. Open-Circuit condition; $I_{D,1} = 0$. This occurs when $R_L = \infty$ leading to a measurement of the open-circuit voltage, $V_{oc}$. Here $V_D = V_{oc}$ and the mathematical expression is:

$$V_{oc} = \frac{1}{\alpha} ln \left[ \frac{I_{isc}}{I_{th}} + 1 \right] \tag{2.48}$$

3. In between-case: $I_{isc} < I_{D,1} < 0$. This occurs when $0 < R_L < \infty$. Here $V_D$ is between 0 and $V_{oc}$, i.e. or $0 < V_D < V_{oc}$

The bias points are of particular importance because they indicate the minimum and maximum power that can be extracted from the photodiode. This power is also indicated in figure (2.25) with the symbol $P_{D,1}$. As is seen $P_{D,1}$ is a function of both $R_L$ and $I_{D,1}$. Using the discussed three DC bias points the power extracted at these points are:

1. Short-Circuit condition; $I_{D,1} = -I_{isc}$, $V_D = 0$ and $P_{D,1} = 0$
2. Open-Circuit condition; $I_{D,1} = 0$, $V_D = V_{oc}$ and $P_{D,1} = 0$
3. In between-case: $I_{isc} < I_{D,1} < 0$, $0 < V_D < V_{oc}$ and $0 < P_{D,1} < P_{max}$; where $P_{max} \sim |V_{oc} I_{sc}|$ and occurs for $R_L \sim \frac{V_{oc}}{I_{isc}}$

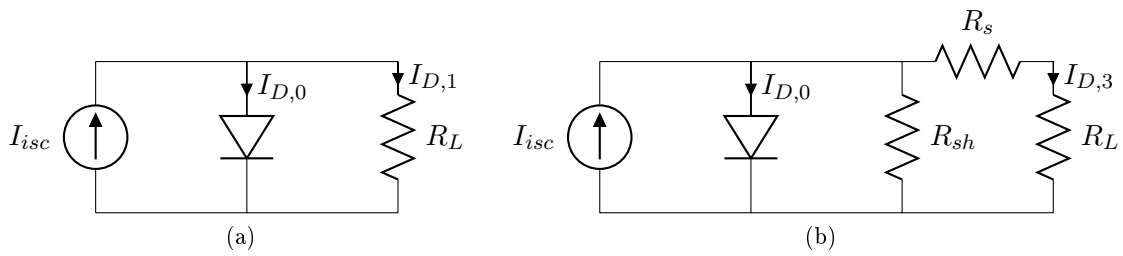


Figure 2.26: Single Diode DC PV Model: (a) Ideal circuit and (b) Real/Non-Ideal circuit. $I_{isc}$ is the photogenerated current. In the real circuit $R_{sh}$ and $R_s$ account for current losses due to manufacturing defects and poor contacts. $R_L$ is the load resistance. $I_{D,1}R_L$ or $I_{D,3}R_L$ biases the respective diode model at an operating point, $V_D$, on the illuminated IV curve given in figure (2.25) [6]

From equations (2.47) and (2.48), generally, as the intensity of light increases $I_{isc}$, $V_{oc}$ and $P_{D,1}$ increases.

In a real or non-ideal photodiode current losses exist which alter the diode IV curves. These losses are represented in terms of a shunt resistance across the diode, $R_{sh}$, and a series resistance, $R_s$, in series with the load resistance $R_L$ [6]. Figure (2.26)(b) is the diode circuit with these added components. Equation (2.49) is the altered diode equation with the losses taken into consideration. Here $R_3 = R_s + R_L$. Ref [6] details the affect of $R_{sh}$ and $R_s$. Generally $R_{sh}$ and $R_s$ will have the affect of reducing $I_{D,3}$ and $P_{D,3}$. The subscript 3 is used in equation (2.49) to keep consistency with the AC PV model, to be discussed next. In both the DC and AC models the subscript 3 indicates the load branch.

$$I_{D,3} = I_{th}\left[exp\left(\alpha\left(I_{D,3}R_3\right)\right) - 1\right] + \frac{I_{D,3}R_3}{R_{sh}} - I_{isc} = I_{th}\left[exp\left(\alpha V_D\right) - 1\right] + \frac{V_D}{R_{sh}} - I_{isc} \quad (2.49)$$

Equations (2.47) and (2.49) can be re-expressed as equations (2.51) and (2.52) for the ideal and the non-ideal diode models. In re-expressing $I_{D,1}$, $I_{D,3}$ is $I_{D,1}$ multiplied by ratio of resistances as determined by circuit analysis. This re-expression has the advantage that analyzing the non-ideal model is as simple as the ideal model. The re-expression of equation (2.47) is achieved by using the definition for the open-circuit voltage, equation (2.48), which makes it possible to re-arrange for $I_{th}$:

$$I_{th} = \frac{I_{isc}}{exp\left(\alpha V_{oc}\right) - 1} \quad (2.50)$$

The advantage of this is $I_{th}$ is expressed in terms of measurable parameters: $I_{isc}$ and $V_{oc}$.

$$I_{D,1} = I_{isc}\left[\frac{exp\left(\alpha V_D\right) - exp\left(\alpha V_{oc}\right)}{exp\left(\alpha V_{oc}\right) - 1}\right] = I_{isc}\left[\frac{exp\left(\alpha V_D\right) - A}{A - 1}\right] \quad (2.51)$$

where $V_D = -I_{D,1}R_L$ and $A = exp\left(\alpha V_{oc}\right)$.
Through circuit analysis:

$$I_{D,3} = I_{isc}\left[\frac{exp\left(\alpha V_D\right) - exp\left(\alpha V_{oc}\right)}{exp\left(\alpha V_{oc}\right) - 1}\right]\frac{R_t}{R_3} = I_{isc}\left[\frac{exp\left(\alpha V_D\right) - A}{A - 1}\right]\frac{R_t}{R_3} \tag{2.52}$$

where $R_3$ is the resistance of the load branch, $V_D = -I_{D,3}R_3 = -I_{D,3}\left(R_s + R_L\right)$ and $R_t$ is the total resistance.

#### 2.4.3.2 Single Diode AC PV Model

Using the mathematical expressions for the single diode DC PV model the mathematical expressions for the AC generated current and power are derived for the single diode AC PV model. Before delving into the derivations the nomenclature used is discussed next then a literature review is presented specifically focusing on the ideas listed above.

**2.4.3.2.1 Nomenclature** The general circuit for the AC model is given in figure (2.27)(a). In this figure and equations above and below $i_{D,x}$ ,equation (2.53), is the total current which is the superposition of DC and AC currents $I_{D,x}$ and $i_{d,x}$, respectively. Here the nomenclature used is as follows - capital letters are chosen for DC while small letters are chosen for AC. The combination of small and large letters indicate the variable has both DC and AC components. x in the subscript is a numerical value for the branches of the circuit right of the diode. For the diode branch x has a value of 0 and the value of x increases to the right of the diode.

$$i_{D,x} = I_{D,x} + i_{d,x} \tag{2.53}$$

**2.4.3.2.2 Literature Review** The works reviewed here are a thesis and a paper published by the same author [47, 48]. The scarcity of work on the topic, as will be elucidated in the review, arises from the fact that operating a photodiode in its 4th quadrant results in reducing the bandwidth of the photodetector. Photodetectors, as mentioned above, are operated in the 3rd quadrant in order to achieve large bandwidths. For modulations below 10 MHz a photodiode can be operated at $I_{isc}$. This is also elucidated below.

In the thesis Silicon Solar Cell as an optical detector[47] and the paper[48] the objective of the work is to demonstrate that silicon solar cells can be used as an economical alternative to standard photodiodes in low to medium data rate systems. The author achieves this by measuring the current and voltage response of a solar cell to light modulated from DC up to 100 MHz. The response was measured at two bias points: $I_{isc}$ and $V_{oc}$. These two points are chosen in order to use the DC equations (2.48) and (2.47), along with the small signal approximation to derive an expression for the AC photovoltage at $V_{oc}$ and the AC photocurrent at $i_{d,3}$. The derived expression are: $\partial V_D = \frac{V_{oc}}{T} - \frac{\partial I_{isc}}{\alpha I_{isc}}$ and $\partial I_{d,3} = \partial I_{isc}$. Here $\partial V_D$ and $\partial I_{d,3}$ are the small signal AC voltage and AC short circuit current and $T$ is the temperature. It was concluded that since the AC voltage is inversely related to the short circuit current this limits the use of operating a photodetctor at $V_{oc}$. However; operating at $I_{isc}$ the AC photocurrent exhibits a perfectly linear response. This linear response is experimentally verified but the theoretical assertion at $V_{oc}$ is not.

To analyze the response speed of the photodiode an equivalent circuit model similar to figure (2.27)(b) was stated. The time constant is given by: $\tau = R_t C_J$. $R_t$ is the combination of load, shunt and series resistance. At the $I_{isc}$ bias point a cutoff frequency of 3.75 MHz was measured while at $V_{oc}$ bias point a cutoff frequency of 909 Hz was measured. The reduction at $V_{oc}$ is due to the fact that $R_t$ has as value of $25\,k\Omega$ while at $I_{isc}$ $R_t$ has a value of $6\Omega$. In both cases $C_J = 7.0\,nF$ which is the value of the junction capacitance of the solar cell.

In conclusion the author showed that bandwidth decreases when operating at $V_{oc}$ and that the AC response at $I_{isc}$ is linear. The shortcomings of the author's works are:

1. A general expression for the AC generated current is not derived
2. The response of the solar cell is measured only for a resistive load
3. Power extraction and maximum power point are not discussed

In the next section a general expressions for current and power are derived for the AC PV model. These equation are then verified for resistive and reactive loads.

**2.4.3.2.3 AC PV Model** The general circuit for the AC model is given in figure (2.27)(a). This model is similar to the real single diode DC PV model discussed above with the addition of $i_{isc_1}$, the modulated current resulting from the modulation of light, $C_J$ is the junction capacitance and $Z_L$ is the load impedance. To reduce mathematical complexity the AC real/non-ideal single diode PV circuit, figure (2.27)(a), is reduced to AC single diode ideal PV circuit, figure (2.27)(b), by combining $R_{sh}$, $R_s$, $C_J$ and $Z_L$ to $Z_t$ via circuit analysis. Please note that $Z_t$ is a function of voltage because of $C_J$, equation (2.45). The reduction of the real/non-ideal model to ideal model follows from the previous section. As a result of the reduction $i_{d,1}$ is now derived and $i_{d,3}$ is recovered via circuit analysis. The equations are derived in the limit that the AC current is smaller than the DC current, i.e. $i_{isc_1} < I_{isc}$. Equations (2.65) and (2.67) are the expressions for $i_{d,1}$ and $i_{d,3}$. Their derivation is discussed next.

The derivation of $i_{d,1}$ begins by taking the derivative of the ideal diode equation (2.47) yielding:

$$dI = BdV - dI_{isc} \tag{2.54}$$

where

$$B = \alpha I_{th} exp\left(\alpha V_D\right) = \frac{\alpha I_{isc} exp\left(\alpha V_D\right)}{exp\left(\alpha V_{oc}\right) - 1} = \frac{\alpha I_{isc} exp\left(\alpha V_D\right)}{A - 1} \tag{2.55}$$

Here $dI$, $dV$ and $dI_{isc}$ are the AC current, voltage and short-circuit current. These terms are assumed to be sinusoidal; i.e. a sinusoidal modulation of light is only considered. Equations (2.56), (2.57) and (2.58) are the expressions for these terms where $\phi$ is the phase between the real and imaginary parts of the impedance, $Z_t$ and $\phi_1$ is the phase between $i_{d,1}$ and $i_{isc_1}$. In the expression for $B$, equation (2.55), equation (2.50) is substituted for $I_{th}$. The motivation for doing this is to reduce the number of independent parameters. $B$ has units of $\frac{1}{\Omega}$.

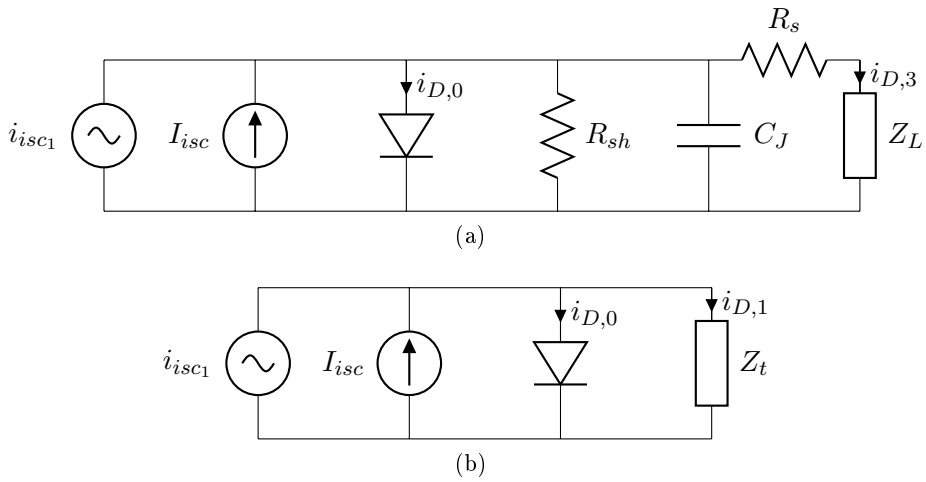


Figure 2.27: AC Single Diode Model. (a) Real/Non Ideal AC PV circuit (b) Ideal AC PV circuit. (a) and (b) are the extensions of the DC PV models, given in figures (2.26)(a) and (b), with the addition of junction capacitance, $C_J$, AC short circuit current, $i_{isc_1}$, and load impedance, $Z_L$. (a) is reduced to (b) by combining $R_{sh}$, $C_J$, $R_s$ and $Z_L$ into a total resistance $Z_t$.

$$dI_{isc} = i_{isc_1} exp\left(j\omega t\right) \tag{2.56}$$

$$dI = i_{d,1} exp\left(j\left(\omega t + \phi_1\right)\right) \tag{2.57}$$

$$dV = v_d exp\left(j\left(\omega t + \phi + \phi_1\right)\right) \tag{2.58}$$

Substituting (2.56)-(2.58) into equation (2.54) results in equation (2.59) after simplification. Equations (2.60) and (2.61) are the real and imaginary parts of equation (2.59). Here $v_d = -i_{d,1} Z_t$ and the expression for $cos\phi$ and $sin\phi$ are determined for equations (2.62) and (2.63). These expressions are voltage dependent because $C_J$, equation (2.45), is voltage dependent. Next an expression for $\phi_1$ is derived.

$$i_{d,1} exp\left(j\phi_1\right) = B v_d exp\left(j\left(\phi + \phi_1\right)\right) - i_{isc_1} \tag{2.59}$$

$$i_{d,1} cos\phi_1 = B v_d cos\left(\phi + \phi_1\right) - i_{isc_1} \tag{2.60}$$

$$i_{d,1} sin\phi_1 = B v_d sin\left(\phi + \phi_1\right) \tag{2.61}$$

$$R = Re\left(Z_t\right) = Z_t cos\phi \tag{2.62}$$

$$X = Im\left(Z_t\right) = Z_t sin\phi \tag{2.63}$$

Using equation (2.61), the sine sum identity and the expression for $v_d$; $\phi_1$ is derived below and the final expression is given in equation (2.64):

$$i_{d,1}sin\left(\phi_1\right) = Bv_d sin\left(\phi + \phi_1\right)$$

$$i_{d,1}sin\phi_1 = -Bi_{d,1}Z_t\left[sin\phi cos\phi_1 + sin\phi_1 cos\phi\right]$$

$$i_{d,1}sin\phi_1 = -Bi_{d,1}\left[Xcos\phi_1 + Rsin\phi_1\right]$$

$$sin\phi_1 = -BXcos\phi_1 - BRsin\phi_1$$

$$BXcos\phi_1 = -BRsin\phi_1 - sin\phi_1$$

$$BXcos\phi_1 = -sin\phi_1\left[BR + 1\right]$$

$$tan\phi_1 = \frac{-BX}{1+BR} \tag{2.64}$$

$$sin\phi_1 = \frac{-BX}{\sqrt{\left(1+BR\right)^2 + \left(BX\right)^2}},\ cos\phi_1 = \frac{1+BR}{\sqrt{\left(1+BR\right)^2 + \left(BX\right)^2}}$$

Using equations (2.60), (2.64), the cosine sum identity and the expression for $v_d$ the expression for $i_{d,1}$ is derived below and given in equation(2.65):

$$i_{d,1}cos\phi_1 = -Bi_{d,1}Z_t\left[cos\phi cos\phi_1 - sin\phi sin\phi_1\right] - i_{isc_1}$$

$$i_{d,1}cos\phi_1 = -Bi_{d,1}\left[Z_t cos\phi cos\phi_1 - Z_t sin\phi sin\phi_1\right] - i_{isc_1}$$

$$i_{d,1}cos\phi_1 = -Bi_{d,1}\left[Rcos\phi_1 - Xsin\phi_1\right] - i_{isc_1}$$

$$i_{isc_1} = -Bi_{d,1}\left[Rcos\phi_1 - Xsin\phi_1\right] - i_{d,1}cos\phi_1$$

$$i_{isc_1} = -Bi_{d,1}Rcos\phi_1 - i_{d,1}cos\phi_1 + Bi_{d,1}Xsin\phi_1$$

$$i_{isc_1} = -i_{d,1}cos\phi_1\left[BR + 1\right] + Bi_{d,1}Xsin\phi_1$$

$$i_{isc_1} = -i_{d,1}\left(\frac{1+BR}{\sqrt{\left(1+BR\right)^2 + \left(BX\right)^2}}\right)\left[BR+1\right] + i_{d,1}\left(\frac{-BX}{\sqrt{\left(1+BR\right)^2 + \left(BX\right)^2}}\right)BX$$

$$i_{isc_1} = -i_{d,1}\left(\frac{(1+BR)^2}{\sqrt{(1+BR)^2+(BX)^2}}\right) - i_{d,1}\left(\frac{(BX)^2}{\sqrt{(1+BR)^2+(BX)^2}}\right)$$

$$i_{d,1} = \frac{-i_{isc_1}}{\sqrt{(1+BR(w))^2+(BX(w))^2}} \tag{2.65}$$

In the above expression $R$ and $X$ are replaced with $R(\omega)$ and $X(\omega)$ to explicitly show that these parameters are dependent on angular frequency, $\omega$. The dimensionless form of $i_{d,1}$ is:

$$\frac{i_{d,1}}{i_{isc_1}} = \frac{-1}{\sqrt{(1+BR(\omega))^2+(BX(\omega))^2}} \tag{2.66}$$

Using equation (2.65) equation (2.67) is the expression for $i_{d,3}$. This equation is derived from circuit analysis. Here $Z_t$ is the total impedance and $Z_3$ is the impedance of the load branch, i.e. $Z_3 = R_s + Z_L$.

$$i_{d,3} = \frac{-i_{isc_1}}{\sqrt{(1+BR(\omega))^2+(BX(\omega))^2}}\frac{Z_t}{Z_3} \tag{2.67}$$

Both $i_{d,1}$ and $i_{d,3}$ are functions of four parameters - $V_D$, $I_{isc}$, $i_{isc_1}$, and $w$, i.e. the DC bias point, the DC short circuit current, the AC short circuit current and the modulation frequency of light. The equations for $i_{d,1}$ and $i_{d,3}$ indicate an increase in AC current as $i_{isc_1}$ increases and as $V_D$ or $I_{isc}$ decreases.

Equation (2.53) for the small signal approximation can be thought of as an AC current with a DC offset. In a measurement the root mean square (RMS) of this current is measured and is:

$$i_{D,x} = \sqrt{I_{D,x}^2 + i_{d,x}^2} \tag{2.68}$$

**2.4.3.2.4 AC Power** As mentioned a PV device is used to extract DC power and as such can also be used to extract AC power. Having derived $i_{D,x}$ the AC power is:

$$p_{D,x} = i_{D,x}^2 Z \tag{2.69}$$

where $Z$ is either the total impedance, $Z_t$, or the load impedance $Z_L$. This is explored in the next section.

Like DC power AC power can be dissipative if the impedance is purely resistive but unlike DC power AC power can be non-dissipative and occurs for a purely reactive load. This non-dissipative power is called reactive power. A reactive power stores energy for half a cycle and returns the energy back to the source the rest half of the cycle. Hence there is no net transfer of energy to the load. In the photodiode case the source is an illuminating object external to the photodiode. A finite energy is returned back to the source via radiation but most of the energy will be dissipated by the diode. This is understood as follows:

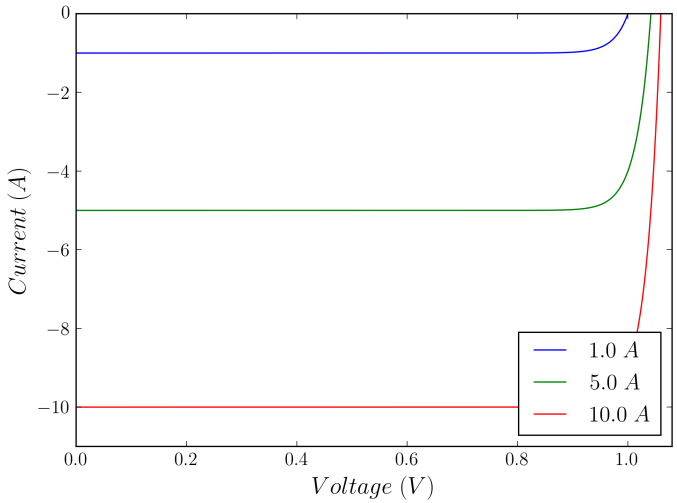


Figure 2.28: Theoretical IV Curves. The curves are generated using equation (2.51) for the following $I_{isc}$ values 1.00 ,5.0 and 10.0 $A$. The associated $V_{oc}$ values are 1.00, 1.04 and 1.06 $V$. The increase in $V_{oc}$ is logarithmic with $I_{isc}$ as expected from equation (2.48)

1. A real photodiode has some finite resistance, $R_s$ or $R_{sh}$; hence the absorbed AC optical power will always be dissipated
2. In the case of a diode having $R_s = 0$ and $R_{sh} = \infty$ the AC voltage resulting from the AC current flowing through the reactive element will bias the diode causing power dissipation

**2.4.3.2.5 Analytical Predictions** In this part predictions of equations (2.51), (2.66) and (2.69) are given for three regimes: purely resistive, purely reactive and mixture of both resistive and reactive. The ideal case is considered because of ease of analysis. However the non-ideal response is easily recovered through circuit analysis. In all three regimes an IV curve is required for determining the bias point. Hence these curves are first discussed.

**2.4.3.2.5.1 Diode IV Curves** The diode IV curves given in figure (2.28) are generated using equation (2.51). In these curves $I_{isc}$ is increased and as expected $V_{oc}$ also increases. The increase in $V_{oc}$ is logarithmic with $I_{isc}$ as expected from equation (2.48). Three different values for $I_{isc}$ are chosen 1.00, 5.0 and 10.0 $A$ and the corresponding values for $V_{oc}$ are 1.00, 1.04 and 1.06 $V$.

**2.4.3.2.5.2 Resistive Regime**

**DC Analysis**

Figure (2.29) is the above IV curves with lines intersecting the curves. These lines are called DC load lines and are determined using ohm's law for $R_L$ equivalent to 0.1, 0.2 and

1.0 Ω. The intersection of the DC load lines with the IV curves is a graphical method used to determine the DC operating point or the DC bias, $V_D$. Figure (2.30) is a plot of the DC bias point, $I_{D,1}R_L \, vs \, I_{isc}R_L$. This plot collapses the distinct IV curves of figure (2.29) with loads lines into an overlapping family of curves. The motivation for this plot comes from equation (2.51). Equation (2.51) is a function of both $I_{isc}$ and $R_L$. A 3-D plot could be made but by combining $I_{isc}$ and $R_L$, as a product, a 2D plot is made. The advantage of combining the two as a product will become clear in the next few lines. The x-axis in this figure is $I_{isc}R_L$ while the y-axis is a product of $I_{D,1}$ and $R_L$. This product is the bias voltage, $V_D$. The plot indicates that for a fixed $I_{isc}$ or $R_L$ as $R_L$ or $I_{isc}$ increases $V_D$ initially increases linearly. For a certain value of $R_L$ or $I_{isc}$ a saturation point is reached after which an increase in either $R_L$ or $I_{isc}$ results in a logarithmic increase in $V_D$. These two regions are separated by a knee. The knee in these plots corresponds to the knee in the IV curves, figure (2.29), and indicate that an increasing $I_{isc}$ corresponds to a decreasing $R_L$. Mathematically this can be understood as follows:

$$I_{isc}R_L = V$$

Using the approximation that the bend in the knee occurs when $V \sim V_{oc}$ the above equation is:

$$I_{isc}R_L = V_{oc}$$

Using the expression for $V_{oc}$; equation (2.48):

$$I_{isc}R_L = \frac{1}{\alpha} \ln \left[ \frac{I_{isc}}{I_{th}} + 1 \right]$$

Rearranging for $R_L$:

$$R_L = \frac{\left( \frac{1}{\alpha} \ln \left[ \frac{I_{isc}}{I_{th}} + 1 \right] \right)}{I_{isc}} \tag{2.70}$$

Therefore as $I_{isc}$ increases the denominator increases the same amount while the numerator increases logarithmically hence $R_L$ decreases. For the $I_{isc}$ chosen, 1.0, 5.0, and 10.0 $A$ the respective $R_L$ values at the knee are 1.0, 0.2 and 0.11 Ω. As discussed below the knee region is also the region for extracting maximum power. Figure (2.30) is generated by sweeping DC load lines, with resistance values in the range of 0.01 to 2.00 Ω, across the three IV curves.

Having showed a collapsed plot for $V_D$ figures (2.31)(a) and (b) is a collapsed plot for $\frac{I_{D,1}}{I_{isc}}$. The x-axis is the logarithm of $I_{isc}R_L$ and the y-axis is $I_{D,1}$ divided by its respective $I_{isc}$. Figure (2.31)(a) indicates that for a fixed $I_{isc}$ or $R_L$ as $R_L$ or $I_{isc}$ increases $I_{D,1}$ is initially equivalent to $I_{isc}$. After a certain value for $R_L$ or $I_{isc}$ an increase in either results in a decrease in $I_{D,1}$. This decrease in $I_{D,1}$ corresponds to the section of the IV curves past the knee. Figure (2.31)(b) is the exploded section of figure (2.31)(a) highlighting the lack of overlap in these curves. These curves elucidate two ideas:

1. As $I_{isc}$ increases the knee moves to the right and $R_L$ at the knee point decreases. This is mathematically shown in equation (2.70)

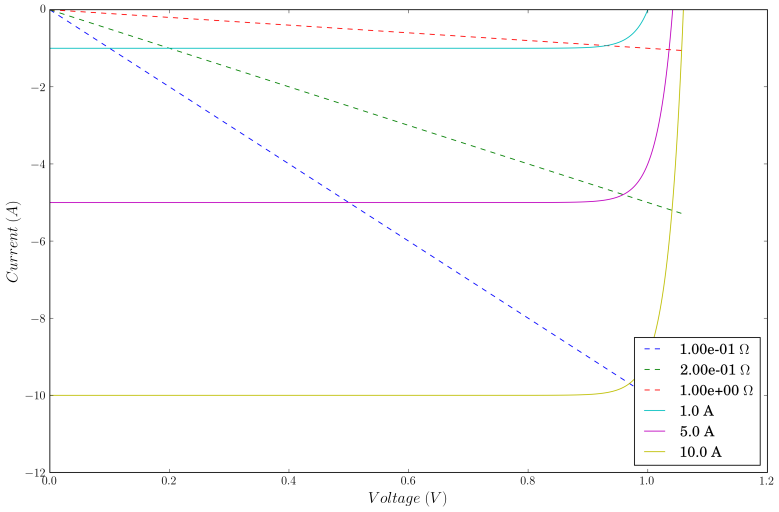


Figure 2.29: IV Curves with load lines. The load lines are for $R_L$ of 0.1, 0.2 and 1.0 $\Omega$

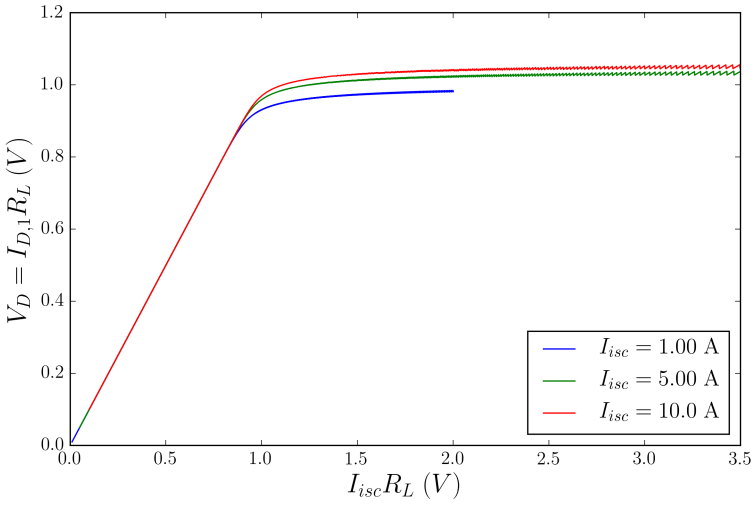


Figure 2.30: $I_{D,1}R_L\, vs\, I_{isc}R_L$ for $I_{isc} = 1$, 5 and 10 $A$. Two linear regions exist separated by a knee. The voltage to the left of the knee increases linearly with $I_{isc}$ ,or optical power, while the voltage to the right of the knee increases logarithmically with $I_{isc}$. As $I_{isc}$ increases the knee shifts to the right and $V_D$ increases

2. Lack of overlap after the knee region and the separation between the curves decreases as $I_{isc}$ increases. The former is attributed to the difference in $V_{oc}$ and the latter is attributed to the logarithmic increase in $V_{oc}$ as $I_{isc}$ increases. This relationship is captured in equation (2.48). As $I_{isc}$ increases from 1.0 to 5.0 $A$ $V_{oc}$ increases by roughly 4.0% while an increase of $I_{isc}$ from 5.0 to 10.0 $A$ results in an increase of $V_{oc}$ by roughly 1.7%. Hence the decrease in separation between the 5.0 $A$ and 10.0 $A$ curves.

### DC Power

The total power is given in equation (2.69). Here only the DC case is considered, i.e. $i_{d,1} = 0$. Hence equation (2.69) reduces to:

$$P_{D,1} = I_{D,1}^2 R_L$$

$P_{D,1}$ is a function of both $I_{isc}$ and $R_L$ and is plotted in figure (2.32). The x-axis is the logarithm of $I_{isc}R_L$ and the y-axis is $P_{D,1}$. Also plotted is the maximum power point as determined from equation (2.71)[49]. The plot show that $P_{D,1}$ increases as $I_{isc}$ increases which is as expected.

$$P_{max} = I_{isc}V_{oc}\left[\frac{\alpha V_{oc} - \ln\left(\alpha V_{oc} + 0.72\right)}{\alpha V_{oc} + 1}\right] \tag{2.71}$$

Figure (2.33) combines all the above plots, i.e. $IV$, $I_{D,1}R_L$, $\frac{I_{D,1}}{I_{isc}}$ and $P_{D,1}$, for the $I = 1.0\,A$ and $V_{oc} = 1.0\,V$ case into a single plot. This is done to emphasize the point that the knee corresponds to the maximum power that can be extracted. The intersection of the vertical and horizontal dotted lines in this figure indicates the maximum power point on the $IV$ curve. The voltage at the maximum power point is[49]:

$$V_{mp} = V_{oc}\left[\frac{\alpha V_{oc} - \ln\left(\alpha V_{oc} + 0.72\right)}{\alpha V_{oc} + 1}\right] \tag{2.72}$$

### AC Analysis

Following the same analysis as the DC case figure (2.34)(a) and (b) are plots of $\frac{i_{d,1}}{i_{isc_1}}$ given in equation (2.73). This equation is derived from equation (2.66) by setting $X(w) = 0$ to reflect the purely resistive case considered. Similar to the DC case the x-axis is the product of $I_{isc}R_L$ and is chosen because $i_{d,1}$ is a function of both these variables. The y-axis is $i_{d,1}$ divided by $i_{isc_1}$. Figure (2.34)(b) is the exploded section of figure (2.34)(a) highlighting the separation between the curves. As explained in the DC case above the separation occurs because of differences in $V_{oc}$. Similar to the DC case as $I_{isc}$ increases the separation between the curves decreases. The values of $V_D$ used to generate these plots are acquired from figure (2.30).

$$\frac{i_{d,1}}{i_{isc_1}} = -\frac{1}{1 + BR_L} = \frac{exp\left(\alpha V_{oc}\right) - 1}{exp\left(\alpha V_{oc}\right) + \alpha I_{isc} exp\left(\alpha V_D\right) R_L - 1} \tag{2.73}$$

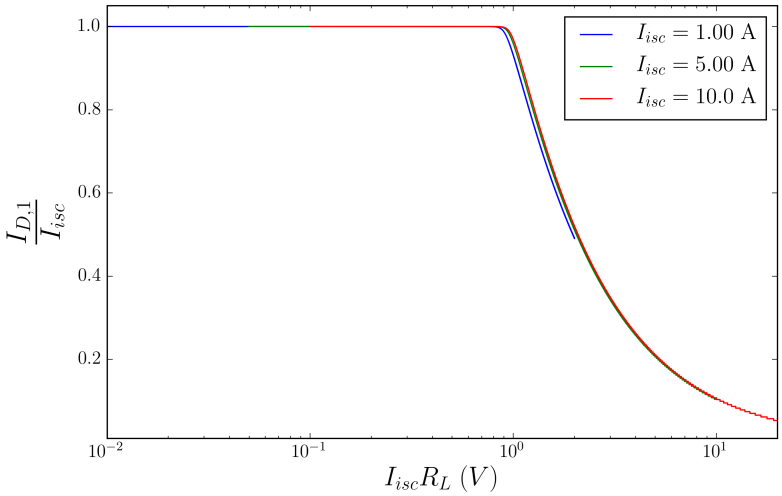


(a)

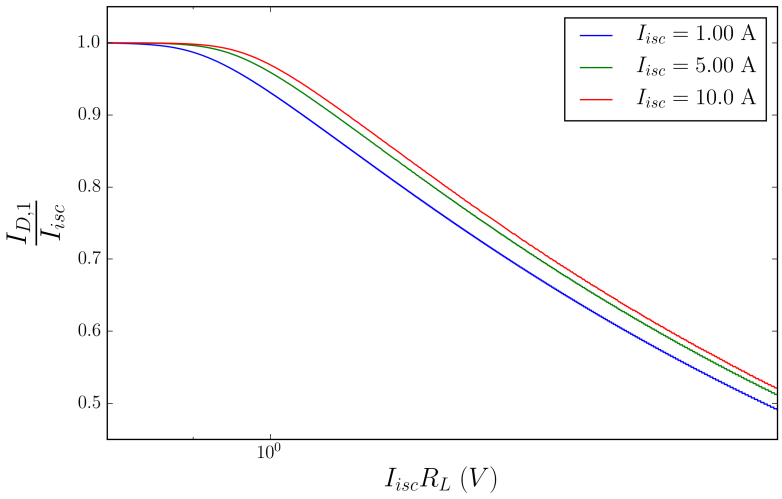


(b)

Figure 2.31: $\frac{I_{D,1}}{I_{isc}}$ *vs* $I_{isc}R_L$ for $I_{isc} = 1$, 5 and 10 $A$. (a) Two distinct regions exist separated by a knee. To the left of the knee $\frac{I_{D,1}}{I_{isc}} = 1$ and to the right of the knee $\frac{I_{D,1}}{I_{isc}}$ decreases. The former corresponds to the flat or horizontal part of the IV curve, figure (2.28), while the latter corresponds to the vertical part of the IV curve. The lack of overlap in $\frac{I_{D,1}}{I_{isc}}$ past the knee is due to differences in $V_{oc}$. As $I_{isc}$ increases the knee shifts to the right. This is emphasized in (b) which is the exploded section of (a) around the knee

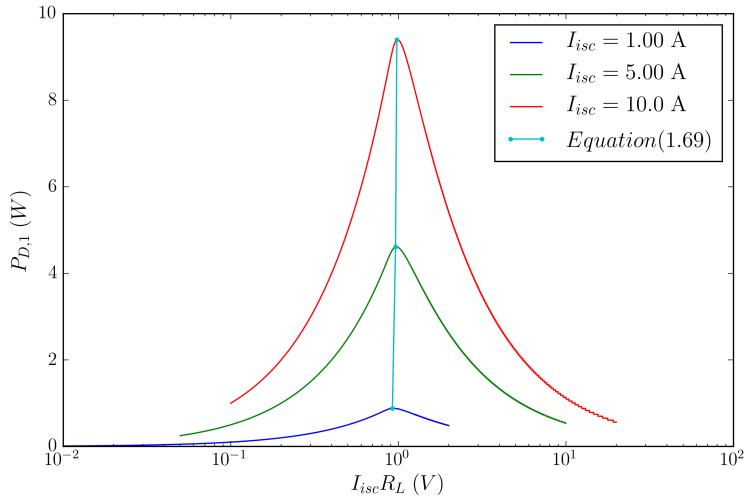


Figure 2.32: $P_{D,1}$ *vs* $I_{isc}R_L$ As $I_{isc}$ or optical power increases the extracted DC power, $P_{D,1}$, also increases. The maximum power point is indicated on the plots and is determined using equation (2.71). Using this equation maximum power point is extracted for $R_L$ = 0.88, 0.18 and 0.09 $\Omega$ for $I_{isc} = 1$, 5 and 10 $A$

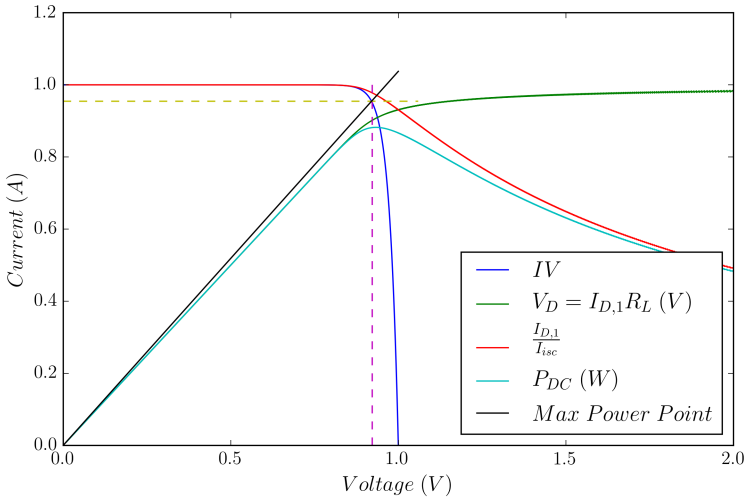


Figure 2.33: $IV$, $I_{D,1}R_L$, $\frac{I_{D,1}}{I_{isc}}$ and $P_{D,1}$ are plotted for $I = 1.0\,A$ and $V_{oc} = 1.0\,V$. The knee indicates the maximum power that can be extracted. The dotted line indicates the maximum power point on the IV curve

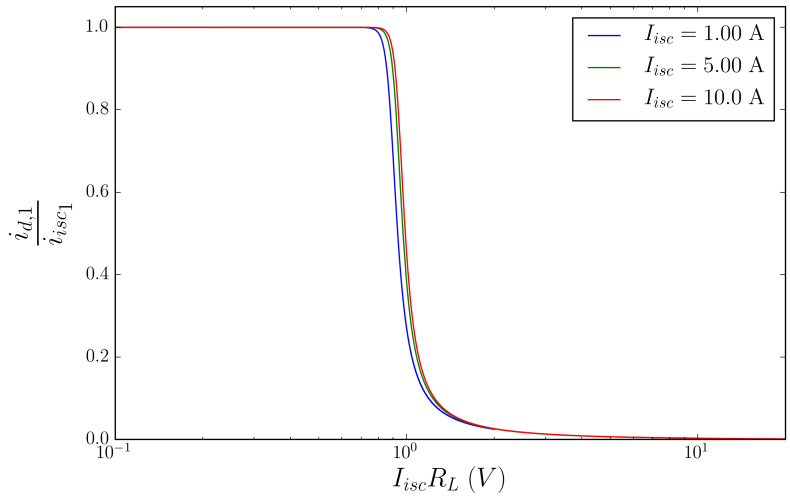


(a)

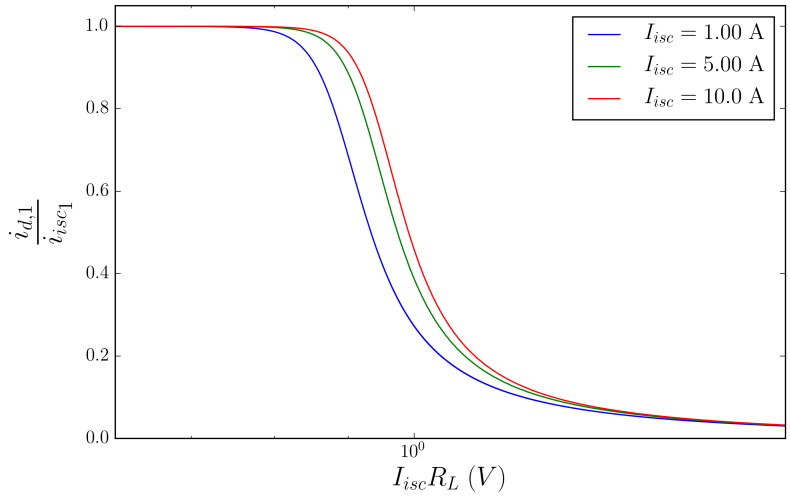


(b)

Figure 2.34: $\frac{i_{d,1}}{I_{isc_1}}$ $vs$ $I_{isc}R_L$ This plot is similar to DC plot in figure (2.31)(a). Similar to the DC case two distinct regions are separated by a knee. The lack of overlap right of the knee is due to the differences in $V_{oc}$. This is emphasized in (b) which is the exploded section of (a) in the vicinity of the knee

Figure (2.35) is a comparison of $\frac{I_{D,1}}{I_{isc}}$ and $\frac{i_{d,1}}{i_{isc_1}}$ for the IV curve having $I_{isc} = 1.0\,A$ and $V_{oc} = 1.0\,V$. The x-axis, unlike the previous plots above, is simply $I_{isc}R$. The non-logarithmic choice is made to highlight the difference between the two curves. The differences between the two are:

1. The knee for $\frac{i_{d,1}}{i_{isc_1}}$ case is shifted towards lower $I_{isc}R_L$ values

2. The $\frac{i_{d,1}}{i_{isc_1}}$ current reduces faster than the DC current. This can be understood by substituting for $B$, equation (2.55), and $V_D = -I_{D,1}R_L$ into equation (2.73) reducing this equation to:

$$\frac{i_{d,1}}{i_{isc_1}} = -\frac{exp\left(\alpha V_{oc}\right) I_{D,1}}{exp\left(\alpha V_{oc}\right) I_{D,1} - \alpha V I_{isc} exp\left(\alpha V_D\right)}$$

Substituting equation (2.51) for $I_{D,1}$ in the denominator and using the approximation $A >> 1$ reduces the above equation to:

$$\frac{i_{d,1}}{i_{isc_1}} = -\frac{exp\left(\alpha V_{oc}\right) I_{D,1}}{I_{isc}\left(exp\left(\alpha V_D\right) - exp\left(\alpha V_{oc}\right)\right) - \alpha V_D I_{isc} exp\left(\alpha V_D\right)}$$

Factoring $\left(\frac{I_{D,1}}{I_{Isc}}\right)$ and $exp\left(\alpha V_D\right)$:

$$\frac{i_{d,1}}{i_{isc_1}} = -\left(\frac{I_{D,1}}{I_{isc}}\right) \frac{exp\left(\alpha V_{oc}\right)}{exp\left(\alpha V_D\right)\left[1 - \alpha V_D\right] - exp\left(\alpha V_{oc}\right)}$$

$$\frac{i_{d,1}}{i_{isc_1}} = -\left(\frac{I_{D,1}}{I_{isc}}\right) C \tag{2.74}$$

where

$$C = \frac{exp\left(\alpha\left(V_{oc} - V_D\right)\right)}{\left[1 - \alpha V_D\right] - exp\left(\alpha\left(V_{oc} - V_D\right)\right)} \tag{2.75}$$

As is seen from equation (2.74) $\frac{i_{d,1}}{i_{isc_1}}$ differs $\frac{I_{D,1}}{I_{isc}}$ by the $C$ factor. This $C$ factor is a function of $V_{oc}$ and $V_D$. For low $V_D\,C's$ numerator and denominator are equivalent to each other; hence the normalized AC and DC currents, as illustrated in figure (2.35), are the same. As $V_D$ increases the exponential term in both the numerator and denominator of equation (2.75) decreases exponentially but the $\alpha V_D$ term in the denominator increases linearly. This exponential decrease and linear increase in the denominator results in the denominator being greater than the numerator and hence the $C$ factor decreasing. Therefore using equation (2.74) the dimensionless AC response, $\frac{i_{d,1}}{i_{isc_1}}$ can be predicted from the DC response of the photodiode.

This shifting of the knee in figure (2.35) is indicative of a shift in the maximum power point. This is explored in the next section.

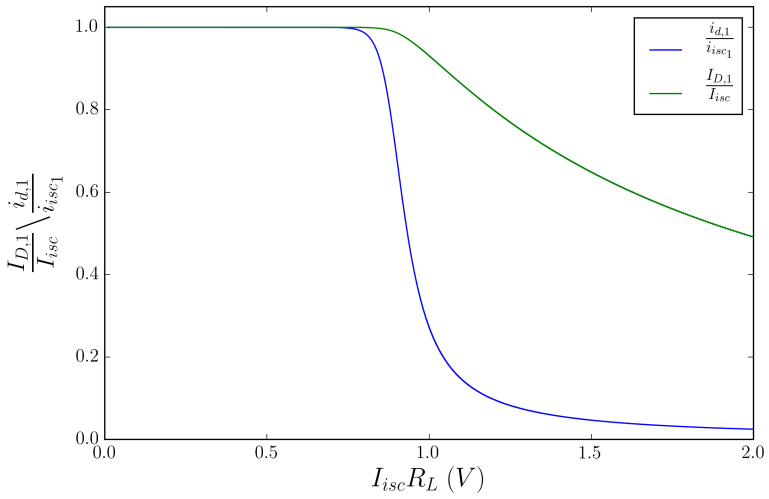


Figure 2.35: $\frac{I_{D,1}}{I_{isc}}\ vs\ I_{isc}R$ and $\frac{i_{d,1}}{i_{isc_1}}\ vs\ I_{isc}R$ for the IV curve having $I_{isc} = 1.0\,A$. The knee for $\frac{i_{d,1}}{i_{isc_1}}$ is shifted towards lower $I_{isc}R_L$ and $\frac{i_{d,1}}{i_{isc_1}}$ reduces faster than $\frac{I_{D,1}}{I_{isc}}$

### AC Power

The total power is given in equation (2.69). Considering only the AC case, i.e. $I_{D,1} = 0$ equation (2.69) reduces to:

$$p_{D,1} = p_{d,1} = i_{d,1}^2 R_L$$

$$p_{D,1} = p_{d,1} = i_{d,1}^2 R_L = \left(\frac{i_{isc_1}}{1 + BR_L}\right)^2 R_L$$

substituting for $B$

$$p_{d,1} = \left(\frac{Ai_{isc_1}}{A + \alpha I_{isc} R exp\,(\alpha V)}\right)^2 R_L \tag{2.76}$$

Figure (2.36) is a plot of $p_{d,1}$ vs $I_{isc}R_L$. In this plot $i_{isc_1}$ is chosen to be 10% of $I_{isc}$ in keeping with the assumption that the optically generated AC current is lower than the optically generated DC current. The x-axis is the logarithm of $I_{isc}R_L$. The plot shows $p_{d,1}$ increases as $i_{isc_1}$ increases.

Figure (2.37) is a plot comparing normalized DC and AC power. Here the x-axis is just $I_{isc}R_L$. The maximum power point for the AC case has shifted to the left by roughly 8.83% from the DC case. The shift for the AC power point is given in equation (2.77) and is derived below. Table (2.4) compares the voltage required to achieve maximum power point for the AC and DC cases.

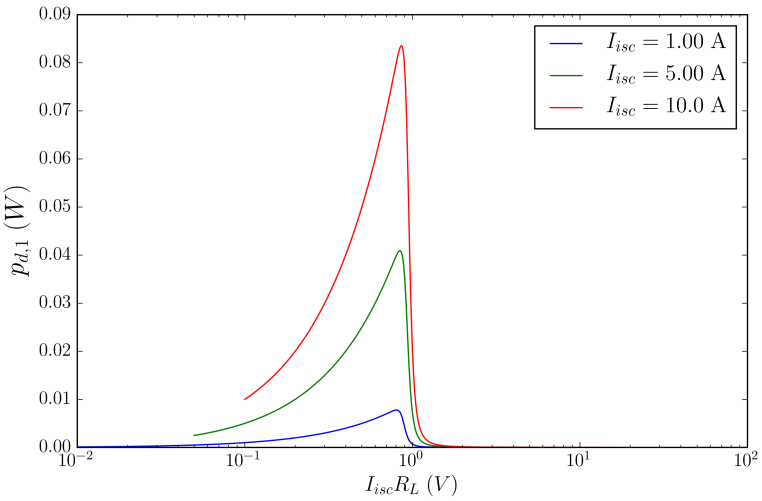


Figure 2.36: $p_{d,1}\, vs\, I_{isc}R_L$ The plot is generated using equation (2.76) where $i_{isc_1}$ is 10% of $I_{isc}$. 10% is chosen in keeping with the small signal approximation used to derive equation (2.65). The plot shows that $p_{d,1}$ increases as $i_{isc_1}$ increases

| $V_{mp}^{DC}$ $(V)$ | $V_{mp}^{AC}$ $(V)$ | $\Delta V_{mp}$ $(V)$ |
|---|---|---|
| $8.821\times10^{-1}$ | $8.042\times10^{-1}$ | $7.791\times10^{-2}$ |
| $9.221\times10^{-1}$ | $8.427\times10^{-1}$ | $7.992\times10^{-2}$ |
| $9.400\times10^{-1}$ | $8.606\times10^{-1}$ | $7.941\times10^{-2}$ |

Table 2.4: AC and DC comparison of voltage at the maximum power point. The values are determined graphically. The subscript $mp$ stands for maximum power point. $\Delta V_{mp} = V_{mp}^{DC} - V_{mp}^{AC}$

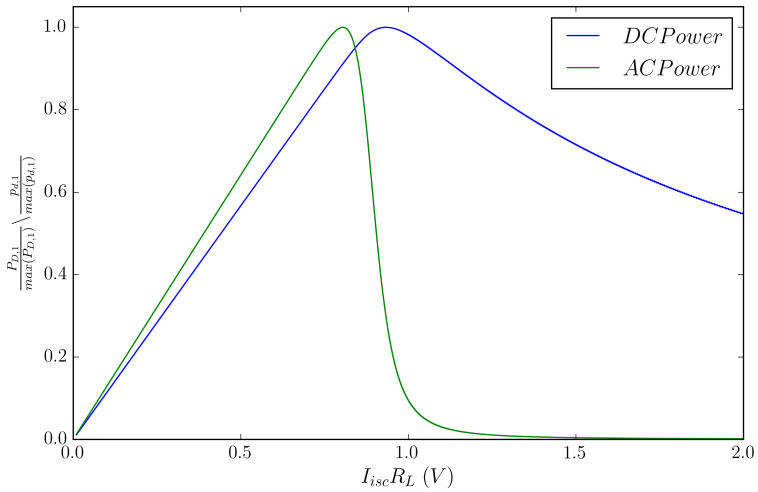


Figure 2.37: $\frac{P_{D,1}}{max(P_{D,1})}\ vs\ I_{isc}R_L$ and $\frac{p_{d,1}}{max(p_{d,1})}\ vs\ I_{isc}R_L$. The maximum power point for the AC power does not coincide with the DC maximum power point. For the AC case the power point is shifted to the left by roughly 8.83% which indicates a reduction in $R_L$ or $I_{isc}$ if $I_{isc}$ or $R_L$ is kept fixed

An expression for the voltage resulting in the maximum power point for the AC case is derived by taking the derivative of equation (2.76) with respect to voltage. But first, substituting equation (2.51) for $I_{D,1}$ and $R_L = \frac{-V}{I_{D,1}}$ yields:

$$p_{d,1} = \left(\frac{Ai_{isc_1}}{A + \alpha I_{isc}R_L exp\left(\alpha V\right)}\right)^2 R_L = \frac{-i_{isc_1}^2 VA}{I_{isc}\left(exp\left(\alpha V\right) - A\right)\left(1 - \frac{\alpha V exp(\alpha V)}{exp(\alpha V) - A}\right)^2}$$

Taking the derivative of the above expression with respect to voltage yields:

$$\begin{aligned}\frac{dp_{d,1}}{dV} &= \frac{-i_{isc_1}^2 A}{I_{isc}\left(exp\left(\alpha V\right) - A\right)\left(1 - \frac{\alpha V exp(\alpha V)}{exp(\alpha V) - A}\right)^2} + \frac{\alpha V i_{isc_1}^2 A exp\left(\alpha V\right)}{I_{isc}\left(exp\left(\alpha V\right) - A\right)^2\left(1 - \frac{\alpha V exp(\alpha V)}{exp(\alpha V) - A}\right)^2} \\ &+ \frac{2V i_{isc_1}^2 A\left(\frac{\alpha^2 V exp(\alpha V)}{exp(\alpha V) - A} - \frac{\alpha exp(\alpha V)}{exp(\alpha V) - A} + \frac{\alpha^2 V (exp(\alpha V))^2}{(exp(\alpha V) - A)^2}\right)}{I_{isc}\left(exp\left(\alpha V\right) - A\right)\left(1 - \frac{\alpha V exp(\alpha V)}{exp(\alpha V) - A}\right)^3}\end{aligned}$$

Setting $\frac{dp_{d,1}}{dV} = 0$ and substituting $A = exp\left(\alpha V_{oc}\right)$ reduces the above expression to:

$$0 = \begin{array}{c} \frac{-exp(\alpha V_{oc})}{(exp(\alpha V)-exp(\alpha V_{oc}))\left(1-\frac{\alpha V exp(\alpha V)}{exp(\alpha V)-exp(\alpha V_{oc})}\right)^2} + \\ \frac{\alpha V exp(\alpha V_{oc}) exp(\alpha V)}{(exp(\alpha V)-exp(\alpha V_{oc}))^2\left(1-\frac{\alpha V exp(\alpha V)}{exp(\alpha V)-exp(\alpha V_{oc})}\right)^2} + \\ \frac{2V exp(\alpha V_{oc})\left(\frac{\alpha^2 V exp(\alpha V)}{exp(\alpha V)-exp(\alpha V_{oc})} - \frac{\alpha exp(\alpha V)}{exp(\alpha V)-exp(\alpha V_{oc})} + \frac{\alpha^2 V (exp(\alpha V))^2}{(exp(\alpha V)-exp(\alpha V_{oc}))^2}\right)}{(exp(\alpha V)-exp(\alpha V_{oc}))\left(1-\frac{\alpha V exp(\alpha V)}{exp(\alpha V)-exp(\alpha V_{oc})}\right)^3} \end{array}$$

Making the following substitutions: $\Delta V = V_{oc} - V$ further simplifies the above expression:

$$0 = \begin{array}{c} \frac{-exp(\alpha\Delta V - 1 + \alpha V_{oc})(-1+exp(\alpha V_{oc}))^2}{(-1+exp(\alpha\Delta V)+\alpha V)^2} + \\ \frac{\alpha V exp(\alpha\Delta V - 2 + 2\alpha V_{oc})(-1+exp(\alpha V_{oc}))^2}{(-1+exp(\alpha\Delta V)+\alpha V)^2} - \\ \frac{2\alpha V exp(\alpha\Delta V)(-1+exp(\alpha\Delta V))^3(\alpha V exp(\alpha V_{oc})-1+exp(\alpha V_{oc}))}{(-1+exp(\alpha V_{oc}))^3(-1+exp(\alpha\Delta V)+\alpha V)^3} \end{array}$$

The motivation for this substitution is to determine the amount of shift from $V_{oc}$ where $V_{oc}$ is assumed to be the maximum power point. The assumption of $V_{oc}$ being the maximum power point arises from assuming the diode IV curve's knee has zero curvature resulting in a rectangular IV curve. If $\Delta V = 0$ the AC and DC maximum power points are the same. Multiplying the expression by $(-1 + exp(\alpha V_{oc}))^3 (-1 + exp(\alpha\Delta V) + \alpha V)^3$, making the approximation $-1 + exp(\alpha V_{oc}) \sim exp(\alpha V_{oc})$ and the substitution $1 - exp(\alpha\Delta V) = D$ results in the following expression:

$$0 = -exp(-1 + 3\alpha V_{oc})(D + \alpha V) + \alpha V exp(-2 + 4\alpha V_{oc})(D + \alpha V) - 2\alpha V D(\alpha V + 1)$$

Solving this expression for $D$ yields:

$$D = \frac{\alpha V exp(2\alpha V_{oc})(-exp(-1 + \alpha V_{oc}) + \alpha V exp(-2 + 2\alpha V_{oc}))}{2\alpha V(1 + \alpha V) + exp(-1 + 3\alpha V_{oc}) - \alpha V exp(-2 + 4\alpha V_{oc})}$$

Solving for $\Delta V$:

$$\Delta V = \frac{1}{\alpha} ln\left(1 - \frac{\alpha V exp(2\alpha V_{oc})(-exp(-1 + \alpha V_{oc}) + \alpha V exp(-2 + 2\alpha V_{oc}))}{2\alpha V(1 + \alpha V) + exp(-1 + 3\alpha V_{oc}) - \alpha V exp(-2 + 4\alpha V_{oc})}\right)$$

$$V_{oc} = V + \frac{1}{\alpha} ln\left(1 - \frac{\alpha V exp(2\alpha V_{oc})(-exp(-1 + \alpha V_{oc}) + \alpha V exp(-2 + 2\alpha V_{oc}))}{2\alpha V(1 + \alpha V) + exp(-1 + 3\alpha V_{oc}) - \alpha V exp(-2 + 4\alpha V_{oc})}\right) \quad (2.77)$$

Using the approximation: $\alpha V_{oc} >> 1$

$$V_{oc} = V + \frac{1}{\alpha} ln\left(1 - \frac{\alpha V exp(2\alpha V_{oc})(-exp(\alpha V_{oc}) + \alpha V exp(2\alpha V_{oc}))}{2(\alpha V)^2 + exp(3\alpha V_{oc}) - \alpha V exp(4\alpha V_{oc})}\right)$$

| $V_{mp}^{DC}$ $(V)$ | $V_{mp}^{AC}$ $(V)$ | $\Delta V_{mp}$ $(V)$ |
|---|---|---|
| 1.000 | $9.072\times10^{-1}$ | $9.280\times10^{-2}$ |
| 1.042 | $9.481\times10^{-1}$ | $9.340\times10^{-2}$ |
| 1.060 | $9.657\times10^{-1}$ | $9.430\times10^{-2}$ |

Table 2.5: DC and AC maximum power point.$V_{mp}^{DC}$is approximated to $V_{oc}$. The same definition as used in table 2.4 is carried over

Table (2.5) are the values for $\Delta V$ and show that the AC maximum power point is lower than the DC maximum power point. The AC maximum power point is shifted by roughly 9.28% of the DC maximum power point. Comparing table (2.4) and (2.5) the predictions made by equation (2.5) do not match the graphical predictions. This is expected because it was assumed that the maximum power point is at $V_{oc}$. However the shift in the AC maximum power point predicted by the equation is close to shift acquired via the graphical method, i.e. 9.28% shift is predicted and via graphical methods a shift of 8.83% is shown.

**DC and AC Power** Accounting for both DC and AC power the total power dissipated is $p_{D,1} = \left(I_{D,1}^2 + \frac{i_{d,1}^2}{2}\right) R_L \sim I_{D,1}^2 R_L$ because $\frac{i_{d,1}^2}{2}$ is smaller than $I_{D,1}^2$. This is the DC power case discussed above.

**2.4.3.2.5.3 Reactive Regime:** The reactive regime is defined as the load being either capacitive or inductive.

**DC Analysis** A capacitor in DC is an open circuit or infinite resistance. Therefore; a capacitive load biases the photodiode at the open circuit point $V_D = V_{oc}$ and $I_D = 0\,A$. An inductor in DC is a short circuit or zero resistance. Therefore an inductive load biases the photodiode at the short circuit point $V_d = 0\,V$ and $I_{D,1} = I_{isc}$.

**AC Analysis** The AC current, $i_{d,1}$equation (2.65) reduces to:

$$i_{d,1} = -\frac{i_{isc_1}}{\sqrt{1 + (BX)^2}} \tag{2.78}$$

where $B = \frac{\alpha I_{isc} exp(\alpha V_{oc})}{exp(\alpha V_{oc})-1}$ for a capacitive load and $B = \frac{\alpha I_{isc}}{exp(\alpha V_{oc})-1}$ for an inductive load. The $B$ parameter for a capacitive load is greater than the inductive load by $exp\,(\alpha V_{oc})$. For similar magnitude of $X$ $i_{d,1}$ for the capacitive load will be less than the inductive load. The dimensionless form of equation (2.78) $\frac{i_{d,1}}{i_{isc_1}}$, is plotted in figure (2.38). The x-axis is the logarithm of $I_{isc}Z_L$ and is chosen because $i_{d,1}$ is a function of $I_{isc}$ and $Z_L = X$. This is similar to what was done in the resistive case. The shape of $\frac{i_{d,1}}{i_{isc_1}}$ is similar to the shape of the resistive case. This is expected because equation (2.78) is similar to equation (2.73). These plots are generated for the IV curve having the following parameters: $I_{isc} = 1.0\,A$ and $V_{oc} = 1.0\,V$. Here $Z_L$ is swept by varying the frequency.

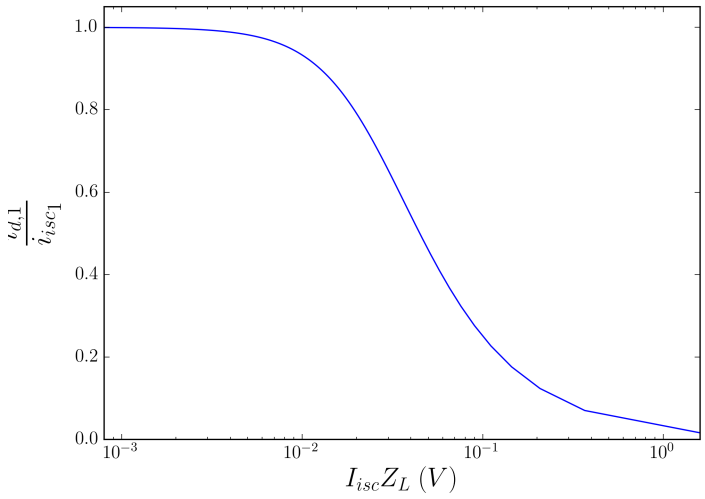


Figure 2.38: $\frac{i_{d,1}}{i_{isc_1}}\ vs\ I_{isc}Z_L$ The shape of the curve is similar to the resistive curve. $\frac{i_{d,1}}{i_{isc_1}}$ is generated using equation (2.78) and the parameters: $I_{isc} = 1.0\,A$ and $V_{oc} = 1.0\,V$. Here $Z_L$ is swept by varying the frequency

**Power Analysis** As mentioned above power is not dissipated in reactive elements but transferred back to the source. For the capacitive and inductive cases the total power, equation (2.69), reduces to $p_{D,1} = \frac{i_{d,1}^2}{\sqrt{2}}\frac{1}{wc}$ and $p_{D,1} = \sqrt{I_{isc}^2 + \frac{i_{d,1}^2}{2}}\,(wL)$, respectively. These are the amount of power that are either radiated away or could be delivered to a potential load. These are not plotted because dissipated power is of interest.

**2.4.3.2.5.4 Mixture case: Resistive and Reactive** Here the response of the photodiode is studied between the two extrema discussed above. The load circuit considered is a resistor $R$ in parallel with a capacitor having an impedance $X$. The IV curve considered has an $I_{isc} = 1.0\,A$ and $V_{oc} = 1.0\,V$. In the analysis the reactive element is $X = Rtan\phi$ where $\phi$ is the phase between $R$ and $X$. For the parallel circuit considered the real and the imaginary impedance are $R\,(w) = \frac{RX^2}{R^2+X^2}$ and $X\,(w) = \frac{-R^2X}{R^2+X^2}$. For $\phi = 0$ the circuit is purely resistive while for $\phi = \frac{\pi}{2}$ the circuit is purely reactive.

**DC Analysis** In DC the capacitor branch is an open circuit and hence the resistive branch dominates. This is the purely resistive case discussed above.

**AC Analysis:** Figure (2.39) is a plot of the AC current $\frac{i_{d,1}}{i_{isc_1}}\ vs\ I_{isc}Z_L$. This plot is generated using equation (2.66). As is seen from the figure an increasing phase results in a shift of the knee to the left. This is expected because an increasing phase results in $V_D$ approaching $V_{oc}$ which causes the $B$ parameter in the denominator of equation (2.66) to become large hence resulting in the shifting of the knee for lower values of $I_{isc}Z_L$.

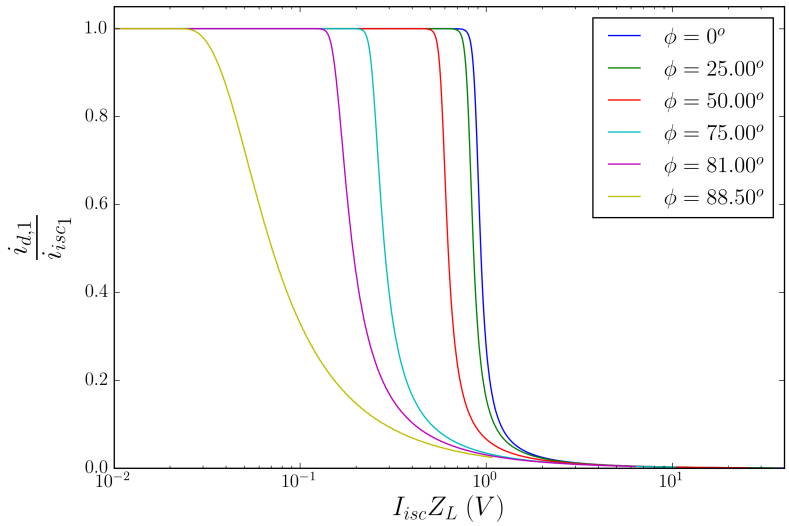


Figure 2.39: $\frac{i_{d,1}}{i_{isc_1}}\ vs\ I_{isc}Z_L$. The plot is generated for a load comprising of a resistor $R$ in parallel with a reactive element $X = Rtan\phi$ and for the IV curves having $I_{isc} = 1.0\,A$ and $V_{oc} = 1.0\,V$. For $\phi = 0$ the circuit is purely resistive and for $\phi = \frac{\pi}{2}$ the circuit is purely capacitive. The knee shifts to the left as $\phi$ increases indicating a shift towards larger $R_L$and therefore towards $V_{oc}$

**Power:** The total power from equation (2.69) is: $p_{D,1}^2 = I_{D,1}^2 R + i_{d,1}^2 R\,(w)$. As mentioned above the case for power dissipation is only considered. This condition reduces $Z\,(w)$ to $R\,(w)$.

**DC Analysis** The same argument holds as above, i.e in DC only the purely resistive branch needs to be considered. The analysis is the same as for the purely resistive case.

**AC Analysis** Figure (2.40) is a plot of $p_{d,1}\ vs\ I_{isc}Z_L$. The x-axis is the logarithm of $I_{isc}Z_L$. Similar to the resistive case for generating this plot $i_{isc_1}$ is chosen to be 10% of $I_{isc}$. Two important points arise:

1. The power dissipated decreases as phase increases
2. The maximum power point shifts to the left or for lower values of $I_{isc}Z_L$

Both are expected because as phase increases the impedance of the reactive branch decreases therefore the circuit becomes reactive. A reactive circuit does not dissipate power.

## 2.5 Conclusion

In this chapter, a brief discussion on the physics of resonators, flexural deformations, piezoelectricity and semiconductor junctions was given. Using the concept of *pn* junctions and band gaps the single diode DC PV model was introduced. From this model an equation

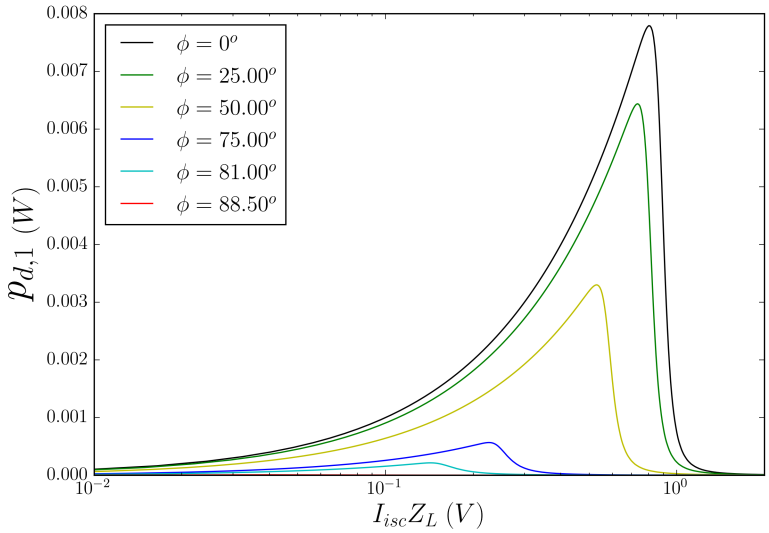


Figure 2.40: $p_{d,1}\, vs\, I_{isc}Z_L$ Power dissipation decreases as the phase increases and the maximum power shifts to the left. The plot is generated for a load comprising of a resistor $R$ in parallel with a reactive element $X = Rtan\phi$ and for the IV curves having $I_{isc} = 1.0\,A$ and $V_{oc} = 1.0\,V$. For $\phi = 0$ the circuit is purely resistive and hence maximum power is dissipated. For $\phi = \frac{\pi}{2}$ the circuit is purely capacitive and zero power is dissipated

was derived that predicts the AC response of a photodiode operated in the fourth or PV quadrant. This equation predicts the expected current and power resulting from a resistive and/or reactive loads and to changes in both DC and AC optical powers. A summary of the predictions are:

1. For a resistive load:
   (a) The AC maximum power point is at lower bias voltage, $V_D$, than for DC
   (b) From the DC IV curves the dimensionless AC current response $\frac{i_{d,1}}{i_{isc_1}}$ can be predicted using the $C$ parameter. The $C$ parameter is a function of two DC parameters - the open circuit voltage, $V_{oc}$ and $V_D$
2. For a reactive load zero power is extracted
3. Extracted AC electrical power decreases non-linearly with an increase of DC optical intensity and increases quadratically with an increase of incident AC optical intensity

The above stated physics and developed physical models are used to design a torsional resonator in GaAs. Using this torsional resonator GaAs's piezoelectric and opto-piezoelectric material properties are demonstrated. In table (2.6) a breakdown of the physics used in the following chapters is given along with the theoretical and experimental objectives for each chapter.

| Chapter Number | Physics used | Objective |
|---|---|---|
| 3 | AC PV Model | To validate the derived model for a resistive and capacitive load |
| 4 | Cantilever modes, bimorphs, *pn* and heterojunctions | Demonstrate and validate the electrical drive and response of the torsional modes using the piezoelectric and inverse piezoelectric effect |
| 5 | Bimorphs, *pn* and heterojunctions; specifically varying the thickness of the depletion region by an applied bias | Demonstrate and validate the interaction between the depletion region and the piezoelectric strain in the linear and non-linear regimes. This is done through electrical drive and detect. Here, the thickness of the depletion regions and hence the piezoelectric strain is varied by an applied DC bias |
| 6 | Bimorphs, *pn* and heterojunctions, AC PV model. For the *pn* and heterojunctions, like above, the varying of the thickness of the depletion region by an applied bias is used | Demonstrate and validate the optical driving of the torsional modes and the interaction between the depletion region and the optically induced piezoelectric strain in the linear regime. As above, the depletion regions and hence the piezoelectric strain is varied by an applied DC bias |

Table 2.6: Physics used and the objectives for the respective chapters

# Chapter 3

# AC PV Model

## 3.1 Introduction

In this chapter equation (2.66) is verified in the resistive and capacitive regimes. Two photodiodes, Newport 818-SL and 818-BB-20, are used to validate the predictions. 818-SL is used for resistive loads while 818-BB-20 is used for capacitive loads. 818-SL is used for resistive loads because it is easily biased with resistors having values between 10s of $\Omega$ to a few $k\Omega$. For 818-BB-20 resistance values between several 100s of $k\Omega$ to 10s of $M\Omega$ are required for biasing the diode. Lower resistances are required for 818-SL because it has a larger photodetector area. The larger photodetector area results in a larger optical generated current for the same bias. The diameter of 818-SL and 818-BB-20 are $10\,mm$[50] and $0.40\,mm$[51] respectively. The larger photodetector area however results in a larger junction capacitance, $C_J$. This $C_J$ limits the bandwidth of the photodetector. Therefore for low frequency experiments 818-SL is used while for high frequency experiments 818-BB-20 is used.

These diodes are illuminated using Marktech MT7318A-UR-A red LED having a dominant wavelength of $643\,nm$. The circuit for driving the LED, figure (3.1), consists of a DC and an AC voltage source. The DC source biases the LED establishing a constant emitted intensity while the AC source modulates the emitted intensity about this bias.

## 3.2 Experiment

Given the circuit in figure (2.27)(a) $i_{D,3}$ is measured. Through circuit analysis $i_{D,1}$ is determined. This requires numerical values for $I_{isc}$, $i_{isc_1}$, $V_{oc}$, $R_{sh}$, $R_s$ and $C_J$. $I_{isc}$, $i_{isc_1}$ and

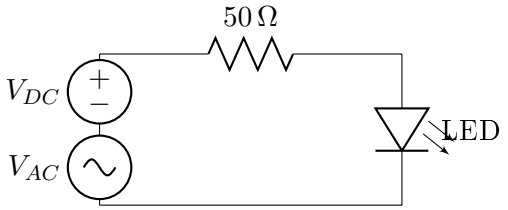


Figure 3.1: LED Drive Circuit

| Current Range ($\mu A$) | Error % |
|---|---|
| 1000 | $\pm\left(0.3\% I_{D,1} + 1.0\mu A + (20\,nA)\,(V)\right)$ |
| 100 | $\pm\left(0.3\% I_{D,1} + 100nA + (2\,nA)\,(V)\right)$ |

Table 3.1: HP-4145B Current Error recreated from HP-4145B Operation Manual

$V_{oc}$ are experimentally measured while $R_{sh}$ and $R_s$ are determined from fitting the diode IV curves to the single diode model. $C_J$ is measured using the Andeen Hagerling 2500A (AH) Capacitance Bridge.

The resistive regime is first considered followed by the capacitive regime. Lastly, using a crystal oscillator AC optical power is measured and compared to theory.

### 3.2.1 Resistive Load:

As mentioned above for resistive loads 818-SL is used. As discussed in section(2.4.3.2) the following are required to verify equation (2.66):

1. IV curves of the illuminated photodetector. From these curves the measured values of $I_{isc}$ and $V_{oc}$ are determined as function of optical power. Additionally, by fitting these curves to equation(2.49) $R_{sh}$ and $R_s$ are determined

2. Bias voltage $V_D$. This is determined using load lines

3. AC short circuit current, $i_{isc_1}$. This is determined by measuring the photodiode current at $R_L = 0$ for incident modulated optical power

#### 3.2.1.1 IV Curves

The IV curves, $I_{D,3}\,vs\,V$, for 818-SL are plotted in figure (3.2) for optical powers, $P_{opt}$, between $66 - 981\,\mu W$. In this plot, the x-axis is voltage and the y-axis is current. These curves are similar to the theoretically generated IV curves shown in figure (2.29). As expected as $I_{isc}$ or the optical power incident on the photodiode increases $V_{oc}$ increases logarithmically. The logarithmic increase in $V_{oc}$ explains the decrease in separation for the higher illuminated IV curves seen in figure (3.2). Equation (2.48) captures this logarithmic relationship.

The IV curves are measured using the HP-4145B semiconductor parameter analyzer. The relative error[1] in the currents are approximately 0.7% and 0.5%. These are determined using the accuracy chart found in the HP-4145B manual for currents in the range of 100 and $1000\,\mu A$. Part of the accuracy chart is recreated in table(3.1). The uncertainty in the voltage is assumed to be small and hence ignored. $P_{opt}$ is measured using the 1815-C power meter. The uncertainty in this value, $\Delta P_{opt}$, is calculated from the table given in the operator's manual. For all ranges the maximum error is 1.7%.

The non-ideal diode model, equation (2.49), is used to fit the IV curves. Here $\alpha = \frac{q}{\eta kT}$ where $\eta$ is the diode ideality factor. The ideality factor accounts for recombination in the junction[2]. A photodiode having $\eta = 1$ is desired Generally, however, photo-diodes having

[1] Relative error is defined as the uncertainty in the value divided by the value, i.e. $\frac{\Delta x}{x}$

[2] The diode equation assumes recombinations of EHPs occur in the bulk

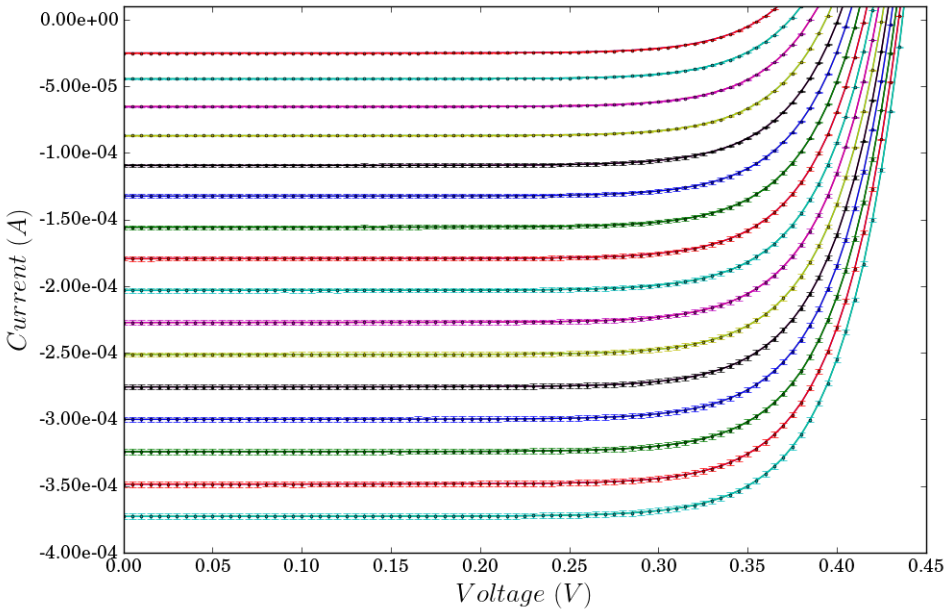


Figure 3.2: 818-SL $I_{D,3}\, vs\, V$ for optical power between $66 - 981\,\mu W$. The non-linear current response follows equation (2.49). As $I_{isc}$ or the optical power incident on the photodiode increases $V_{oc}$ increases logarithmically. The logarithmic increase in $V_{oc}$ explains the decrease in separation at $I_{D,3} = 0$. This logarithmic relationship is captured in equation (2.48). Lines are drawn as a guide to the eye

| $P_{opt}$ $\left(\times 10^{-4} W\right)$ | $\Delta P_{opt}$ $(\mu W)$ | $I_{isc}$ $\left(\times 10^{-4} A\right)$ | $\Delta I_{isc}$ $(\mu A)$ | $V_{oc}$ $(V)$ |
|---|---|---|---|---|
| 0.659 | 1.12 | 0.250 | 0.175 | 0.355 |
| 1.17 | 1.99 | 0.444 | 0.233 | 0.375 |
| 1.72 | 2.92 | 0.653 | 0.296 | 0.385 |
| 2.29 | 3.89 | 0.871 | 0.361 | 0.935 |
| 2.88 | 4.89 | 1.10 | 1.33 | 0.400 |
| 3.48 | 5.92 | 1.33 | 1.40 | 0.405 |
| 4.10 | 6.97 | 1.56 | 1.47 | 0.410 |
| 4.72 | 8.02 | 1.79 | 1.54 | 0.415 |
| 5.35 | 9.09 | 2.03 | 1.61 | 0.420 |
| 5.98 | 10.2 | 2.27 | 1.68 | 0.420 |
| 6.61 | 11.2 | 2.51 | 1.75 | 0.425 |
| 7.25 | 12.3 | 2.76 | 1.83 | 0.430 |
| 7.89 | 13.4 | 3.00 | 1.90 | 0.430 |
| 8.53 | 14.5 | 3.24 | 1.97 | 0.435 |
| 9.17 | 15.6 | 3.49 | 2.05 | 0.435 |
| 9.81 | 16.7 | 3.73 | 2.12 | 0.435 |

Table 3.2: Measured $I_{isc}$ and $V_{oc}$ for the respective measured incident optical power. $\Delta P_{opt}$ and $\Delta I_{isc}$ are the measured uncertainties in $P_{opt}$ and $I_{isc}$. $\Delta V_{oc}$ is assumed to be small and hence ignored.

$1 \leq \eta \leq 2$ is acceptable. The fit for these curves yields the values for $R_{sh}$ and $R_s$. The fit values and the uncertainty in the fits for the illuminated intensities are given in table (3.3). As is seen, $R_{sh}$ and $R_s$ decrease as the intensity increases. A similar trend was also noticed by Chenvidhya et al[52]. The value of $C_J$ is also given in this table. The uncertainty in $C_J$ is ignored because according to the AH manual the accuracy is 5 parts per million. Given the values for the non-ideal circuit $R_L$ is chosen to meet two requirements:

1. For some of the incident power the photo-diode should be biased at the maximum power point. The values of $R_L$ at maximum power point are determined from figure (3.2) and are in the range of $1 - 10\,k\Omega$

2. The bandwidth of the photodetector, $R_t C_J$, should be greater than 1 KHz. This frequency is chosen because it is large enough to be away from the line frequency and its harmonic, i.e 60 and $120\,Hz$, and an electrical amplifier with the appropriate gain and noise floor is available. $R_t$ is the total resistance determined from circuit analysis of the non-ideal diode circuit. The circuit is given in figure (2.27). Here $Z_L = R_L$. The range of $R_L$ from the point above satisfies this bandwidth requirement

The $R_L$ values chosen are: 1, 2.2, 5 and $10\,k\Omega$. These values correspond to the maximum power point for incident powers of 981, 410, 172 and $66\,\mu W$, respectively. Given these values of $R_L$ for the DC and AC analysis $R_{sh}$ can be ignored because its resistance is roughly 100 - 1000 times greater than the rest of the circuit elements. For the DC case considered next $I_{D,3} = I_{D,1}$. For the AC case the impedance of $C_J$ at $1.0\,kHz$ for the 1 and $2.2\,k\Omega$ resistors is large enough that $i_{d,3} = i_{d,1}$ while for 5 and $10\,k\Omega$ the impedance of $C_J$ at $1.0\,kHz$ is such

| $P_{opt}\ (\times 10^{-4} W)$ | $R_{sh}\ (M\Omega)$ | $\Delta R_{sh}\ (k\Omega)$ | $R_s\ (\Omega)$ | $\Delta R_s\ (\Omega)$ | $\eta$ | $\Delta\eta \times 10^{-3}$ | $C_J\,(nF)$ |
|---|---|---|---|---|---|---|---|
| 0.659 | 15.2 | 759 | 40.8 | 2.03 | 1.15 | 1.36 | 4.74 |
| 1.17 | 12.7 | 634 | 22.6 | 1.13 | 1.17 | 1.38 | 4.74 |
| 1.72 | 8.10 | 405 | 18.7 | 0.937 | 1.17 | 1.56 | 4.74 |
| 2.29 | 6.24 | 312 | 13.3 | 0.664 | 1.18 | 1.81 | 4.74 |
| 2.88 | 5.44 | 272 | 13.4 | 0.671 | 1.18 | 2.16 | 4.74 |
| 3.48 | 2.60 | 130 | 9.82 | 0.419 | 1.19 | 2.18 | 4.74 |
| 4.10 | 1.92 | 95.9 | 10.4 | 0.52 | 1.19 | 2.21 | 4.74 |
| 4.72 | 3.14 | 15.7 | 11.1 | 0.553 | 1.18 | 2.19 | 4.74 |
| 5.35 | 1.59 | 79.3 | 10.7 | 0.537 | 1.19 | 2.18 | 4.74 |
| 5.98 | 1.16 | 57.9 | 9.61 | 0.481 | 1.20 | 2.20 | 4.74 |
| 6.61 | 1.51 | 75.3 | 10.2 | 0.512 | 1.19 | 2.30 | 4.74 |
| 7.25 | 1.45 | 72.5 | 10.2 | 0.511 | 1.19 | 2.66 | 4.74 |
| 7.89 | 1.25 | 62.5 | 10.0 | 0.501 | 1.20 | 2.42 | 4.74 |
| 8.53 | 1.05 | 52.2 | 10.4 | 0.519 | 1.19 | 2.48 | 4.74 |
| 9.17 | 2.06 | 103 | 10.1 | 0.508 | 1.20 | 3.81 | 4.74 |
| 9.81 | 1.11 | 103 | 9.73 | 0.508 | 1.20 | 3.79 | 4.74 |

Table 3.3: Values for $R_{sh}$, $R_s$ and $\eta$ for the respective incident optical power. These values are determined by fitting equation (2.49) to measured $I_{D,3}$. $\Delta R_{sh}$, $\Delta R_s$ and $\Delta\eta$ are the error in the fits

that $i_{d,3}$ is 98.9 and 95.8% of $i_{d,1}$. Hence for the AC case $i_{d,3}$ is assumed to be equivalent to $i_{d,1}$.

#### 3.2.1.2 DC Case

Figure (3.3) is similar to figure (3.2) with the addition of load lines pertaining to the chosen values of $R_L$. The values of $R_L$ are verified using the slope of its measured IV curves. These curves are also measured using the HP-4145B. The measured values of $R_L$ are 1.032, 2.185, 5.018 and $10.08\,k\Omega$. These values are within the rated 10% tolerance. The relative errors for the respective resistances are: 0.62%, 1.06%, 2.11% and 0.66%. The uncertainty is calculated using the error propagation equation(3.1)[53]. In this equation $x = f(u, v)$ and the uncertainty in $x$ is determined from the uncertainties in $u$ and $v$. $\sigma$ is the standard deviation. The third term is 0 in the absence of correlation between $u$ and $v$.

$$\sigma_x^2 = \sigma_u^2 \left(\frac{\partial x}{\partial u}\right)^2 + \sigma_v^2 \left(\frac{\partial x}{\partial v}\right)^2 + 2\sigma_u\sigma_v \left(\frac{\partial x}{\partial u}\right)\left(\frac{\partial x}{\partial v}\right) \tag{3.1}$$

The uncertainty in $R$ is calculated using ohm's law, i.e. $R(V, I) = \frac{V}{I}$. In this calculation it is assumed that the uncertainties in the voltage and current are independent of each other, i..e the third term in the above equation is 0. A change of notation is made from $\sigma$ to $\Delta$. The uncertainty in $R$ is:

$$\Delta R^2 = \Delta I^2 \left(\frac{\partial R}{\partial I}\right)^2 + \Delta V^2 \left(\frac{\partial R}{\partial V}\right)^2$$

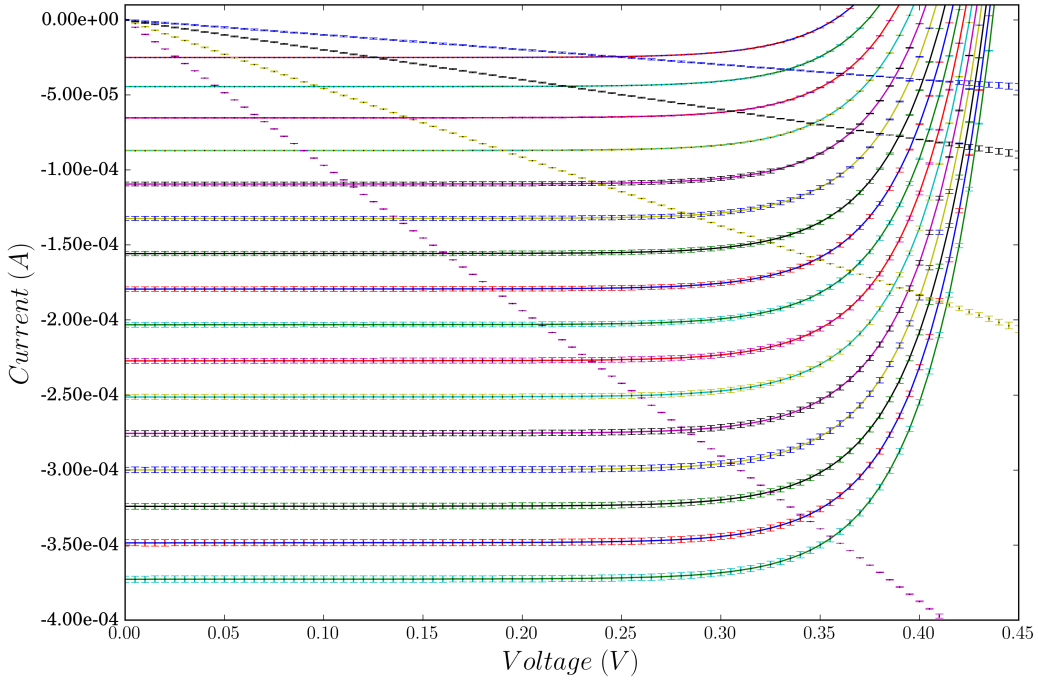


Figure 3.3: 818-SL IV Curves with Load Lines for $R_L = 1$, 2.2, 5 and $10\,k\Omega$ from bottom to top. Lines are drawn as a guide to the eye

$$\Delta R^2 = \Delta I^2 \left(-\frac{V}{I^2}\right)^2 + \Delta V^2 \left(\frac{1}{I}\right)^2$$

The relative error in $R$ is:

$$\frac{\Delta R^2}{R^2} = \frac{\Delta I^2}{R^2} \left(-\frac{V}{I^2}\right)^2 + \frac{\Delta V^2}{R^2} \left(\frac{1}{I}\right)^2$$

$$\frac{\Delta R^2}{R^2} = \frac{\Delta I^2}{I^2} + \frac{\Delta V^2}{V^2}$$

$\frac{\Delta V}{V}$ is assumed to be smaller than $\frac{\Delta I}{I}$ therefore the uncertainty in $R$ and the relative error is the same as the uncertainty and relative error in the measured current, i.e.

$$\Delta R = \Delta I$$

$$\frac{\Delta R}{R} = \frac{\Delta I}{I}$$

Using figure (3.3) plots of $I_{D,1}R_t \, vs \, I_{isc}R_t$ and $\frac{I_{D,1}}{I_{isc}} \, vs \, I_{isc}R_t$ are generated next followed by a short discussion on DC power.

Figures (3.4) (a) and (b) are a plot of $I_{D,1}R_t \, vs \, I_{isc}R_t$. This figure is similar to figure (2.30) discussed in the theoretical prediction section. As expected as both $I_{isc}$ and $R_t$ increases $I_{D,1}R_t$ also increases. Two linear regions exist separated by a knee. The region to the left of the knee represents linear increase of voltage with optical power while the region right of the knee is the logarithmic increase of voltage with optical power. For lower resistances the knee shifts to the right indicating an increase in $V_{oc}$. This shift is emphasized in figure (3.4)(b). The error bars are determined using equation (3.1) and the values from tables(3.2) and (3.3)

Figure (3.5) (a) and (b) are a plot of $\frac{I_{D,1}}{I_{isc}} \, vs \, I_{isc}R_t$. This figure is similar to figure (2.31) discussed in the theoretical predictions section. As expected as both $I_{isc}$ and $R_t$ increases $\frac{I_{D,1}}{I_{isc}}$ decreases. Similar to above, two distinct regions exist separated by a knee. To the left of the knee $\frac{I_{D,1}}{I_{isc}}$ is 1 and to the right of the knee $\frac{I_{D,1}}{I_{isc}}$ decreases. The former corresponds to the flat or the horizontal part of the IV curve, figure (3.3), while the latter corresponds to the vertical part of the same curve. Similar to figure(3.4) as the resistance is decreased the knee of the $\frac{I_{D,1}}{I_{isc}}$ curves shifts to the right. This point is emphasized in figure (3.5)(b) by plotting the curves associated with $R_L = 1$ and $10\,k\Omega$. A lack of overlap between these curves is also seen past the knee. Again this is as expected due to the differences in $V_{oc}$. The error bars are determined using the method discussed above.

In both these plots for the fixed $R_L$ the x-axis represents increasing $I_{isc}$.

**3.2.1.2.1 DC Power** Figure (3.6) is a plot of maximum DC power that can be extracted from the photodiode for the given incident optical powers. The x-axis is $I_{isc}$ and the y-axis is $P_{D,1}$. The solid line in this plot is generated from equation (2.71) using the measured $V_{oc}$ and $I_{isc}$ values in table (3.2). The symbol 'x' on the plot are the maximum power that can be extracted for each $I_{isc}$. This is determined from the product of the measured current and voltage, $P_{D,1} = I_{D,1}V_D$ corresponding to the respective $I_{isc}$. The solid circle are the dissipated power due to $R_L$. In general, as expected, as $P_{D,1}$ increases $I_{isc}$ increases. Good agreement is seen between the predicted values and the calculated $P_{D,1}$ values from the data. This plot also shows that the dissipated power due to $R_L$ corresponds to with in 5% of the maximum power point. This is expected because $R_L$ was chosen to best match the maximum power point for the respective $I_{isc}$.

Using this curve and the measured optical power the efficiency of the photodiode is approximately 12%. Efficiency is defined as the ratio of electrical power to optical power.

Having characterized the DC response of the photodiode to various $R_L$ and optical powers the AC case is discussed next.

### 3.2.1.3 AC Case

In this section equation (2.66) is verified using the AC circuit in figure (2.27)(a) where $Z_L$ is equivalent to $R_L$. To verify this equation the following are required: (1) DC bias point $V_D$ and (2) an AC generated current. The former requirement is met by using the above discussed $R_L$ and optical powers and the latter requirement is met by adding a small modulating voltage to the existing DC bias on the LED. The measured current from the photodiode is $i_{d,3}$. Using tables (3.2) and (3.3) $i_{d,1}$ is recovered. $i_{isc_1}$ is measured at the short-circuit point. At this point $R_L = 0\,\Omega$ and $i_{d,3} = i_{isc_1}$.

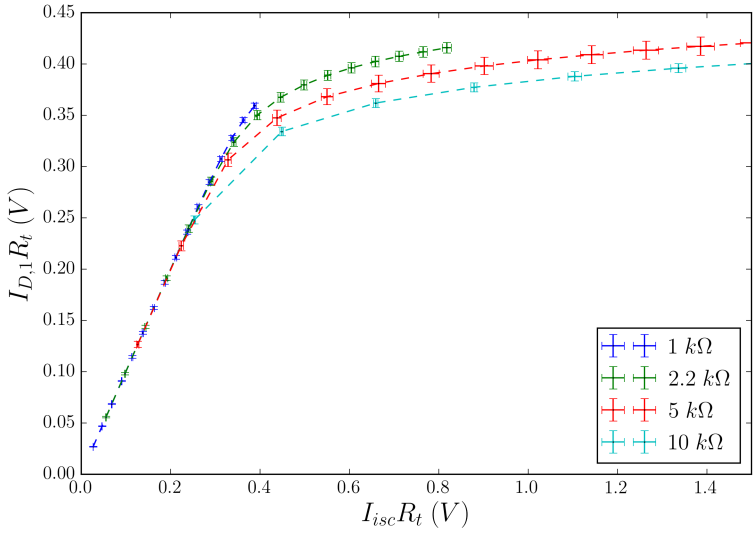


(a)

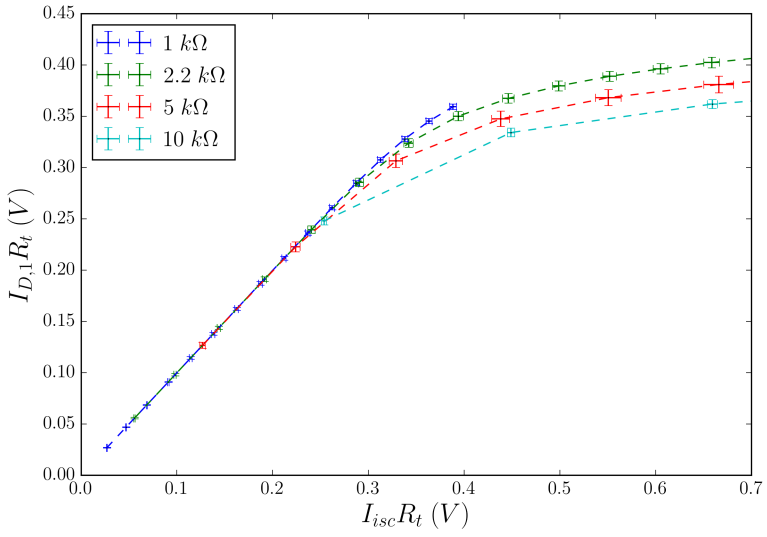


(b)

Figure 3.4: $I_{D,1}R_t\, vs\, I_{isc}R_t$ for $R_L = 1, 2.2, 5.$ and $10\,k\Omega$ (a) Two linear regions separated by a knee are seen. The voltage to the left of the knee increases linearly with optical power while the voltage to the right of the knee increases logarithmically with optical power (b) Exploded section of (a) in the vicinity of the knee. This is done to emphasize the point that the knee shifts to the right as $R_L$ decreases. The shifting to the right is indicative of increasing $I_{isc}$ or an increasing incident optical power. The dotted line is drawn as an aid to the eye

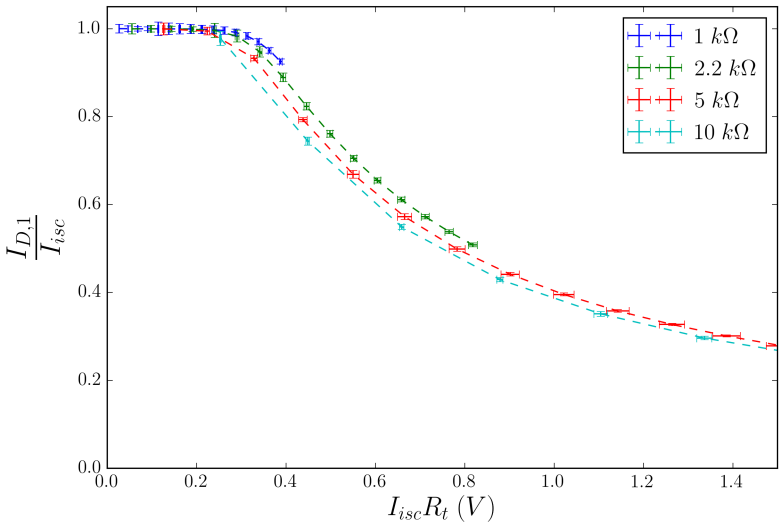


(a)

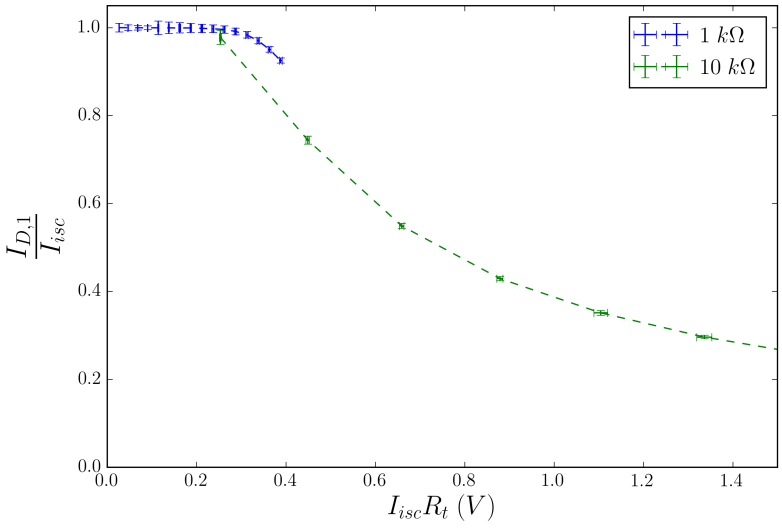


(b)

Figure 3.5: $\frac{I_{D,1}}{I_{isc}}$ *vs* $I_{isc}R_t$ for $R_L = 1, 2.2, 5.$ and $10\,k\Omega$: (a) Two distinct regions are seen separated by a knee. To the left of the knee $\frac{I_{D,1}}{I_{isc}} = 1$ and to the right $\frac{I_{D,1}}{I_{isc}}$ decreases. The former corresponds to the flat or horizontal part of the IV curve, (3.3), while latter corresponds to the vertical part of the same curve. The lack of overlap past the knee is due to differences in $V_{oc}$. The knee shifts to the right as $R_L$ decreases. This is emphasized in (b) and is indicative of increasing $I_{isc}$ or an increasing incident optical power. The dotted line is drawn as an aid to the eye

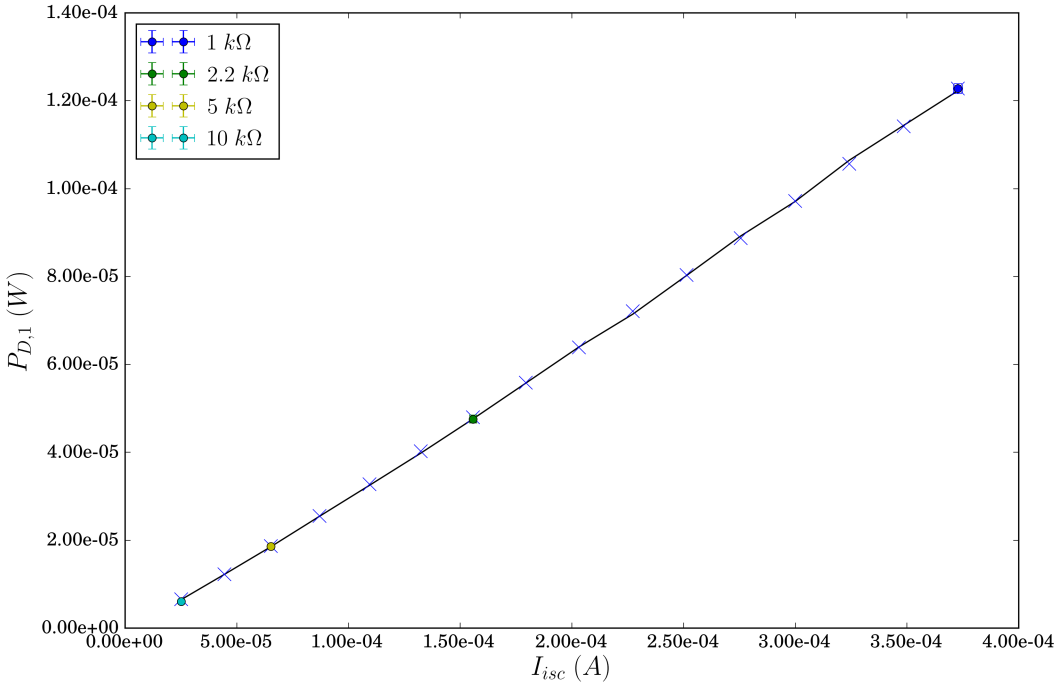


Figure 3.6: $P_{D,1}\, vs\, I_{isc}$ The solid line is generated from equation (2.71) using the measured $V_{oc}$ and $I_{isc}$ values. Symbol 'x' is the maximum power that can be extracted for each $I_{isc}$. The solid circle are the dissipated power due to $R_L$. Good agreement is seen amongst the three

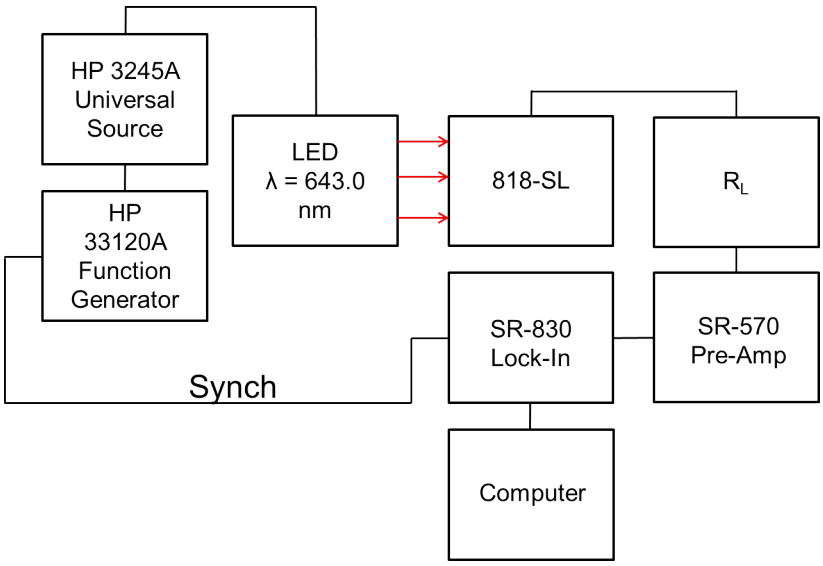


Figure 3.7: Block Diagram of experimental setup used for measuring the AC response of 818-SL biased by a resistive load, $R_L$. The HP-3425A and 33120A supply the DC and AC voltage required bias and modulate the LED. The light modulated light from the LED is incident on the $R_L$ biased 818-SL photodetector. The current, $i_{D,3}$, generated by the biased photodetector is amplified by the SR-570 low current noise pre-amp. The output of the amplifier is fed into the SR-830 lock-in. The lock-in is synchronized to the HP-33120A. The data from the lock-in is collected on a computer. The arrows in the diagram indicate light being emitted from the LED onto the 818-SL

The experimental setup is first discussed followed by analysis of the data.

**3.2.1.3.1 Experimental Setup** Figure (3.7) is the block diagram of the experimental setup. HP-3245A is used to bias the LED and the HP-33120A is used to modulate the LED via an AC voltage. The current, $i_{D,3}$, is first amplified by the SR-570 and the output is fed into the SR-830 lock-in amplifier. The input of the SR-830 is set to AC couple in order to reject $I_{D,3}$. Therefore $i_{d,3}$ is measured. The SR-830 is locked to the synchronization signal of the HP-33120A. The modulation optical power, $p_{opt}$, from the LED is kept between $12.91 - 18.30\,\mu W$ which is at maximum 26% of the total optical power. The modulation power is measured using 1815-C power meter. This justifies the comparison of the measured data with theory. The transimpedance gain factor on the SR-570 is set to $1\frac{mA}{V}$.

**3.2.1.3.2 AC Analysis** Figure (3.8) is the theoretical and experimental plot for $\frac{i_{d,1}}{i_{isc_1}} vs I_{isc}R_t$. This figure is similar to figure (2.34) discussed in the theoretical prediction section. The x-axis is logarithm of $I_{isc}R_t$. The theoretical curve is generated using equation (2.66) along with the values for circuit elements and the DC bias points discussed above. The experimental data follows the same trend as predicted by theory. In general good agreement is seen between the two. Similar to DC case the curves do not overlap past the knee and the knee shifts to the right as $R_L$ decreases. The former and latter are expected due to the changes

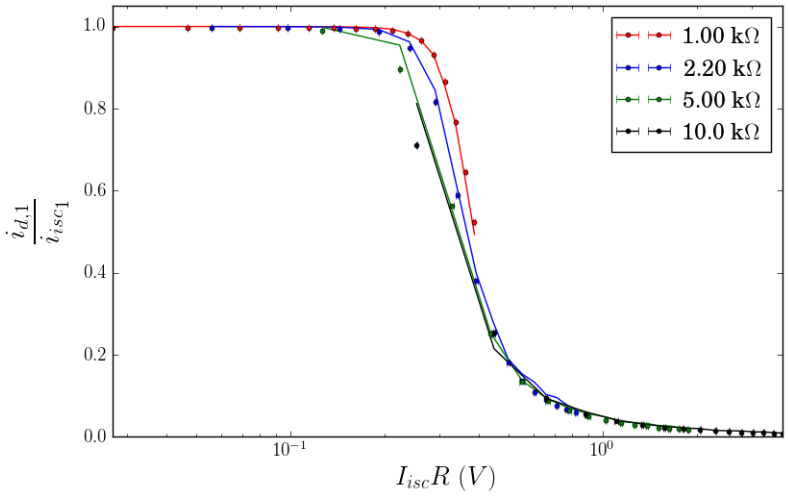


Figure 3.8: $\frac{I_1}{I_{sc_1}}$ *vs* $I_{sc}R_t$ for $R_L = 1, 2.2, 5.\text{and}\,10\,k\Omega$. Good agreement is seen between experimental data and theoretical predictions. Similar to the DC case two distinct regions are separated by the knee. The region to the left of the knee corresponds to the horizontal section of the IV curves while to the right of the knee corresponds to the vertical section of the IV curves. The lack of overlap past the knee is due to differences in $V_{oc}$. The knee shifts to the right as $R_L$ decreases.

in $V_{oc}$ resulting from an increase in $I_{isc}$. The uncertainty in the x-axis follows from before. Uncertainties in $i_{d,1}$ as a result of statistical fluctuations is ignored. The justification for this is given below in the noise section.

**3.2.1.3.3 $C$ Parameter** As was shown in equation (2.74) $\frac{I_{D,1}}{I_{isc}}$ and $\frac{i_{d,1}}{i_{isc_1}}$ are related by the $C$ parameter. In figures (3.9) - (3.12) the experimental $C$ is plotted along with the predictions from equation (2.75). The x-axis is the natural $I_{isc}R_t$. In general an agreement is seen between the two validating the idea that $\frac{I_{D,1}}{I_{isc}}$ and $\frac{i_{d,1}}{i_{isc_1}}$ are related by the $C$ parameter. That is to say knowing the DC response of a photodiode the AC response can be predicted using the $C$ parameter. The experimental $C$ is determined by dividing $\frac{i_{d,1}}{i_{isc_1}}$ and $\frac{I_{D,1}}{I_{isc}}$ as seen from equation (2.74). The prediction from equation (2.75) is generated using the experimentally determined DC parameters: $V_{oc}$, $\eta$ and $V_D = I_{D,1}R_t$. The values for $I_{D,1}R_t$ are from figure (3.4). The error bars are determined using the method discussed above.

**3.2.1.3.4 AC Power** Figure (3.13) and (3.14) is the a plot of the normalized DC and AC power for the $1\,k\Omega$ and $2.2\,k\Omega$ resistor. These plot are similar to figure (2.37) with the difference being in figures (3.13) and (3.14) the DC curve is plotted only up to the maximum power point. As expected the maximum power point for AC is different than for DC. This is discussed in the analytical prediction section above. The maximum power point for AC power is shifted to the left of the DC power by approximately 33% and43%; respectively.

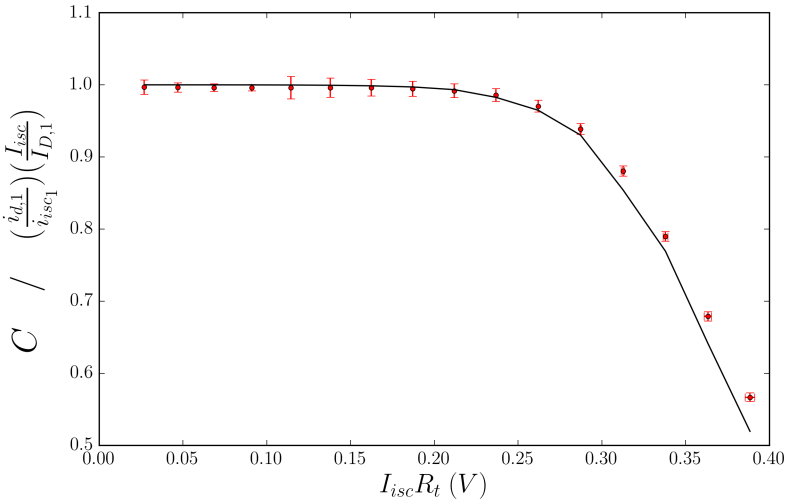


Figure 3.9: $C$ parameter for $1\,k\Omega$. The solid dots are the experimental $C$ generated by dividing $\frac{i_{d,1}}{i_{isc_1}}$ and $\frac{I_{D,1}}{I_{isc}}$. The solid line is determined from equation (2.75) using the experimentally determined $V_{oc}$, $\eta$ and $V_D$ DC parameters.

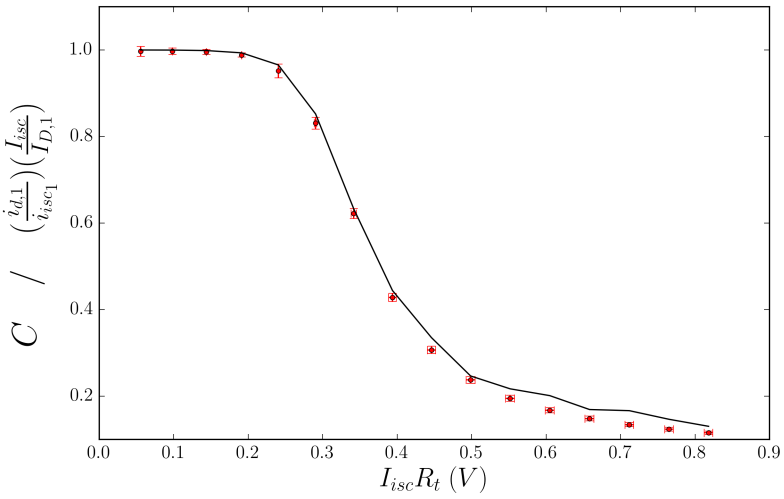


Figure 3.10: $C$ parameter for $2.2\,k\Omega$. The solid dots are the experimental $C$ generated by dividing $\frac{i_{d,1}}{i_{isc_1}}$ and $\frac{I_{D,1}}{I_{isc}}$. The solid line is determined from equation (2.75) using the experimentally determined $V_{oc}$, $\eta$ and $V_D$ DC parameters.

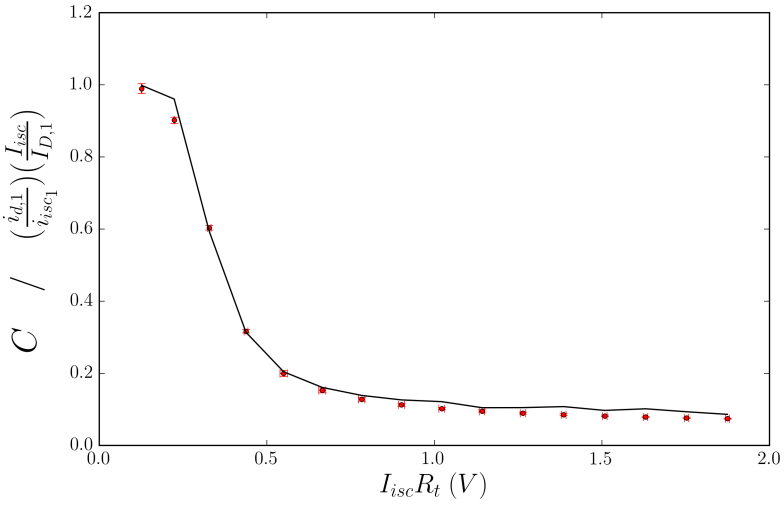


Figure 3.11: $C$ parameter for $5\,k\Omega$. The solid dots are the experimental $C$ generated by dividing $\frac{i_{d,1}}{i_{isc_1}}$ and $\frac{I_{D,1}}{I_{isc}}$. The solid line is determined from equation (2.75) using the experimentally determined $V_{oc}$, $\eta$ and $V_D$ DC parameters.

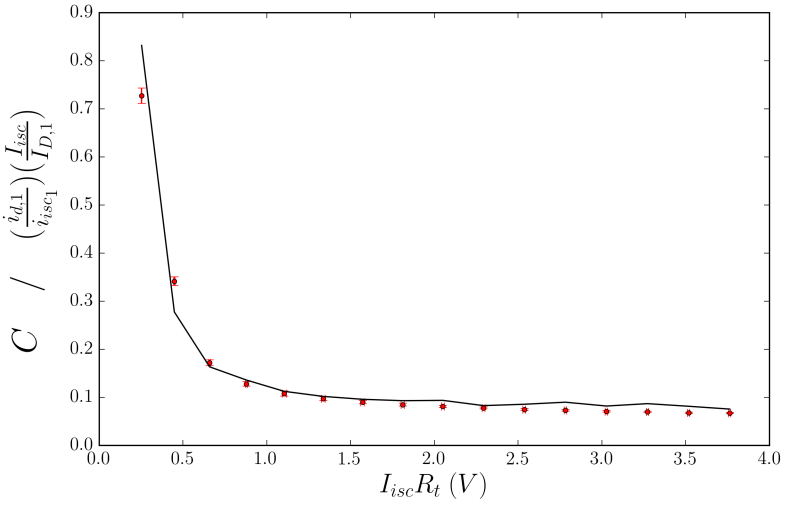


Figure 3.12: $C$ parameter for $10\,k\Omega$. The solid dots are the experimental $C$ generated by dividing $\frac{i_{d,1}}{i_{isc_1}}$ and $\frac{I_{D,1}}{I_{isc}}$. The solid line is determined from equation (2.75) using the experimentally determined $V_{oc}$, $\eta$ and $V_D$ DC parameters.

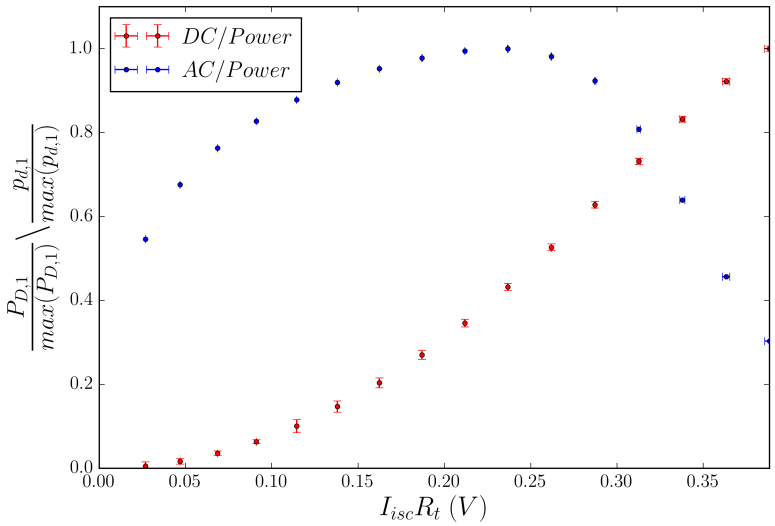


Figure 3.13: Normalized DC and AC Power for $1\,k\Omega$. The maximum power point for AC is shifted to the left by approximately 33% indicating that for the $1\,k\Omega$ $R_L$ an $I_{isc}$ of approximately $250\,\mu A$ is required. For the same $R_L$ an $I_{isc}$ of approximately $370\mu A$ is required for the DC maximum power point

Using equation (2.77) a shift of 18% and 19% is expected for the respective resistances. The discrepancy between the theoretical expectations and measurements is due to the discrete number of $I_{isc}$ or optical powers used. This finite number also prevented observing a shift for $R_L = 5\,k\Omega$ and $10\,k\Omega$.

**3.2.1.3.5 Noise** For the AC data presented above uncertainty bars related to the statistical fluctuation are not shown. This is because the signal to noise ratio (SNR) is on the order of $1.0 \times 10^6$. The noise floor is determined by considering the circuit in figure(2.27)(a) in the absence of a drive signal. From circuit theory the noise sources are: Johnson noise[54] due to the $R_{sh}$ and $R_3$ and shot noise of the 818-SL[50]. Johnson noise is given by equation (3.2) and the shot noise of the 818-SL is $76\frac{fA}{\sqrt{Hz}}$. This value is determined by multiplying the responsivity of 818-SL at $633\,nm$ with its noise equivalent power (NEP) $0.2\frac{pW}{\sqrt{Hz}}$. Both of these values are given in the specification sheets. In addition to these three noise sources the input voltage noise of the SR-570 also needs to be considered. Its noise floor is $150\frac{pA}{\sqrt{Hz}}$. This value is acquired from the SR-570 user manual. Having determined the noise sources the total noise is the response of each noise source added in quadrature. This response is calculated from circuit theory and is the noise at the output of the amplifier. The total noise is plotted in figure (3.15). The x-axis is frequency and the y-axis is voltage noise. As is seen the noise floor is approximately $3.0\frac{nV}{\sqrt{Hz}}$ at the operation frequency of $1\,kHz$. The dominant source of noise is the voltage noise of the SR-570. As mentioned above AC measurements are made using a lock-in amplifier. The filter time constant on the lock-in is set to 1 second. Therefore the noise floor in the measurement is $3.0\,nV$ and the AC signal being measured is

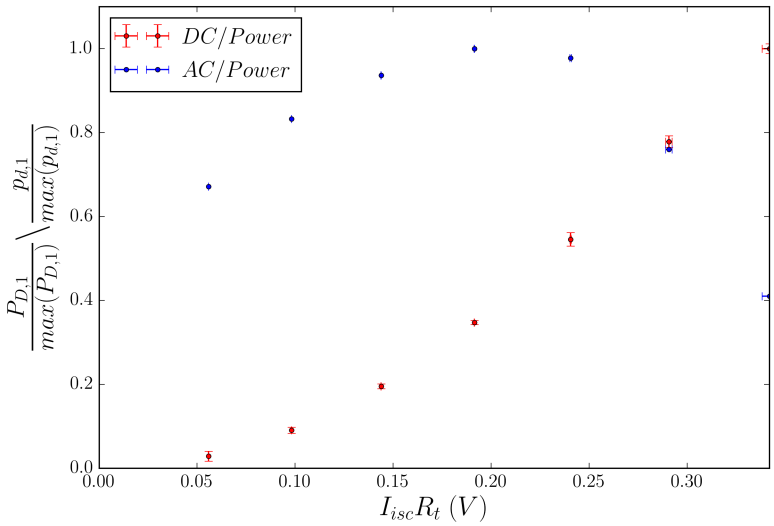


Figure 3.14: Normalized DC and AC Power for $2.2\,k\Omega$. The maximum power point for AC is shifted to the left by approximately 43% indicating that for the $2.2\,k\Omega$ $R_L$ an $I_{isc}$ of approximately $89\,\mu A$ is required. For the same $R_L$ an $I_{isc}$ of approximately $160\,\mu A$ is required for the DC maximum power point

greater than a $mV$. This gives a SNR of greater than 1.0$e$6.

$$\frac{V_T}{\sqrt{f}} = \sqrt{4K_BTR} \tag{3.2}$$

### 3.2.2 Capacitive Loads:

As mentioned above for capacitive loads Newport 818-BB-20 photodiode is used to verify equation (2.66). A capacitive load biases the photodiode at the open circuit voltage, i.e $V_D = V_{oc}$. Therefore a DC analysis is not required. Figure (2.27)(a) is the circuit used for analysis. In this circuit $Z_L = C_L$. Similar to the previous section:

1. $i_{d,3}$ is measured and using circuit analysis $i_{d,1}$ is determined
2. $I_{isc}$, $i_{isc_1}$ and $V_{oc}$ are experimentally measured using the HP-4145B while $R_{sh}$ and $R_s$ are determined from fitting the diode IV curves to the single diode model
3. $C_J$ is measured using the AH 2500 A

#### 3.2.2.1 Experimental Setup

The block diagram of the experimental setup used is given in figureă(3.16). This setup is similar to the previous setup, figure (3.7), with the difference being the current $i_{d,3}$ is

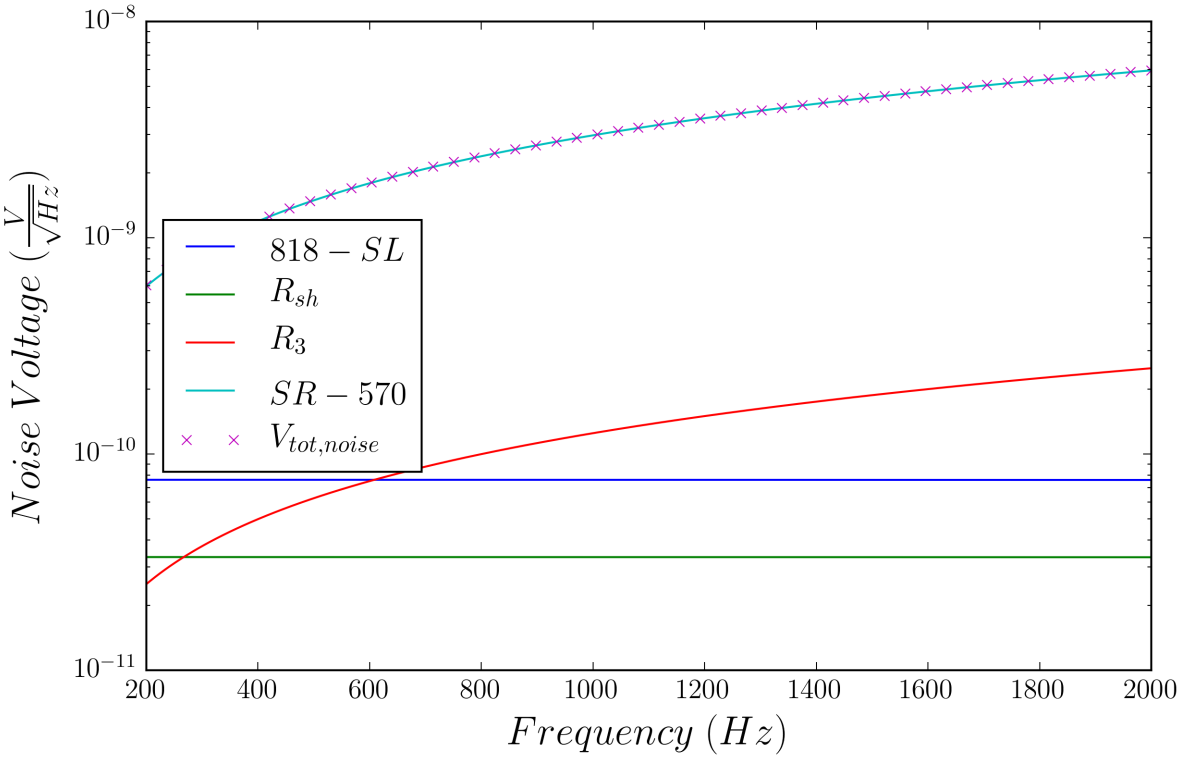


Figure 3.15: Voltage Noise vs Frequency. Plotted are the individual contributions from the noise sources: shot noise of 818-SL, Johnson noise of $R_{sh}$ and $R_3$ and the noise floor of SR-570. Also plotted is the total noise, $V_{tot,noise}$. As is seen the SR-570 is the major contribution to the noise floor. $V_{tot,noise}$ is the quadrature sum of the four noise sources

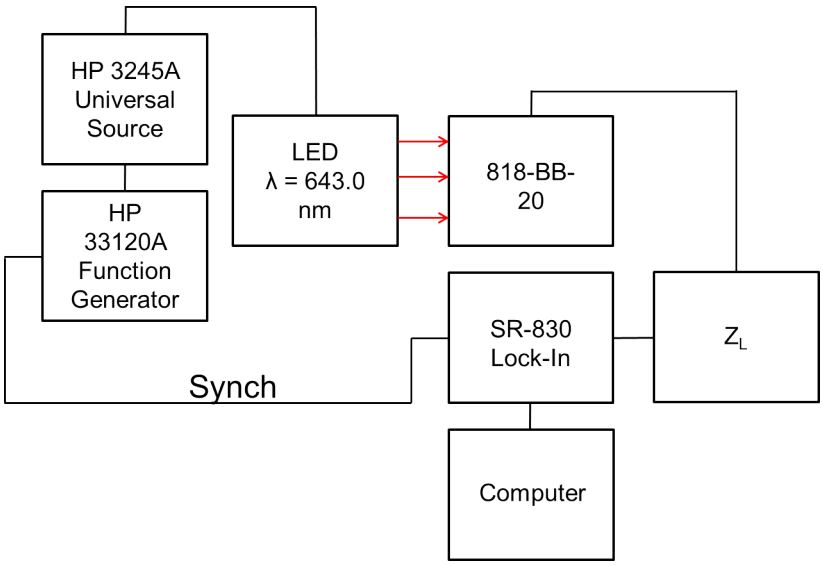


Figure 3.16: Block Diagram of experimental setup used for measuring the AC response of 818-BB-20 biased by a capacitive load, $Z_L$. The HP-3425A and 33120A supply the DC and AC voltage required to bias and modulate the LED. This light is incident on the $Z_L$ biased 818-BB-20 photodetector. The current, $i_{d,3}$, generated by the biased photodetector is fed into the current input of the SR-830 lock-in amplifier. The lock-in is synchronized to the HP-33120A. The data from the lock-in is collected on a computer. The arrows in the diagram indicate light being emitted from the LED onto the 818-BB-20

measured using the built-in current amplifier of the SR-830. Unlike the previous experiment the optical power is kept fixed and the modulation is varied. The frequency is varied from $60\,Hz - 21\,kHz$.

#### 3.2.2.2 AC Results and Analysis

Figure (3.17) is the theoretical and experimental plot of the normalized AC current, $\frac{i_{d,1}}{i_{isc_1}} vs\ I_{isc}Z_t$. The choice of axis is the same as discussed above in the capacitive analysis part of the analytical prediction section. As is seen the theoretical predictions agree well with the measured data. The uncertainty in the x-axis of the experimental data is plotted as well and is due to measurement accuracy of the HP-4145B. $i_{d,3}$ is measured using a $C_L$ of $105.62\,pF$ and a DC and AC LED illumination power of $P_{opt} = 1.65\,\mu W$ and $p_{opt} = 99.10\,nW$. This illumination corresponds to an $I_{isc}$ of approximately 215 nA and an $i_{isc_1}$ of approximately 12.9 nA. The values for $R_{sh}$, $R_s$ and $V_{oc}$ at this DC illumination are $49.5\,M\Omega \pm 2.56\%$, $0.443\,\Omega \pm 2.23\%$ and $0.36\,V$. $C_J$ has a value of $228.25\,pF$. These are used for generating the theoretical curve. The value of $C_L$ is chosen to best match $C_J$.

#### 3.2.2.3 Noise

Here, the same methodology as described in the resistive case is followed for determining the noise floor. The SNR in this experiment is approximately $1.0 \times 10^6$. The circuit used

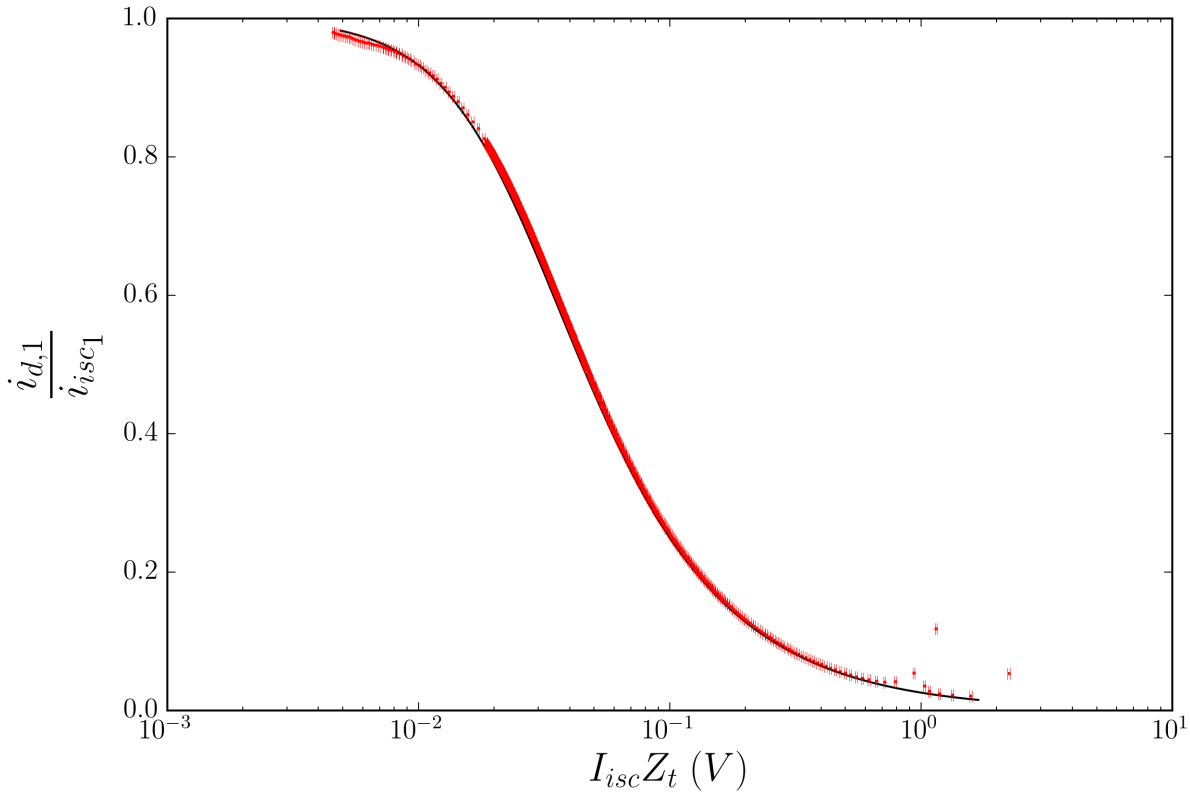


Figure 3.17: $\frac{i_{d,1}}{i_{isc_1}}\ vs\ \alpha I_{sc} Z_t$ for $C_L = 105.62\,pF$ The solid line matches the experimental data. This line is generated using equation (2.66) along with the following measured and fitted values of $2.15 \times 10^{-7}\,A \pm 0.97\%$, $49.5\,M\Omega \pm 2.56\%$, $0.443\,\Omega \pm 2.23\%$, $0.36\,V$, $228.25\,pF$ and $105.62\,pF$ for $I_{isc}$, $R_{sh}$, $R_s$, $V_{oc}$, $C_J$ and $C_L$

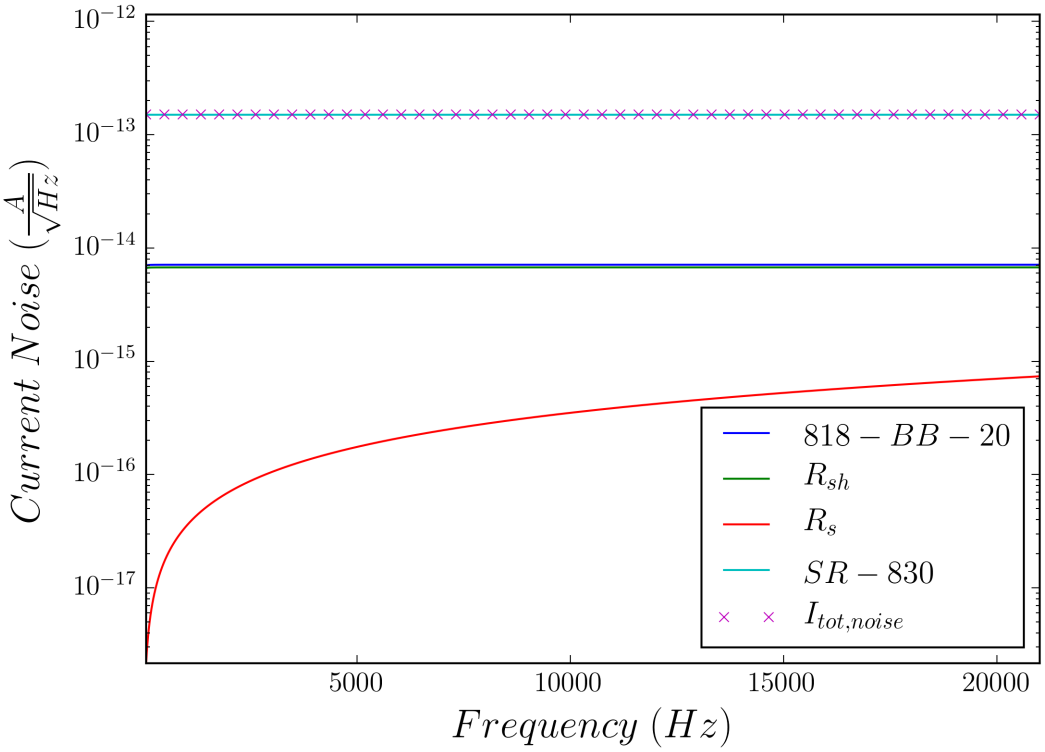


Figure 3.18: Current Noise vs Frequency. Plotted are the individual contributions from the noise sources: shot noise of 818-BB-20, Johnson noise of $R_{sh}$ and $R_s$ and the noise floor of SR-830. Also plotted is the total noise, $I_{tot,noise}$. As is seen the SR-830 is the major contribution to the noise floor. $I_{tot,noise}$ is the quadrature sum of the four noise sources

for this analysis is similar to the resistive case with the difference being $Z_L$ is $C_L$. There are four sources of noise: Johnson noise of $R_{sh}$ and $R_s$, shot noise of 818-BB-20 and the noise floor of the SR-830. The shot noise of 818-BB-20 is $19.5\frac{fA}{\sqrt{Hz}}$ and is determined from the specification sheet. The noise floor of the SR-830 is $130.0\frac{fA}{\sqrt{Hz}}$. This value is acquired from the SR-830 user manual. Figure (3.18) is the plot of the total noise floor and the contribution from each source. The total noise is the quadrature sum of the individual contributions. In this figure the x-axis is frequency and the y-axis is current noise, i.e. $\frac{A}{\sqrt{Hz}}$. The plotted noise is the noise at the input of the SR-830. Similar to the resistive case the noise floor of the amplifier is the dominant source of noise.

### 3.2.3 QTF Load:

In this section the extraction of AC electrical power from an illuminated photodiode is demonstrated. This extraction of AC power is demonstrated by driving a Quartz Tuning Fork (QTF) resonator into resonance. To achieve this the QTF is placed on the load branch

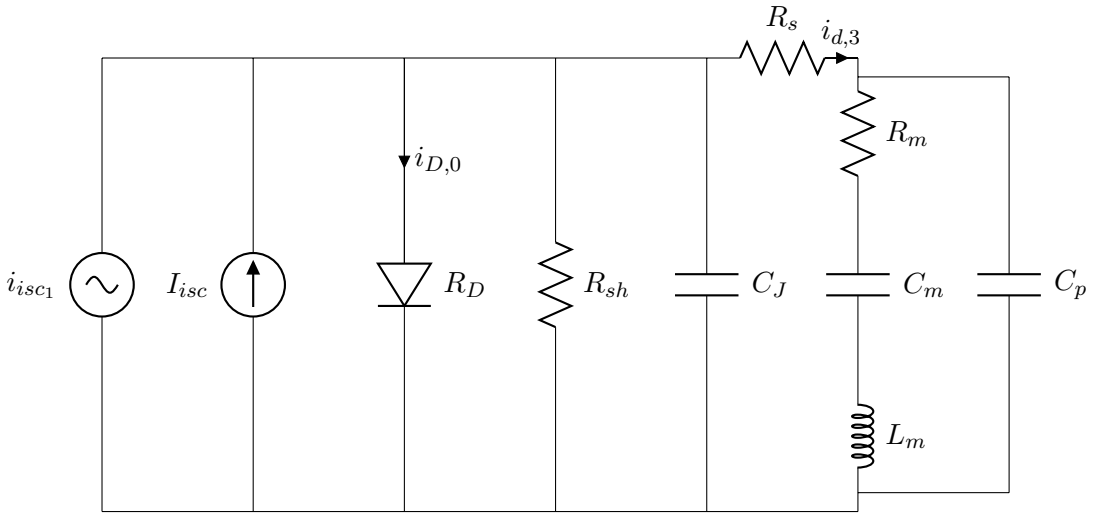


Figure 3.19: AC Single Diode PV Model with QTF Load

of the photodiode. A QTF is a capacitive device hence $V_D = V_{oc}$. In addition to demonstrating the extraction of AC electrical power, the experiment also demonstrates conversion of optical to mechanical power. The optical to mechanical power conversion is mediated by the piezoelectric effect. This experiment is the discrete version of the work presented in chapter 5. Here discrete means two separate devices are used to demonstrate the opto-piezo effect. In chapter 6 a single device that is both a mechanical resonator and a photodiode is used to demonstrate the opto-piezo effect.

#### 3.2.3.1 QTF Circuit Parameters

In order to use the derived theoretical framework a knowledge of the QTF circuit and its values are required. The equivalent circuit of the QTF is the BVD circuit given in figure (2.12). The values of the circuit components are determined by fitting the measured response of the QTF to this model. The measured response is acquired electrically, i.e. by driving the QTF using a function generator. The resulting current is then amplified, using an Amptek A-250 charge sensitive amplifier and the amplified voltage is measured using the SR-830 which is locked to the function generator. Figure (3.20)(a) and (3.20)(b) are the current and phase response of the QTF. This response is similar to that discussed in section (2.3.4). As seen from the figures the QTF has a resonance frequency of $f_r = 32764\,Hz$, an anti-resonance frequency of $f_a = 32800\,Hz$, and a quality factor of $Q \sim 100,000$. The circuit parameters determined from fitting to the BVD model are: $L_m = 7.69430 \times 10^3\,H \pm 2.92 \times 10^{-1}\%$, $C_m = 3.06662 \times 10^3\,F \pm 2.91 \times 10^{-1}\%$ and $R_m = 1.59533e4\,\Omega \pm 4.12\%$. $C_p$ is measured using the AH-2500A and its value is $1.41783e-12\,F$.

#### 3.2.3.2 Experimental Setup

Given the fit parameters and the operation frequency, 818-BB-20 is chosen as the power source to drive the QTF. The experimental setup is given in figure (3.21). This setup is

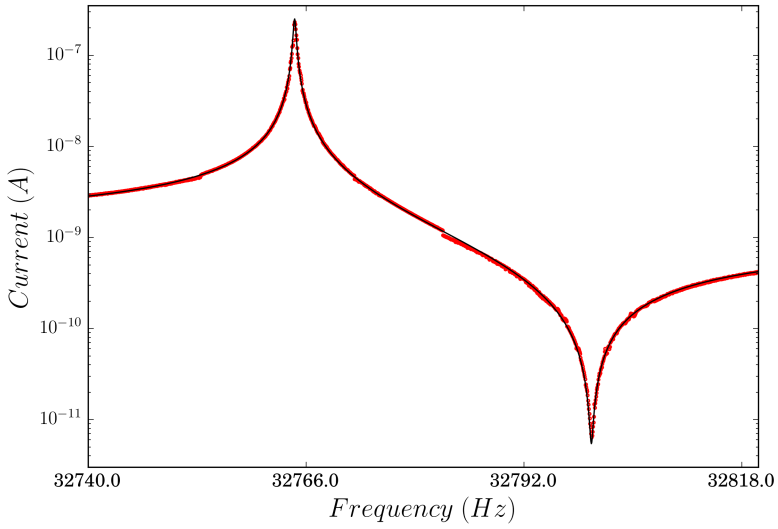


(a)

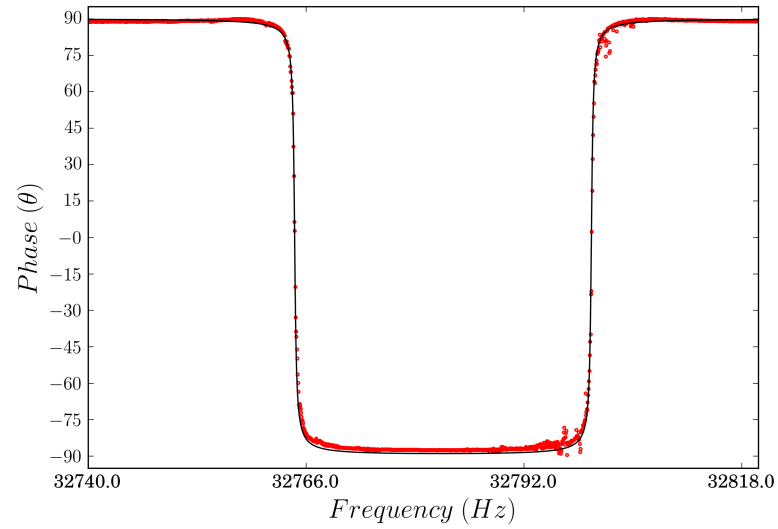


(b)

Figure 3.20: Electrically Driven QTF (a) Measured current and fit, (b) Measured phase. The resonance frequency of $f_r = 32764\,Hz$, an anti-resonance frequency of $f_a = 32800\,Hz$, and a quality factor of $Q = 100,000$. The circuit parameters determined from the fit to the BVD model are:$L_m = 7.69430 \times 10^3\,H \pm 2.92 \times 10^{-1}\%$, $C_m = 3.06662 \times 10^3\,F \pm 2.91 \times 10^{-1}\%$ and $R_m = 1.59533e4\,\Omega \pm 4.12\%$. $C_p = 1.41783e-12\,F$ is measured using AH-2500A capacitance bridge

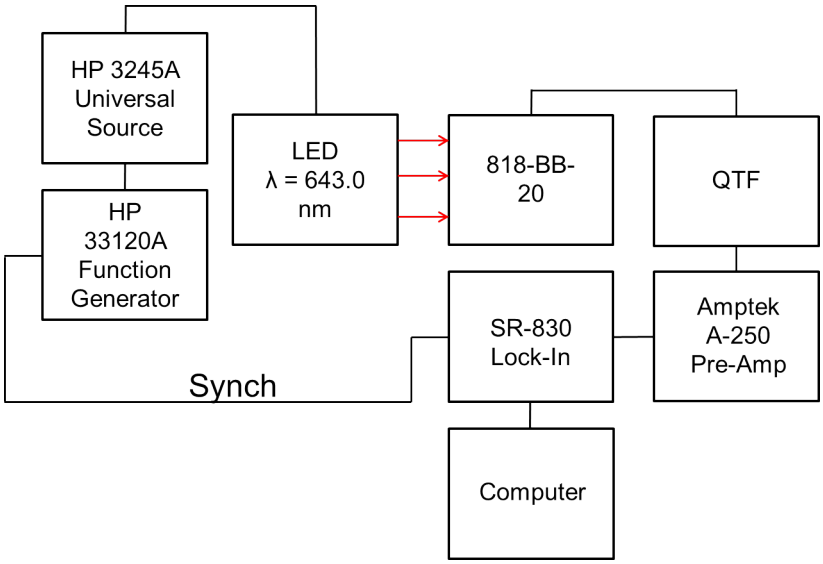


Figure 3.21: Block Diagram of experimental setup used for measuring the AC response of 818-BB-20 biased by the Quartz Tuning Fork (QTF) which is a capacitive load. The HP-3425A and 33120A supply the DC and AC voltage required to bias and modulate the LED. This light is incident on the 818-BB-20 photodetector which is biased by the QTF at $V_{oc}$. The current, $i_{d,3}$, generated by the biased photodetector is amplified by the Amptek A-250. The output of the A-250 is connected to the SR-830 lock-in amplifier. The lock-in is synchronized to the HP-33120A. The data from the lock-in is collected on a computer. The arrows in the diagram indicate light being emitted from the LED onto the 818-BB-20

| $P_{opt}$ $(\mu W)$ | $\Delta P_{opt}$ $(nW)$ | $I_{isc}$ $(nA)$ | $\Delta I_{isc}$ $(nA)$ | $V_{oc}$ $(V)$ | $p_{opt}$ $(nW)$ | $\Delta p_{opt}$ $(nW)$ | $i_{isc_1}$ $(nA)$ |
|---|---|---|---|---|---|---|---|
| 0.314 | 5.34 | 40.8 | 0.304 | 0.306 | 27.1 | 0.461 | 3.53 |
| | | | | | 135 | 2.29 | 17.5 |
| 3.13 | 53.4 | 407 | 3.04 | 0.366 | 34.0 | 0.579 | 4.43 |
| | | | | | 170 | 2.90 | 2.21 |
| | | | | | 341 | 5.79 | 44.3 |

Table 3.4: 818-BB-20 measured $I_{isc}$, $V_{oc}$ and $i_{isc_1}$ for the incident DC and AC optical powers - $P_{opt}$ and $p_{opt}$. $\Delta P_{opt}$, $\Delta I_{isc}$ and $\Delta p_{opt}$ are the measured uncertainties in $P_{opt}$, $I_{isc}$ and $p_{opt}$. Both $\Delta V_{oc}$ and $\Delta i_{isc_1}$ are assumed to be small and hence ignored. The justification for ignoring $\Delta i_{isc_1}$ is given below. Notice the DC and AC optical powers used vary by an order of magnitude

| $P_{opt}$ $(\mu W)$ | $R_{sh}$ $(\times 10^7 \Omega)$ | $\Delta R_{sh}$ $(M\Omega)$ | $R_s$ $(\Omega)$ | $\Delta R_s$ $(m\Omega)$ | $\eta$ | $\Delta \eta$ $(\times 10^{-3})$ | $C_J$ $(pF)$ |
|---|---|---|---|---|---|---|---|
| 0.314 | 21.9 | 1.29 | 0 | 0 | 1.08 | 0.693 | 170 |
| 3.13 | 2.89 | 1.42 | 0.443 | 9.73 | 1.15 | 2.79 | 201 |

Table 3.5: 818-BB-20 values for $R_{sh}$, $R_s$, $\eta$ are determined from fitting the IV curves to equation (2.49).$C_J$ is measured using AH. $\Delta R_{sh}$, $\Delta R_s$ and $\Delta \eta$ are the errors in the fitting to the mentioned equation. $\Delta C_J$ is small and hence ignored

similar to the above discussed resistive and capacitive cases with the difference being the Amptek A250 is used to amplify $i_{d,3}$. The DC, AC optical powers, $P_{opt}$, $p_{opt}$, used and the resulting $I_{isc}$, $i_{isc_1}$ and $V_{oc}$ are given in table (3.4). The optical power is measured using the 1815-C power meter, $I_{isc}$ is measured using the HP4145B and $i_{isc_1}$ is measured using the setup in figure (3.7). $\Delta P_{opt}$, $\Delta p_{opt}$ and $\Delta I_{isc}$ are the instrumental uncertainties acquired from the respective manuals. The uncertainty in $\Delta i_{isc_1}$ is smaller than the rest as was discussed in the noise section in the resistive analysis above. As seen from the table the experiment is conducted with DC and AC optical powers that vary by an order of magnitude. Table (3.5) are the values for $R_{sh}$, $R_s$, $\eta$ and $C_J$ for the incident optical powers. As seen these values decrease with increasing optical power. A similar trend is also seen for the 818-SL as discussed in the resistive case above. $R_{sh}$, $R_s$ and $\eta$ are determined by fitting the IV curves to equation (2.49). The IV curves are not shown but are similar to figure (3.2). $C_J$ is determined using AH.

#### 3.2.3.3 AC Results and Analysis

**3.2.3.3.1 $i_{d,3}$ Measurement and Analysis** Figure (3.19) is the circuit used for analysis. This circuit is similar to figure (2.27)(a) with $Z_L$ replaced by the BVD circuit. Figures (3.22)(a) and (b) are the measured QTF response to DC and AC incident optical powers of $P_{opt} = 3.13 \mu W$ and $p_{opt} = 341\, nW$ respectively. Also plotted are the theoretical predictions from equation (3.3) for figure (3.22)(a) and equation (2.41) for figure (3.22)(b).

In figure (3.22)(a) the x-axis is frequency and the y-axis is $i_{d,3}$. As can be seen from figure (3.22) (a) the measured current varies over 5 orders of magnitude and an agreement between theory and experiment is seen over this range. Notice that $i_{d,3}$ is measured and not $i_{D,3}$. This is because QTF is a capacitive device hence 818-BB-20 is biased at $V_{oc}$ and therefore $I_{D,3} = 0$. Using this, the $B$ parameter in equation (2.67) is $\alpha I_{isc}$ reducing equation (2.67) to

$$i_{d,3} = \frac{-i_{isc_1}}{\sqrt{\left(1 + \alpha I_{isc} R\left(w\right)\right)^2 + \left(\alpha I_{isc} X\left(w\right)\right)^2}} \frac{Z_t}{Z_3} \tag{3.3}$$

$Z_t$, $Z_3$, $R\left(w\right)$ and $X\left(w\right)$ are determined from circuit analysis, table(3.4) and the electrically determined values for $R_m$, $L_m$ and $C_m$. The Q for the optical drive is reduced by 40.78% compared to the electrical drive. This reduction is due to the comparable impedance of $C_J$, i.e. at the resonance frequency the impedance of $C_J$ is 41.92% greater than $R_m$.

The phase of $i_{d,3}$ is given in figure (3.22) (b) along with the theoretical predictions. The x-axis in this plot is in frequency and the y-axis is the phase in degrees. At $f_r$ and $f_a$ the phase is $0^\circ$ indicating the circuit is becoming purely resistive and hence the source is delivering power to a resistive element; i.e. the 818-BB-20 is delivering power to drive the QTF. At frequencies away from $f_r$ and $f_a$ the phase of $i_{d,3}$ is $-90^\circ$ which indicates that the circuit is capacitive. In these plots, similar to the resistive and capacitive sections, uncertainties in $i_{d,3}$ and $\vartheta$ are ignored. The justification for this is given below in the noise section.

**3.2.3.3.2 $p_{d,3}$ Analysis** Figure (3.23) is a plot of the theoretically predicted and experimentally determined $p_{d,3}$ at resonance. This is a log-log plot where the x-axis is $i_{isc_1}$. The resonance point is chosen because the QTF is purely resistive and hence maximum power dissipation occurs. In general, the theoretical predictions agrees well with the experimentally determined $p_{d,3}$. The equation used for both is (3.4) where $Z_{real}$, given in equation (2.35), is the real part of the QTF's impedance and $i_{d,3}$ is either the experimentally measured or the theoretically determined current. There are two important points to note from this figure:

1. As $I_{isc}$ increases $p_{d,3}$ decreases, i.e. as the DC optical power increases AC power delivered to the load decreases. Here, an order of magnitude increase in $I_{isc}$ results in a factor of 2.81 reduction in $p_{d,3}$. From equation (3.4) $I_{isc}$ is in the denominator hence reduction in $p_{d,3}$ is expected.

2. As $i_{isc_1}$ increases $p_{d,3}$ increases, i.e. as the AC optical power increases AC power delivered to the load increases. Here, an order of magnitude increase in $i_{isc_1}$ results in a two orders of magnitude increase in $p_{d,3}$. From equation (3.4) $i_{isc_1}^2$ is in the numerator hence $p_{d,3}$ is expected to increase and the observe trend is also expected

$$p_{d,3} = i_{d,3}^2 Z_{real} = \left( \frac{i_{isc_1}^2}{\left(1 + \alpha I_{isc} R\left(w\right)\right)^2 + \left(\alpha I_{isc} X\left(w\right)\right)^2} \left(\frac{Z_t}{Z_3}\right)^2 \right) Z_{real} \tag{3.4}$$

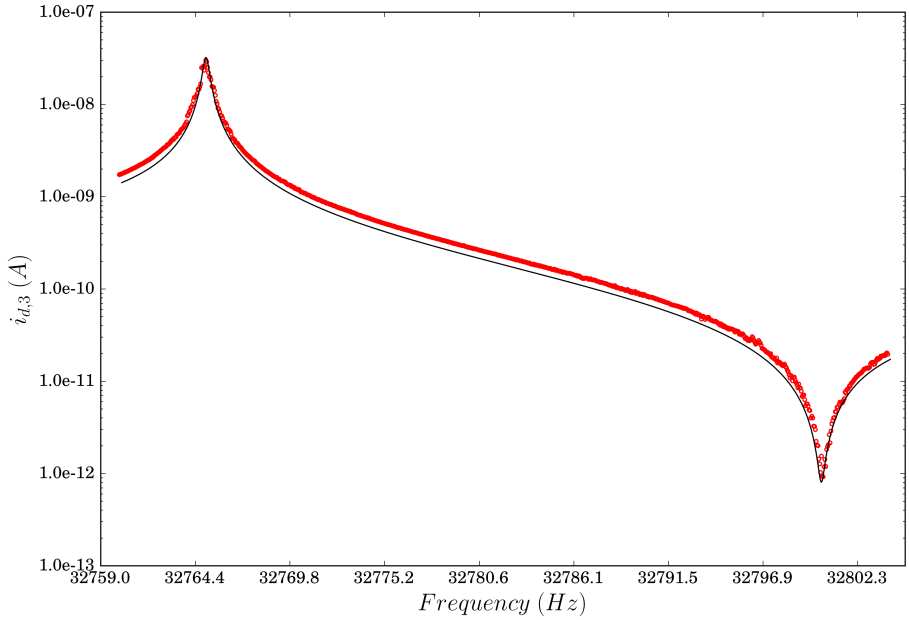


(a)

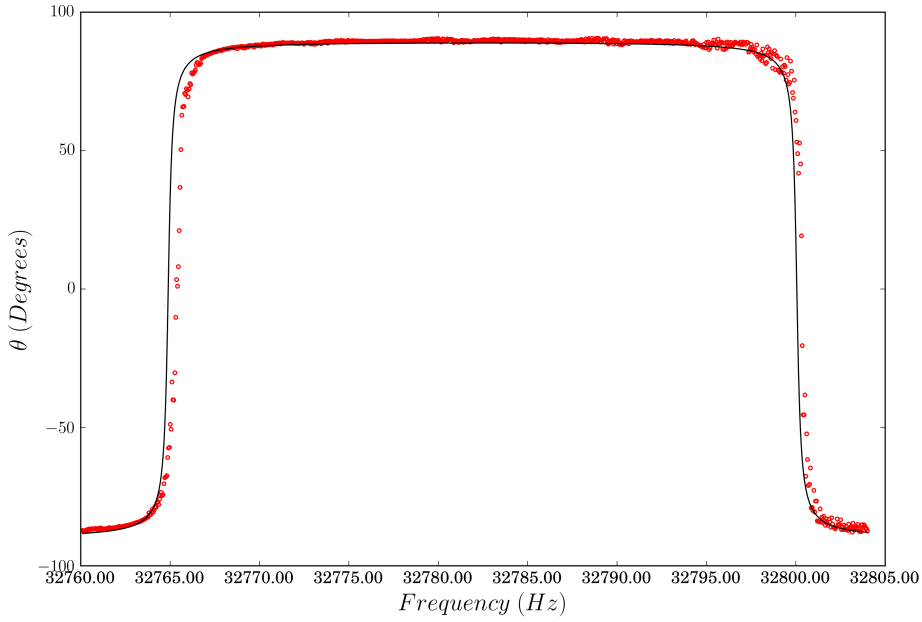


(b)

Figure 3.22: Optically Driven QTF for $P_{opt} = 3.13\,\mu W$ and $p_{opt} = 341\,nW$. (a) $i_{d,3}$ *vs Frequency* The theoretical prediction is made using equation (3.3 (b) $\vartheta$ *vs Frequency* The theoretical prediction is made using equation (2.41). In general for both good agreement is seen between the theoretical prediction and the measured response

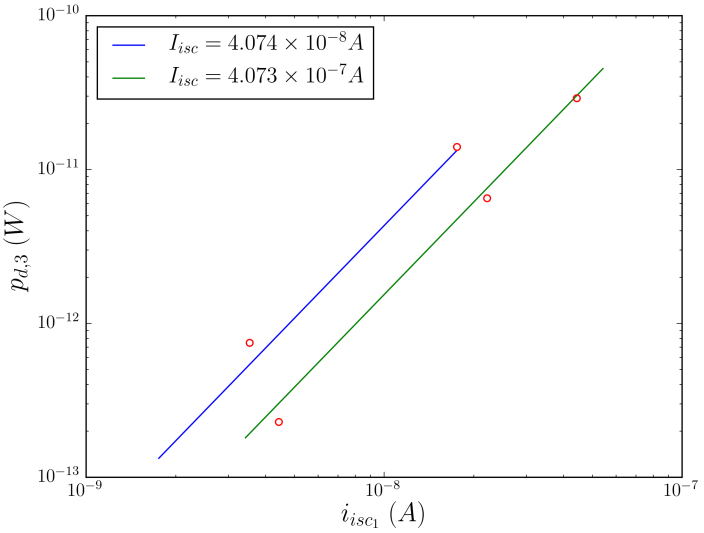


Figure 3.23: Power dissipated at resonance, $p_{d,3}\, vs\, i_{isc_1}$. The $I_{isc}$ and $i_{isc_1}$ used in the experiment are given in table(3.4). The theoretical lines are generated using equation (3.4) for $i_{isc_1}$ values ranging from approximately $2 \times 10^{-9}$ - $2 \times 10^{-8}$ $A$ for an $I_{isc} = 4.074 \times 10^{-8}\, A$ and $i_{isc_1}$ values ranging from approximately $4.5 \times 10^{-9}$ - $5.2 \times 10^{-8}$ $A$ for an $I_{isc} = 4.074 \times 10^{-9}\, A$. The ranges of $i_{isc_1}$ are chosen to be lower than the respective $I_{isc}$

#### 3.2.3.4 Noise

Here, the same methodology as described in the resistive and capacitive case is followed for determining the noise floor. The SNR in this experiment is greater than $1.0 \times 10^4$. The circuit used for this analysis is similar to both cases with the difference being $Z_L$ is the QTF. There are five sources of noise: Johnson noise of $R_{sh}$, $R_s$ and$R_m$, and the shot noise of 818-BB-20 and the A-250. The shot noise of the A250 is $1\frac{nV}{\sqrt{Hz}}$. This value is acquired from the data sheet. Figure (3.24) is the plot of the total noise floor of the experiment and the contributions from each source in the vicinity of resonance. The area around resonance is chosen because in this region maximum power dissipation occurs. The total noise is the quadrature sum of the individual contributions. In this figure the x-axis is frequency and the y-axis is current noise, i.e. $\frac{A}{\sqrt{Hz}}$. The plotted noise is the noise at the input of the A-250. The dominant source of noise is the Johnson noise of $R_{sh}$. This is unlike the resistive and capacitive cases where the amplifier is the dominant source of noise.

## 3.3 Conclusion

In this chapter, the AC response of a photodiode operated in the fourth or PV quadrant was measured for a resistive and capacitive loads. The results from the measurements were compared to the theoretical predictions made by the AC PV model. It was found that the experimental results agrees well with theoretical predictions.

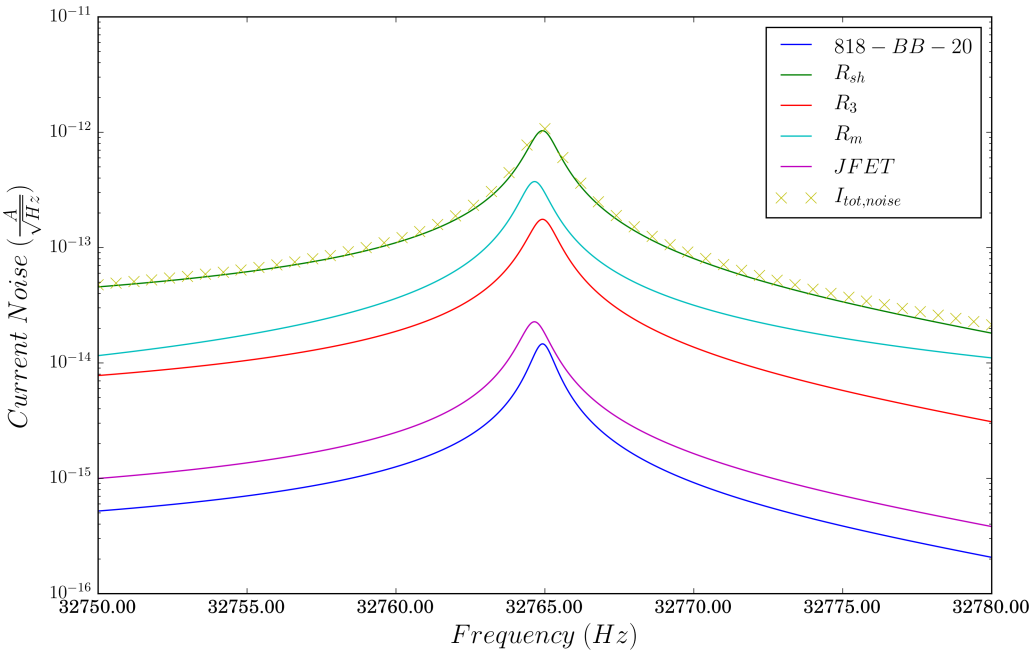


Figure 3.24: Current Noise vs Frequency in the vicinity or resonance. Plotted are the individual contributions from the noise sources: shot noise of 818-BB-20 and A-250, Johnson noise of $R_{sh}$, $R_m$ and $R_s$. Also plotted is the total noise, $I_{tot,noise}$. As is seen the dominant source of noise is the Johnson noise of $R_{sh}$

# Chapter 4

# Driving and Detecting of Torsional modes using Flexural Deformation of tines

## 4.1 Introduction

In this chapter the design, fabrication and experimental validation of a torsional resonator fabricated from a $GaAs$ heterostructure is presented. The torsion modes of the resonator are driven and detected using asymmetrical flexural deformation of two tines. This asymmetrical flexural deformation is achieved using a combination of the unique piezoelectric properties in $GaAs$ and $In_{0.485}Ga_{0.515}P$ and their semiconductor properties. Their semiconductor properties are used for creating a bimorph from a heterojunction and an asymmetrical $pn$ junction. The depletion regions resulting from the heterojunction and $pn$ junction exhibits the piezoelectric property. This property is used to drive and detect the torsional modes.

Next, a literature review on $GaAs$ heterostructure resonators and torsional resonators is given.

### 4.1.1 Literature Review

#### 4.1.1.1 GaAs heterostructure resonator

The earliest work demonstrating the piezoelectric effect in a $GaAs\,pn$ junction was done by White[31]. In this work White used the piezoelectric property of the depletion region in a $GaAs$ $pn$ junction to demonstrate an ultrasonic transducer. He qualitatively demonstrated the operation of this transducer between frequencies of 0.5 to 1.0 GHz.

After this demonstration publications on depletion layer piezoelectric GaAs resonators is sparse till the early 2000s.

In 2002 Knobel et al[55] fabricated a 1.0 GHz doubly clamped resonator in a GaAs heterostructure. The heterostructure consists of a $GaAs - Al_{0.3}Ga_{0.7}As - GaAs$ epitaxially grown heterostructure with a 2DEG between the $GaAs - Al_{0.3}Ga_{0.7}As$ interface. In this structure the $Al_{0.3}Ga_{0.7}As$ is the piezoelectric region. The motivation for using the heterostructure was to integrate an amplifier and a resonator onto a single structure. The

advantage of integrating the two is to reduce the contributions to noise from parasitic capacitive and resistive elements. This was done in order to be able to measure quantized vibrations of the resonator. The measurements were done in a dilution refrigerator achieving a temperature of 10 mK.

In 2007 Masmanidis et al [34] fabricated a single and double clamped resonators using a GaAs *pin* junction. The $p$ and $n$ are the $p$ and $n$ doped regions while the $i$ is the intrinsic region. This region is piezoelectric. The singly clamped heterostructure has a resonance frequency of 8 MHz and the double clamped structure has a resonance frequency of approximately 34 MHz. These structure were electrically driven and the displacement was optically measured. The device was held at a pressure of approximately $5\,mTorr$.

#### 4.1.1.2 Torsional Resonators

Torsional resonators due to their lack of coupling to the environment have high Qs and therefore can be used as sensitive probes to measure weak forces. Some examples of weak forces measured using micro-torsional resonators are:

1. Casimir Force - using a torsional resonator Chan et al[56] measured the attractive force between an uncharged metal surface comprising the resonator and an uncharged metal ball. The casimir force measured ranged from 10s to up to 800 pN depending on the distance between the two uncharged surface. The resonator having a Q of approximately 7150 was fabricated from highly doped polysilicon layers on a silicon substrate. Under 1g this force is equivalent to mass of up to $81\,pg$

2. Nuclear Magnetic Forces - A torsional resonator is used to measure the spin flip of electrons at the interface of a ferromagnetic and a non-magnetic material. This torsional resonator[57] is fabricated from single crystal silicon having a Q of 28,000 and a resonance frequency of $6.7\,MHz$. Using the torsional resonator they were able to measure 76,000 spin flip events which roughly corresponds to a torque of $2.3 \times 10^{-22}\,Nm$ or a force of approximately $0.46\,pN$. Under 1g this force is equivalent to mass of up to $47\,fg$

The inspiration for the design of the torsional resonator described in this chapter came from the work of Kleiman et al[58]. In their work, a torsional resonator was fabricated from single crystal silicon. This torsional resonator is designed to have a symmetric torsional mode and anti-symmetric torsional modes. The Q of the first anti-symmetric torsional mode of the fabricated resonators were found to be between the ranges of $10^4 - 10^8$.

### 4.1.2 Motivation

As mentioned above torsional resonators have high Q. However, they suffer from having complicated non-planar fabrication processes or complicated experimental setups. The experimental setups generally involve either three or more electrical terminals or having measurement apparatuses, that verify deflection, external to the resonator. In contrast, microresonators, e.g. cantilevers, bridges etc, designed to excite and measure flexural deformations are less complicated to fabricate and measure but suffer from low $Qs$.

The torsional resonator presented here is a 2-terminal device, fabricated using planar semiconductor processing, with the capability for in situ deflection measurements. Additionally, the torsional modes are driven and detected using flexural deformations of the structure.

### 4.1.3 Outline

The outline of this chapter is as follows: the mechanical, electrical and heterostructure design of the resonator is discussed in section(4.2). The electromechancial analytical model for the resonator is presented in section(4.3). Section(4.4) outlines the fabrication steps used to build the actual devices. Section(4.5) presents the experimental results and compares them to theoretical predictions. In section (4.6) piezoelectric matrices of common piezoelectric materials are compared to the piezoelectric matrix of III-Vs in order to emphasize its uniqueness. Section(4.7) concludes this chapter.

## 4.2 Design

### 4.2.1 Structural Design

Figure (4.1) is a cartoon of the mechanical structure designed for flexurally exciting and measuring the torsional modes. This structure is called Y and is fabricated from a photodiode heterostructure grown on a $p^+$ GaAs substrate. The heterostructure is chosen as a result of the piezoelectric properties of $GaAs$ and $In_{0.485}Ga_{0.515}P$. These properties and the choices for the grown layers of the heterostructure will be discussed in the following sections.

The Y structure or resonator is comprised of three sections: pad, spine and Y tines. The word tine is used to differentiate between the structure of the spine which is a cantilever and the structure of the Y which are two angled cantilevers. The resonator has two principal modes of oscillation: low frequency flexural mode, resulting from cantilever motion of the spine, and a high frequency torsional coupled motion of the Y structure. The expected torsional mode shapes for the Y structure are shown in figure (4.2). The first mode is the symmetric mode, i.e. the pad and the tines move symmetrically while the second and third modes are the anti-symmetric modes; i.e. the pad and the tines move anti-symmetrically. The commonality amongst these three modes is that the tines exhibit anti-symmetric flexural deformation about the spine resulting in a circular motion about the spine. A pad extended from the spine is added to give rise to anti-symmetric torquing modes - modes 2 and 3. In the first torsional mode the deformed shape of the tines resemble the shape of a cantilever in its fundamental mode, i.e. 0 nodes. In the second torsional mode the shape of the deformed shape of the tines resemble the shape of a cantilever in its first harmonic mode, i.e. 1 node. The third torsional mode the deformed shape of the tines resembles the second harmonic cantilever mode, i.e. 2 nodes. The shapes of the deformed tines are of importance because they are used in section (4.3) to derive the analytical model used for predicting the current at resonance.

In the following section, the unique piezoelectric property of III-V materials is discussed. Using this unique piezoelectric property and III-Vs semiconductor properties the epitaxial layers, comprising the photodiode structure, required for achieving torsional oscillation is discussed.

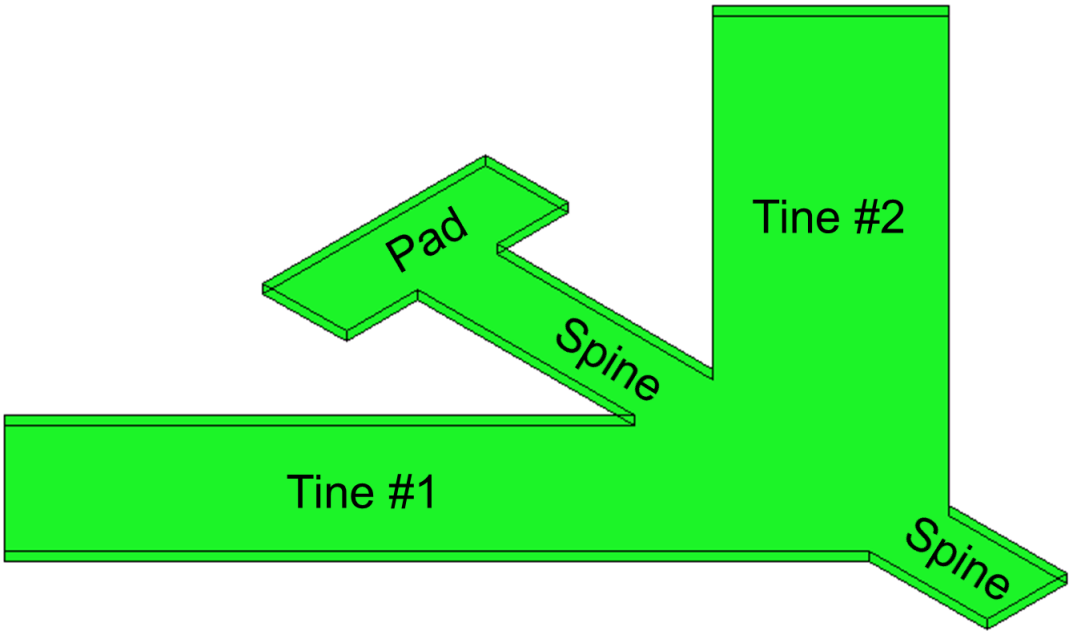


Figure 4.1: Y Structure. The structure is comprised of three sections: Pad, Spine and Tines. The Spine is parallel to [100] while the tines are parallel to $[\bar{1}\bar{1}0]$ and $[1\bar{1}0]$

### 4.2.2 Piezoelectric properties

III-Vs belong to a class of materials lacking symmetry between the positive and negative ions of the crystal lattice. In GaAs, for example, there is a tendency for the electron clouds to shift towards the arsenic atoms resulting in a dipole along the [111] axis. This deviation from inversion symmetry results in non-vanishing piezoelectric coefficients.

To determine the piezoelectric coefficients required to achieve torsional motion the wafer orientation needs to be considered. The most common wafer orientation for GaAs is (100). A top view of this wafer orientation is illustrated in figure (4.3). In this wafer orientation, [100] is the normal axis $x_3$ or the z-axis, $[\bar{1}10]$ is the $x_2$ or y axis and $[\bar{1}\bar{1}0]$ is the $x_1$ or the x axis. The x and y axis are the primary and the secondary flats. The piezoelectric matrix for this wafer orientation is:

$$d_{iq}(\phi) = \frac{d_{14}}{2} \begin{bmatrix} 0 & 0 & b_2 \\ 0 & 0 & -b_2 \\ 0 & 0 & 0 \\ 2a_2 & -2b_2 & 0 \\ -2b_2 & 2a_2 & 0 \\ 0 & 0 & 2a_2 \end{bmatrix} \frac{pC}{N}$$

where $\phi$ is the rotation of the coordinate system around the $x_3$-axis, $b_2 = cos(2\phi)$ and $a_2 = sin(2\phi)$. $\pm b_2$ is maximized if $\left(\phi = \frac{n\pi}{2}\right)$. This reduces the piezoelectric matrix to:

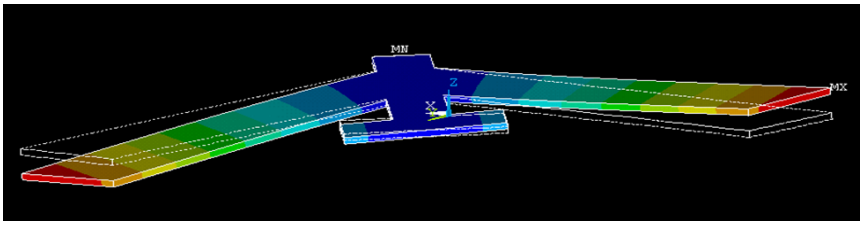


(a)

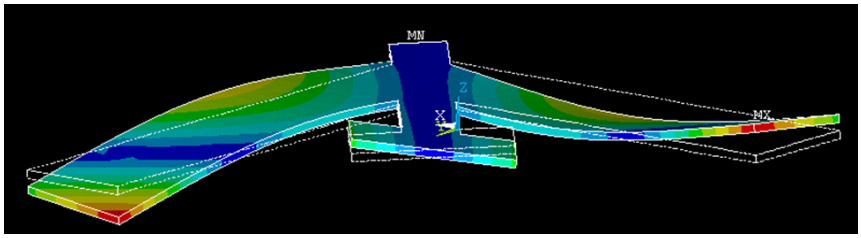


(b)

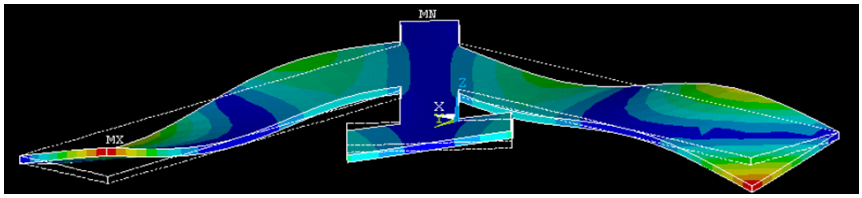


(c)

Figure 4.2: First three torsional Y-Structure Mode Shapes: (a) Symmetric Fundamental, (b) Anti-Symmetric Fundamental and (c) Anti-Symmetric 1st Harmonic. The shape of the tines for the first two torsional modes resemble the first two mode shapes of a cantilever having 0 and 1 node; respectively. The shape of the tine for the 3rd torsional mode is similar to a cantilever's 3rd mode shape only in the number of nodes, i.e. 2.

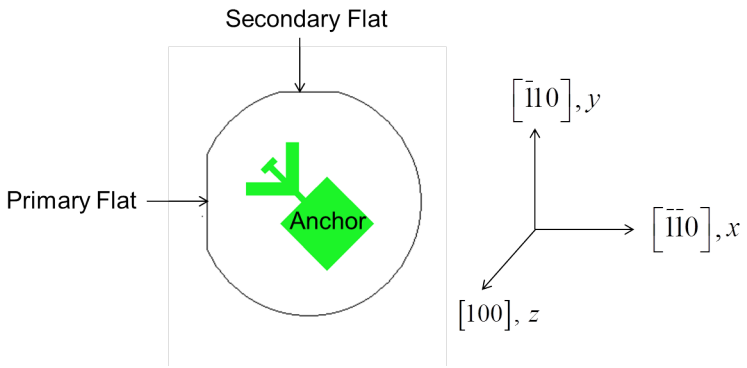


Figure 4.3: Cartoon of the orientation of GaAs Torsional Resonator with respect to the [100] wafer. Beside the cartoon is the coordinate system pertaining to the [100] wafer orientation. The flat lines are the primary and secondary flats on the wafer. They are parallel to $[\bar{1}\bar{1}0]$ and $[\bar{1}10]$. The spine in parallel to [100] while the tines of the resonator are parallel to $[\bar{1}\bar{1}0]$ and $[\bar{1}10]$ or the $x$ and $y$ axis. The spine of the resonator is clamped at the anchor. The corners of the anchor are parallel to [100] and $[\bar{1}00]$

$$d_{iq} = \frac{d_{14}}{2} \begin{bmatrix} 0 & 0 & 1 \\ 0 & 0 & -1 \\ 0 & 0 & 0 \\ 0 & 2 & 0 \\ -2 & 0 & 0 \\ 0 & 0 & 0 \end{bmatrix} \frac{pC}{N} \tag{4.1}$$

which is the piezoelectric matrix for the 100 wafer orientation. The non-zero components of interest are $d_{13}$ and $d_{23}$. For these components a field applied in the z-direction results in an extension/compression in the x-direction and a compression/extension in y-direction. Using this asymmetry, tines that are parallel to these directions can be driven anti-symmetrically. As discussed in chapter(2) using a unimorph or a bimorph structure flexural strain can result from longitudinal strain. Here, a bimorph structure is created by epitaxially growing an asymmetric pn junction and a heterojunction. The chosen epitaxial layers are discussed in the next section.

A cartoon of the orientation of the torsional resonator is illustrated in figure (4.3). As is seen from this figure, the torsional resonator's tines, pad and anchor are parallel to $[\bar{1}\bar{1}0]$ and $[\bar{1}10]$ while the spine is parallel to [100].

### 4.2.3 MBE growth

Figure (4.4) is the cross-sectional view, parallel to 100, of the epitaxial layers comprising the photodiode. This heterostructure is grown using molecular beam epitaxy (MBE). The thickness and the doping concentration of the epitaxial layers are also given in this figure. Table (4.1) replicates this information with the addition of adding the purpose for each layer. The layers are discussed next.

| Layer | Grown Material | Doping Type | Doping Concentration $(cm^3)$ | Thickness $(nm)$ | Purpose |
|---|---|---|---|---|---|
| 1 | $GaAs$ | $p^+$ | $1.9 \times 10^{18}$ | 50 | Buffer |
| 2 | $Al_{0.8}Ga_{0.2}As$ | $i$ | $1.5 \times 10^{15}$ | 1000 | Sacrificial |
| 3 | $GaAs$ | $p^+$ | $2.0 \times 10^{19}$ | 200 | Bottom Contact |
| 4 | $In_{0.485}Ga_{0.515}P$ | $p$ | $1.0 \times 10^{18}$ | 50 | Passivation |
| 5 | $GaAs$ | $p$ | $1.0 \times 10^{17}$ | 1500 | p-junction |
| 6 | $GaAs$ | $n$ | $1.0 \times 10^{18}$ | 100 | n-junction |
| 7 | $In_{0.485}Ga_{0.515}P$ | $n$ | $2.0 \times 10^{18}$ | 25 | Passivation |
| 8 | $GaAs$ | $n^+$ | $5.0 \times 10^{18}$ | 200 | Top Contact |

Table 4.1: Layers comprising the heterostructure, doping type, concentration, thickness and purpose

The photodiode structure is grown on a 3 in. diameter $p^+$ GaAs (100), $1.0 \times 10^{19}\,cm^{-3}$, wafer in Ultra High Vacuum (UHV) under standard set of conditions for III-V material growth. The growth begins with a standard 50 nm $p^+$ GaAs buffer layer upon which the sacrificial and electromechanical layers are grown. The first layer after the buffer layer is a 1000 nm $Al_{0.8}Ga_{0.2}As$ sacrificial layer[1]. The thickness is chosen as a compromise between successfully releasing the mechanical structures and to avoid the presence of dislocations[2] in the electromechanical layers. The released structure is illustrated in figure(4.5)(a). The unetched section of the $Al_{0.8}Ga_{0.2}As$ is the anchor of the mechanical structure and the etched section is the area where the mechanical structure is free to deform.

Following the sacrificial layer a 200 nm $p^+$ GaAs electrical contact layer is grown. The thickness and doping concentration for the contact layer are chosen to achieve low contact resistance. A surface passivation layer, $50\,nm\ p-In_{0.485}Ga_{0.515}P$[3] layer is grown on top of the electrical contact layer. Following the passivation layer is an asymmetric, both in thickness and doping concentration, $GaAs\,pn$ junction having thicknesses of $1.5\,\mu m$ and $100.0\,nm$, respectively. The layers following the $n^-$ junction are $25\,nm\ n-In_{0.485}Ga_{0.515}P$ passivation layer and $200\,nm\ n^+GaAs$ electrical contact layers. The $p^+$ and $n^+$ contacts layers are referred to as bottom and top electrical contacts.

The $In_{0.485}Ga_{0.515}P$ layers, in addition to their role for surface passivation, also form a back surface field (BSF). This will be discussed in chapter 6

The resonator therefore comprises of two semiconductor layers $GaAs$ and $In_{0.485}Ga_{0.515}P$. The thicknesses and the choice of these layers are chosen to ensure successful fabrication of the resonator. This is elaborated below, in the fabrication section.

[1] The term sacrificial layer means this layer is etched or removed during fabrication such that the intended mechanical structure is free to deform

[2] Dislocations occur because $Al_{0.8}Ga_{0.2}As$ is not lattice matched to GaAs. This mismatch results in the growth of strained $Al_{0.8}Ga_{0.2}As$. This strained region relaxes past a critical thickness and the result of this relaxation is dislocation. The layers grown on top of a dislocated region will propagate the dislocations causing failure in fabrication

[3] $In_{0.485}Ga_{0.515}P$ is lattice matched to $GaAs$. Hence avoiding issues regarding dislocations

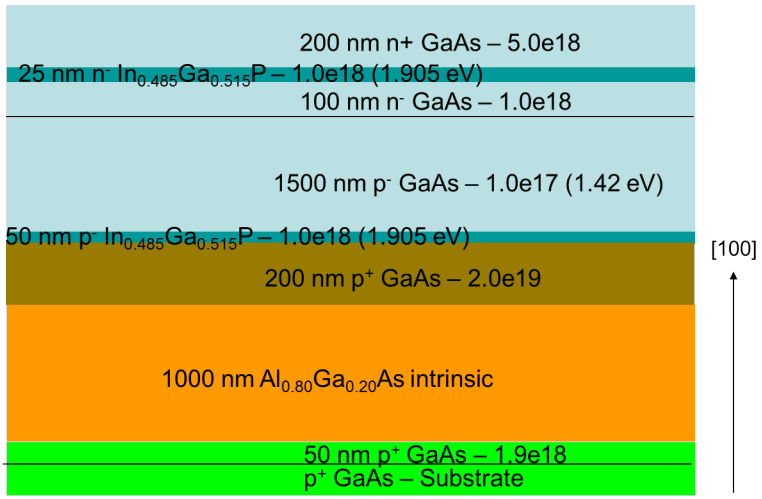


Figure 4.4: Cross-Sectional view of the MBE grown structure parallel to [100]. The arrow is drawn parallel to [100]. $Al_{0.8}Ga_{0.4}As$ is the sacrificial layer. The bottom and top contacts are the $200\,nm\,p^+$ and $n^+$ layers. The $In_{0.485}Ga_{0.515}P$ layers are grown for surface passivation and to create a back surface field (BSF). The $p^-n^-$ $GaAs$ layers comprises the $pn$ junction

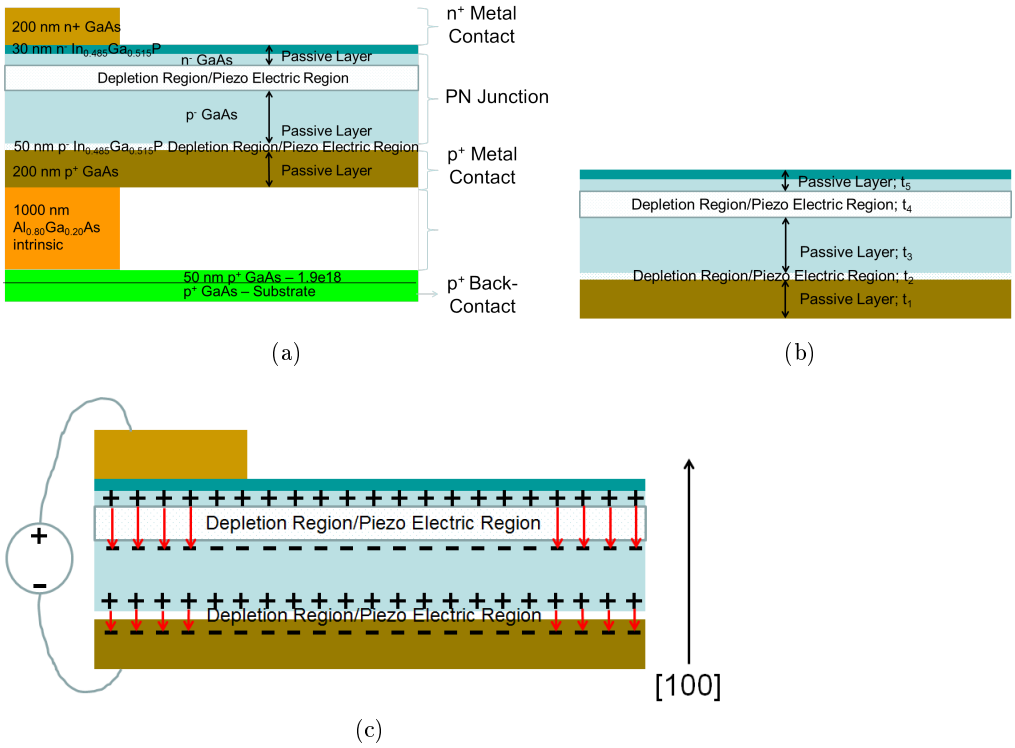


Figure 4.5: Cross-section of a released tine. (a) Location of the depletion width/piezoelectric and passive layers, (b) $t_1$, $t_2$, $t_3$ $t_4$ and $t_5$ are the thickness of passive and piezoelectric layers and (c) The applied potential appears across the depletion widths. The red arrows are the direction of the field going from positive (+) to negative (-) potential

### 4.2.4 Depletion/Piezoelectric Regions

In this section the position of the piezoelectric regions within the photodiode structure is discussed.

In order to efficiently drive and measure piezoelectricity the piezoelectric material should be insulating. In III-V materials, there are two ways of achieving this: doping with iron or using its semiconductor properties to create a depletion region. The former was used by Hjort[1] to fabricate tuning forks as discussed in the introduction chapter of this thesis. In the latter the depletion region has the additional property of piezoelectricity. For the above discussed MBE structure the location of the depletion region is best illustrated using the energy band diagram, figure 4.6. In this figure the x-axis is the thickness of the structure, where $0\,\mu m$ is the the top $n^+$ contact layer and $2.075\,\mu m$ is the bottom $p^+$ contact layer. The y-axis in this figure is the energy of the bands. From, figure 4.6 and as illustrated in the cartoon of figure(4.5)(a), there are two depletion/piezoelectric regions:

1. at the interface between the $p^-n^-$ GaAs
2. the depleted $p^-$ $In_{0.485}Ga_{0.515}P$ region

For convenience the depletion regions, $p^-In_{0.485}Ga_{0.515}P$ and $p^-n^-GaAs$, are referred to as layers 2 and 4. The choice for naming layers 2 and 4 coincides with figure (4.5)(b) where $t_1, \ldots, t_5$ are the thickness of the bottom contact $GaAs$ successively to the top contact $GaAs$. The depleted $p^-n^-$ junction and the depleted $p^-$ $In_{0.485}Ga_{0.515}P$ region in combination with the electrical contact layers is the bimorph required for flexural deformation. This can be seen as follows:

1. A voltage applied across the top and bottom electrical contacts are dropped across the depletion regions, figure(4.5)(c)
2. The voltage in the respective depletion regions results in a longitudinal deformation due to the piezoelectric effect
3. The extent of the longitudinal deformation is restricted by the passive elastic layers resulting in flexural deformation

As discussed above, in the piezoelectric section, the tines are parallel to the x and y axis and thus will undergo asymmetric flexural deformation. This asymmetric flexural deformation is used to drive the torsional modes using the piezoelectric effect and measure the mechanical deformation using the inverse piezoelectric effect.

### 4.2.5 Dimensional constraints

In this section, the dimensions chosen for the resonator are discussed. The motivation for choosing the length and widths of the pad, spine and tines is to maximize the quality factor $Q$. As stated in the theory section, 2.2.2, the $Q$ of a resonator is limited by various intrinsic and extrinsic factors. Anchor loss is one of the extrinsic factors and occurs because a deforming structure connected to an anchor deforms the anchor resulting in a non-recoverable loss of energy from the vibrating structure. By choosing the appropriate dimensions of length and width for the pad, spine and tines this loss can be minimized. The anchor limited $Q$ is

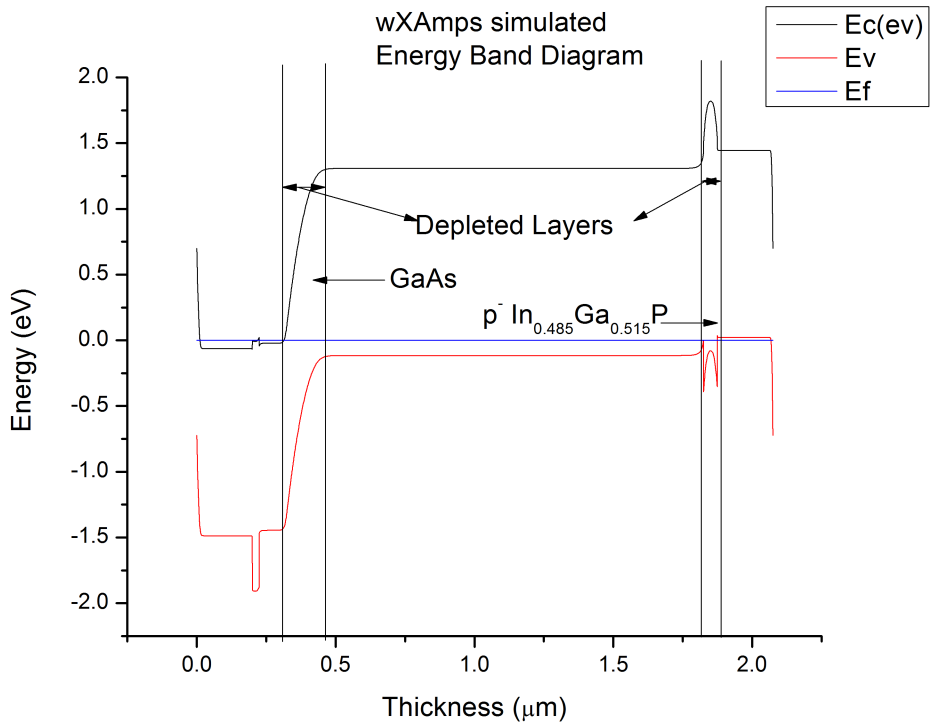


Figure 4.6: wxAmps simulated Energy Band Diagram. The pn and heterojunction depleted regions are indicated

expressed as $Q_{anch} = 2\pi \frac{E_{res}}{E_{anch}}$. Here $E_{res}$ is the strain energy stored in the vibrating structure and $E_{anch}$ is the strain energy stored in the anchors during maximum displacement. The respective strain energies are acquired using Ansys - a finite element analysis (FEA) software. The following restrictions are placed on the dimensions of the pad, spine, tines and anchor:

1. The spine fundamental cantilever mode is greater than $20.0\,KHz$. This restriction is chosen because spine lengths having frequencies below $20.0\,KHz$ have low fabrication yield. The same restriction holds for the tine lengths.

2. A spine width of $10\,\mu m$ is chosen. Ideally the width of the spine should be as thin as possible in order to minimize the loss of strain energy to the anchor and to maximize torque cancellation along the spine in the anti-symmetric modes. A choice of $10.0\mu m$ assures successful fabrication

3. Frequencies between adjacent modes should well separated so as to limit the coupling between adjacent modes. The coupling occurs due to the modes finite $Q$

4. Torsional frequencies of interest are less than $1.5\,MHz$. The restriction is a result of the bandwidth limitation of the amplifier

5. Simulated $Q_{anch} > 1000$; are only chosen. This is because structures having $Q > 1000$ yields a large signal to background ratio. This is discussed in greater detail in the section on electrical modeling, section (4.3)

6. The anchor size has to be greater than $150 \times 150\,\mu m$ but less than $350 \times 350\,\mu m$. The anchor of the mechanical structure also serves the dual purpose of being the top electrical contact. The electrical contacts are made using a wire bonder. The wire bonder restricts the contact size to a minimum of $150\,\mu m$ while the $350\,\mu m$ restriction is required to keep the background signal low. A further explanation of this is given in section (4.3)

7. A tine width of $30.0\,\mu m$ is chosen to maximize the piezo signal as explained in section (4.3)

8. The pad dimensions are kept smaller than the tine dimensions. This is motivated by the work of Kleiman et al[58]

Following the above restrictions the dimensions for the Y structures are given in table (4.2). Two common trends can be seen:

1. Increasing the pad length results in decreasing the frequencies of the torsional mode

2. Increasing spine length results in decreasing the frequency of all the modes

Given the design, the dimensions of the structure and the piezoelectric matrix an analytical model is derived next predicting the expected current at resonance.

| Spine Length ($\mu m$) | Tine Length($\mu m$) | Tine Center($\mu m$) | Pad Width($\mu m$) | Pad Length($\mu m$) | Mode# | Frequency ($Hz$) | Q |
|---|---|---|---|---|---|---|---|
| 92.43 | 100 | 50 | 20 | 40 | 1 | 51,894 | 15,813 |
| | | | | | 2 | 374,658 | 10,780 |
| | | | | | 3 | 1,391,790 | 111,624 |
| 92.43 | 60 | 50 | 10 | 40 | 1 | 98,743 | 14,033 |
| | | | | | 2 | 737,430 | 12,884 |
| | | | | | 3 | 1,666,320 | 389,363 |
| 92.43 | 60 | 50 | 15 | 40 | 1 | 98,478 | 14,397 |
| | | | | | 2 | 725,828 | 14,869 |
| | | | | | 3 | 1,644,870 | 348,365 |
| 102.45 | 80 | 60 | 15 | 40 | 1 | 73,392 | 14,971 |
| | | | | | 2 | 515,127 | 12,196 |
| | | | | | 3 | 1,161,570 | 102,185 |
| 102.45 | 80 | 60 | 15 | 80 | 1 | 68,192 | 15,131 |
| | | | | | 2 | 283,574 | 143,949 |
| | | | | | 3 | 542,748 | 13,277 |
| | | | | | 4 | 1,146,510 | 94,554 |
| 162.43 | 80 | 60 | 15 | 40 | 1 | 45,610 | 24,190 |
| | | | | | 2 | 463,149 | 139,486 |
| | | | | | 3 | 824,750 | 3,147,875 |
| | | | | | 4 | 1,142,140 | 309,761 |

Table 4.2: Y resonator dimensions, mode number, resonant frequency and Q. The increasing mode numbers corresponds to the fundamental symmetric and the fundamental anti-symmetric and 1st harmonic anti-symmetric modes. In general, increasing the pad length results in decreasing the frequencies of the torsional modes and increasing the spine length results in decreasing the frequency of all the modes

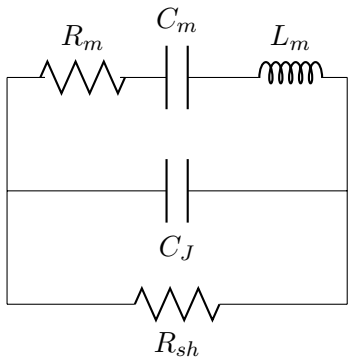


Figure 4.7: Modified Butterworth-Van Dyke (BVD) Electrical Circuit. $R_m$, $L_m$, $C_m$ are the motional terms and $C_J$ is the junction capacitance and $R_{sh}$ is the shunt resistance accounting for the finite resistance in the material

## 4.3 Electrical Prediction

The modified BVD model figure (4.7) is used to describe the current at resonance. The difference between the BVD and modified BVD is the package capacitance is replaced with the junction capacitance and a shunt resistance, $R_{sh}$, is added. $R_{sh}$ accounts for the finite resistance of the diode. In the modified BVD model $C_J$ and $C_m$ are the total junction capacitance and total motional capacitance. As is seen in figure(4.5)(c) for the heterojunction considered here there are two capacitors in series. In the derivation, $C_{J,j}$ and $C_{m,j}$ for each layer is first derived and then using circuit theory an expression for the equivalent $C_J$ and $C_m$ is given. The subscript $j$ is used to indicate the layer of interest. $j$ is either equivalent to 2 or 4. $L_m$ is determined using equation (2.37) where $f_r$ is the resonance frequency of the torsional mode determined from table (4.2).

To determine $C_{m,j}$ and $C_{J,j}$ the piezoelectric and dielectric thicknesses and the location of these layer with in the bimorph is required. As described in section (4.2.4) and figure (4.5)(b) the thickness of the piezoelectric and dielectric regions, $t_2$ and $t_4$, are equivalent to the respective depletion thicknesses because they are one and the same. $t_2$ according to figure(4.5)(b), is the the thickness of layer 2 which is $50\,nm$. $t_4$, is determined using the equation (2.43). The values used for $\epsilon_r$, $N_a$ and $N_d$ are 13.16[59], $1.0 \times 10^{17}\,cm^{-3}$ and $1.0 \times 10^{18}\,cm^{-3}$. The equation for the built-in voltage is equation(2.42). The intrinsic carrier concentration for GaAs is: $2.0 \times 10^{6}\,cm^{-3}$ [60] and a temperature of $300\,K$ is chosen. Using these values the depletion width is: $146.19\,nm$ which agrees with the simulated data in figure 4.6. The extent of the depletion width into the $p^-$ and $n^-$ regions is: 132.90 and $13.290\,nm$ reducing the thickness of $p^-$ and $n^-$ regions to: 1367.10 and $86.710\,nm$. The extent into the $p^-$ and $n^-$ regions is calculated using the following equations[5]: $x_{p0} = \frac{W}{1+\frac{N_a}{N_d}}$ and $x_{n0} = \frac{W}{1+\frac{N_d}{N_a}}$. The individual elastic layer thicknesses are: $t_1 = 200.0$, $t_3 = 1367.10$ and $t_5 = 86.710\,nm$. The locations of $t_1$, $t_3$ and $t_5$ are indicated in figure (4.5)(b).

Having determined the thickness of the piezoelectric and dielectric layers the piezoelectric and inverse piezoelectric effect is used to determine $C_{m,j}$. The overview of the derivation, given in figure (4.8), is as follows: an applied voltage results in a $z$-directed elec-

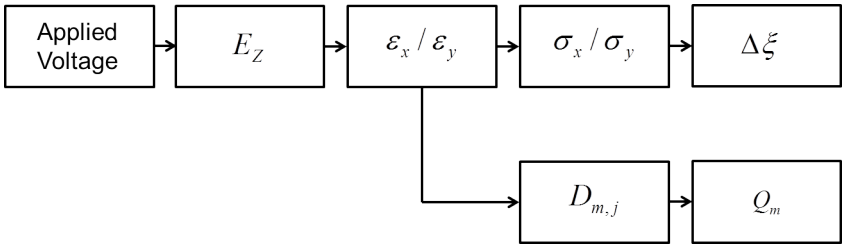


Figure 4.8: Overview of $C_{m,j}$ derivation. An applied voltage results in an z-directed field which produces a $x$ or $y$ directed strain, depending on the orientation of the tine, due to the piezoelectric effect. The resulting strain produces a $x$ or $y$ directed stress. This stress due to the bimorph structure results in a bending moment in the $y$ or $x$ direction which then results in a deflection in the $z$-direction. The x or y directed strain also results in a dipole producing an electric displacement, $D_{m,j}$, in the $z$-direction which can then be integrated to determine the piezoelectric charge, $Q_m$. Using $Q_m$ $C_{m,j}$ is determined

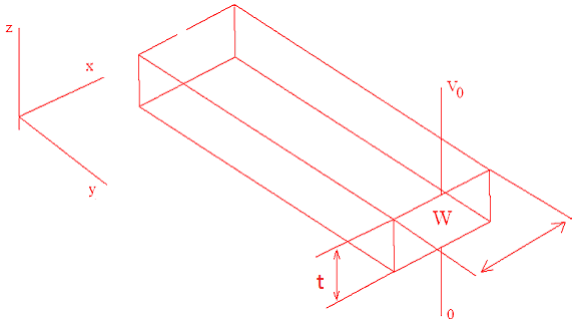


Figure 4.9: GaAs tine geometry coordinate system. The x-axis is the width, y-axis is the length and the z-axis is the thickness

tric field which produces a $x$ or $y$ directed strain, depending on the orientation of the tine, due to the piezoelectric effect. The resulting strain produces a $x$ or $y$ directed stress. This stress due to the bimorph structure results in a bending moment in the $y$ or $x$ direction which then results in a deflection in the $z$-direction. The $x$ or $y$ directed strain also results in a dipole producing an electric displacement, $D_{m,j}$, in the $z$-direction which can then be integrated to determine the piezoelectric charge. This charge, $Q_m$, is the same through both the motional capacitances because the capacitors are in series. Using $Q_m$ $C_{m,j}$ can be determined via $Q_m = C_{m,j}V_j$. Figure (4.9) is the geometry of one of the tines and the associated coordinate system. The x-axis is the width, y-axis is the length and the z-axis is the thickness. Using this geometry and the fact that $Q_m$ is the same for both $C_{m,j}$:

$$\begin{gathered} Q_m = C_{m,2}V_2 = \int_0^L \int_0^W D_{m,2}dydx = Q^1_{m,2} + Q^2_{m,,2} \\ = \int_0^L \int_0^W d_{13,2}Y\epsilon_{6,2}dydx + \int_0^L \int_0^W d_{13,2}Y\epsilon_{1,2}dydx \end{gathered} \tag{4.2}$$

$$\begin{gathered} Q_m = C_{m,4}V_4 = Q^1_{m,4} + Q^2_{m,4} \\ = \int_0^L \int_0^W D_{m,4}dydx \int_0^L \int_0^W d_{13,4}Y\epsilon_{6,4}dydx + \int_0^L \int_0^W d_{13,4}Y\epsilon_{1,4}dydx \end{gathered} \tag{4.3}$$

The $Q^1_{m,j}$ and $Q^2_{m,j}$ terms in equation (4.2) and (4.3) are the motional charge related to the bending and longitudinal strain of the piezoelectric layers. These both need to be considered because the structure undergoes both longitudinal and bending strain. These both strains due to the inverse piezoelectric generates a charge. In these equations $Y_2$ and $Y_4$ are the modulus of elasticity for the $In_{0.485}Ga_{0.515}P$ and $GaAs$ layers. The expressions for $C_{J,2}$ and $C_{J,4}$ are:

$$Q_J = C_{j,2}V_2 = \int_0^L \int_0^W D_{J,2}dydx = \int_0^L \int_0^W \epsilon_{r,2}\epsilon_0 E_3 dydx = \int_0^L \int_0^W \epsilon_{r,2}\epsilon_0 \frac{V_2}{t_2}dydx$$

$$C_{J,2} = \frac{\epsilon_0\epsilon_{r,2}}{t_2}\sum_i L_i W_i \tag{4.4}$$

$$Q_J = C_{J,4}V_4 = \int_0^L \int_0^W D_{J,4}dydx = \int_0^L \int_0^W \epsilon_{r,4}\epsilon_0 E_3 dydx = \int_0^L \int_0^W \epsilon_{r,,4}\epsilon_0 \frac{V_4}{t_4}dydx$$

$$C_{J,4} = \frac{\epsilon_0\epsilon_{r,4}}{t_4}\sum_i L_i W_i \tag{4.5}$$

where $L_i$ and $W_i$ are the length and the width of the pad, spine, tines and the anchor. Unlike the motional capacitance for the junction charge the dimensions of the complete structure needs to be considered because the depletion regions extends to both the resonator and the anchor. This dielectric charge or current is the background signal.

The voltage for $C_{J,j}$ and $C_{m,j}$ is $V_j$. This is expected because the voltage drop is determined by the junction capacitance.

The detected motional charge is $Q_{m,j} = Q^1_{m,j} + Q^2_{m,j}$. The expression for $Q^1_{m,j}$, is given in equation (4.6); where $\bar{z}_j$ is the distance from the neutral axis to the region of

greatest stress/strain in the respective piezoelectric layers and $\xi$ is the deflection of the tine. The mathematical expression for the tine's deflection is given in equation(4.7) where the first term in the sum is the equation for the mode shape equation (4.8) and the second term is the curvature evaluated at some point along the length of the tine, i.e. $y = y_1$. In these equations $(k_i L)$ are numerical values, table (2.2), yielding the familiar cantilever modes. $M_j$ in equation (4.7) is the bending moment and $I_j$ is the moment of inertia.

$$Q^1_{m,j} = \int_0^L \int_0^W d_{23,j} Y \bar{z}_j \frac{\partial^2 \xi}{\partial^2 x^2} dy dx = YW d_{23,j} \bar{z}_j \frac{\partial \xi}{\partial y}\bigg|_{x=L} \tag{4.6}$$

$$\xi(y) = \frac{M_j L^3}{Y_j I_j} \sum \frac{X_i}{(k_i L)^4} \left(\frac{\partial X_i}{\partial y}\right)_{y=y_1} = \frac{M_j L^3}{Y I_j} \psi_i \tag{4.7}$$

$$X_i = cos(k_i y) - cosh(k_i y) - \alpha_i (sin(k_i y) - sinh(k_i y)) \tag{4.8}$$

where

$$\alpha_i = \frac{cosh(k_i L) + cos(k_i L)}{sinh(k_i L) + sin(k_i L)}$$

The expression for $Q^2_{m,j}$ for the two piezoelectric layers are:

$$Q^2_{m,j} = \frac{d_{23,2} L F_2}{t_2} \tag{4.9}$$

$$Q^2_{m,j} = \frac{d_{23,4} L F_4}{t_4} \tag{4.10}$$

where $F_2$ and $F_4$ are the extensional force and $t_2$ and $t_4$ are the thicknesses of the piezoelectric layer.

Therefore expressions for $M_j$, $\bar{z}_j$ and $F_j$ are required in order to obtain numerical values of $Q^1_{j,m}$ and $Q^2_{j,m}$. $M_j$ and $F_j$ are derived using the following assumptions:

1. In static equilibrium $\sum F_j = 0$ and $\sum M_j = 0$; i.e. $M_1+M_2+M_3+M_4+M_5 = F_1\left(\frac{t_1}{2}\right)+F_2\left(t_1+\frac{t_2}{2}\right)+F_3\left(t_1+t_2+\frac{t_3}{2}\right)+F_4\left(t_1+t_2+t_3+\frac{t_4}{2}\right)+F_5\left(t_1+t_2+t_3+t_4+\frac{t_5}{2}\right)$. The condition for the moment is true only at the tip of the tine. $F_j$ represents the axial force while $M_j$ is the bending across each of the five layers

2. Each of the layers comprising the bimorph are assumed to be thin enough such that the radius of curvature, $r$ is the same across all layers; $\frac{1}{r} = \frac{\sum_j M_j}{\sum_j Y I_j}$

3. Total strain at the interface of each of the layers must be equivalent to each other; $\epsilon_1(t_1) = \epsilon_2(t_1)$, $\epsilon_2(t_2) = \epsilon_3(t_2)$, $\epsilon_3(t_3) = \epsilon_4(t_3)$ and $\epsilon_4(t_4) = \epsilon_5(t_5)$

4. The stress or strain at the bottom of the tine is opposite to the top, i.e. if the bottom is in tensile strain the top is in compressive

5. The maximum stress/strain occurs at the bottom to the tines, i.e. $\epsilon_1(0) = -\epsilon_3(t)$

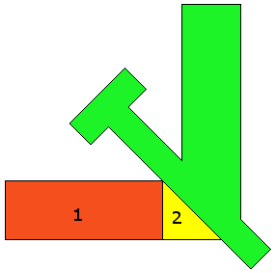


Figure 4.10: Segmentation of the tine's Y-Torsional Resonator tine. The tine is split into two segments. Segment#1 is the standard cantilever geometry and segment#2 is the extra piece of the tine whose length and width are the same, i.e. $W = L = 30\,\mu m$. For the calculations segment#2 is assumed to be clamped

6. A single tine is considered in the calculations. Once an expression for the charge is derived for a single tine that number is double to reflect the consideration of both the tines

7. As depicted in figure (4.10) the second segment of the tine is considered to be clamped; hence allowing for the use of the cantilever modes on the first segment

   Using assumption 3:
   Layers 1 and 2; $\epsilon_1(t_1) = \epsilon_2(t_1)$

$$\frac{F_1}{A_1 Y} - \frac{t_1}{2r} = -d_{23,2}\frac{V_2}{t_2} + \frac{F_2}{A_2 Y} + \frac{t_2}{2r}$$

   Layers 2 and 3; $\epsilon_2(t_2) = \epsilon_3(t_2)$

$$-d_{23,2}\frac{V_2}{t_2} + \frac{F_2}{A_2 Y} - \frac{t_2}{2r} = \frac{F_3}{A_3 Y} + \frac{t_3}{2r}$$

   Layers 3 and 4; $\epsilon_3(t_3) = \epsilon_4(t_3)$

$$\frac{F_3}{A_3 Y} - \frac{t_3}{2r} = -d_{23,4}\frac{V_4}{t_4} + \frac{F_4}{A_4 Y} + \frac{t_4}{2r}$$

   Layers 4 and 5; $\epsilon_4(t_4) = \epsilon_5(t_4)$

$$-d_{23,4}\frac{V_4}{t_4} + \frac{F_4}{A_4 Y} - \frac{t_4}{2r} = \frac{F_5}{A_5 Y} + \frac{t_5}{2r}$$

In the above equations the strain in each layer is a superposition of the longitudinal, bending and piezo strain. The respective strains are due to the longitudinal force, $F_j$, bending moment, $M_j$ and the piezo coefficient equation (2.30). The piezo strain in the above equations has a negative sign to account for the direction of the electric field. The field is pointed from the top to bottom contact which is opposite the chosen positive orientation of the z-axis.

The above four equations have six unknowns, i.e. $F_1$, $F_2$, $F_3$, $F_4$, $F_5$ and $r$. Using assumptions 1 and 2 the above equations can be written in the form of the following matrix:

$$\begin{bmatrix} \frac{1}{A_1Y} & -\frac{1}{A_2Y} & 0 & 0 & 0 \\ 0 & -\frac{1}{A_2Y} & \frac{1}{A_3Y} & 0 & 0 \\ 0 & 0 & \frac{1}{A_3Y} & -\frac{1}{A_4Y} & 0 \\ 0 & 0 & 0 & -\frac{1}{A_4Y} & \frac{1}{A_5Y} \\ 1 & 1 & 1 & 1 & 1 \end{bmatrix} \begin{bmatrix} F_1 \\ F_2 \\ F_3 \\ F_4 \\ F_5 \end{bmatrix}$$
$$+\frac{1}{2YI} \begin{bmatrix} -(t_1+t_2) & -(t_1+t_2) & -(t_1+t_2) & -(t_1+t_2) & -(t_1+t_2) \\ (t_2+t_3) & (t_2+t_3) & (t_2+t_3) & (t_2+t_3) & (t_2+t_3) \\ -(t_3+t_4) & -(t_3+t_4) & -(t_3+t_4) & -(t_3+t_4) & -(t_3+t_4) \\ (t_4+t_5) & (t_4+t_5) & (t_4+t_5) & (t_4+t_5) & (t_4+t_5) \\ 0 & 0 & 0 & 0 & 0 \end{bmatrix}$$
$$\times \begin{bmatrix} \left(\frac{t_1}{2}\right) F_1 \\ \left(t_1+\frac{t_2}{2}\right) F_2 \\ \left(t_1+t_2+\frac{t_3}{2}\right) F_3 \\ \left(t_1+t_2+t_3+\frac{t_4}{2}\right) F_4 \\ \left(t_1+t_2+t_3+t_4+\frac{t_5}{2}\right) F_5 \end{bmatrix}$$
$$= \begin{bmatrix} -d_{23,2}\frac{V_2}{t_2} \\ -d_{23,2}\frac{V_2}{t_2} \\ -d_{23,4}\frac{V_4}{t_4} \\ -d_{23,4}\frac{V_4}{t_4} \\ 0 \end{bmatrix}$$

yielding five equations and five unknowns. Here $I = \frac{w}{12}\left(t_1^3 + t_2^3 + t_3^3 + t_4^3 + t_5^3\right)$. Solving for the unknowns the equation for the force and moment are:

$$F_2 = \frac{YW}{t^3}\left( \begin{array}{c} d_{23,2}V_2 t\left(-t^3 + 4t^2 t_2 + 3t_2\left(t_2 + 2\left(t_3+t_4+t_5\right)\right)\left(\left(t_2 + 2\left(t_3+t_4+t_5\right)\right) - 2\right)\right) \\ d_{23,4}V_4 t_2\left(4t^2 - 3t\left(t_2 + 2t_3 + 3t_4 + 4t_5\right) + 3\left(t_4 + 2t_5\right)\left(t_2 + 2\left(t_3+t_4+t_5\right)\right)\right) \end{array} + \right) \tag{4.11}$$

$$M_2 = \frac{Yt_2^3 W}{2t^3}\left(d_{23,2}V_2\left(-t + t_2 + 2\left(t_3+t_4+t_5\right)\right) + d_{23,4}V_4\left(-t + t_4 + 2t_5\right)\right) \tag{4.12}$$

$$F_4 = \frac{YW}{t^3}\left( \begin{array}{c} d_{23,2}V_2 t_4\left(4t^2 - 3t\left(t_2 + 2t_3 + 3t_4 + 4t_5\right) + 3\left(t_4 + 2t_5\right)\left(t_2 + 2\left(t_3+t_4+t_5\right)\right)\right) \\ d_{23,4}V_4\left(-t^3 + 4t^2 t_4 - 6tt_4\left(t_4 + 2t_5\right) + 3t_4\left(t_4 + 2t_5\right)^2\right) \end{array} + \right) \tag{4.13}$$

$$M_4 = \frac{Yt_4^3 W}{2t^3}\left(d_{23,2}V_2\left(-t + t_2 + 2\left(t_3+t_4+t_5\right)\right) + d_{23,4}V_4\left(-t + t_4 + 2t_5\right)\right) \tag{4.14}$$

where $t = t_1 + t_2 + t_3 + t_4 + t_5$.

To calculate $Q^1_{m,j}$ an expression for $\bar{z}_j$ is required. $\bar{z}$ is defined as the position of zero strain or stress along the length of the tines. Using assumption 5 $\bar{z} = \frac{t}{2}$, i.e. the position of the neutral axis is half of the total thickness. However; the individual piezoelectric regions do

not span the total thickness. Adjusting for this $\bar{z}_1 = t_1 + t_2 - \frac{t}{2}$ and $\bar{z}_2 = t_1 + t_2 + t_3 + t_4 - \frac{t}{2}$. Equations (4.15) and (4.16) are the general expressions for motional charge with substitutions for $M_j$, $\bar{z}_j$, $\frac{\partial \xi}{\partial y}$ and $F_j$. For these expression $\xi(y)$ and $y_1$ are both evaluated at $L$ i.e. the tip of the tine and the expression for $\psi_i$ is given in equation (4.7).

$$Q_m = C_{m,2} V_2$$

$$Q_m = \frac{-Y d_{23,2} LW}{t^3 t_2} \begin{bmatrix} d_{23,2} V_2 \begin{Bmatrix} t^3 + t^2 t_2 (3\psi_i - 4) \\ -3tt_2 (-t_2 (2 - \psi_i) - 4 (1 - \psi_i) (t_3 + t_4 + t_5)) \\ -3t_2 (t_2 + 2 (t_3 + t_4 + t_5)) (t_2 + 2 (1 - \psi_i) (t_3 + t_4 + t_5)) \end{Bmatrix} \\ + d_{23,4} V_4 t_2 \begin{Bmatrix} t^2 (3\psi_i - 4) + 3t (t_2 + (1 - \psi_i) (2t_3 + 3t_4 + 4t_5)) \\ -3 (t_4 + 2t_5) (t_2 + 2 (1 - \psi_i) (t_3 + t_4 + t_5)) \end{Bmatrix} \end{bmatrix} \tag{4.15}$$

$$Q_m = C_{m,4} V_4$$

$$Q_m = \frac{-Y d_{23,4} LW}{t^3 t_4} \begin{bmatrix} d_{23,2} V_2 t_4 \begin{Bmatrix} t^2 (3\psi_i - 4) \\ +t (3 (1 - \psi_i) (t_2 + 2t_3 + 4t_5) + 3t_4 (-2\psi_i + 3)) \\ -3 (t_2 + 2 (t_3 + 2t + t_5)) (t_4 + 2t_5 (1 - \psi_i)) \end{Bmatrix} \\ + d_{23,4} V_4 \begin{Bmatrix} t^3 + t^2 t_4 (3\psi_i - 4) - 3tt_4 (-t_4 (2 - \psi_i) - 4t_5 (1 - \psi_i)) \\ -3t_4 (t_4 + 2t_5) (t_4 + 2t_5 (1 - \psi_i)) \end{Bmatrix} \end{bmatrix} \tag{4.16}$$

Evaluating the first 200 terms in $\psi_i$; $\psi_i = 0.9937 \sim 1$. Using this value equations (4.15) and (4.16) are reduced to equations (4.17) and (4.18).

$$Q_m = C_{m,2} V_2 = \frac{-Y d_{23,2} LW}{t^3 t_2} \begin{bmatrix} d_{23,2} V_2 \left(t^3 - t^2 t_2 + 3tt_2^2 - 3t_2^2 (t_2 + 2 (t_4 + t_3 + t_5))\right) \\ + d_{23,4} V_4 t_2 \left(-t^2 + 3tt_2 - 3t_2 (t_4 + 2t_5)\right) \end{bmatrix} \tag{4.17}$$

$$Q_m = C_{m,4} V_4 = \frac{-Y d_{23,4} LW}{t^3 t_4} \begin{bmatrix} d_{23,2} V_2 t_4 \left(-t^2 + 3tt_4 - 3t_4 (t_2 + 2 (t_3 + t_4 + t_5))\right) \\ + d_{23,4} V_4 \left(t^3 - t^2 t_4 + 3tt_4^2 - 3t_4^2 (2t_5 + t_4)\right) \end{bmatrix} \tag{4.18}$$

Equations (4.19) and (4.21), determined using equations (4.4) and (4.5), are the junction capacitance for layers 2 and 4. The values used for $\epsilon_{2,r}$ and $\epsilon_{4,r}$ are given in table(4.3) and $t_2$ and $t_4$ are 50.0 and 146.19 $nm$. Expressions for $C_{m,2}$ and $C_{m,4}$, (4.20) and (4.22), are derived using equations (4.17) and (4.18). 2 is multiplied to the expressions for $C_{m,j}$ to account for the second tine. $\beta_2$ and $\beta_4$ in these expressions represent the amount of the total voltage dropped across 2 and 4 and have values of 0.2650 and 0.7350, respectively. These values are determined by using the off resonance series circuit and the assumption that the junction capacitances are greater than their respective motional capacitances. This assumption will be justified later.

| Constants | Values |
|---|---|
| $\epsilon_{r,2}$ | 12.50 [59] |
| $\epsilon_{r,4}$ | 13.18 [60] |
| $d_{23,2}$ | 0.579 $\frac{pm}{V}$ [59] |
| $d_{23,4}$ | 1.345 $\frac{pm}{V}$ [60] |

Table 4.3: Table of constant for $GaAs$ and $In_{0.485}Ga_{0.515}P$

Geometrically the major contribution to the junction capacitance is the area of the electrical pad. Considering a pad having dimensions of $250 \times 250\,\mu m^2$ $C_{J,4}$ and $C_{J,2}$ are approximately $54.99$ and $152.50\,pF$. $C_{m,2}$ and $C_{m,4}$ have values ranging from $1.08 - 0.32\,fF$ for tine lengths given in table (4.2), width of $30.0\,\mu m$ and values for $d_{2,23}$ and $d_{4,23}$ are given in table(4.3). The ratio of $C_J$ to $C_m$ is $10^4 - 10^5$. Therefore; (1) the signal to the background is small necessitating a high Q in order to get an appreciable signal to background ratio and (2) this ratio justifies the assumption made in determining values for $\beta_2$ and $\beta_4$.

$$C_{J,2} = \frac{\epsilon_0 \epsilon_{r,2}}{t_2} \sum_i L_i W_i = 2212.50 \left( \sum_i L_i W_i \right) \mu F \tag{4.19}$$

$$\begin{aligned} C_{m,2} = & \frac{-2Y d_{23,2} LW}{t^3 t_2} \left[ \begin{array}{c} d_{23,2} \left( t^3 - t^2 t_2 + 3 t t_2^2 - 3 t_2^2 \left( t_2 + 2 \left( t_3 + t_4 + t_5 \right) \right) \right) \\ + d_{23,4} \frac{\beta_4}{\beta_2} t_2 \left( -t^2 + 3 t t_2 - 3 t_2 \left( t_4 + 2 t_5 \right) \right) \end{array} \right] \\ & = -26.103 \left( L \right) \, pF \end{aligned} \tag{4.20}$$

$$C_{J,4} = \frac{\epsilon_0 \epsilon_{r,4}}{t_4} \sum_i L_i W_i = 797.914 \left( \sum_i L_i W_i \right) \mu F \tag{4.21}$$

$$\begin{aligned} C_{m,4} = & \frac{-2Y d_{23,4} LW}{t^3 t_4} \left[ \begin{array}{c} d_{23,2} \frac{\beta_2}{\beta_4} t_4 \left( -t^2 + 3 t t_4 - 3 t_4 \left( t_2 + 2 \left( t_3 + t_4 + t_5 \right) \right) \right) \\ + d_{23,4} \left( t^3 - t^2 t_4 + 3 t t_4^2 - 3 t_4^2 \left( t_4 + 2 t_5 \right) \right) \end{array} \right] \\ & = -54.790 \left( L \right) \, pF \end{aligned} \tag{4.22}$$

Equations (4.23) and (4.24) are expressions for $C_J$ and $C_m$ required for the BVD model. These are determined by considering the circuits for the junction and motional capacitances independently of each other. $L_m$ can be ascertained using equation (2.37) and equation(4.24).

$$C_J = 586.42 \left( \sum_i L_i W_i \right) \mu F \tag{4.23}$$

$$C_m = -17.6799 \left( L \right) \, pF \tag{4.24}$$

Equation(4.25) and (4.26) are the expected $C_m$ for the second and third modes. They are derived from equations (4.15) and (4.16) only considering the second and the third mode

shapes, i.e. $\psi = 0.1883 \, \text{and} \, 0.6473e - 1$ respectively. Using equations (4.15) and (4.16) is justified because the field across the tines and hence the moment does not change.

$$C_m^{Mode\,2} = -70.2610\,(L)\;pF \tag{4.25}$$

$$C_m^{Mode\,3} = -71.7428\,(L)\;pF \tag{4.26}$$

## 4.4 Fabrication

In this section, the steps required for fabricating the resonators is discussed. As mentioned above the heterostructure is grown on a 3in. diameter GaAs (100) wafer. This wafer is cleaved into $14 \times 14$ mm chips on which the torsional resonators are fabricated. Each of these $14 \times 14$ mm chips consists of 326 isolated devices. The resonators are fabricated in a clean room facility using standard fabrication techniques - chemical vapor deposition (CVD), photolithography, wet chemical etching and metalization. The resonators are fabricated using a six step process involving 4 masking steps, a back-contact step and finally resonator release.

Figure(4.11)(a) is the optical micrograph of the fabricated torsional resonator where sections A-A and B-B represents the tine and the $n^+$, $p^+$ electrical contact pads. Figure (4.11)(b) is the cross-section view of the heterostructure at sections A-A and B-B. Using this cross-section view and figure (4.11)(c), which is a legend of the MBE heterostructure and the additional layers used for fabrication. Figure (4.12) is the mask used to fabricate the chips. This figure only serves to illustrate that the complete mask consists of 21 tiles. To fabricate the torsional resonator discussed in this chapter four tiles are required. Figure (4.13) is an image of a small section of a single tile. In this image there are a bunch of resonators and an alignment marker. Figure (4.14) is an image of a single device belonging to this tile. This device will be used as top view for the device process steps. They are:

1. **Cleaning**: The fabrication begins with cleaning the chips. The following recipe is used: 5 minutes dip each in acetone and methanol followed by a 5 minute deionized $H_2O$ rinse. The chips are then placed in a UV-Ozone environment for 10 minutes followed by a 1 minute buffered hydrogen fluoride (BHF) dip and 5 minute DI water rinse

2. **Mask#1 - Defines the geometry of resonator and anchor**: A $100.0\,nm$ of CVD $SiO_2$ is first grown over the sample, figure (4.15)(a). Using mask #1 the patterns for MEMS torsional resonators and their respective anchors are transferred to a positive photo-resist (PR). After development of PR exposed $SiO_2$ is etched using BHF exposing $n^+\,GaAs$. PR is removed and the heterostructure layers, $n^+GaAs$, $n^-In_{0.485}Ga_{0.515}P$, $n^-GaAs$, $p^-GaAs$ and $p^-In_{0.485}Ga_{0.515}P$ are wet-chemically etched using $C_6H_8O_7 : H_2O_2$ $(7:1)$, $(100\%)HCl$, $C_6H_8O_7 : H_2O_2$ $(7:1)$, $(100\%)\,HCl$. The underlying $p^+$ GaAs layer is now exposed as seen in figure (4.15)(b). In section A-A the non-etched part represents one of the tines of the resonator while the etched section of B-B opens the bottom contact for metalization and the unetched section is the top contact. The top view figure (4.15)(c) shows the torsional resonators and their respective anchors.

3. **Mask#2 - Preparation for Release**: In this step the $Al_{0.8}Ga_{0.2}As$ layer between the devices and the regions required for releasing the torsional resonators is exposed. First; the remaining $SiO_2$ layer from the previous step is etched using BHF. A new $100.0\,nm\,CVD\,SiO_2$ layer is deposited. Using mask#2 the pattern is transferred to a positive PR. Following the development of PR the exposed $SiO_2$ is etched using BHF and the PR is removed. The exposed $p^+\,GaAs$ is wet chemically etched using $C_6H_8O_7 : H_2O_2$ $(7:1)$. As seen in figure (4.16) $Al_{0.8}Ga_{0.2}As$ required for releasing the resonator and isolating the devices is exposed for etching

4. **Mask#3 - Metalization of Bottom Contact:** Using mask#3 the patterns for the $p^+$ metal contact is transferred to a positive PR. Following the development of PR the exposed $SiO_2$ is wet-chemically etched using BHF exposing the underlying $p^+GaAs$. 25/50/200 nm of Ti/Pt/Au is deposited using a metal evaporator in UHV. The sample is then removed and placed in an Acetone bath for 24 hrs for lift-off. This is seen in figure(4.17)

5. **Mask#4 - Metalization of Top Contact:** Using mask#4 the patterns for the $n^+$ metal contact is transferred to a positive PR. The same procedure follows as above with the exception of the metals used. They are 25/50/200 nm of Ni/Ge/Au. The finished cross-section view is seen in figure (4.18). This is the final mask step.

6. **Back contact**: A metal contact to the substrate is made by depositing 25/50/200 nm of Ti/Pt/Au using the evaporator. This is seen in figure (4.19)

7. **Release of resonator**: In the final fabrication step the torsional resonators are released by etching the exposed $Al_{0.8}Ga_{0.2}As$ layer from step 3. The chip is placed in a bath of $(49\%)\,HF : H_20$ $(1:9)$ for 5 minutes and 30 seconds. This timed etch removes $Al_{0.8}Ga_{0.2}As$ from underneath the tines, spine and the pad of the resonator. The etch is followed by a 10 minute $DI\,H_2O$ rinse. The chip is immersed in HLPC grade propanol and transferred to a critical point dryer (CPD) for successful release of the torsional resonators. A critical point dryer is used to avoid stiction. Stiction is the adhesion of the mechanical structure to the substrate. This occurs during the drying step after the sample has been removed from the $DI$ rinse process. During drying capillary forces pull the mechanical structure towards the substrate. The mechanical structure due to the van-der waals forces stick to the substrate. To avoid this the sample is placed in a CPD which displaces the propanol with liquid $CO_2$. By raising the temperature and pressure of the chamber to the critical point liquid $CO_2$ becomes gaseous $CO_2$. The cross-section of the released device is shown in figure (4.20)

Figure (4.21) is the SEM image of the fabricated Y torsional resonator.

## 4.5 Experimental Setup and Results

This section describes the experimental setup used to drive and measure the response of the two terminal torsional resonator at the above discussed three torsional modes. The experimental results are then compared to the theoretical predictions of the measured frequency, motional capacitance and inductance dielectric capacitance and Q of the Y resonator.

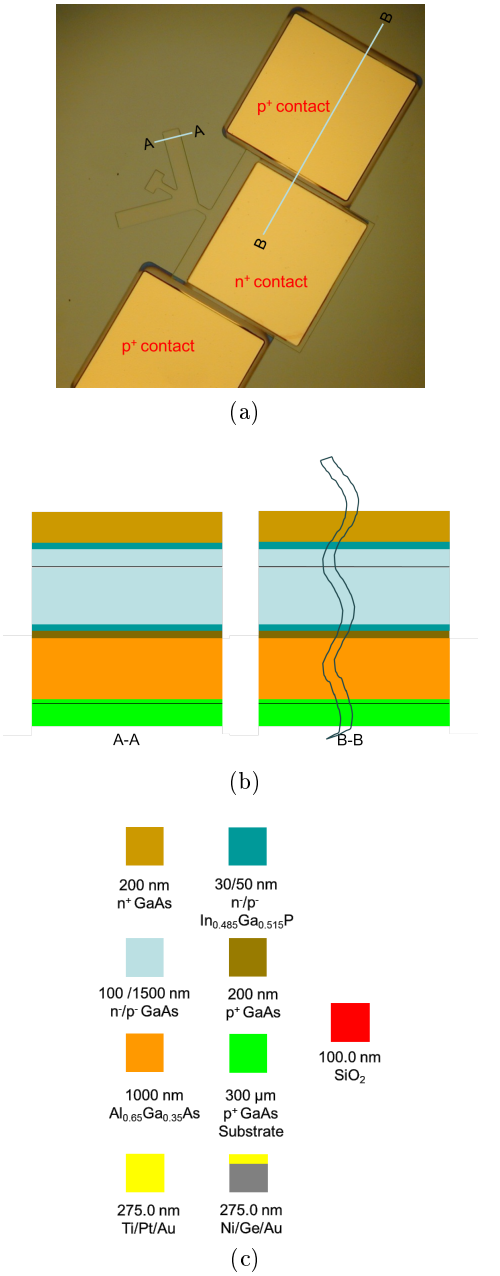


Figure 4.11: Steps for fabrication of Y Torsional Resonator. (a) Optical Micrograph of a fabricated Y-Torsional Resonator where cross-sections A and B are the tine and the top and bottom contacts, (b) is the cross-section view of the heterostructure at sections A-A and B-B and (c) is a legend of the MBE heterostructure layers and additional layers used for fabrication

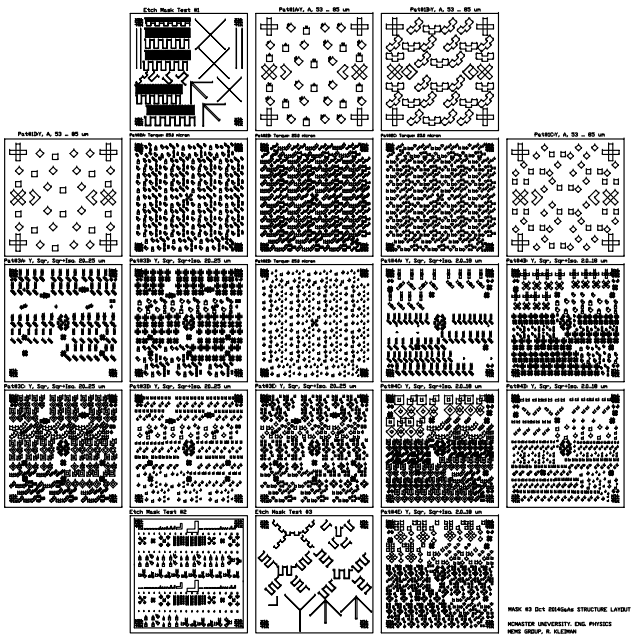

Figure 4.12: Mask to fabricate torsional resonators. This is a 3' mask on a 4' plate. Each tile is a $14\,mm$ square. There are 21 tiles. To fabricate the resonator discussed in this chapter four tiles are used

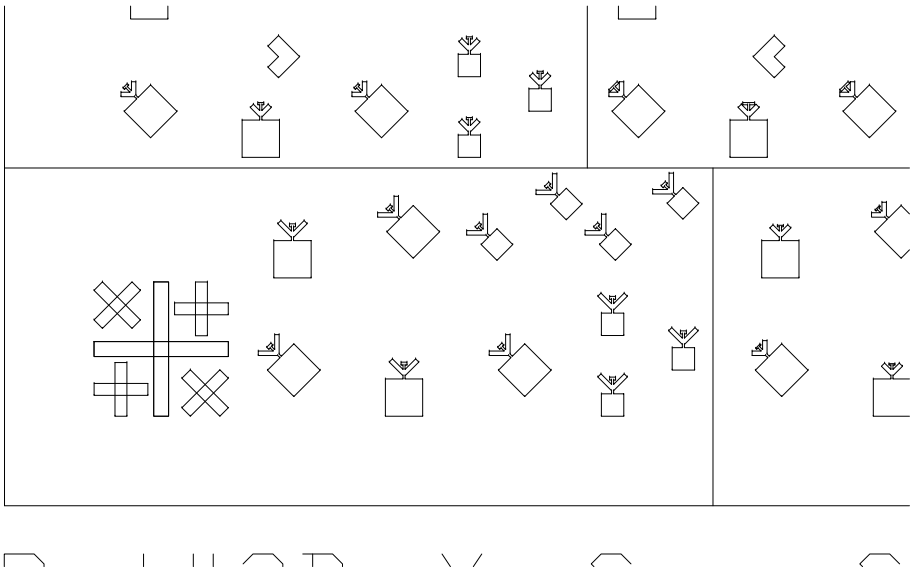

Figure 4.13: A small section of a single tile. In this image there are a bunch of resonators. The large cross pattern is an alignment marker

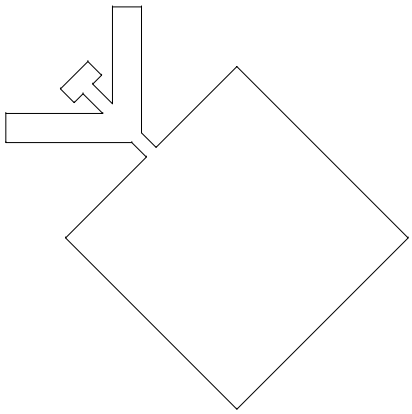

Figure 4.14: Single device belonging to the above tile

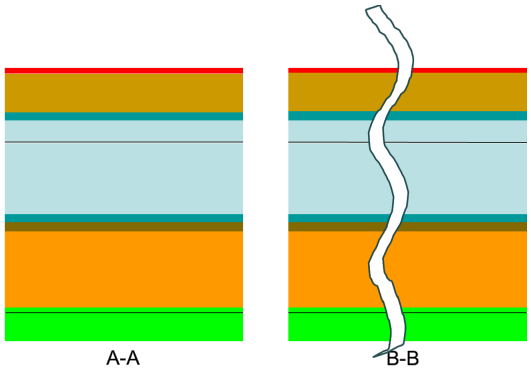


(a)

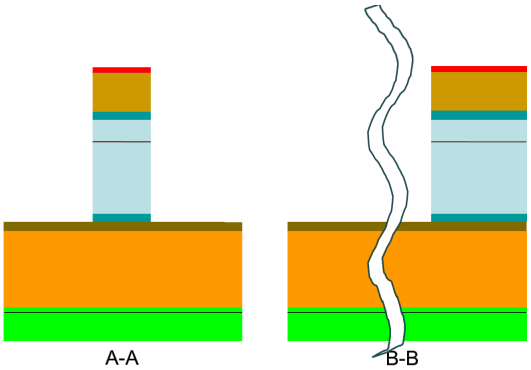


(b)

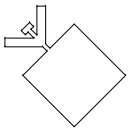

(c)

Figure 4.15: Mask#1: (a) Chemical vapor deposition (CVD) of 100.0 $nm$ $SiO_2$. $SiO_2$ is represented by the color red. Using mask #1 (d) the patterns for torsional resonators and their respective anchors are transferred to a positive photo-resist (PR). After development of PR exposed $SiO_2$ is etched using BHF exposing $n^+GaAs$. PR is removed and the heterostructure layers, $n^+GaAs$, $n^-In_{0.485}Ga_{0.515}P$, $n^-GaAs$, $p^-GaAs$ and $p^-In_{0.485}Ga_{0.515}P$ are wet-chemically etched using $C_6H_8O_7 : H_2O_2$ (7 : 1), (100%)$HCl$, $C_6H_8O_7 : H_2O_2$ (7 : 1) and (100%) $HCl$. (c) The top view of the structure

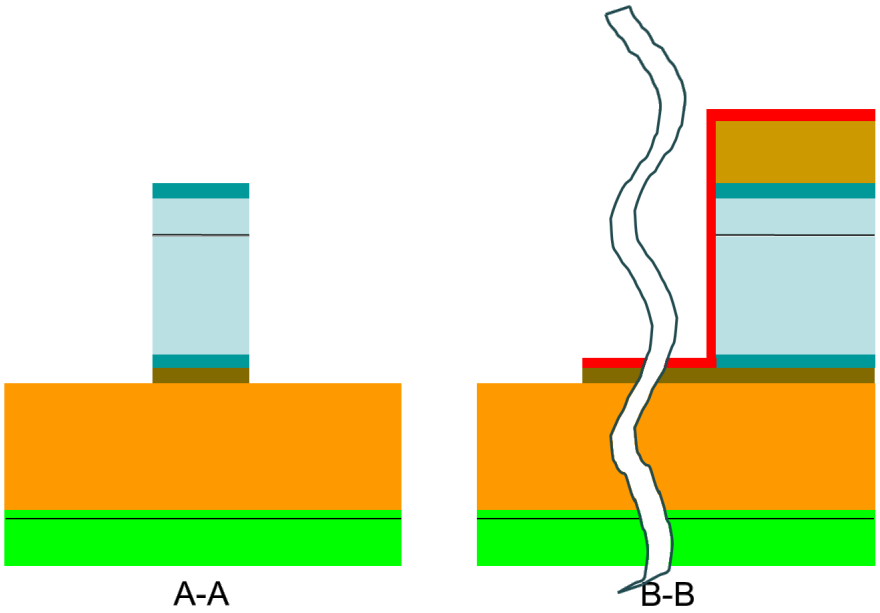


(a)

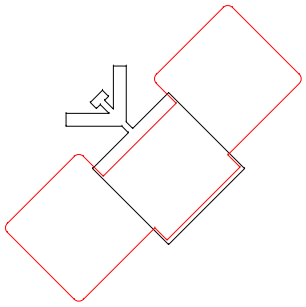

(b)

Figure 4.16: Mask#2: Preparation for release: $Al_{0.8}Ga_{0.2}As$ layer between the devices and the regions required for releasing the torsional resonators is exposed. First; the remaining $SiO_2$ layer from the previous step is etched using BHF. A new $100.0\,nm\,CVD\,SiO_2$ layer is deposited. Using mask#2 the pattern is transferred to a positive PR. Following the development of PR the exposed $SiO_2$ is etched using BHF and the PR is removed. The exposed $p^+\,GaAs$ is wet chemically etched using $C_6H_8O_7 : H_2O_2$ $(7:1)$. (b) The top view of the structure. Here the red line indicates the outline of the $p^+$ contacts. The region surrounding the $p^+$contacts have been etched

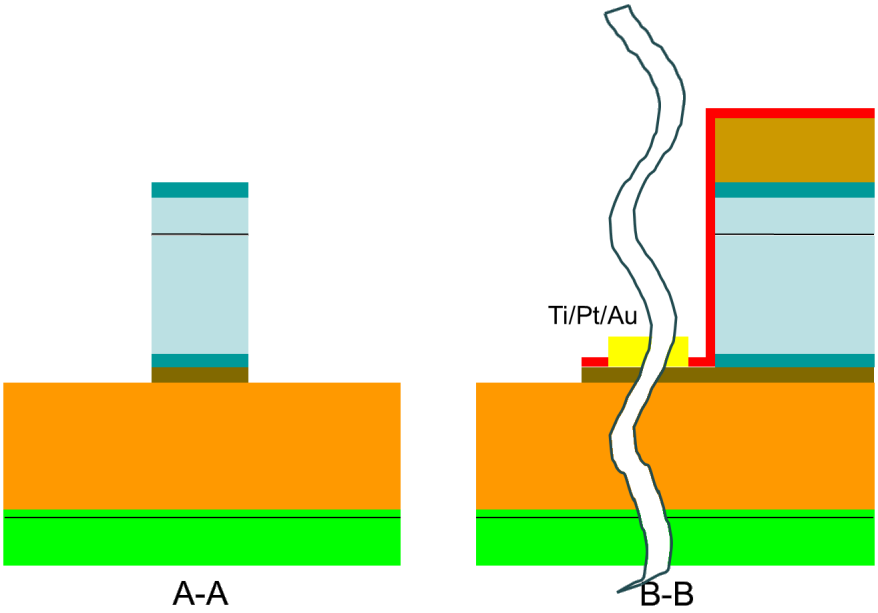


(a)

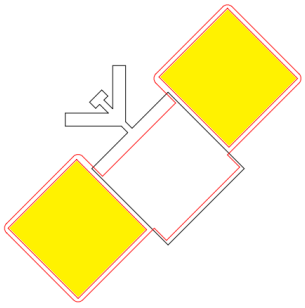

(b)

Figure 4.17: Mask#3: Using mask#3 the patterns for the $p^+$ metal contact is transferred to a positive PR. Following the development of PR the exposed $SiO_2$ is wet-chemically etched using BHF exposing the underlying $p^+GaAs$. 25/50/200 nm of Ti/Pt/Au is deposited using a metal evaporator in UHV. The sample is then removed and placed in an Acetone bath for 24 hrs for lift-off. (b) the top view of the structure

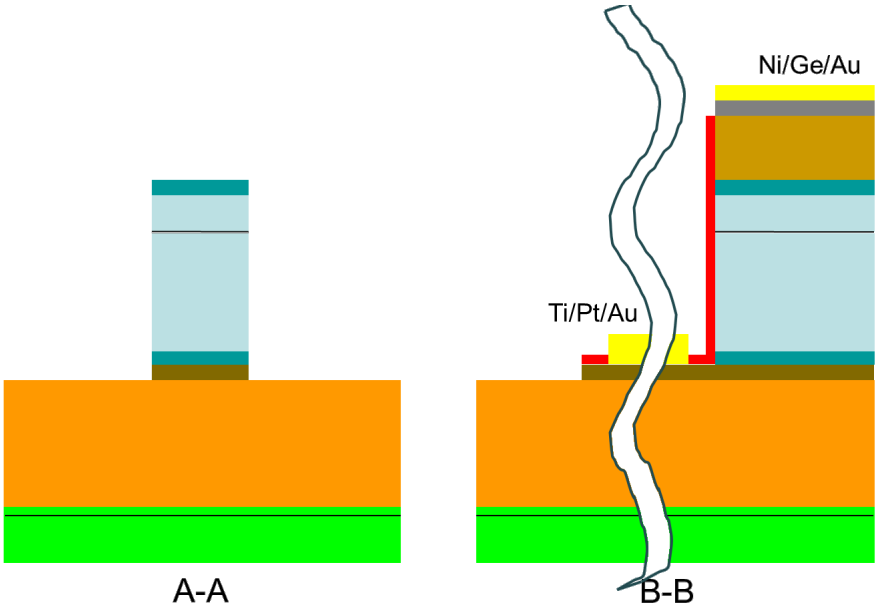


(a)

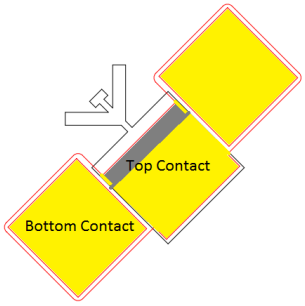


(b)

Figure 4.18: Mask#4: Using mask#4 the patterns for the $n^+$ metal contact is transferred to a positive PR. The same procedure follows as above with the exception of the metals used. They are 25/50/200 nm of Ni/Ge/Au. (b) the top view of the structure. The bottom and top contacts are indicated.

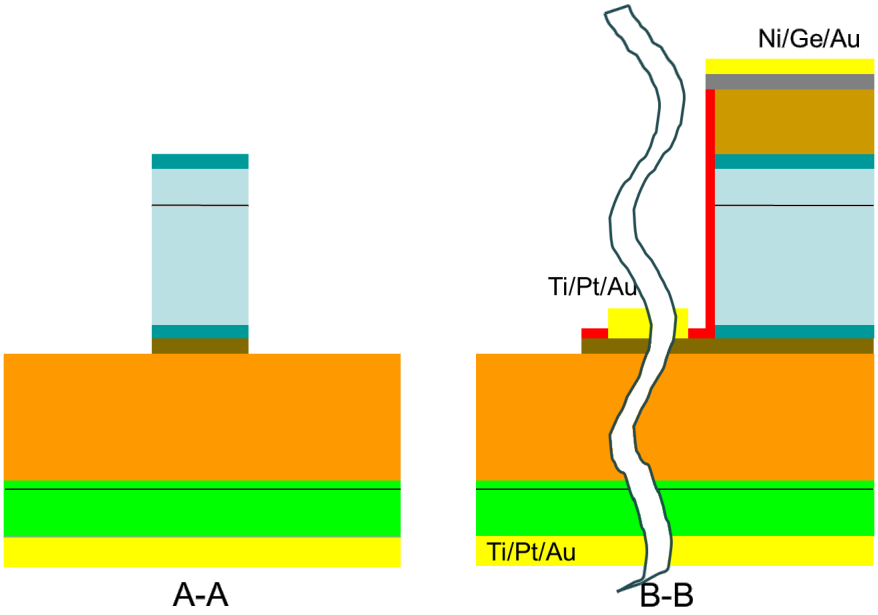


(a)

Figure 4.19: Back contact: A metal contact to the substrate is made by depositing 25/50/200 nm of Ti/Pt/Au using the evaporator

### 4.5.1 Experimental Setup

An overview of the experimental setup is given in figure(4.22). The experimental setup consists of a Keysight 33522B function generator generating sinusoidal signals that are used to drive the device. The response is measured using an SR-844 lock-in amplifier synchronized with the function generator. Labview is used to automate the experiment and save the acquired data for analysis. Using this setup a frequency sweeping experiment is conducted on the two terminal resonators to determine the resonant modes.

The fabricated chip, consisting of 326 isolated devices, mounted on a printed circuit board (PCB) using silver paste. A wire bonder is used to bond gold wires from the top and bottom contacts of the device to the electrical pads on the PCB. The PCB consists of 13 electrical pads connected to their respective SMA connectors via a transmission line. The SMA connectors connect the device to the function generator and amplifier. The current from the device is amplified using an Amptek A-250 charge sensitive amplifier. The amplifier is connected to the device via a 10.0 nF DC blocking capacitor. The DC blocking capacitor is required to block the $-0.82\,V$ at the input port of the Amptek A-250. The amplifier and the DC blocking capacitor are placed as close as possible to the SMA connector in order to minimize contribution from stray capacitances, cable impedance etc. The device along with the A-250 and 10.0 nF capacitor are placed in a vacuum chamber. A pressure of ~ 2 mTorr is achieved in the chamber.

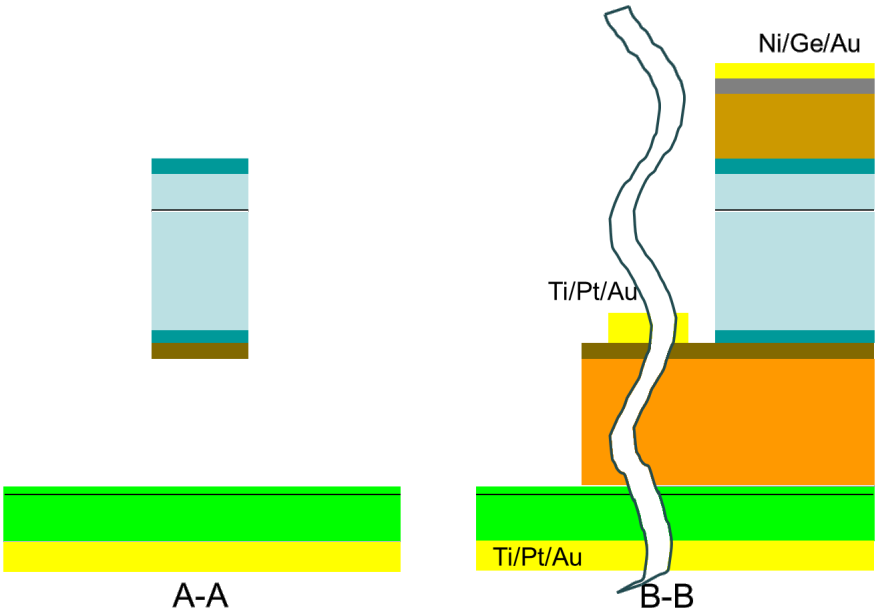


(a)

Figure 4.20: Release of resonator: In the final fabrication step the torsional resonators are released by etching the exposed $Al_{0.8}Ga_{0.2}As$ layer from step 3. The chip is placed in a bath of $(49\%)\,HF : H_20\ (1:9)$ for 5 minutes and 30 seconds. This timed etch removes $Al_{0.8}Ga_{0.2}As$ from underneath the tines, spine and the pad of the resonator. The etch is followed by a 10 minute $DI\,H_2O$ rinse. The chip is immersed in HLPC grade propanol and transferred to a critical point dryer (CPD) for successful release of the torsional resonators. A critical point dryer is used to avoid stiction. Stiction is the adhesion of the mechanical structure to the substrate. This occurs during the drying step after the sample has been removed from the $DI$ rinse process. During drying capillary forces pull the mechanical structure towards the substrate. The mechanical structure due to the van-der waals forces stick to the substrate. To avoid this the sample is placed in a CPD which displaces the propanol with liquid $CO_2$. By raising the temperature and pressure of the chamber to the critical point liquid $CO_2$ becomes gaseous $CO_2$.

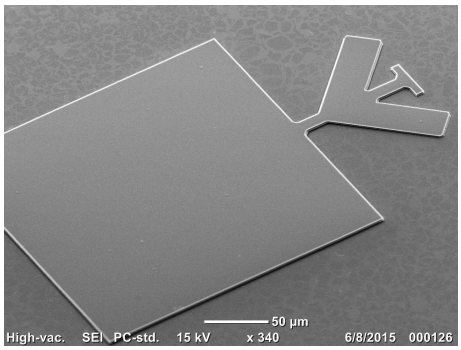


Figure 4.21: SEM image of Y Torsional Resonator. The large square is the anchor. The spine, tines and pad are on top of the anchor

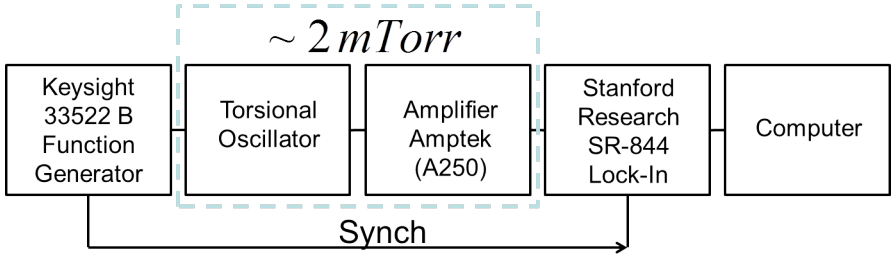


Figure 4.22: Experimental setup used for frequency sweeping experiments. The function generator drives the torsional oscillator and supplies the synchronization signal to the SR-844 Lock-in Amplifier. The experiment is controlled by the computer using labview. The data from the lock-in is stored for later processing. The blue dash line indicates the components placed in the vacuum chamber. A vacuum pressure of $\sim 2\,mTorr$ is achieved

### 4.5.2 Electrical Circuit

The complete electrical circuit for the two terminal device is given in figure(4.22)(a). The diode is the two terminal device and the circuit to the right of the 10.0 nF DC block capacitor is the circuit for the A-250. At resonance the diode reduces to the BVD circuit; figure(4.22)(b). The electrical parameters of this circuit $R_m$, $C_m$, $L_m$ and $C_J$ are determined by fitting this model to the experimental data. $Q$ is calculated using equation: $Q = \frac{1}{2\pi f_r R_m C_m}$

### 4.5.3 Experimental Results

Figures (4.24) (a), (b) and (c) are the response of the device at the fundamental, first and 2nd harmonic modes. The fit parameters and Q for the respective modes along with the theoretical and simulated predictions are given in table (4.4). The fit values are acquired by fitting the data to the modified BVD model. In general the frequency results from simulation agrees well with the experimental data and the trend for the simulated Q-values agrees with experimental results. For the latter the error between the predicted and measured Q-values are large. This is because in the simulation only anchor loss is considered. There are other extrinsic factors that contribute to lowering the Q such as thermo-elastic dissipation, surface losses from fabrication, inhomogeneous etching of the heterostructure layers resulting in non-straight side walls, etc.

The theoretically predicted results for $C_J$ at the fundamental and the harmonic modes are within 10% of the measured results. The theoretical predicted results for $C_m$ at the fundamental mode differs by 65% of the measured value. This is puzzling because the same geometry is used to determine both $C_J$ and $C_m$. Therefore; this reduces arguments for variations in the thickness of the depletion region and the dimensions of the structure. Some possible explanations are:

1. the piezoelectric constants used are incorrect. The piezoelectric constant for GaAs is well established [60, 1, 34, 55] however piezoelectric constants for $In_{0.485}Ga_{0.515}P$ have been determined using extrapolation methods

2. there could be trap states whose effects are only seen when measuring small currents

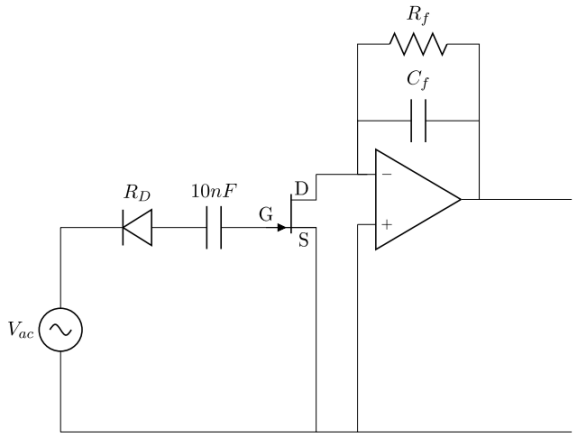


(a)

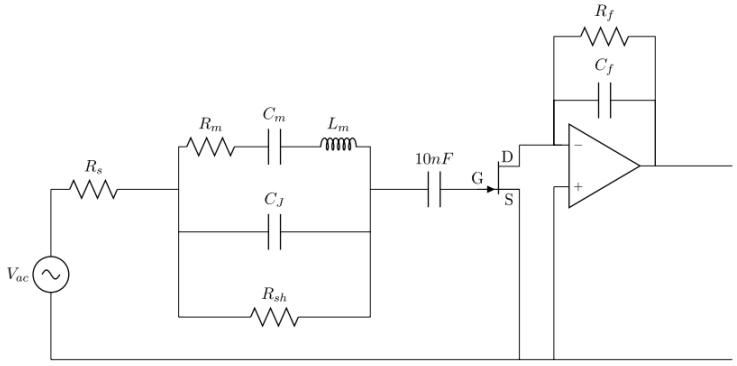


(b)

Figure 4.23: Electrical Circuit of the two terminal device and the the A-250 amplifier (a) Diode circuit (b) Diode equivalent circuit around resonance. In (b) the diode is replaced by the modified BVD model. In this model $R_m$, $C_m$, $L_m$, $C_J$ and $R_{sh}$ are the motional resistances, capacitances, inductances, the junction capacitance and the shunt resistance. The shunt resistance accounts for the leakage current across the depletion regions. $R_s$ is the series resistance accounting for the finite resistance of the semiconductor metal contacts. The $10\,nF$ capacitor is placed to block the DC bias the output of the amplifier. The amplifier is a charge sensitive amplifier consisting of a JFET at the input stage and a feedback resistance and capacitance $R_f$ and $C_f$ respectively. Their values are $300\,M\Omega$ and $1.5\,pF$

| | Theoretical Prediction | Experimental Results | %Error |
|---|---|---|---|
| $f_r\ (Hz)$ | 73,392.00 | 76,696.63 | 4.31 |
| $C_m\ (fF)$ | 1.4142 | 0.4924 | 65.18 |
| $L_m\ (H)$ | 3276.96 | 8747.25 | 62.54 |
| $C_J\ (pF)$ | 40.418 | 38.0858 | 5.77 |
| $Q$ | 14,971.15 | 10,116.30 | 32.43 |

(a)

| | Theoretical Prediction | Experimental Results | %Error |
|---|---|---|---|
| $f_r\ (Hz)$ | 515,127.00 | 590,284.52 | 12.73 |
| $C_m\ (fF)$ | 1.5675 | 0.3846 | 75.46 |
| $L_m\ (H)$ | 67.79 | 189.051 | 67.78 |
| $C_J\ (pF)$ | 40.418 | 37.709 | 6.70 |
| $Q$ | 12,196.35 | 5,768.03 | 52.71 |

(b)

| | Theoretical Prediction | Experimental Results | %Error |
|---|---|---|---|
| $f_r\ (Hz)$ | 1,161,570.00 | 1,221,620.50 | 4.92 |
| $C_m\ (fF)$ | 1.5822 | 0.1918 | 87.88 |
| $L_m\ (H)$ | 11.87 | 88.4933 | 86.59 |
| $C_J\ (pF)$ | 40.418 | 36.025 | 10.87 |
| $Q$ | 102,185.24 | 9,002.91 | 91.19 |

(c)

Table 4.4: Comparison of Experimental Results and Theoretical predictions for the three Torsional modes for a resonator with a tine length of $80.0\mu m$: (a) Symmetric Torsional Mode, (b) 1st Anti-Symmetric Torsional Mode, (c) 2nd Anti-Symmetric Torsional Mode

For higher modes the theoretical predictions gets progressively worse. This is attributed to two reasons

1. The theoretical equations are derived for the case where segment#2, figure(4.10), is considered to be clamped. For higher order cantilever modes the deflection close to the clamp are higher than for the fundamental tine mode. This is qualitatively illustrated in the torsional mode shape; figures 4.2 $(a)$, $(b)$ and $(c)$

2. In equations(4.25) and (4.26) the charge due to the longitudinal strain is considered to be the same across all modes. This is an incorrect assumption

Not shown in the table are the fitted values for $R_{sh}$ and $R_s$ for the three modes. These values are approximately: $1.0\,G\Omega$ and $3.0\,k\Omega$, $1.0\,G\Omega$ and $888\,\Omega$ and $2.0\,M\Omega$ and $1\,k\Omega$ for the fundamental, first and second harmonic modes.

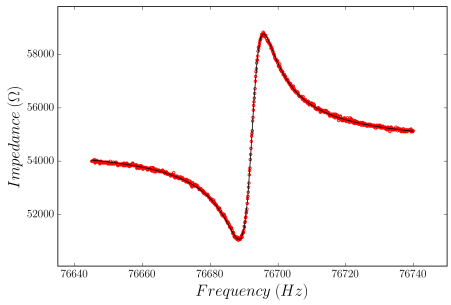


(a)

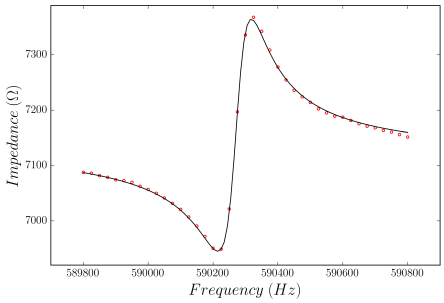


(b)

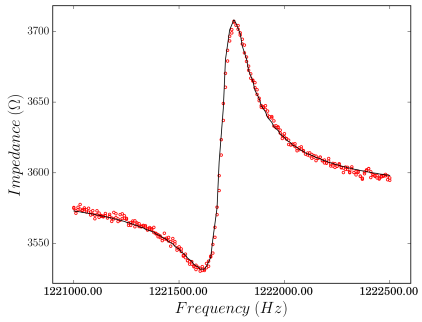


(c)

Figure 4.24: Harmonic response of the device at the fundamental, 1st and 2nd harmonic torsional modes. The x-axis is frequency and y-axis is impedance. The solid line is a fit to the modified BVD model and the dotted circles are the experimental results. The y-axis is determined by first converting the measured voltage to a current using the transfer function of the amplifier and then converting the current to impedance using the drive voltage

| Material Name/Composition | Piezoelectric Matrix |
|---|---|
| Lithium niobate, $LiNbO_3$ | $d_{iq} = \begin{bmatrix} 0 & -20.8 & 0.863 \\ 0 & 20.8 & 0.863 \\ 0 & 0 & 16.2 \\ 0 & 74 & 0 \\ 74 & 0 & 0 \\ -20.8 & 0 & 0 \end{bmatrix} \frac{pm}{V}$ |
| Quartz, $SiO_2$ | $d_{iq} = \begin{bmatrix} -2.27 & 0 & 0 \\ 2.27 & 0 & 0 \\ 0 & 0 & 0 \\ -0.67 & 0 & 0 \\ 0 & 2.27 & 0 \\ 0 & 4.54 & 0 \end{bmatrix} \frac{pm}{V}$ |
| Lead zirconate titanate, $PZT$ | $d_{iq} = \begin{bmatrix} 0 & 0 & -171 \\ 0 & 0 & 0 \\ 0 & 0 & 374 \\ 0 & 0 & 0 \\ 584 & 0 & 0 \\ 0 & 0 & 0 \end{bmatrix} \frac{pm}{V}$ |

Table 4.5: Piezoelectric matrix for $LiNbO_3$ [10], $SiO_2$ [11] and $PZT$ [12]

## 4.6 Comparison to other Piezoelectric materials

Table (4.5) is a list of common piezoelectric materials used for making devices. The piezoelectric matrix for the respective materials are also listed in this table. Equation (4.1) is the piezoelectric matrix for [100] III-V materials. Upon comparing these piezoelectric matrices III-Vs have this unique characteristic that a field applied in the z-direction not only results in an orthogonal response but this response is anti-symmetric. Using this unique characteristic of III-Vs and with proper heterostructure design mechanical modes that are traditionally difficult to drive and detect in micro-resonators are now easily accessible.

As is seen from the table, both $LiNbO_3$ and $SiO_2$ have a parallel and orthogonal response. In $LiNbO_3$ a field applied in the y-direction results in a deformation in the y-direction and x-direction. In $SiO_2$ a field applied in the x-direction results in a deformation in the x-direction and y-direction. The resulting deformations have opposite polarity much like III-Vs, i.e. the direction of the strain in one axis is opposite the other. Using this opposite polarity high Q resonators, similar to what is described in this chapter, can be made but the placement of the electrodes required to achieve this is complicated and is not amenable to planar processing. Quartz tuning fork resonators[61] are an example of using complicated electrode geometry to achieve high Q.

## 4.7 Conclusion

In conclusion, the design, fabrication and the subsequent experimental results of a novel torsional resonator driven and detected using the asymmetric flexural deformation of two tines was demonstrated. This was made possible by using a combination of $GaAs$ and $In_{0.485}Ga_{0.515}P$ semiconductor properties and their unique piezoelectric properties. The latter was used for driving and detecting the torsional mode while the former allowed for the creation of a bimorph via the growth of an asymmetrical $pn$ junction and a heterojunction. Modeling the tines as cantilevers and using the inverse piezoelectric effect equations for the motional charge were derived. The predictions from these equations were compared to experimental results.

The torsional resonator was chosen to highlight the fact that using the combination of III-Vs orientation dependent piezoelectric properties and heterostructure design, modes that are traditionally difficult to drive and detect in micro-resonators are now simple. Additionally, using the above mentioned two combinations and some imagination other geometries of resonators can be designed to access previously inaccessible or hard to detect mechanical modes. Examples of these are given in section(7.2).

Having successfully demonstrated the operation of the torsional resonator in the next chapter the interaction between the piezoelectric and depletion region is explored.

# Chapter 5

# Electro-mechanical coupling in a GaAs Torsional Resonator

## 5.1 Introduction

In this chapter, electro-mechanical coupling is investigated in the fabricated torsional resonator. Electro-mechanical coupling is defined as the interaction between the piezoelectric strain and the variation in the thickness of the depletion region. This interaction results in

1. DC tuning of the magnitude of the resonant AC current
2. actuation of the resonator using the harmonics of the applied voltage

The former and latter are possible because the depletion thickness changes as a function of the applied voltage. Applying a DC voltage results in a non-linear change in the depletion thickness while applying an AC voltage also varies the depletion thickness. A small AC voltage results in a small change in depletion thickness. This change in thickness can be ignored. Additionally, the AC current response is linear with the applied AC voltage. However; for a large AC voltage the change in the depletion thickness cannot be ignored. This change results in a non-linear AC current response which enables the generation of harmonic frequencies of the applied AC fundamental frequency.

Therefore two regions of operation exist with respect to the magnitude of AC drive - linear and non-linear. For shortness linear drive is called $f$ and nonlinear drive is called harmonic drive or $2f$. The impetus for $f$ is the AC current response is measured at the same frequency as the AC voltage drive while $2f$ implies the AC current response is measured at twice the AC drive frequency.

Next, literature review is presented on the electro-mechanical coupling of GaAs resonators and the generation of harmonics from a diode.

### 5.1.1 Literature Review

#### 5.1.1.1 Electro-mechanical coupling

Masmanidis et al[34] demonstrated the electro-mechanical coupling in a $pinGaAs$ heterostructure for an $f$ drive. They did this by optically measuring the change in amplitude

of a fabricated resonator in response to a DC bias. They found the amplitude of vibration increased as the DC bias increased from reverse to forward bias.

This is the only published demonstration of the coupling till now. A demonstration of $2f$ or harmonic drive for piezoelectric-semiconductors to this date does not exit. However; $2f$ drive is used in capacitive resonators. This is discussed next.

#### 5.1.1.2 Harmonic Drive

Capacitive resonators can be thought of as a parallel plate capacitor where either one of the two plates is free to move. The movement of the plate results from the non-linear electrostatic force[62] $F = \frac{1}{2}V^2\frac{dC}{dx}$. Here $V$ is the applied voltage, $C$ is the capacitance and $x$ is the deflection of the parallel plate. As a result of this $V^2$ effect on $F$ harmonics of the applied AC voltage can be used to drive the resonator. The response at the harmonics can then be measured. This is useful when measuring small currents (resulting from small changes in capacitance) on top of a large background current (resulting from feedthrough and parasitic impedances). To elucidate: for a $\frac{f}{2}$ drive the background current will be at $\frac{f}{2}$ while the resonance signal is at $f$. On the measurement side this background current can be filtered leaving only the desired signal at $f$.

This $\frac{f_r}{2}$ actuation has been utilized in gyroscopes[62] where small capacitance changes due to the Coriolis force at the resonator's vibration frequency, $f_r$, is measured. In such cases measuring at a different frequency than the drive eliminates the contribution from the drive hence making it easier to measure the small capacitance change

#### 5.1.1.3 Harmonic signals from diodes

Generating harmonic signals from a diode have been explored since the 1950s. Leenov et al[63] used a silicon graded junction diode to generate harmonics up to the 3rd of applied frequency. The applied frequencies ranged from $320 - 35000\,Hz$ and the harmonic generated frequencies ranged from $960 - 105,000\,Hz$.

With the advent of GaAs gunn diodes harmonically generated signals up to 110 GHz is possible. Barth[64] and Haydl[65] demonstrated the generation of these harmonic frequencies using gunn oscillators.

### 5.1.2 Motivation

The motivation in this chapter is to demonstrate $2f$ drive for piezoelectric semiconductors. As mentioned in the literature review section this has not been done. The advantage of using non-linear drive is the drive signal can be separated from the detect signal thereby improving the signal to background ratio. Additionally, this separation of drive and detect also eliminates contributions from feedthrough impedances thereby also improving the signal to background ratio. This demonstration of $2f$ can also lead to making a parametric amplifier. Parametric amplifiers have low noise floors and take advantage of the Q of the resonator to amplify a signal. The low noise floor makes it easy to measure small or weak signals. Traditionally parametric amplifiers are made from discrete components involving a diode and a resonant circuit. Here, the two are integrated thus making it a single device.

### 5.1.3 Outline

The outline of this chapter is as follows: the analytical model and the prediction from this model for the $f$ and $2f$ case is derived and discussed in section (5.2). Following this, the experimental setup, results and comparison to the analytical predictions are given in section (5.3). Section (5.4) concludes the chapter.

## 5.2 Analytical Model

One of the motivations of this work is to measure the current resulting from the electromechanical coupling. This current, called the motional current, is related to the motional capacitance, $C_m$, via the modified BVD model. Therefore an expression for the motional capacitance for the $f$ and $2f$ case is derived below. Additionally an expression for the junction capacitance is also derived for the $f$ and $2f$ case. The expressions for junction capacitance is derived because the associated current dominates away from resonance.

### 5.2.1 $f$ Case

The depletion thickness change as a function of voltage is given in equation(2.43). Since the depletion and the piezoelectric regions are the same the piezoelectric thickness also changes by the same amount. In the photodiode structure, figure 4.5(c), two depletion/piezoelectric regions, exist $t_2$ and $t_4$. Therefore, the thickness of these regions will change as a function of the applied bias - $t_2(V)$ and $t_4(V)$. As a result of the change in thicknesses in these regions the thickness of the adjacent transition/elastic regions, $t_3(V)$ and $t_5(V)$, will also change. These changes in thicknesses affect the values of the motional capacitance. Equations (5.5) and (5.6) capture this change for the former and the latter. Their derivation follows.

#### 5.2.1.1 $C_{m,x}(V)$

Here expressions for $C_{m,x}(V)$, i.e. the piezoelectric capacitance in layers 2 and 4, are derived. The nomenclature used is the same as in the previous chapter.

The general expression for depletion thickness as a function of voltage is rewritten from equation (2.43) as: $d(V) = d^0\sqrt{1-\frac{V}{V_{bi}}}$; where $d^0$ is the thickness at $0\,V$, and $V_{bi}$ is the built in voltage. For $pn$ junctions $d^0$ or $t_4^0$ is given by equation (2.43) and $V_{bi}$ is given by equation (2.42) For the heterojunction wXAmps[66] is used to determine $t_2^0 = 50\,nm$ and $V_{bi,2} = 0.387\,V$. According to the simulator at $V_{DC} = 0\,V$ the $p^- In_{0.485}Ga_{0.515}P$ layer is completely depleted. $t_2$, and $t_4$ can be expressed as:

$$t_2(V) = t_2^0\sqrt{1-\frac{\beta_2 V}{V_{bi,2}}} = (50e-9)\sqrt{1-\frac{\beta_2 V}{0.387}} \tag{5.1}$$

$$t_4(V) = t_4^0\sqrt{1-\frac{\beta_4 V}{V_{bi,4}}} = (146.185e-9)\sqrt{1-\frac{\beta_4 V}{1.33}} \tag{5.2}$$

The thickness of the transitions regions, $t_3$ and $t_5$ can be expressed as a function of the depletion regions.

For a $pn$ junction the respective depleted thickness of the $p$ and $n$ layer are: $d_p = d\frac{N_d}{N_d+N_a}$ and $d_n = d\frac{N_a}{N_d+N_a}$[5]. For the heterostructure again wXAmps is used and found that the depletion region does not extend into the $p^+ - GaAs$ or $t_1$ layer. This is expected because this layer is degenerately doped. Hence $t_1$ remains fixed and is expressed as: $t_1 = t - (t_2 + t_3 + t_4 + t_5)$. At zero bias $t_2$ is completely depleted with minimal extension into the $p^- - GaAs$ or $t_3$ region. The thickness of $t_3$ is dependent on changes to both $t_2$ and $t_4$. Therefore $t_3$ and $t_5$ are expressed as:

$$t_3(V) = t_3^0 - t_4\frac{N_d}{N_d+N_a} - \left(t_2 - t_2^0\right) \tag{5.3}$$

$$t_5(V) = t_5^0 - t_4\frac{N_a}{N_d+N_a} \tag{5.4}$$

where $t_3^0$ and $t_5^0$ are the undepleted thicknesses, i.e. $1.5\,\mu m$ and $125\,nm$.

Using the above definitions for the bias dependent thicknesses of each layer and accounting for the thickness of each layer the simplified forms of equations(4.17) and (4.18) are:

$$C_{m,2}(V) = \frac{-2Yd_{23,2}LW}{t^3t_2}\left(d_{23,2}\left(t^3 - t^2t_2\right) + d_{23,4}\frac{\beta_4}{\beta_2}t_2\left(-t^2 + 3tt_2 - 3t_2\left(t_4 + 2t_5\right)\right)\right)$$

$$C_{m,4}(V) = \frac{-2Yd_{23,4}LW}{t^3t_4}\left(d_{23,4}\left(t^3 - t^2t_4 + 3tt_4^2\right)\right)$$

In the above expressions only the dominant terms are considered. Additionally, $t_2(V)$, $t_3(V)$, $t_4(V)$ and $t_5(V)$ are written as $t_2$, $t_3$, $t_4$ and $t_5$ . Unless otherwise stated these terms are functions of voltages.

#### 5.2.1.2 $C_{J,x}$

For $C_{J,2}$ and $C_{J,4}$ the change in $t_2$ and $t_4$ only needs to be considered. Therefore these expressions are:

$$C_{J,2} = \frac{\epsilon_0\epsilon_{r,2}}{t_2}L_TW_T$$

$$C_{J,4} = \frac{\epsilon_0\epsilon_{r,4}}{t_4}L_TW_T$$

#### 5.2.1.3 $C_J$ and $C_m$

Accounting for the series circuit the total junction and motional capacitances are:

$$C_J = \frac{\epsilon_0\epsilon_{2,r}\epsilon_{4,r}}{t_2\epsilon_{4,r} + t_4\epsilon_{2,r}}L_TW_T \tag{5.5}$$

$$C_m = \frac{2Yd_{23,2}d_{23,4}^2LW\beta_4\left(t^2-tt_4+3t_4^2\right)\left(d_{23,4}t_2\beta_4\left(t^2-3t_2\left(t-t_4-2t_5\right)\right)+d_{23,2}t^2\beta_2\left(-t+t_2\right)\right)}{t^2\left(d_{23,4}t_2\beta_4\left[d_{23,4}t\left(t^2-tt_4+3t_4^2\right)-d_{23,2}t_4\left(t^2-3t_2\left(t-t_4-2t_5\right)\right)\right]-d_{23,2}^2t^2t_4\beta_2\left(-t+t_2\right)\right)} \tag{5.6}$$

Therefore, the equation for the total current for the $f$ case is:

$$I^f = I_p^f + I_m^f = \left[C_J + C_m\right]V_{ac}wcos\left(wt\right) \tag{5.7}$$

$C_J$ and $C_m$ are expressions for the capacitance for the $f$ case and from this point on wards will be written as $C_J^f$ and $C_m^f$ to distinguish from the $2f$ case

### 5.2.2 $2f$ Case

Using equations (5.5) and (5.6) expressions for $C_J^{2f}$ and $C_m^{2f}$ are derived. The superscript $2f$ corresponds to the $2f$ case. The derivation begins with considering the total charge:

$$Q = C_TV = \left(C_J^f + C_m^f\right)V \tag{5.8}$$

which consists of contributions from both $C_J^f$ and $C_m^f$. Here

$$V = V_{DC} + V_{AC}$$

The total current is:

$$I = \frac{dQ}{dt} = \frac{d}{dt}\left(C_TV_{AC}\right) = \frac{dC_T}{dV_{AC}}\frac{dV_{AC}}{dt}V_{AC} + C_T\frac{dV_{AC}}{dt} = \left[\frac{dC_T}{dV_{AC}}V_{AC} + C_T\right]\frac{dV_{AC}}{dt} \tag{5.9}$$

To determine the current at $2f$ due to the harmonic drive $C_T$ is expanded as a Taylor series

$$C_T = C_T^f + \frac{d}{dV}C_T^f|_{V=V_{DC}}V_{AC} + \frac{1}{2}\frac{d^2}{dV^2}C_T^f|_{V=V_{DC}}V_{AC}^2 + \ldots$$

Substituting this into equation (5.9) and ignoring contributions greater than $V_{AC}$ yields:

$$I = \left[C_T^f + 2\frac{d}{dV}C_T^f|_{V=V_{DC}}V_{AC}\right]\frac{dV_{AC}}{dt} \tag{5.10}$$

where $C_T^f$ is a sum of equations (5.5) and (5.6). The first term is the current measured at the driven frequency $f$. The second term is the current measured at $2f$, i.e. twice the driven frequency. The current equation for $2f$ is written as follows:

$$I^{2f} = 2\left[\frac{d}{dV}C_T^f|_{V=V_{DC}}V_{AC}\right]\frac{dV_{AC}}{dt} = I_J^{2f} + I_m^{2f} = \left[\frac{d}{dV}C_J^f|_{V=V_{DC}} + \frac{d}{dV}C_m^f|_{V=V_{DC}}\right]V_{ac}^2wsin\left(2wt\right) \tag{5.11}$$

Here the following substitution is made $V_{AC} = V_{ac}cos\left(wt\right)$. The superscript $2f$ indicates junction or motional currents are generated at twice the drive frequency. This results from the product of $V_{AC}$ and $\frac{dV_{AC}}{dt}$.

The expression for $\frac{d}{dV}C_J^f$ is:

$$\frac{d}{dV}C_J^f = -\frac{\epsilon_0\epsilon_{2,r}\epsilon_{4,r}\left(t_2^{'}+t_4^{'}\right)}{\left(\epsilon_{4,r}t_2+\epsilon_{2,r}t_4\right)^2}L_tW_t \tag{5.12}$$

where $t_2^{'} = -\frac{t_2^0\beta_2}{2V_{bi,2}}\left(1-\frac{\beta_2 V}{V_{bi,2}}\right)^{-\frac{1}{2}}$ and $t_4^{'} = -\frac{t_4^0\beta_4}{2V_{bi,4}}\left(1-\frac{\beta_4 V}{V_{bi,4}}\right)^{-\frac{1}{2}}$

The expression for $\frac{d}{dV}C_m^f$ is:

$$\frac{d}{dV}C_m^f = \frac{\alpha}{V_{23,4}} \tag{5.13}$$

where

$$\alpha = \frac{-\begin{pmatrix}\beta_4 d_{23,2}\left(d_{23,4}\right)^2\\ \times YL_tW_t\end{pmatrix}\gamma}{t^2\left(\begin{pmatrix}\beta_4 d_{23,4}t_2\left(d_{23,4}t\eta_5 - d_{23,2}t_4\eta_6\right)\\ +t^2\beta_2\left(d_{23,2}\right)^2 t_4\eta_8\end{pmatrix}^2\right)}$$

where

$$\gamma = \begin{pmatrix} -\beta_4\begin{pmatrix}\beta_4 d_{23,2}t^2\eta_{12}\\ +\beta_4 d_{23,4}t_2\eta_6\end{pmatrix}\\ \times\eta_7\begin{pmatrix}\beta_4 d_{23,4}t_2\left(d_{23,4}t\eta_5 - d_{23,2}t_4\eta_6\right)\\ +\beta_2\left(d_{23,2}\right)^2 t^2 t_4\eta_8\end{pmatrix}\\ +\frac{\eta_5}{\left(N_{ad}\right)^2 V_{2,23}}\begin{pmatrix}\beta_2\left(d_{23,2}\right)^2 N_{ad}t^2t_4\eta_8\\ +\beta_4 d_{23,4}t_2\begin{pmatrix}d_{23,4}N_{ad}t\eta_5\\ -d_{23,2}t_4\left(N_a\eta_{10}+N_d\eta_{11}\right)\end{pmatrix}\end{pmatrix}\\ \times\begin{pmatrix}\beta_2^2 d_{23,2}N_{ad}t^2\gamma_{22}V_{4,23}\\ +\beta_2\beta_4 d_{23,4}\gamma_{22}V_{4,23}\left(N_d\eta_4+N_a\eta_9\right)\\ +3\left(\beta_4\right)^2 d_{23,4}\left(t_2\right)^2\gamma_{44}V_{2,23}\left(-N_a+N_d\right)\end{pmatrix}\\ +\frac{\eta_5}{\left(N_{ad}\right)^2 V_{2,23}}\begin{pmatrix}\beta_2 d_{23,2}N_{ad}t^2\eta_8\\ -\beta_4 d_{23,4}t_2\left(N_a\eta_{10}+N_d\eta_{11}\right)\end{pmatrix}\\ \times\begin{pmatrix}-\left(\beta_2 d_{23,2}t\right)^2 N_{ad}t_4\gamma_{22}V_{4,23} - \left(\beta_2\right)^2 d_{4,23}t_2V_{2,23}\\ \times\begin{pmatrix}d_{23,2}\gamma_{44}\left(N_a\left(t^2-3tt_2+6t_2\left(t_5^0-t_4\right)\right)+N_d\left(t^2-3tt_2+6t_2\left(t_5^0+t_4\right)\right)\right)\\ +d_{23,4}N_{ad}t\eta_7\end{pmatrix}\\ +\beta_1\beta_2\begin{pmatrix}\left(d_{23,4}\right)^2 N_{ad}t\gamma_{22}\eta_5V_{4,23} - d_{23,2}d_{23,4}V_{4,23}\gamma_{22}t_4\left(N_d\eta_4+N_a\eta_9\right)\\ +V_{2,23}\left(d_{23,2}\right)^2 N_{ad}t^2\gamma_{44}\eta_8\end{pmatrix}\end{pmatrix}\end{pmatrix}$$

where $t_2 = t_2^0\sqrt{1-\frac{\beta_1 V}{V_{bi,2}}}$ $t_4 = t_4^0\sqrt{1-\frac{\beta_2 V}{V_{bi,4}}}$ $\left(\gamma_4\right)^2 = \left(t_4^0\right)^2\left(1-\frac{\beta_2 V}{V_{4,bi}}\right)^2$ $\gamma_{22} = t_2^0\left(1-\frac{\beta_1 V}{V_{2,bi}}\right)^{-\frac{1}{2}}$ $\gamma_{44} = t_4^0\left(1-\frac{\beta_2 V}{V_{4,bi}}\right)^{-\frac{1}{2}}$ $N_{ad} = N_a + N_d$ $\eta_1 = -3tt_2 - 3t_2t_4 + 6t_2t_5^0$ $\eta_2 = -3tt_2 + 3t_2t_4 + 6t_2t_5^0$ $\eta_3 = \frac{3t_2\left(-N_at_2\left(-N_at_4+N_dt_4+2N_at_5^0+2N_dt_5^0\right)\right)}{N_{ad}}$ $\eta_4 = t^2 - 6tt_2 + 6t_2\left(t_4+2t_5^0\right)$ $\eta_5 = t^2 - tt_4 + 3\left(t_4\right)^2$ $\eta_6 =$

$t^2-3tt_2+\eta_3\ \eta_7=-6\left(t_4^0\right)^2+t\gamma_{44}\ \eta_8=t-t_2\ \eta_9=t^2-6tt_2-6t_2t_4+12t_2t_5^0\ \eta_{10}=t^2+\eta_1\ \eta_{11}=t^2+\eta_2\ \eta_{12}=-t+t_2$

Using equation(5.11) expressions for $C_J^{2f}$ and $C_m^{2f}$ are (5.14) and (5.15). These are determined as follows:

$$I^{2f}=I_J^{2f}+I_m^{2f}=\left[\frac{d}{dV}C_J^f|_{V=V_{DC}}+\frac{d}{dV}C_m^f|_{V=V_{DC}}\right]V_{ac}^2 wsin\left(2wt\right)$$

Substituting for $\frac{d}{dV}C_m^{2f}$:

$$I^{2f}=I_J^{2f}+I_m^{2f}=\left[\frac{d}{dV}C_J^f|_{V=V_{DC}}+\frac{\alpha}{V_{23,4}}\right]V_{ac}^2 wsin\left(2wt\right)$$

Factoring $V_{23,4}$ from the expression

$$I^{2f}=I_J^{2f}+I_m^{2f}=\left[V_{23,4}\frac{d}{dV}C_J^f|_{V=V_{DC}}+\alpha\right]\frac{V_{ac}^2}{V_{23,4}}wsin\left(2wt\right)$$

Therefore the first term is $C_J^{2f}$ and the second term is $C_m^{2f}$. These are:

$$C_J^{2f}=V_{23,4}\frac{d}{dV}C_J^fV_{ac}=-V_{23,4}\frac{\epsilon_0\epsilon_{2,r}\epsilon_{4,r}\left(t_2^{'}+t_4^{'}\right)}{\left(\epsilon_{4,r}t_2+\epsilon_{2,r}t_4\right)^2}L_tW_t \tag{5.14}$$

and

$$C_m^{2f}=\alpha \tag{5.15}$$

Having derived $C_p^{2f}$ and $C_m^{2f}$ in the next section the prediction of equations (5.5), (5.6), (5.14) and (5.15) are plotted.

### 5.2.3 Analytical Predictions

The analytical predictions for $C_J^f$, $C_m^f$, $C_J^{2f}$ and $C_m^{2f}$ are first plotted. This is called the electrical response. Using these the mechanical response to the varying $C_m^f$ and $C_m^{2f}$ are plotted. This is called the electro-mechanical response. For the plots below the following parameters are used: For both the plots the following parameters are used $V_{bi,2}=0.387\,V$, $V_{bi,4}=1.33\,V$, $d_{23,2}=0.57905\,\frac{pC}{N}$, $d_{23,4}=-1.345\frac{pC}{N}$, $L=80.0\mu m$, $W=30.0\mu m$, $t_2^0=50.0\,nm$, $t_4^0=146.185\,nm$, $t_5^0=125.00\,nm$, $Y=80.0\,GPa$, $t=1.875\,\mu m$, $L_TW_T=68.9245e-9\,m^2$, $\beta_2=0.2650,\beta_4=0.7350$ and $\epsilon_{r,2}$ and $\epsilon_{r,4}$ are 12.50 [59] and 13.18 [60]. The square anchor has dimensions of $250\times250\,\mu m^2$

#### 5.2.3.1 Electrical Response

**5.2.3.1.1 $C_J^f$ and $C_m^f$** Figures (5.1) (a) and (b) are the plot of equations (5.5) and (5.6). Here the x-axis is dc voltage, $V_{DC}$, and the y-axis is junction capacitance in figure (a) and motional capacitance in figure (b) for the case of $f$. $V_{DC}$ ranges from $-0.5$ to $0.5\,V$ . In general, the capacitances increases as $V_{DC}$ increases. The junction and motional capacitances at $0.5\,V$ are roughly 1.35 and 1.46 times greater than their respective values at $-0.5\,V$. In

figure (5.2) the two capacitances are compared by normalizing to their respective values at $V_{DC} = 0\,V$. In the figure the superscript in $C^f_{J,m}$ signifies either junction or motional capacitance. As is seen, the motional capacitance is lower than the junction capacitance for $V_{DC}$ below $0\,V$. Above $0\,V$ the motional capacitance is greater. In figure (5.3) $\left(\frac{C^f_J(0)}{C^f_J(V_{DC})}\right)^2$ and $\left(\frac{C^f_m(0)}{C^f_m(V_{DC})}\right)^2$ vs $V_{DC}$ are plotted. The motivation for doing this is to:

1. show that both $C^f_J$ and $C^f_m$ varies as $\frac{1}{\sqrt{1-\left(\frac{V_{DC}}{V_{bi}}\right)}}$. This is the familiar diode capacitance relationship, equation(2.45), with respect to $V_{DC}$. The relationship was discussed in the pn junction section of chapter 2
2. show that as expected from figure (5.3) and reflected in figure (5.3) the slope for the motional capacitance is higher than for the junction capacitance.

**5.2.3.1.2 $C^{2f}_J$ and $C^{2f}_m$** Figures (5.4) (a) and (b) are a plot of equations (5.14) and (5.15). The x-axis is the same as for the above plots. As expected the two capacitances increase as $V_{DC}$ increases. The capacitances values, $C^{2f}_J$ and $C^{2f}_m$, at $0.5\,V$ are 2.5 and 2.6 times greater than their values at $-0.5\,V$. This increase is larger than at $f$ however the magnitude of $C^{2f}_J$ and $C^{2f}_m$ is approximately half of $C^f_J$ and $C^f_m$. The trend in figure (5.5) is similar to figure (5.2) but the variation between $C^{2f}_J$ and $C^{2f}_m$ is smaller. This is seen from figure (5.6) where the slope of the junction and motional capacitance are similar. Figure (5.6) is plotted to show both $C^{2f}_J$ and $C^{2f}_m$ vary as $\frac{1}{\sqrt{\left(1-\frac{V_{DC}}{V_{bi}}\right)^3}}$ which is the first derivative of $\frac{1}{\sqrt{1-\left(\frac{V_{DC}}{V_{bi}}\right)}}$.

#### 5.2.3.2 $V^{2f}$

Figure (5.7) is a plot of the harmonic generated voltage at $2f$ using $\frac{V^2_{ac}}{V_{bi,4}}$ where $V_{ac}$ is the drive voltage applied at $f$. This plot illustrates that for an appreciable generation of harmonic voltage at $2f$ a minimum drive voltage of $2.30\,mV_{rms}$ is required. Here appreciable is defined as the minimum voltage required to measure a signal at resonance. This limit is set by the noise floor of the amplifier and the acquisition time. Hence; a minimum voltage of $4.0\,\mu Vrms$ is generated for a drive voltage of $2.30\,mV_{rms}$

#### 5.2.3.3 Electro-Mechanical Response

Mechanically, as the depletion thickness decreases with an increasing $V_{DC}$ the deformation and hence the motional current also increases. This is because as $t_2$ and $t_4$ decreases with $V_{DC}$ the associated piezoelectric strain, $\epsilon_2$ and $\epsilon_4$, increases which results in a larger motional current. This motional current is related to the motional capacitance. This ability to in situ vary the piezoelectric thickness and hence the deflection is unique to semiconductor-piezoelectric materials. Conventionally to vary the piezoelectric thickness requires either chemically removing the piezoelectric layer or depositing a new piezoelectric layer using techniques such a sputtering or CVD. Both are time consuming and limit the thickness that can be achieved.

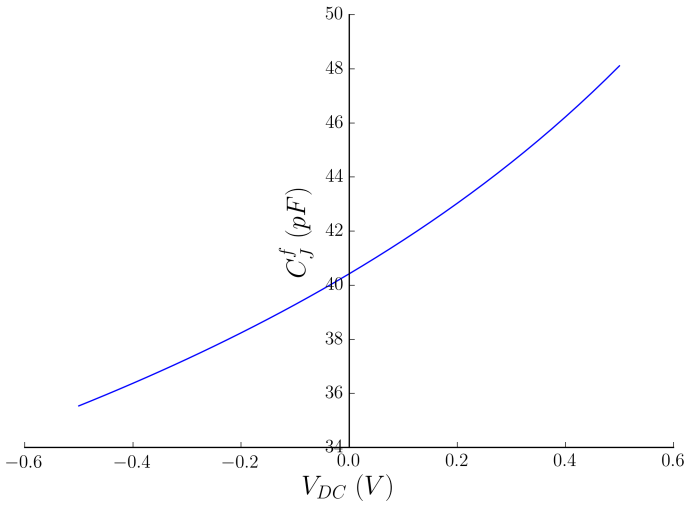


(a)

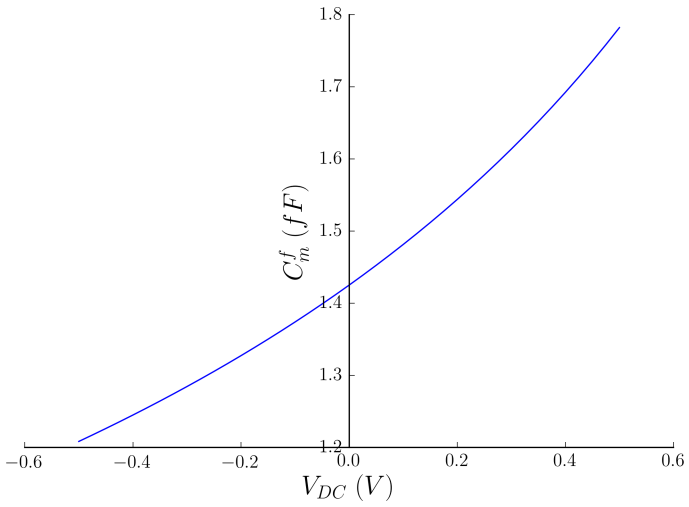


(b)

Figure 5.1: $C_J^f$ and $C_m^f$ as a function of $V_{DC}$: (a) and (b) are the plot of equations (5.5) and (5.6). In general, the capacitances increases as $V_{DC}$ increases

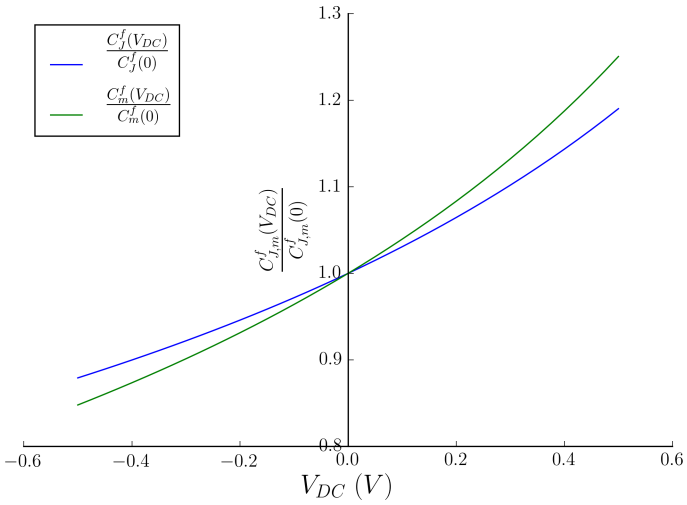


Figure 5.2: Comparison of $\frac{C_J^f(V_{DC})}{C_J^f(0)}$ and $\frac{C_m^f(V_{DC})}{C_m^f(0)}$ vs $V_{DC}$. The motional capacitance is lower than the junction capacitance for $V_{DC}$ below $0\,V$. Above $0\,V$ the motional capacitance is greater

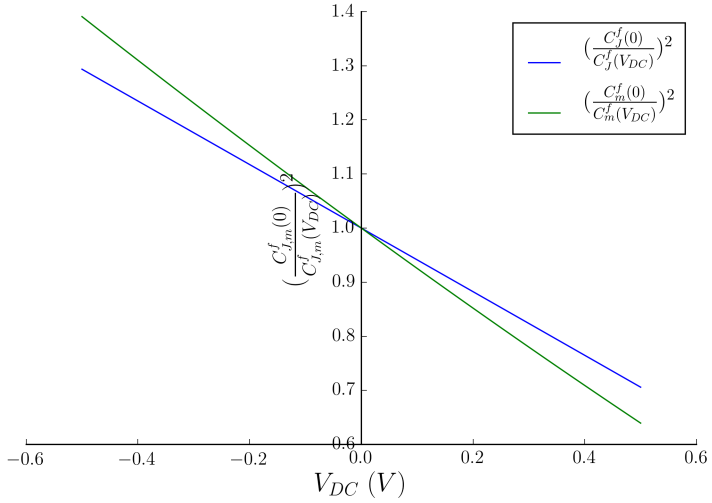


Figure 5.3: Comparison of $\left(\frac{C_J^f(0)}{C_J^f(V_{DC})}\right)^2$ and $\left(\frac{C_m^f(0)}{C_m^f(V_{DC})}\right)^2$. The two are linear lines indicating that both $C_J^f$ and $C_m^f$ varies as $\frac{1}{\sqrt{1-\left(\frac{V_{DC}}{V_{bi}}\right)}}$. This is the familiar diode capacitance relationship, equation(2.45), with respect to $V_{DC}$. The slope of the normalized $C_J^f$ is lower than $C_m^f$

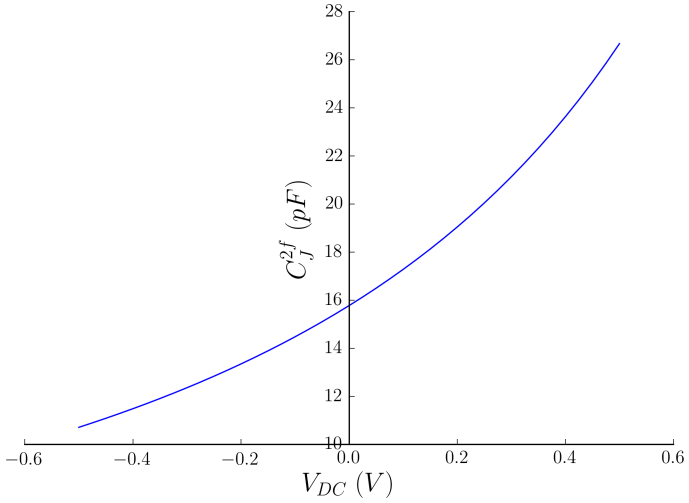


(a)

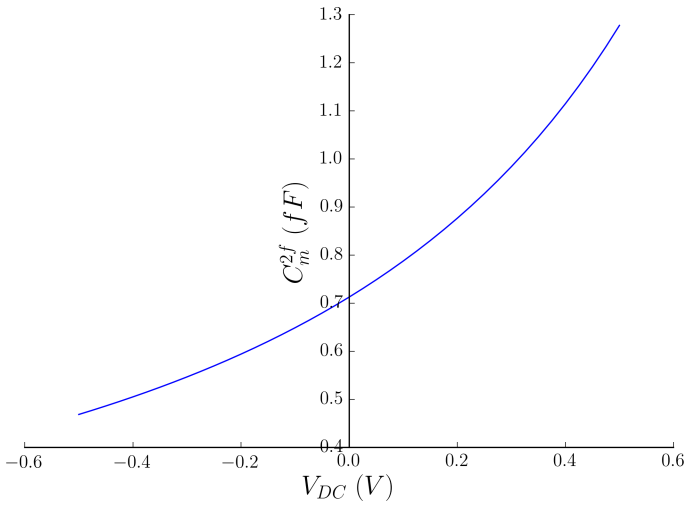


(b)

Figure 5.4: $C_J^{2f}$ and $C_m^{2f}$ as a function of $V_{DC}$: (a) and (b) are the plot of equations (5.14) and (5.15). In general, the capacitances increases as $V_{DC}$ increases

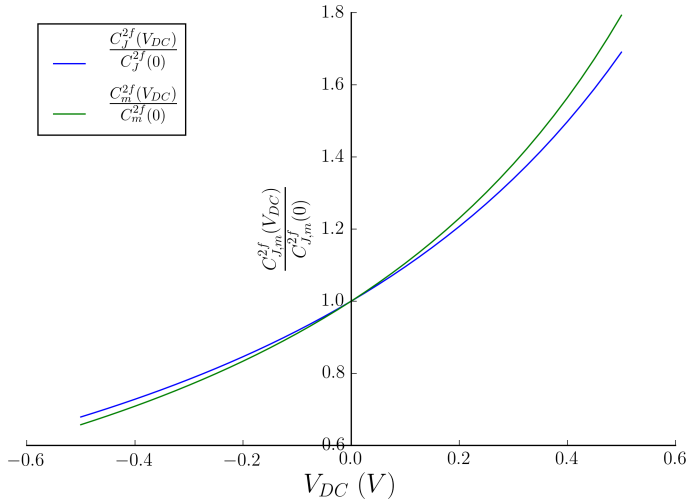


Figure 5.5: Comparison of $\frac{C_J^{2f}(V_{DC})}{C_J^{2f}(0)}$ and $\frac{C_m^{2f}(V_{DC})}{C_m^{2f}(0)}$ vs $V_{DC}$. The capacitance follow the similar trend, i.e the nomalized capacitance increases with $V_{DC}$

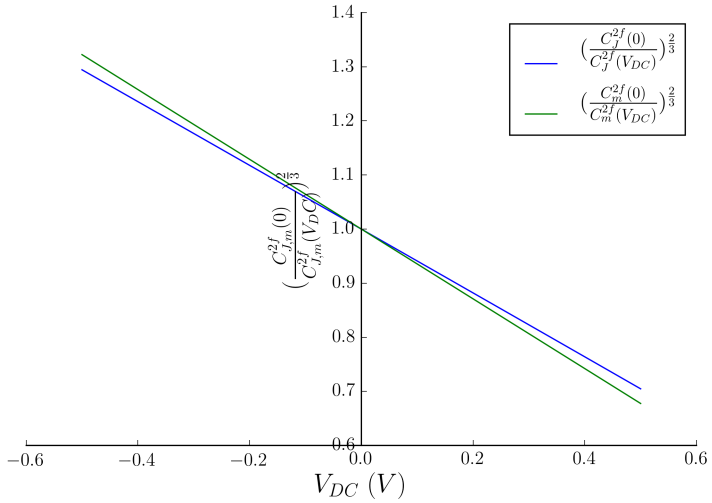


Figure 5.6: Comparison of $\left(\frac{C_J^{2f}(0)}{C_J^{2f}(V_{DC})}\right)^{\frac{2}{3}}$ and $\left(\frac{C_m^{2f}(0)}{C_m^{2f}(V_{DC})}\right)^{\frac{2}{3}}$. The two are linear lines indicating that both $C_J^f$ and $C_m^f$ varies as $\frac{1}{\sqrt{\left(1-\frac{V_{DC}}{V_{bi}}\right)^3}}$

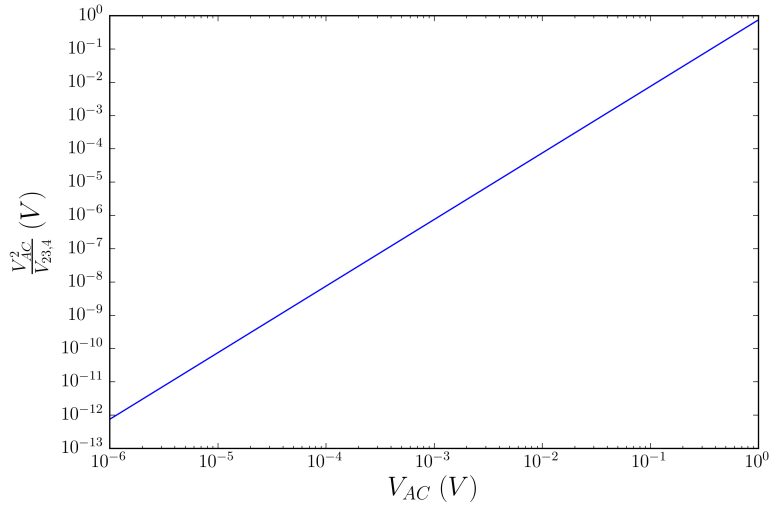


Figure 5.7: $V_{AC}^{2f}$ *vs* $V_{AC}^{f}$ Generated AC voltage at $2f$ as a result of an AC drive voltage at $f$. The $\frac{V_{AC,Drv}}{2.66}$ line is plotted for reference

Figures (5.8)(a) and (b) are plots of this increasing motional current for the following $V_{DC}$ values: $-0.5$, $0$ and $0.5\,V$. The x-axis in these plots is frequency and the y-axis is motional current. Figure(5.8)(a) is the response at $f$ and (b) is the response as $2f$. In these plots the contribution from the background is subtracted. For the $f$ case the motional current predicted for $V_{DC} = 0.5\,V$ is 1.6 times greater than predicted for $V_{DC} = -0.5\,V$. At $2f$, the predicted motional current is 2.8 times greater. This is as expected and is because $C_m^f$ varies approximately as $\frac{1}{\sqrt{1-\frac{V_{DC}}{V_{bi}}}}$ while $C_m^{2f}$ varies approximately as $\frac{1}{\sqrt{\left(1-\frac{V_{DC}}{V_{bi}}\right)^3}}$. Although the increase is larger at $2f$ the current is half or quarter of the current at $f$ for $V_{DC} = 0.5$ and$-0.5\,V$; respectively.

## 5.3 Experimental Setup and Results

Frequency sweeping experiments are conducted to validate the theoretical predictions for $C_J^f$, $C_m^f$, $C_J^{2f}$ and $C_m^{2f}$. In these experiments as the frequency is swept across resonance the current response of the device is recorded. The recorded data is fit to the modified BVD circuit model, figure (4.7), allowing for verifying the predicted $C_J^f$, $C_m^f$, $C_J^{2f}$ and $C_m^{2f}$; respectively.

The setup used, figure 5.9 is similar to that described in the previous chapter with the exception of the change in lock-in amplifier. SR-830 is used instead of SR-844.

For $2f$ experiment the same span in the frequency range is used as the $f$ experiment however in the $2f$ experiment driving frequencies are half of that used in the $f$ experiment. The lock-in is set to measure the 2nd harmonic of the sync signal provided from the function generator.

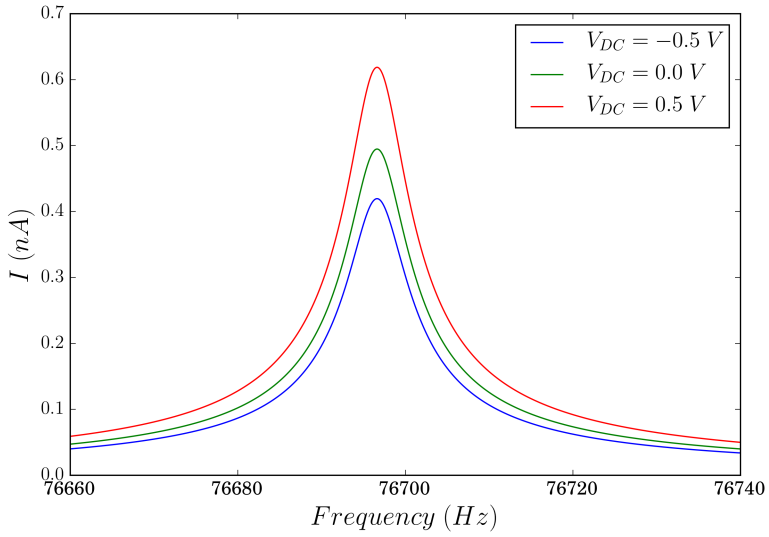


(a)

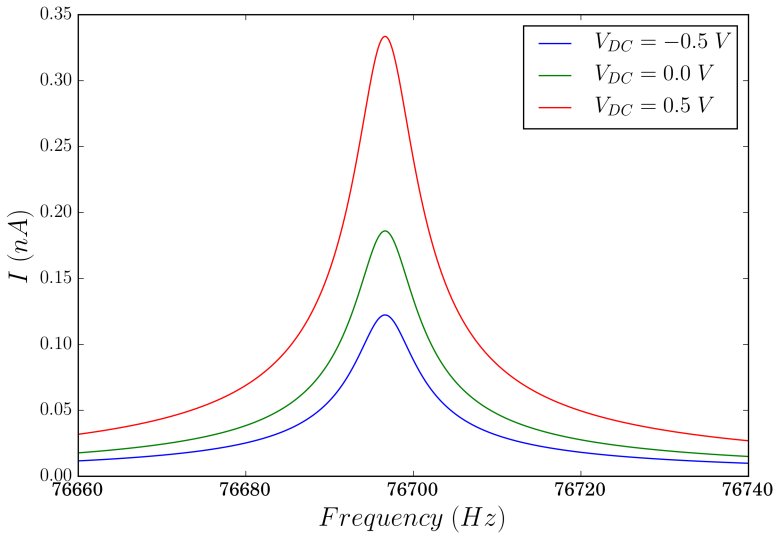


(b)

Figure 5.8: $I^f$ and $I^{2f}$. The motional current for the $f$ and $2f$ case. Generally, in both these plots the motional current increases as $V_{DC}$ increases. For the $2f$ this increase is larger.

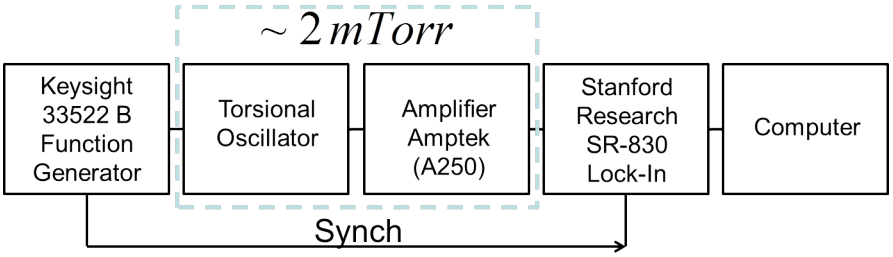


Figure 5.9: Experimental setup used for frequency sweeping experiments both at $f$ and $2f$. The function generator drives the torsional oscillator and supplies the synchronization signal to the SR-830 Lock-in Amplifier. The experiment is controlled by the computer using labview. The data from the lock-in is saved for later processing

### 5.3.1 Equivalent Electrical Circuit

Figure (5.10) is the equivalent circuit models for $f$ and $2f$. The circuit comprise of the BVD circuit, a $1.0\,M\Omega$ DC path to ground and the Amptek A-250 circuit. The A250's circuit consists of a 2SK152 JFET, an op-amp and in the feedback path $C_F$ and $R_F$. Their values are $1.5\,pF$ and $300.0\,M\Omega$; respectively.

### 5.3.2 Experimental Results

The span for the DC bias is determined from the $IV$ curves of the diode; figure (5.11). A bias range of $-0.5 \ldots 0.5\,V$, is chosen to minimize the contributions from the forward bias current of the diode.

Figure (5.12)(a), (b), (c) and (d) are the response of the resonator at $f$ and $2f$. In all these figures the x-axis is frequency. In figures (5.12)(a) and (c) the y-axis is current and in figures (b) and (d) the y-axis is phase in degrees. The drive voltage used for $f$ is $66.67\,\mu V_{rms}$ while for $2f$ the $\frac{f}{2}$ voltage is $21.21\,mV_{rms}$ which generates a harmonic drive voltage of $112.75\,\mu V_{rms}$. This harmonic drive voltage is approximately three times smaller than the expected drive voltage. The theoretical relationship between the two is given in figure (5.7).

From the current plots of $f$ and $2f$ the resonance and anti-resonance are switched between $f$ and $2f$. Anti-resonance curve occurring before resonance is indicative of either $C_J^{2f}$ or $C_m^{2f}$ having a negative value. According to equation (5.14) $C_J^{2f}$ has a negative value for capacitance. From the phase plot a $\frac{\pi}{2}$ phase shift is measured between $f$ and $2f$. This is as expected from the negative $C_J^{2f}$.

#### 5.3.2.1 AC Noise

Figure (5.13) is a plot of the measured AC current noise using the experimental setup. The x-axis is frequency and the y-axis is the current noise. The range of the plotted frequency is the same as the range chosen for measuring resonance. The noise measurements are made in vacuum, in the dark and in the absence of any external electrical excitation. The noise voltage from the amplifier is measured using the lock-in. The current noise is determined by

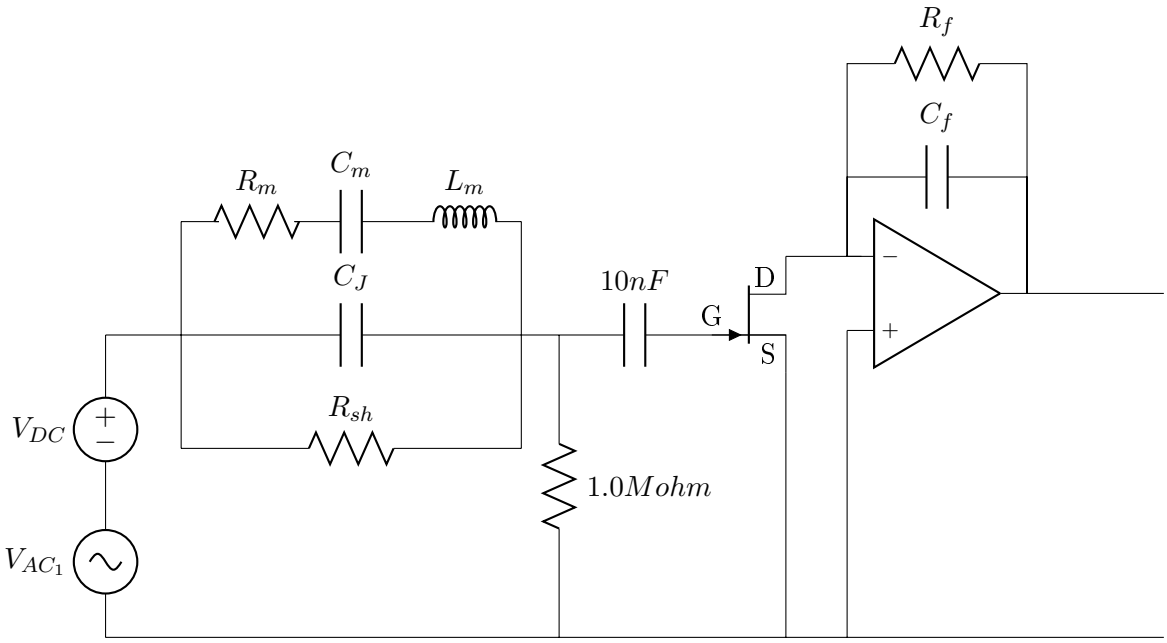


Figure 5.10: Electrical Circuit of the two terminal device and amplifier Equivalent circuit with drive voltage, $V_{AC}$. The $1.0\,M\Omega$ to ground provides a DC path to ground and $R_{sh}$ is the shunt resistance

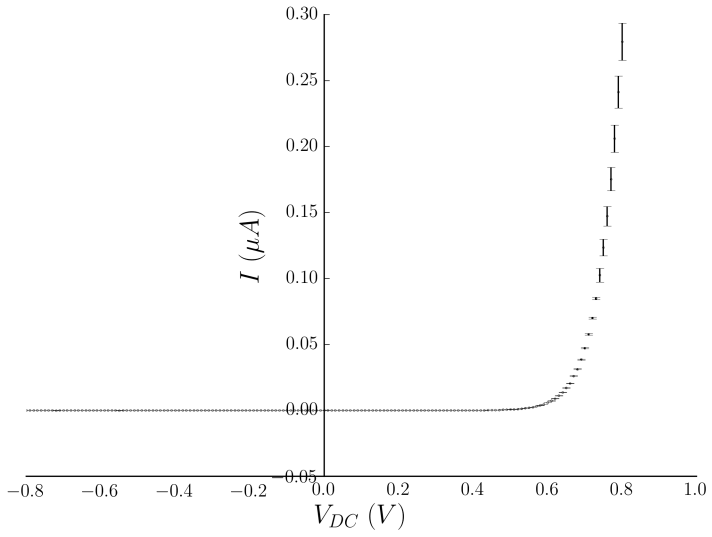


Figure 5.11: Torsional Resonator IV curve measured using the semiconductor parameter analyzer - HP4145-B

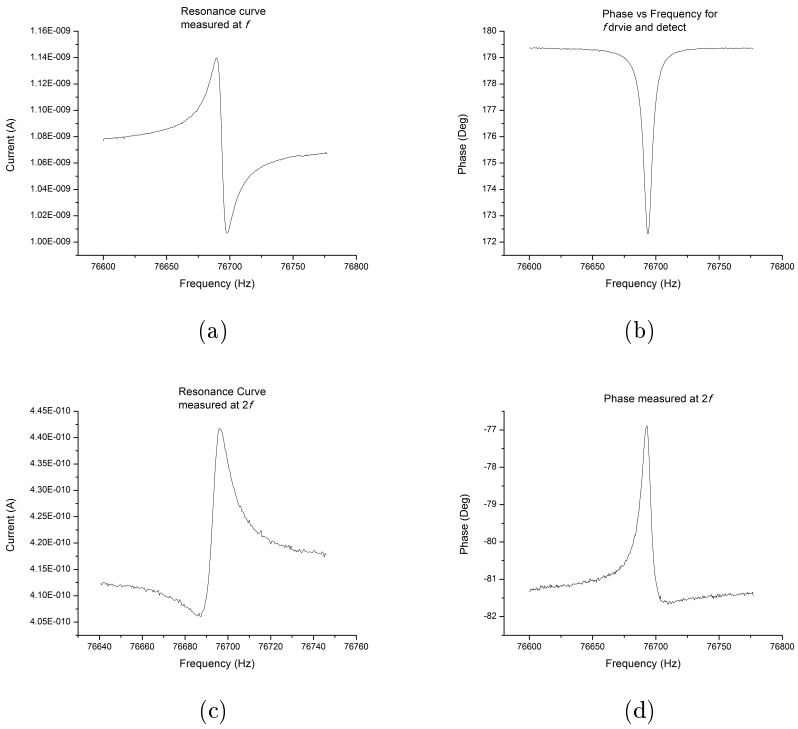


Figure 5.12: Resonance curve at $f$ and $2f$. (a) and (b) Current and Phase vs Frequency at $f$ (c) and (d) Current and Phase frequency at $2f$. The resonance and the anti-resonance peaks are switched between $f$ and $2f$ and a $\frac{\pi}{2}$ phase shift exists between the phase of $f$ and $2f$

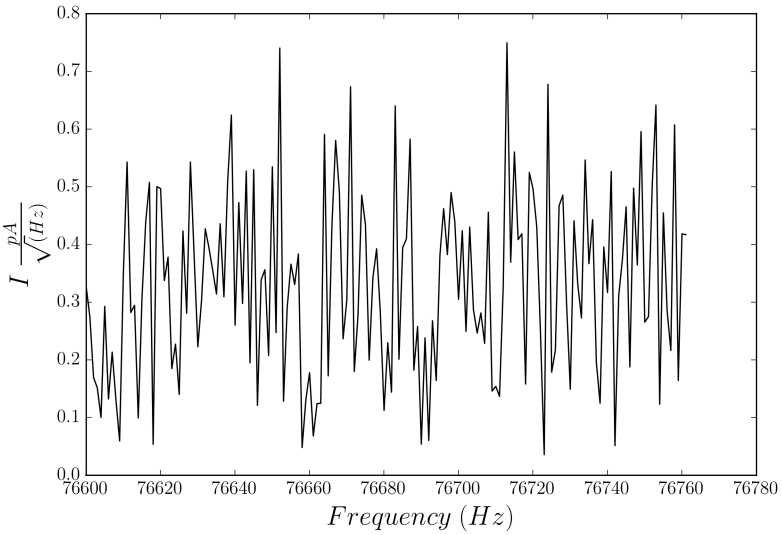


Figure 5.13: Measured Noise. The solid line is drawn as a guide to the eye

applying the amplifier's transfer function to the measured data. As is seen from the figure, the noise floor across the chosen range of frequencies is approximately $0.330\,\frac{pA}{\sqrt{Hz}}$. In the experiment the time constant of the filter on the lock-in amplifier is chosen to be 1.0 sec. Therefore the current noise is $0.330\,pA$

#### 5.3.2.2 Electro-Mechanical Response

Figure (5.14) (a) and (b) are the electro-mechanical response of the device at $f$ and $2f$ for $V_{DC}$ equivalent to $-0.5$, 0.0 and $0.5\,V$. The x-axis is frequency and the y-axis is motional current. In these figures the current due to the non-motional impedances are subtracted. Hence; the curves in these figures are similar to the current response of a voltage driven RLC circuit. From figure (5.14) (a), the $f$ case, as $V_{DC}$ increases the motional current decreases. This is the opposite trend as seen in figure (5.8)(a). For the $2f$ case the motional current increases as $V_{DC}$ increases. This is exactly as predicted. The prediction is plotted in figure (5.8)(b).

In the next few sections the trends of the measured junction and motional capacitances with respect to $V_{DC}$ are compared to trends from analytical predictions. The trends are compared instead of the magnitudes because the derived equations overestimate the magnitude of the motional current. This was shows in table(4.4) of the previous chapter. The experimental values of the junction and motional capacitances are extracted from the experimental data using the modified BVD model.

#### 5.3.2.3 Analysis at $f$

Figure (5.15)(a) and (b) are the plots of the normalized experimental data and normalized analytical predictions for $C_J^f$ and $C_m^f$. The x-axis in these plots is $V_{DC}$. The data in the y-

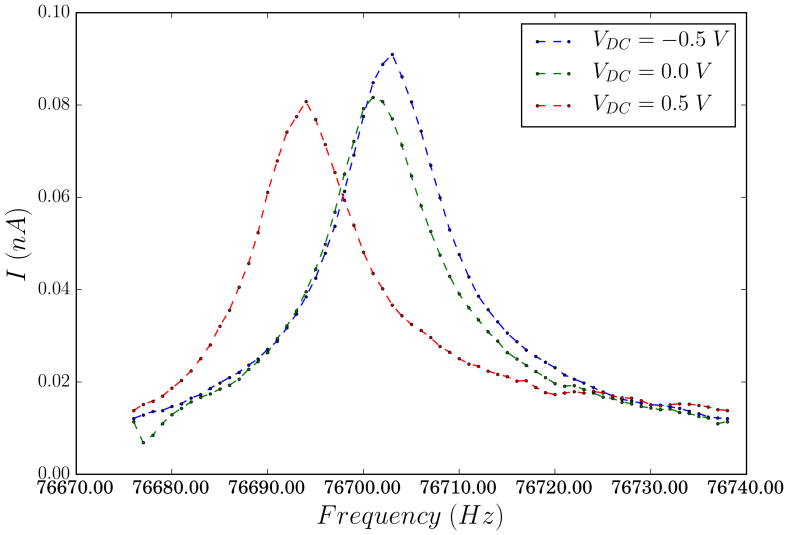


(a)

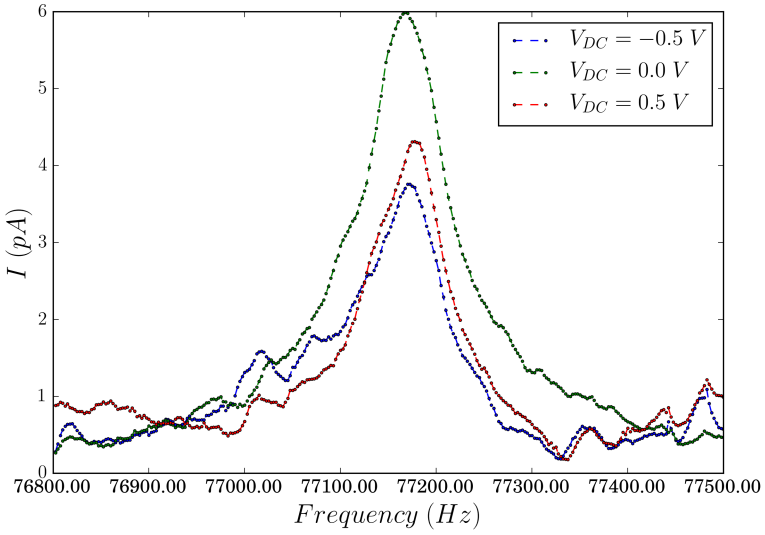


(b)

Figure 5.14: Motional current at $f$ and $2f$. These curves are acquired by subtracting the current contribution due to background impedances. (a) $f$ case: as $V_{DC}$ increases the motional current decreases. This is the opposite trend as seen in figure (5.8)(a), (b) $2f$ case: the motional current increases as $V_{DC}$ increases. This is exactly as predicted. The prediction is plotted in figure (5.8)(b)

axis is normalized to the respective, $C_J^f$ and $C_m^f$, capacitance values at $0\,V$. For the analytical predictions, the values used for the equations are the same as stated in the introduction to the analytical prediction section.

**5.3.2.3.1** $C_J^f$ As seen form (5.15)(a) the trends of the experimental results agrees well with the theoretical predictions. For $V_{DC} > 0.4\,V$ a deviation is seen between the two. This deviation occurs because the turn-on voltage for the diode is approximately $0.45\,V$ and not the equivalent $1.6\,V$ used for the theoretical predictions. The turn on voltage is deduced from the IV curve given in figure (5.11). Error bars for the experimental data in figure (5.15)(a) are not shown because they are below 1%.

**5.3.2.3.2** $C_m^f$ As seen form (5.15)(b) the trend of the experimental results is opposite from the theoretical predictions. This is also seen in figure (5.14) (a). The points in this data are an average of 5 data sets. The error bars are a result of this average.

### 5.3.2.4 Analysis at $2f$

Figure (5.16)(a) and (b) are the plots of the normalized experimental data and normalized analytical predictions for $C_J^{2f}$ and $C_m^{2f}$. Similar to above, the data in these plots are normalized to the capacitance value at $0\,V$. For the analytical predictions, the values used for the equations are the same as stated in the introduction to the analytical prediction section.

**5.3.2.4.1** $C_J^{2f}$ As seen form (5.16)(a) the trends of the experimental results agrees well with the theoretical predictions. For $V_{DC} > 0.2\,V$ a deviation is seen between the two. The reason for the deviation is the same as discussed for the $C_J^f$ case. The early occurrence of the deviation however is due to the $\frac{1}{\sqrt{\left(1-\frac{V_{DC}}{V_{bi}}\right)^3}}$ term in the $2f$ case. The denominator becomes larger for smaller $V_{DC}$. The error bars in the experimental data are not shown because they are below 1%.

**5.3.2.4.2** $C_m^{2f}$ As seen form (5.16)(b) the trends of the experimental results agrees well with the theoretical predictions. This trend was also seen in figure (5.14) (b). The pronounced deviation seen for $C_p^{2f}$ is not seen here. The points in this data are an average of 5 data sets. The error bars shown are a result of this average.

**5.3.2.4.3 Comment about $C_m^f$ and $C_m^{2f}$** The agreement in trend at $2f$ and not at $f$ for the motional capacitance seems to indicate that this phenomena is voltage dependent. That is to say greater the voltage lower the contribution from this phenomena. This is indicative of cases dealing with charge trapping. From figure (4.6) at the $p^- In_{0.485}Ga_{0.515}P$ and $p^-$ $GaAs$ interface there seems to be a condition for hole pile up. This will be explored in the next chapter.

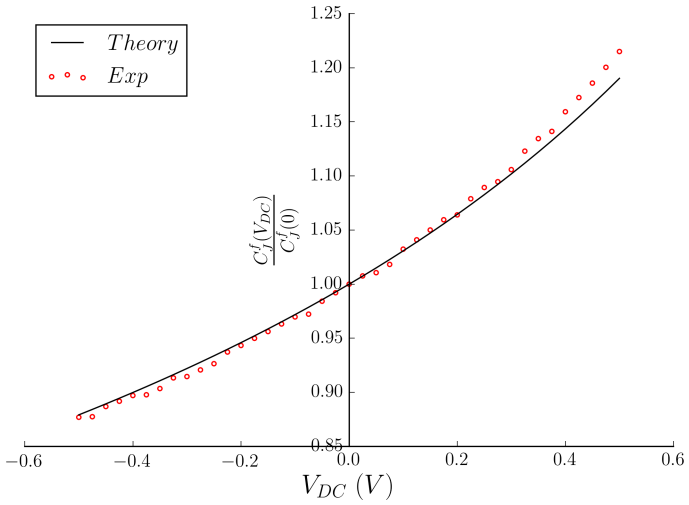


(a)

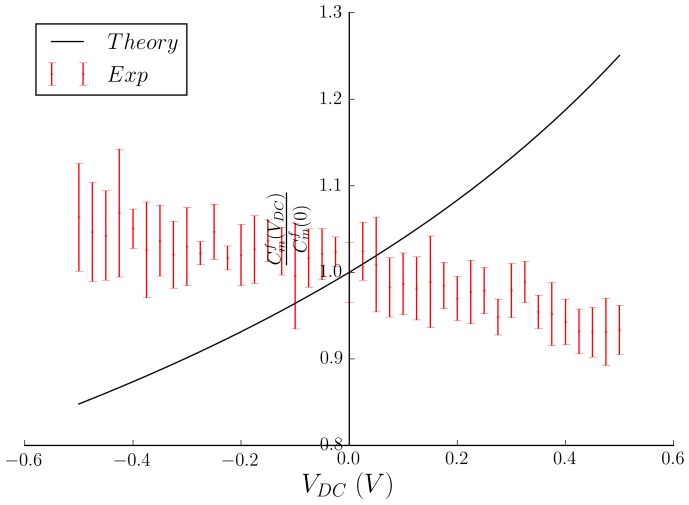


(b)

Figure 5.15: Comparison of experimental and theoretical trends for $C_J^f$ and $C_m^f$ (a) $C_J^f$: trends of the experimental results agrees well with the theoretical predictions. For $V_{DC} > 0.4\,V$ a deviation is seen between the two. This deviation occurs because the turn-on voltage for the diode is approximately $0.45\,V$ and not the equivalent $1.6\,V$ used for the theoretical predictions (b)$C_m^f$: the trend of the experimental results is opposite from the theoretical predictions. This is also seen in figure (5.14) (a)

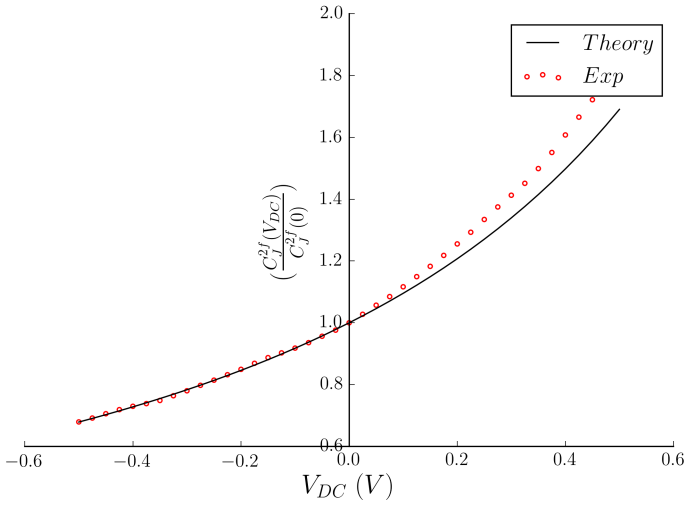


(a)

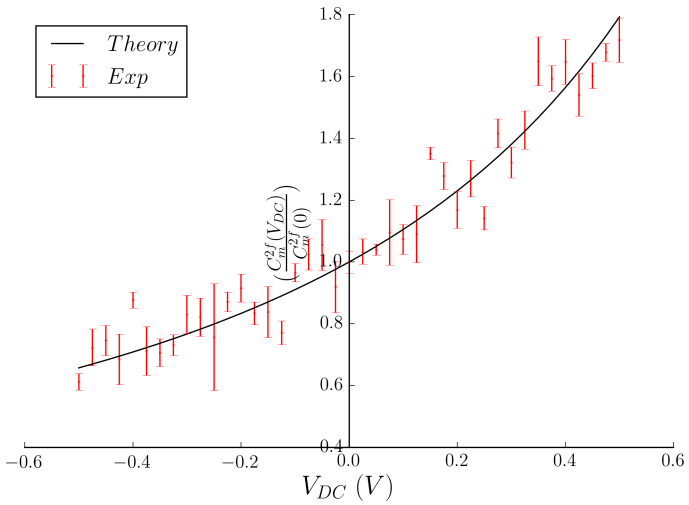


(b)

Figure 5.16: Comparison of experimental and theoretical trends for $C_J^{2f}$ and $C_m^{2f}$ (a) $C_J^{2f}$: trends of the experimental results agrees well with the theoretical predictions. For $V_{DC} > 0.2\,V$ a deviation is seen between the two. The reason for the deviation is the same as discussed for the $C_J^f$ case. The early occurrence of the deviation however is due to the $\frac{1}{\sqrt{\left(1-\frac{V_{DC}}{V_{bi}}\right)^3}}$ term in the $2f$ case. The denominator becomes larger for smaller $V_{DC}$ (b)$C_m^{2f}$: the trends of the experimental results agrees well with the theoretical predictions

## 5.4 Conclusion

In this chapter, the electro-mechanical coupling in the fabricated torsional resonator was investigated. The electro-mechanical coupling was defined as the interaction between the piezoelectric strain and the variation in the thickness of the depletion region. This interaction was investigated in the linear and non-linear regimes of the diode. These regimes were called $f$ and $2f$. The coupling between the two regimes is measured as a motional current. This motional current, through the BVD model, is related to the motional capacitance. Therefore, $C_m^f$ and $C_m^{2f}$ were derived. Additionally; $C_J^f$ and $C_J^{2f}$ were also derived. From the derived theoretical predictions it was found that for the $f$ case both $C_J^f$ and $C_m^f$ increases as inverse square root of the depletion thickness while for $2f$ case both $C_J^{2f}$ and $C_m^{2f}$ increases as the inverse $\frac{3}{2}$ of the depletion thickness. Good agreement was found between the theoretical predictions and measured data for the $f$ and $2f$ junction capacitance and $2f$ motional capacitance. The experimental motional capacitance at $f$ was found to have an opposite trend. A clear reason for this was not found.

# Chapter 6

# Opto-Electro-Mechanical Coupling

## 6.1 Introduction

In this chapter, the opto-electro-mechanical coupling is investigated using the fabricated photodiode torsional resonator. This coupling is defined as the interaction between the optical, mechanical and electrical domains in $GaAs$. The interaction results in:

1. the actuation of the torsional resonator as a result of the opto-piezo effect. That is to say the energy of the incident light is converted into a mechanical force which then causes the torsional resonator to deform

2. the tuning of the opto-piezo effect or opto-mechanical force as a function of the change in the depletion width

The opto-piezo effect belongs to a class of light-matter interaction defined as the photostrictive effect. This effect is a nonthermal effect and is discussed in the literature review section.

### 6.1.1 Literature Review

Light incident on a material can be reflected, transmitted or absorbed. The reflection and absorption of light can lead to a mechanical strain via the radiation pressure, photothermal and photostrictive effects.

#### 6.1.1.1 Radiation Pressure

The concept of the radiation pressure effect was first put forth by Johannes Kepler in 1619 to explain the observation that the tail of a comet always points away from the sun. This is seen in figure (6.1). Maxwell, in 1862, asserted that light has the property of momentum and thus must exert a pressure on an exposed surface[67]. This force is given as $F = \frac{P}{c}$ where $P$ is the power of the incident light and $c$ is the speed of light. Therefore the force is feeble. Due to this weakness of this force light is often used as a probe for measuring various phenomena of interest. For e.g. interferometric setups are used to measure the deflection of mechanical structures without effecting the deformation.

Figure 6.1: Hale-Bopp Comet. The primary tail of the comet is in white and the secondary is in blue. This picture was taken in 1997

Radiation pressure force has also been used to actuate mechanical resonators. In [68] radiation pressure force is used to actuate a microtoroid into resonance. The fourth mechanical mode of the toroid was driven with a $500\,\mu W$ tuneable laser. The resonance frequency of this mode is 54 MHz and its Q is 2100. These measurements were made in ambient pressure and temperature.

#### 6.1.1.2 Photothermal

Zalalutdinov et al [69] demonstrated the actuation of a polysilicon disc resonator using the photothermal effect. The disc has a radius of $20\,\mu m$ and a thickness of $200\,nm$ with a drum mode frequency of 8.6 MHz. The drum mode in the resonator is actuated using modulated laser having power of $30\mu W$. The authors engineered the disc such that the thermal relaxation time is roughly $0.7\,\mu s$ allowing them to thermally actuate the structure in the MHz frequency range. The resonator has a Q of 10,000. The vertical motion of the surface of the disc was measured interferometerically. Using this technique the resonance frequency is determined. They found: increasing the optical power by roughly 17 times results in a roughly 7 times increase in deflection. Similar to above this experiment was also performed at ambient pressures and temperatures.

#### 6.1.1.3 Photostrictive

The photostrictive effect is defined as light-matter interaction leading to nonthermal changes in size of the sample[70]. This effect is observed in ferroelectrics, polar and non-polar semiconductors and organic based materials.

In polar semiconductors the mechanism for photostriction is a combination of piezoelectricity and the PV effect, i.e. the photogenerated voltage causes a photoinduced strain in the material due to the piezoelectric effect. This is termed the opto-piezo effect.

In ferroelectrics, in addition to the opto-piezo effect, a comparable electrostrictive effect is also present[1]. The interplay between the two effects lead to hysteresis behavior [71].

In non-polar semiconductors wavelengths greater than the band gap develops EHPs throughout the surface at the thickness of the light penetration depth. The light generated

[1]Electrostriction is the deformation of a dielectric due to an applied field

| Compounds | | Light irradiance | Strain | Reference |
|---|---|---|---|---|
| Ferroelectrics | SbSI single crystals | Not Reported | -7.0e-3 | [74] |
| | $BiFeO_3$ | $2\ \frac{mJ}{cm^2}$ | 3.0e-3 | [75] |
| | $PbTiO_3$ | $4.8\ \frac{mJ}{cm^2}$ | 0.25 | [76] |
| Polar Semiconductors | CdS | Not Reported | 7.5e-3 | [77] |
| | GaAs(111) | Not Reported | 4.0e-5 | [78] |
| Non-Polar Semiconductors | Germanium crystal | Not Reported | 7.84e-8 | [79] |
| | Silicon | $30\ \frac{mJ}{cm^2}$ | -4.14e-5 | [80] |
| Organic Polymers | Poly-(4,4'-diamino azobenzene pyromellitimide) Films | Not Reported | -1.2 | [81] |
| | Poly(ethylacrylate) networks with azo-aromatic crosslinks | Not Reported | 0.25 | [73] |
| | Nematic Elastomers | Not Reported | 20 | [82] |

Table 6.1: Comparison of photostrictive properties of different compounds

electrons in the conduction band can contribute to the atomic bonding energy, whereas holes in the valence band can decrease the energy of covalent bonds. Because a volume of semiconductor can depend on the occupation of the electronic energy levels [72], the material can deform in the illuminated region.

In organic materials there are various reasons for photostriction[70] but the dominant ones are: light-induced chemical structure transitions[73] or different kinds or molecular reorientation (cooperative motion and alignment) under light irradiation[70].

Table (6.1) is a comparison of the reported strains for ferroelectrics, polar semiconductors, non-polar semiconductors and ogranic polymers. The largest strain occurs for organic polymers however their response times are usually in the range of seconds to minutes. Ferroelectrics and polar semiconductors have lower strains than organic polymers but their response time is generally greater than pico-seconds owing to large carrier mobilities.

#### 6.1.1.4 Opto-piezo effect in GaAs

As seen from table (6.1) Łagowski et al [78] demonstrated the opto-piezo effect in $GaAs$. To this date, theirs is the only published work demonstrating this effect in $GaAs$. The resonator used is a single clamped structure fabricated from [111] $GaAs$. The surface of the structure is unpassivated and hence results in a surface depletion. The absorption of light results in a surface voltage due to surface depletion. This surface voltage results in a strain due to the piezoelectric effect. The fundamental frequency of this structure is $104\,Hz$. The measurements of the deflection was verified optically.

### 6.1.2 Motivation

The motivation for this work is to experimentally and theoretically validate the opto-piezo effect in a $GaAs$ heterostructure. Most electronic and photonic devices in $GaAs$ are made from heterostructures. Therefore validating the opto-piezo effect in a heterostructure can lead to photonic devices having mechanical degrees of freedom. Using the mechanical degree of freedom novel photonic devices such as an optical transistor could be made which could pave the way for an optical computer.

### 6.1.3 Outline

The outline of this chapter is as follows: the heterostructure design presented in chapter (4) is discussed, in section(6.2), in the optical domain. The analytical predictions using the AC PV model is presented in section(6.3). Section(6.4) presents the experimental setup and the comparison between the experimental results and analytical predictions. In section(6.5), the opto-mechanical transduction coefficients for the radiation pressure, photothermal and opto-piezo effect are derived and compared. Section(6.6) concluded the chapter.

## 6.2 Design

### 6.2.1 Heterostructure Design

In section(4.2), the design of the photodiode heterostructure was discussed with respect to mechanical and electrical domains. As a result of this trends quantitative predictions could be made for the motional and junction capacitance values at $f$ and $2f$ for a varying DC bias. These trends were then compared to experimental results. Here, the discussion of the design is extended to include the optical domain. The motivation is to allow for predicting trends and making quantitative prediction at $f$ for a varying DC bias using the AC PV circuit model discussed in section(2.4.3.2). The prediction from the model are then compared to measurements.

The cartoon of the heterostructure is given in figure (4.4) and is used to explain the operation of the photodiode in the optical domain. The photodiode is designed as a GaAs solar cell. The layers grown and the thickness of each of the layers are chosen in order to maximize the absorption of light, the generation of EHPs and extraction of photogenerated current. To understand this better the absorption properties of GaAs and $In_{0.485}Ga_{0.515}P$ are first reviewed followed by an explanation of the opto-electrical design.

#### 6.2.1.1 Absorption Properties of $GaAs$ and $In_{0.485}Ga_{0.515}P$

The absorption properties of a material are defined by the absorption coefficient. This coefficient determines the depth of propagation into a material that light of a particular wavelength can penetrate before it is absorbed. Mathematically this is defined as[83]:

$$I = I_0 (1 - R) exp(-\alpha x)$$

where $I_0$ is the incident intensity, $R$ is the reflection at the incident face, $\alpha$ is the absorption coefficient, $x$ is the thickness of the material and $I$ is the intensity of light trans-

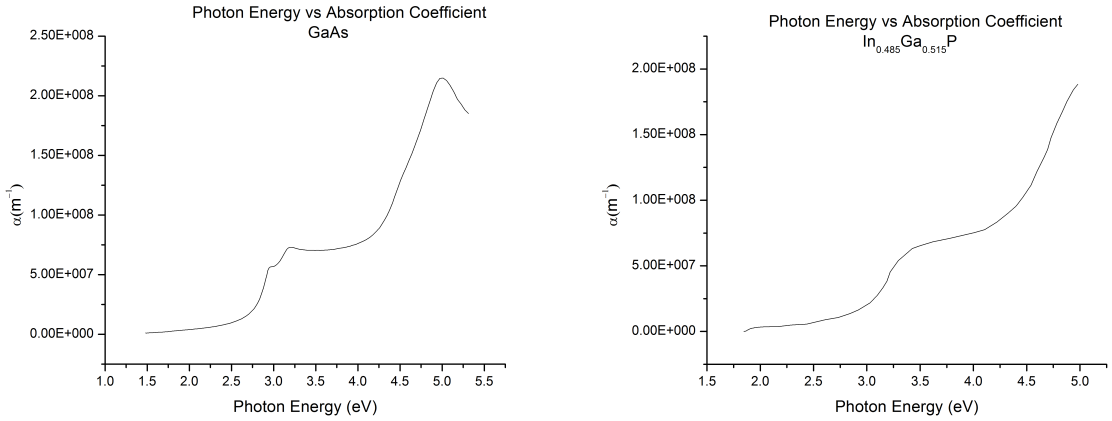


(a) (b)

Figure 6.2: Photon Energy vs Absorption Coefficient. *GaAs* data has been recreated from[7] and $In_{0.485}Ga_{0.515}P$[8]

mitted through the material. The absorption coefficient of *GaAs* as a function of photon energy is given in figure (6.2)(a). From this figure:

1. Photons having energies greater than 1.42 eV are absorbed. This is as expected since the band gap energy of GaAs is 1.42 eV[60]. This energy corresponds to a wavelength of 875 nm

2. The absorption coefficient increases with photon energy indicating that light of shorter wavelengths have decreasing probability of propagating into the material. For the bandedge wavelength, 875 nm, the absorption coefficient is approximately $1.0e6\,m^{-1}$. Therefore, for GaAs thickness of greater than $1.0\mu m$ 100% of the non-reflected light will be absorbed

Also plotted in Figure (6.2)(b) is the absorption coefficient of $In_{0.485}Ga_{0.515}P$. This curve is similar to GaAs. The difference is photons having energies greater than 1.905 eV are absorbed. This energy corresponds to the bandgap energy of $In_{0.485}Ga_{0.515}P$ and also corresponds to a wavelength of approximately 653 nm.

Given these absorption layers and the thicknesses of: (1) the GaAs pn junction, (2) $n^-$and $p^-In_{0.485}Ga_{0.515}P$ layers the probability of photogenerated carriers from $In_{0.485}Ga_{0.515}P$ can be ignored. The thicknesses of the respective layers are $1.5\mu m$, 25 and 50 nm; respectively.

#### 6.2.1.2 Opto-Electrical Design

As mentioned above the photodiode is designed as a *GaAs* solar cell. EHPs created within the pn junction or a diffusion length away from the junction will contribute to the photocurrent. The $In_{0.485}Ga_{0.515}P$ layers, as mentioned in section(4.2), are grown for surface

passivation and to create a back surface field (BSF). These both help in increasing the collection probability of optically generated EHPs. Surface passivation does this by reducing the number of dangling bonds at the surface while BSF introduces a barrier height such that minority carriers are repelled from the p and n contacts and collected at the their respective junctions.

The role of the BSF in the photodiode is better understood from the energy band diagram, figure(6.3). The x-axis in this figure is thickness of the heterostructure and the y-axis is energy. The fermi-level, conduction and valence bands are indicated by the blue, black and red lines respectively. In the x-axis 0 thickness refers to the top of the $n+\ GaAs$ layer in figure (4.4). The vertical lines in figure(6.3) roughly indicate the pn junction depleted region. As is seen from the figure at the $n^-$GaAs and $n^-In_{0.485}Ga_{0.515}P$ interface a barrier height is created for holes but not for electrons. This barrier height repels holes from propagating towards the n-contact while the electrons encounter a tunnel barrier and are successfully collected at the n-contact. At the $p^-In_{0.485}Ga_{0.515}P$ and $p^-$GaAs interface a barrier height is created for electrons, as intended, but a barrier height is also created for holes, as not intended. The barrier height for holes results in phenomena called hole pile-up[84]. Hole-pile up has the effect of reducing the extraction of holes and hence reducing the photogenerated current. This was experimentally observed by[84]. They also showed that hole pile-up can be reduced by increasing the applied electric field.

Using this opto-electrical design and the single diode AC PV model the electrical circuit is discussed next.

#### 6.2.1.3 Electrical Circuit

Figure (6.4) is the opto-piezo electrical circuit. This circuit is similar to the AC PV circuit given in figure (2.27)(a). Following the AC PV circuit trend described in chapter(2) figure (6.4) consists of three branches after the diode. The nomenclature for the current follows from section(2.4.3.2.1) while the nomenclature for the circuit elements follow from chapter 4. The numbers in the circuit elements are associated with the layers of the heterostructure as discussed in chapter 4. The components of this circuit are:

1. $i_{isc_1}$ and $I_{isc}$ are the AC photocurrent and DC short circuit photocurrent
2. $R_{sh,4}$ is the shunt resistance of the $pn$ junction and $Z_{j,4}$ is the respective BVD circuit, figure (2.12). This circuit accounts for the junction capacitance and the motional components
3. $R_{sh,2}$ and $R_{j,2}$ are the shunt and hole-pile up resistances associated with the depleted $p^-In_{0.485}Ga_{0.515}P$ layer. $R_{j,2}$ is chosen as the equivalent circuit element representing hole pile-up because hole pile-up results in reduction of current
4. $Z_{j,2}$ is the BVD circuit related to the depleted $p^-In_{0.485}Ga_{0.515}P$-$GaAs$ heterojunction
5. $R_s$ is the series resistance
6. $i_{D,3} = I_{D,3} + i_{d,3}$ is the total current comprised of the superposition of DC and AC current, respectively. This is the current measured at the load branch of the AC PV circuit

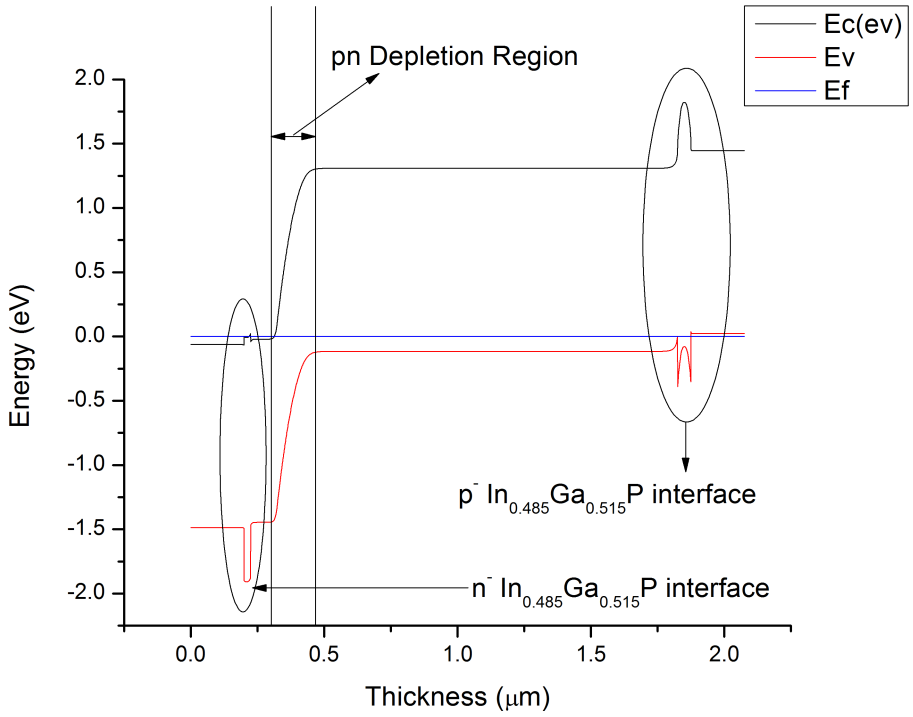


Figure 6.3: Heterostructure Band Diagram: The x-axis in this figure is thickness of the heterostructure and the y-axis is energy. The fermi-level, conduction and valence bands are indicated by the blue, black and red lines respectively. In the x-axis 0 thickness refers to the top of the $n+$ $GaAs$ layer in figure (4.4). The vertical lines in figure(6.3) roughly indicate the pn junction depleted region. As is seen from the figure at the $n^-$GaAs and $n^-In_{0.485}Ga_{0.515}P$ interface a barrier height is created for holes but not for electrons. At the $p^-In_{0.485}Ga_{0.515}P$ and $p^-$GaAs interface a barrier height is created for electrons and holes

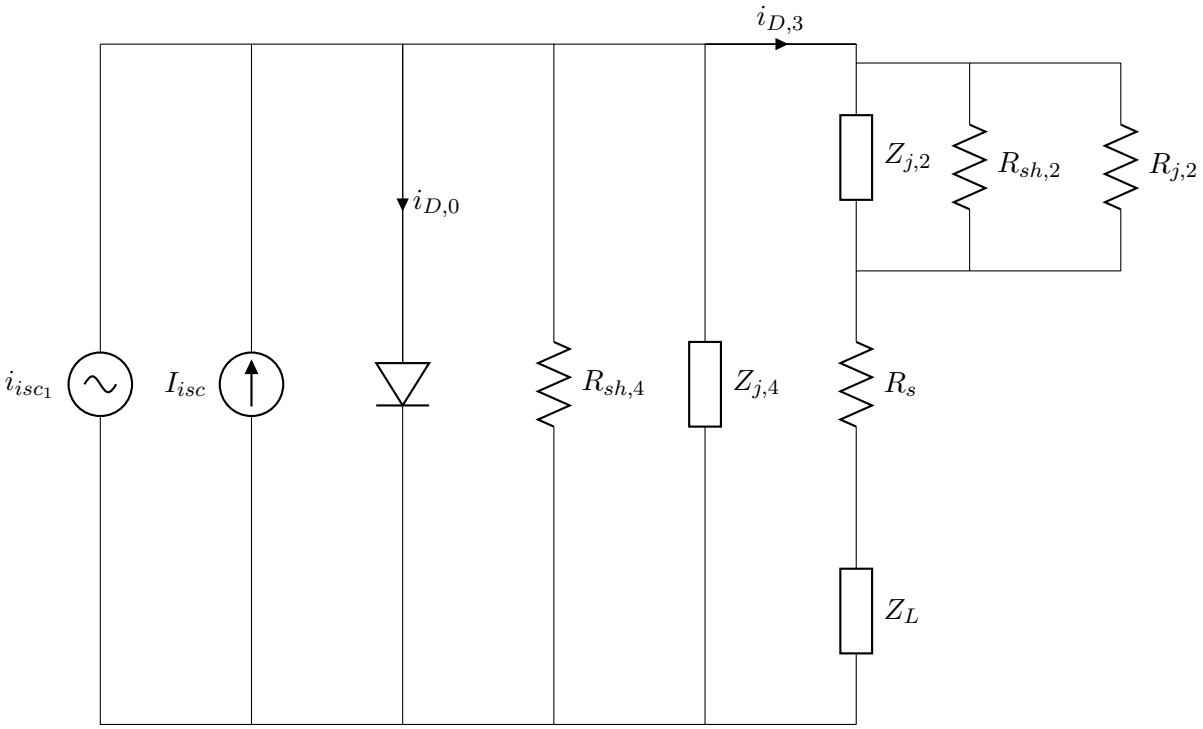


Figure 6.4: Equivalent circuit of Opto-Piezo Resonator. Here $i_{isc_1}$ and $I_{isc}$ are the AC photocurrent and DC short circuit photocurrent, $R_{sh,4}$ is the shunt resistance of the pn junction and $Z_{j,4}$ is the respective BVD circuit, figure (2.12), $R_{sh,2}$ and $R_{j,2}$ are the shunt and hole-pile up resistances associated with the depleted $p^{-}In_{0.485}Ga_{0.515}P$ layer, $Z_{j,2}$ is the BVD circuit related to the depleted $p^{-}In_{0.485}Ga_{0.515}P$-$GaAs$ heterojunction, $R_s$ is the series resistance and $i_{D,3} = I_{D,3} + i_{d,3}$ is the total current comprised of the superposition of DC and AC current, respectively. This is the current measured at the load branch of the AC PV circuit

The justification for this circuit is the photocurrent, $I_{isc_1}$ and $I_{isc}$ are generated from the pn junction while the resistance and impedance of the other layers represent a load to the pn junction or the photogeneration layer. Hence they are placed in the load or the third branch of the circuit. This circuit is similar to the AC PV resonator circuit figure (3.19) discussed in chapter 3. The difference between the two are in this circuit there are two BVD circuits instead of one and one of the BVD circuits is not in the load branch. The analytical predictions of this circuit is given in section (6.3).

Next; the advantages of the torsional design for demonstration of the opto-piezo effect is discussed.

### 6.2.2 Resonator Design

Most of the light incident on the photodiode will be absorbed for wavelengths greater than the band gap energy. Some of the absorbed light gets converted to heat leading to a photothermal effect which can cause a photothermal deformation. The resulting photothermal deformation

could result in an opto-piezo-thermal current. The torsional design negates the occurrence of such a current because the photothermal effect cannot drive the torsional mode. To elucidate: the torsion mode requires the expansion of one tine and the contraction of other. This antisymmetric driving cannot occur thermally because the expansion coefficient for the two tines are the same in both magnitude and direction. By heating or cooling the structure both the tines either expand or contract.

## 6.3 Analytical Predictions

The opto-piezo actuation is measured using $i_{d,3}$. Therefore analytical predictions are given for $i_{d,3}$. Following this, the predictions for the opto-electro-mechanical coupling will be presented. Predictions are made for both the ideal and non-ideal cases.

### 6.3.1 Opto-Piezo Actuation

The predicted current $i_{d,3}$ from the opto-piezo circuit, figure (6.4), is presented below. Here only the AC current is considered because this is the current measured at resonance. The predictions for the AC current are made using the AC PV equation (2.67):

$$i_{d,3} = \frac{i_{isc_1}}{\sqrt{(1+BR)^2 + (BX)^2}} \frac{Z_t}{Z_3}$$

where

$$B = \frac{\alpha I_{isc} exp\left(\alpha V\right)}{exp\left(\alpha V_{oc}\right)}$$

First the ideal case for measuring the opto-piezo current is presented. Following this the non-ideal cases are discussed.

#### 6.3.1.1 Ideal Case

In the ideal case the shunt and series resistances, the effects due to hole pile-up and $Z_{j,2}$ are all ignored. This is the ideal case because the resistances and $Z_{j,,2}$ are parasitic. The ideal opto-piezo circuit given in figure (6.5). Figure (6.6) is a plot of $i_{d,,3}$ for a range of capacitive loads . The x-axis in this plot is frequency and the y-axis is current. The plots are generated using the following values $I_{isc} = 55\,nA$, $I_{isc_1} = 1\,nA$, $V_{oc} = 1.33\,V$, $f_r = 76676\,Hz$, $Q = 10,000$, $C_{J,4} = 55\,pF$ and $C_{m,4} = 3.22\,fF$. The value for the currents were chosen from experimental data and the rest are determined either from simulations or from derived analytical expressions discussed in the previous chapters. A capacitive load is used for the calculations and measurements. This type of load is desired because it minimizes the effects due to RC time constant. There are two important observations from this figure:

1. The resonance and anti-resonance peaks are switched. The lowest current is at the resonance frequency while the highest current is at the anti-resonance frequency. This is expected because at resonance the impedance of the $Z_{j,4}$ branch is the lowest and hence most of the current flows through that branch. In anti-resonance the impedance

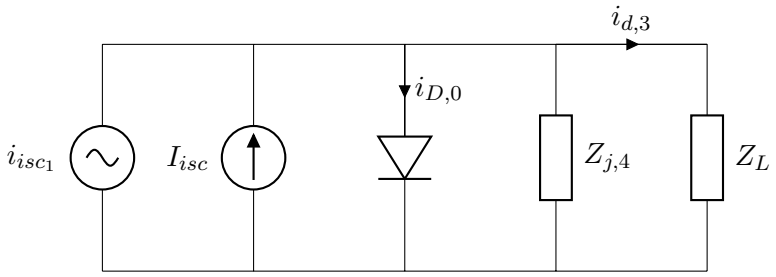


Figure 6.5: Ideal Opto-Piezo circuit. In this circuit the shunt and series resistances are ignored and the effects due to hole pile-up are also ignored

of the $Z_{j,4}$ branch is the highest and hence most of the current flows through the load branch

2. As $C_L$ increases or $Z_L$ decreases $i_{d,3}$ increases. This is as expected. However, to measure maximum current at resonance an optimal load impedance is required. This impedance is equivalent to $C_J$.For the case considered $C_L = C_J = 55\,pF$. This is the familiar impedance matching condition required in high frequency circuits. Figure (6.7) better elucidates the idea of impedance matching. This figure is similar to figure (6.6) except the background current resulting from the junction and load capacitances is subtracted from the current comprising the BVD and background impedances. As is seen from this figure, as the capacitance is increased from 10 to $55\,pF$ the current measured at resonance increases. Beyond $55\,pF$ the current again begins to decrease

#### 6.3.1.2 Non-Ideal Case

In the non-ideal case the shunts and series resistances, the resistance due to hole pile up and $Z_{j,2}$ cannot be ignored. Generally; having finite values for shunts, series and hole pile-up resistances reduces $i_{d,3}$. The effect of $Z_{j,2}$ however is a bit more complicated and is explored next.

In figures(6.8) (a) - (c) and figure(6.9) (a) - (c) $i_{d,3}$ and the phase are plotted. In these plots the x-axis is frequency. The plots are generated using the same values as used to generate figure (6.6). In these plots the shunts and series resistances are ignored. Figures (a) - (c) are plotted for $R_{j,2}$ having values of 1, 10 and $100\,k\Omega$ respectively. The following observations are made:

1. As $R_{j,,2}$ is increased the contribution of $Z_{j,2}$ to $i_{d,3}$ increases

2. For small values of $R_{j,2}$ the contribution form $Z_{j,2}$ can be ignored. This is as expected

3. In figures (b) and (c) as $C_{m,2}$ increases $i_{d,3}$ initially decreases till a cross-over point is reached where the contribution due to $Z_{j,2}$ becomes prevalent. In this case the current at resonance is larger than at anti-resonance. This is similar to what is observed for the optical driven QTF, figure(3.22)(a)

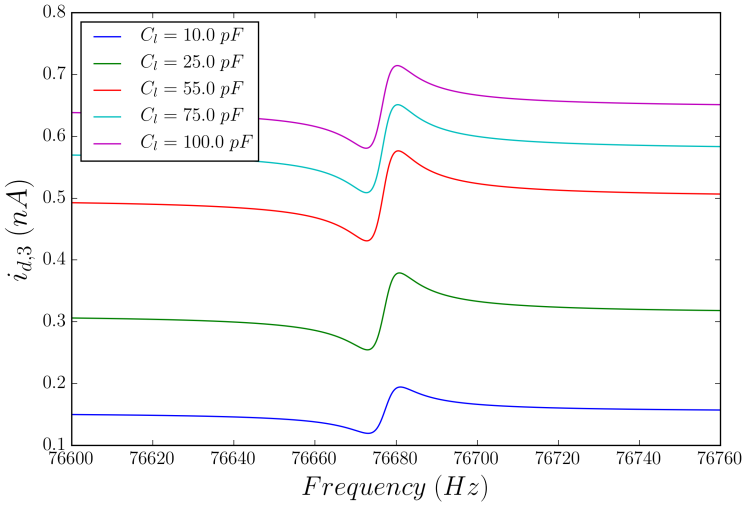


Figure 6.6: $i_{d,3}$ for the ideal circuit given in figure 6.5. The x-axis is frequency. $i_{d,3}$ is determined using equation (2.67) for the range of capacitive loads gives in the legend. The resonance and anti-resonance peaks are switched. The lowest current is at the resonance frequency while the highest current is at the anti-resonance frequency. This is expected because at resonance the impedance of the $Z_{j,4}$ branch is the lowest and hence most of the current flows through that branch. In anti-resonance the impedance of the $Z_{j,4}$ branch is the highest and hence most of the current flows through the load branch

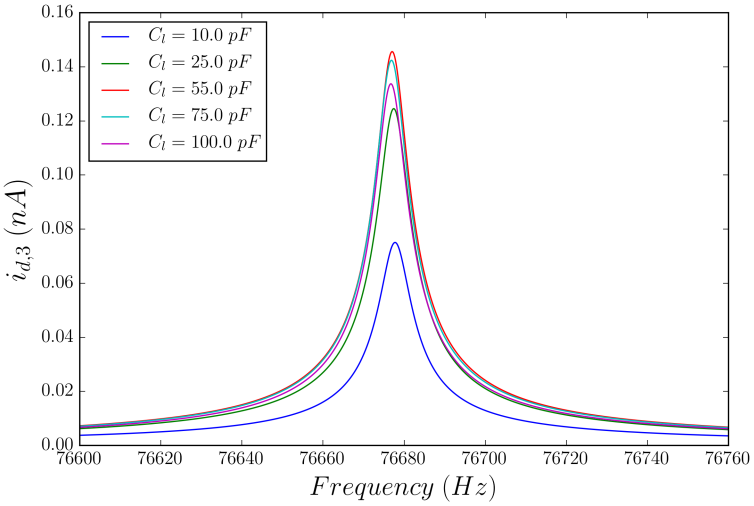


Figure 6.7: Background subtracted $i_{d,3}$. The current contributions to $i_{d,3}$ from the junction and load capacitances are subtracted from $i_{d,3}$. The remaining current is the motional current. This plot elucidates the idea of impedance matching. The largest current in the load branch occurs when $C_L = C_J = 55\,pF$

4. As $C_{m,2}$ increases a splitting is observed between the two resonances resulting in a symmetric and anti-symmetric modes. This is similar to the result of the double resonator case. This splitting is also observed in the phase plot

### 6.3.2 Opto-Electro-Mechanical Coupling

The opto-electro-mechanical coupling is demonstrated by changing the depletion width of the resonator and measuring $i_{d,3}$. The depletion width of the resonator is varied by applying a DC bias, $V_{DC}$. As discussed in the previous chapter as the DC bias is increased the depletion width decreases resulting in a large motional current. In the optical case an additional effect needs to be considered. As the depletion width decreases the photogenerated current also decreases. This decrease in the photogenerated current will result in a decrease in the motional current. The photogenerated current changes as [85]: $i\left(x\right) = i_o\left(1 - exp\left(-\alpha x\right)\right)$ where $i$ is current, $i_0$ is the current measured at reverse bias, $x$ is the depletion width and $\alpha$ is the absorption coefficient. Therefore $i_{d,3}$ is:

$$i_{d,3} = \frac{i_{isc_1}\left(1 - exp\left(-\alpha x\right)\right)}{\sqrt{\left(1+BR\right)^2 + \left(BX\right)^2}} \frac{Z_t}{Z_3} \tag{6.1}$$

#### 6.3.2.1 Ideal Case

Following the same conditions as discussed in the ideal case for the opto-piezo effect, figure (6.10) is a plot of $\frac{i_{d,3}}{i_{isc_1}}$ . The x-axis in this plot is $V_{DC}$. In the ideal case it is assumed that 100% of the applied $V_{DC}$ is dropped across $Z_{j,4}$. As is seen, and expected, as the DC bias is increased $\frac{i_{d,3}}{i_{isc_1}}$ decreases. Therefore, unlike the electro-mechanical case, the favorable operating point for the opto-piezo actuation is in the reverse bias regime. The reverse bias regime for an illuminated photodiode is called the photoconductive regime while the forward bias is called the photovoltaic regime. This tuning of the opto-piezo actuation is unique to III-V materials.

#### 6.3.2.2 Non-Ideal Case

For the non-ideal case, finite resistance for $R_{j,2}$ is considered thereby adding contribution from $Z_{j,2}$. The finite impedances decreases the amount of voltage that is dropped across $Z_{j,4}$ therefore requiring a higher bias voltage to achieve the depletion thickness as in the ideal case. Figure (6.11) is a plot of $\frac{i_{d,3}}{i_{isc_1}}$. The x-axis is the same as above. Again $\frac{i_{d,3}}{i_{isc_1}}$ decreases as the bias goes from the photoconductive to the photovoltaic regime. The difference here is $\frac{i_{d,3}}{i_{isc_1}}$ is smaller than for the ideal case for the same applied $V_{DC}$

## 6.4 Experimental Setup and Results

Similar to previous chapters frequency sweeping experiments are conducted. Here these experiments are conducted in order to validate the theoretical predictions for $i_{d,3}$.

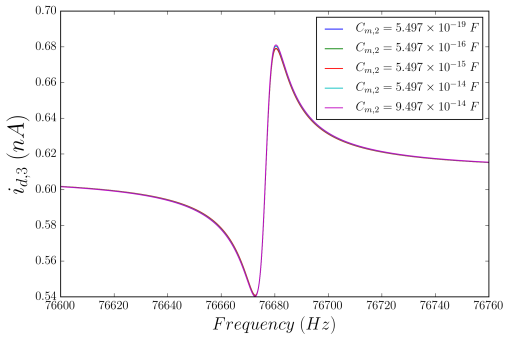


(a)

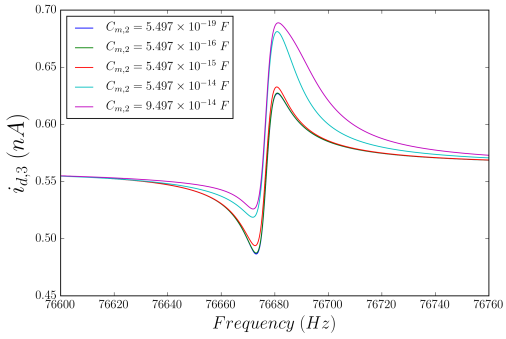


(b)

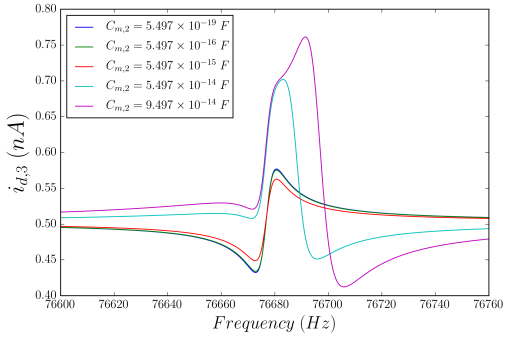


(c)

Figure 6.8: $i_{d,3}$ for the non-ideal case. $i_{d,3}$ is determined using equation (2.67) and the circuit in figure (6.4). In these plots the x-axis is frequency. (a), (b) and (c) are generated for $R_{j,2}$ having values of 1, 10 and 100 $k\Omega$ respectively. The following can be observed: as $R_{j,,2}$ is increased from (a) to (c) the contribution of $Z_{j,2}$ to $i_{d,3}$ increases. In (a) the contribution of $Z_{j,2}$ to $i_{d,3}$ can be ignored.In figures (b) and (c) as $C_{m,2}$ increases $i_{d,3}$ initially decreases till a cross-over point is reached where the contribution due to $Z_{j,2}$ becomes prevalent. In this case the current at resonance is larger than at anti-resonance. This is similar to what is observed for the optical driven QTF, figure(3.22)(a). In (c) as $C_{m,2}$ increases a splitting is observed between the two resonances resulting in a symmetric and anti-symmetric modes

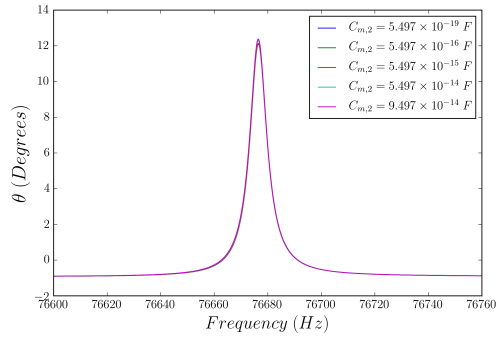


(a)

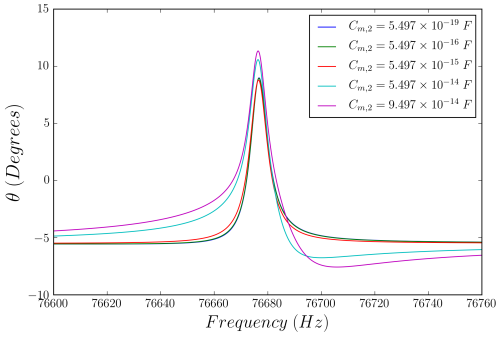


(b)

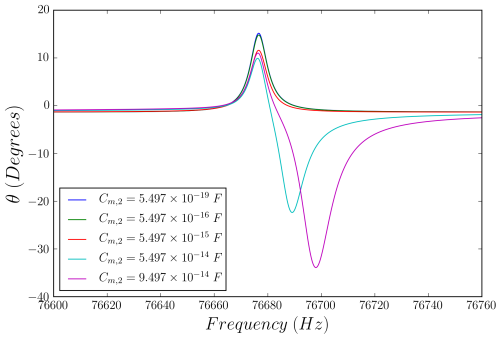


(c)

Figure 6.9: $\theta$ for the non-ideal case. In these plots the x-axis is frequency. (a), (b) and (c) are generated for $R_{j,2}$ having values of 1, 10 and 100 $k\Omega$ respectively. The following can be observed: as $R_{j,,2}$ is increased from (a) to (c) the contribution of $Z_{j,2}$ to $\theta$ increases. In (a) the contribution of $Z_{j,2}$ to $\theta$ can be ignored. In figures (b) and (c) as $C_{m,2}$ increases a cross-over point is reached where the contribution due to $Z_{j,2}$ becomes prevalent. In this case a second peak in (b) and (c) is seen

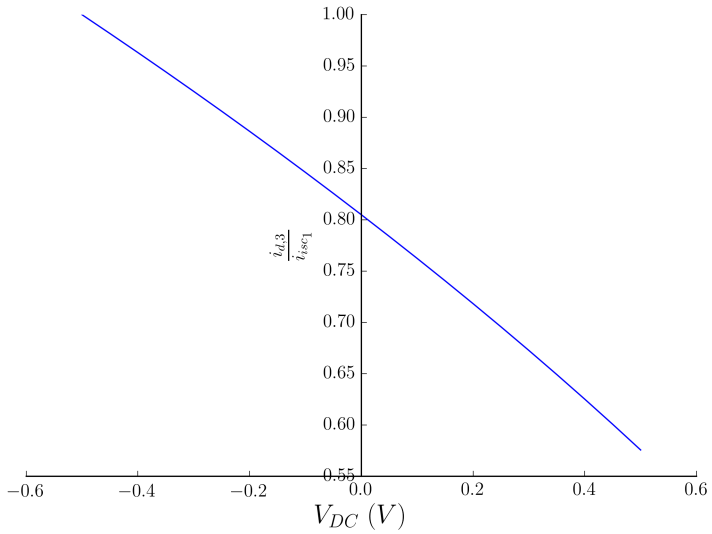


Figure 6.10: $\frac{i_{d,3}}{i_{isc_1}}$ vs $V_{DC}$. $i_{isc_1}$is defined as the current at $V_{DC} = -0.5\,V$. This plot was generated using equation (6.1). As $V_{DC}$ increases the normalized current, $\frac{i_{d,3}}{i_{isc_1}}$ decreases

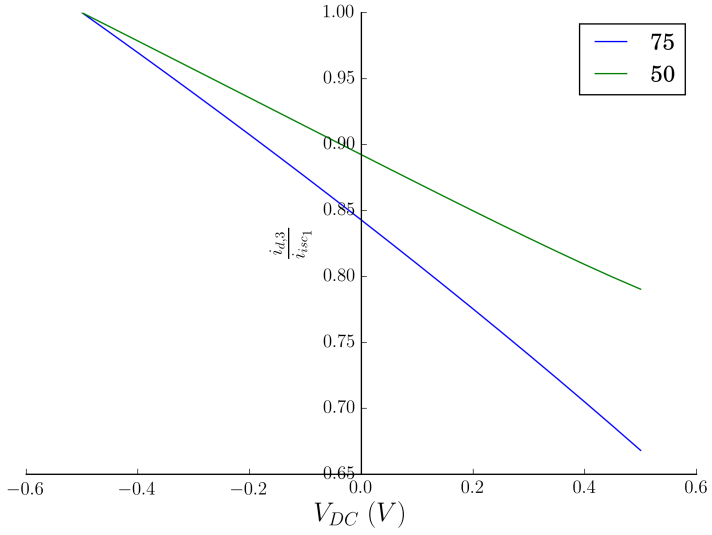


Figure 6.11: $\frac{i_{d,3}}{i_{isc_1}}$ vs $V_{DC}$. $i_{isc_1}$is defined as the current at $V_{DC} = -0.5\,V$. This plot was generated using equation (6.1). As $V_{DC}$ increases the normalized current, $\frac{i_{d,3}}{i_{isc_1}}$ decreases. Finite $R_{j,2}$ is considered such that the voltage drop across $Z_{j,4}$ decreases. In these plots a voltage drop of 75% and 50% is considered. For a 50% voltage drop the normalized current is higher than for a 75% voltage drop

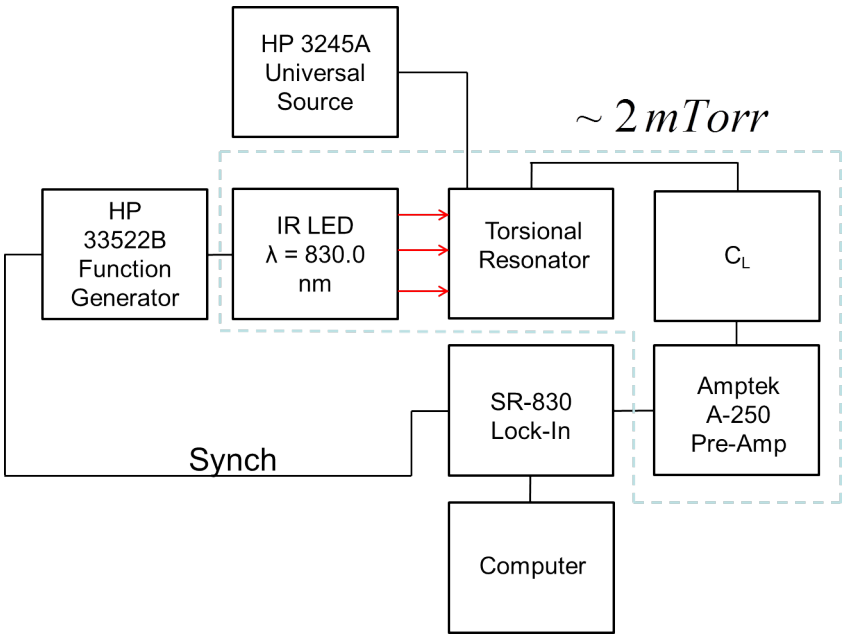


Figure 6.12: Block diagram of the experimental setup used to measure opto-piezo actuation. The HP-3352B supplies the DC and AC voltage required to bias and modulate the LED. This light is incident on the torsional resonator. The DC bias for the torsional resonator is supplied by the HP-3245A. $C_L$ is the load capacitor serving the purpose of a DC block and an AC load for the torsional resonator. The current, $i_{d,3}$, generated is amplified by the Amptek A-250. The output of the A-250 is connected to the SR-830 lock-in amplifier. The lock-in is synchronized to the HP-3352B. The data from the lock-in is collected on a computer. The arrows in the diagram indicate light is being emitted from the LED onto the torsional resonator. The dotted blue lines indicate the components held in vacuum. A vacuum pressure of $\sim 2\,mTorr$ is achieved

### 6.4.1 Experimental Setup

The experimental setup is similar to the previous chapter with the difference being the drive source is replaced with an IR LED, model TSHG5510-ND, emitting light at a peak wavelength of $\lambda = 830.0\,nm$. As discussed above this wavelength is absorbed by $GaAs$ and not by $In_{0.485}Ga_{0.515}P$. Figure (6.12) is the block diagram of the experimental setup. The dotted blue line indicates the components placed in vacuum. A vacuum pressure of $\geq 2\,mTorr$ is achieved in the chamber. A brief description of the setup is as follows: the Keysight 33522B function generator supplies both the DC bias and the AC voltage required for modulating the LED. The bias voltage for the device is supplied by the HP-3245A. The current, $i_{d,3}$ is amplified and converted into a voltage by the Amptek A-250. The amplified voltage is measured using the SR-830. The SR-830 is locked to the synchronization signal of the Keysight 33522B. The modulation optical power is kept to below 25% of the total optical power. Hence justifying the use of equation (2.67) which was derived based on the small signal approximation.

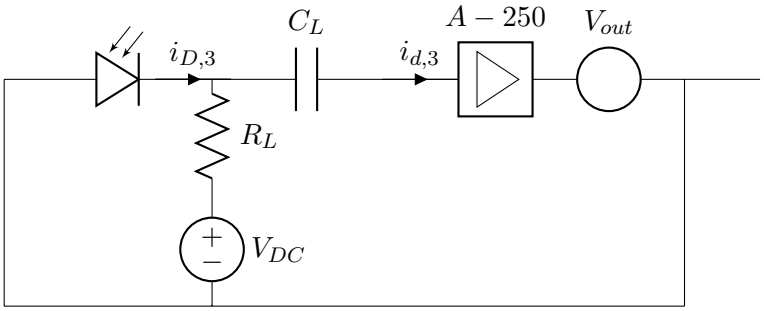


Figure 6.13: Opto-Piezo resonator circuit used for measuring $i_{d,3}$. The opto-piezo resonator is represented by the photo-diode and the amplifier circuit is represented by the box labeled A-250. The amplifier circuit was discussed in chapter 4. The bias voltage to photodiode is supplied via $R_L$

### 6.4.2 Electrical Circuit

Figure (6.13) is the electrical circuit used for measuring $i_{d,3}$. In this circuit the opto-piezo resonator is represented by the photo-diode and the amplifier circuit is represented by the box labeled A-250. The amplifier circuit was discussed in the previous chapter. The photodiode and the amplifier are separated by the load capacitance, $C_L$. $C_L$ serves two purposes:

1. DC block from the Amptek
2. AC load for the device

The bias voltage to photodiode is supplied via $R_L$. The value for $R_L$is $1.0\,M\Omega$ and is chosen such that

1. its resistance is much larger than the impedance of $C_L$. This assures little to no loss of signal
2. its resistance is lower than the DC resistance of the photodiode. This ensures that most of the applied voltage drops across the photodiode

The values for $C_L$ chosen are 220, 140 and $38\,pF$. For the frequency of operation, i.e. $76.6 - 76.8\,KHz$, the impedance is between $10 - 50\,k\Omega$.

### 6.4.3 IR LED Power

Figure (6.14)(a) is a plot of the measured DC LED power, $P_{opt}$. The x-axis is the LED bias voltage and the y-axis is the LED power measured using the 818-BB-20[51] diode and the 1815-C Newport Power Meter. The uncertainty in the measured power, $\Delta P_{opt}$, is calculated from the table given in the operator's manual. As reported in the manual the maximum error is 1.7%. The LED is placed 0.5 cm away from the photodiode. Figure (6.14)(b) is a plot of $P_{opt}$ incident on the opto-piezo resonator. This values is determined determined mathematically, i.e. taking the ratio of the absorption area of the opto-piezo resonator to the area of the 818-BB-20. The illuminated area of the 818-BB-20 is approximately $1.3 \times 10^{-7}\,m^2$ while the illuminated area of the opto-piezo resonator is approximately $2.1 \times 10^{-8}\,m^2$. The opto-piezo resonator is also placed 0.5 cm away from the LED.

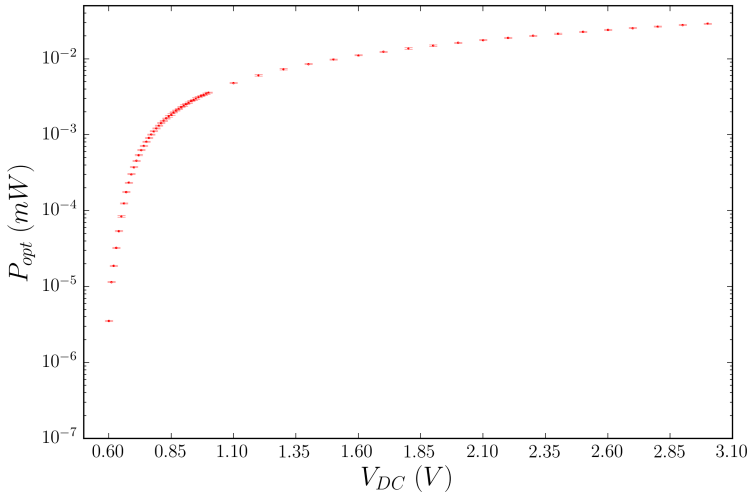


(a)

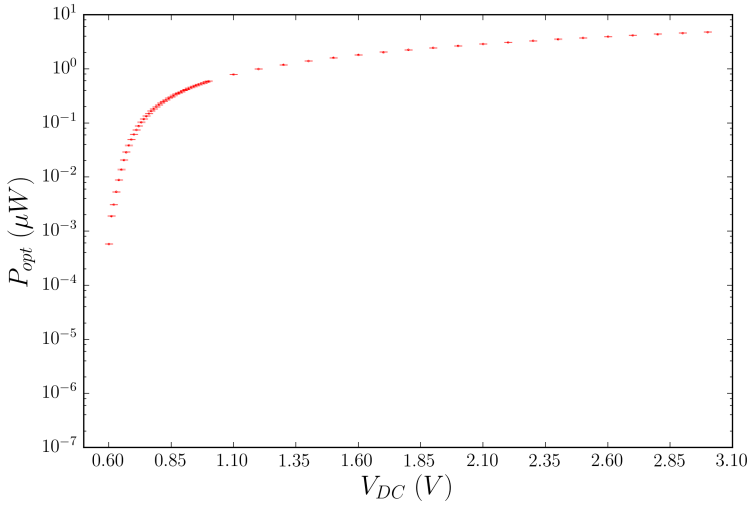


(b)

Figure 6.14: LED Power: (a) LED illuminated power measured using 818-BB-20, (b) LED illuminated power incident on the opto-piezo device. The values in this plot are determined mathematically, i.e. taking the ratio of the absorption area of the opto-piezo resonator to the area of the 818-BB-20. The illuminated area of the 818-BB-20 is approximately $1.3 \times 10^{-7}\, m^2$ while the illuminated area of the opto-piezo resonator is approximately $2.1 \times 10^{-8}\, m^2$. The 818-BB-20 and opto-piezo device are placed 0.5 cm away from the LED

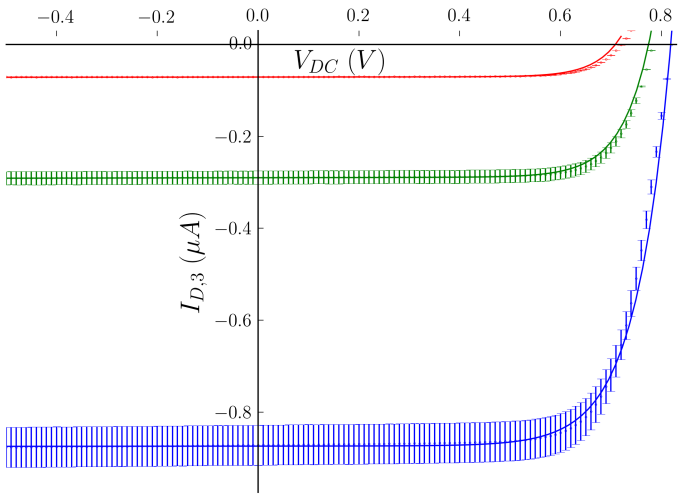


Figure 6.15: Diode IV Curves for an incident powers of 0.3, 1.61 and 4.84 $\mu W$. As the optical power increases the optically generated current also increases

### 6.4.4 Photodiode DC response

The IV curves for the photodiode are plotted in figure (6.15) for incident optical powers of 0.3, 1.61 and 4.84 $\mu W$. The x-axis is voltage and the y-axis is current. The solid lines in this figure are the fit to the curves using the non-ideal single diode DC PV equation (2.49). The measured and fit values are given in tables (6.2) and (6.3). In this equation $\alpha = \frac{q}{\eta kT}$ where $\eta$ is the diode ideality factor. An ideality factor is introduced to account for recombination of EHPs not occurring in the bulk. This was discussed in section (2.4.3).

In table (6.3) the fitted values for the series resistance is a 100,000 times greater than the expected value. The expected value for the series resistance is approximately 0.14 $\Omega$. This value is determined using the resistance equation $R = \frac{L}{wt\sigma}$ where $\sigma$ is the conductivity of the $n^+$ and $p^+$ GaAs. The conductivity of $n^+$ GaAs is 800 $\frac{1}{\Omega - cm}$ and for $p^+$ GaAs is 320 $\frac{1}{\Omega - cm}$. These values are calculated using the following equation $\sigma_n = qn\mu_n$for the $n^+$ GaAs and $\sigma_p = qp\mu_p$ for $p^+$ GaAs. In these equations $q$ is charge, $n$ and $p$ are the doping concentration, $5.0 \times 10^{18}\, cm^{-3}$ and $2.0 \times 10^{19}\, cm^{-3}$ respectively, and $\mu_n$ and $\mu_p$ are the electron and hole mobilities. These values are 1000 and 100 $\frac{cm^2}{Vs}$[5]. Therefore the major contribution to the resistance is the $p^+$-doped layer. Assuming the series resistance is low the large value could be attributed to either $R_{sh,2}$ or $R_{j,2}$ .

From these curves the DC resistance of the diode for a DC bias between $-0.5$ and $0.5\, V$ ranges from about $10\, M\Omega$ for an incident optical power of $0.3\, \mu W$ to about $0.5\, M\Omega$ for an incident optical power of $4.8\, \mu W$. Therefore for the circuit discussed above the incident optical power is kept between $0.3 - 1.6\, \mu W$ to ensure that most of the applied bias appears across the diode.

| $P_{opt}$ $(\mu W)$ | $\Delta P_{opt}$ $(nW)$ | $I_{isc}$ $\left(\times 10^{-7} A\right)$ | $\Delta I_{isc}$ $\left(\times 10^{-9} A\right)$ | $V_{oc}$ $(V)$ |
|---|---|---|---|---|
| 0.304 | 5.174 | 0.707 | 3.640 | 0.705 |
| 1.614 | 27.44 | 2.900 | 15.49 | 0.780 |
| 4.787 | 81.34 | 8.723 | 42.62 | 0.820 |

Table 6.2: Measured $I_{isc}$ and $V_{oc}$ for the respective incident powers. $\Delta P_{opt}$ and $\Delta I_{isc}$ are the measured uncertainties in $P_{opt}$ and $I_{isc}$. $\Delta V_{oc}$ is assumed to be small and hence ignored

| $P_{opt}$ $(nW)$ | $R_{sh}$ $(G\Omega)$ | $\Delta R_{sh}$ $\left(\times 10^{8}\Omega\right)$ | $R_s$ $(k\Omega)$ | $\Delta R_s$ $(k\Omega)$ | $\eta$ | $\Delta\eta$ $\left(\times 10^{-2}\right)$ |
|---|---|---|---|---|---|---|
| 0.304 | 1 | 2.029 | 19.00 | 1.759 | 1.933 | 2.935 |
| 1.614 | 1 | 3.121 | 17.852 | 7.523 | 2.110 | 5.370 |
| 4.787 | 1 | 2.851 | 13.978 | 7.946 | 2.642 | 18.332 |

Table 6.3: Values for $R_{sh}$, $R_s$ and $\eta$ for the respective incident optical powers. These values are determined by fitting equation (2.49) to measured $I_{D,3}$. $\Delta R_{sh}$, $\Delta R_s$ and $\Delta\eta$ are the errors in the fit

### 6.4.5 AC Noise

Figure (6.16) is a plot of the measured AC current noise, $i_{d,3}$, using the experimental setup. The x-axis is frequency and the y-axis is the current noise. The range of the plotted frequency is the same as the range chosen for measuring resonance. The noise measurements are made in vacuum, in the dark and in the absence of any external optical or electrical excitation. The noise voltage from the amplifier is measured using the lock-in. The current noise is determined by applying the amplifier's transfer function to the measured data. As is seen from the figure, the noise floor across the chosen range of frequencies is approximately $0.175\,\frac{pA}{\sqrt{Hz}}$. In the experiment the time constant of the filter on the lock-in amplifier is chosen to be 1.0 sec. Therefore the current noise is $0.175\,pA$

### 6.4.6 Resonance Measurements

Figure (6.17) (a) is a plot of the measured AC current $i_{d,3}$ for an incident $P_{opt}$ and $p_{opt}$ of $304\,nW$ and $21\,nW$. $p_{opt}$ is a representation for the AC optical power. This data corresponds to a circuit having $C_L$ of $222\,pF$, $R_L$ of $1\,M\Omega$ and for a zero DC bias. In this figure the x-axis is frequency. The measurements agree with expectation from theory, i.e. the lowest measured current occurs at resonance while the highest measured current occurs at anti-resonance. The Q of the resonator is approximately 6000. Figure (6.17) (b) is a plot of the measured phase, $\theta$. The measurements, again, agree with the expectation for theory. The fit values are $C_{J,2} = 55\,pF$, $R_{sh,2} = 19.0\,k\Omega$, $C_{J,4} = 155\,pF$, $R_{sh,4} = 1.0\,G\Omega$, $C_{m,2} = 1.24fF$, $C_{m,4} = 0.89\,fF$, $Q = 5922.5$ and resonance frequency of $f_r = 76677.5\,Hz$.

### 6.4.7 Impedance Matching

Figure (6.18) is a plot of the motional current for $C_L$ equivalent to 222, 140 and $38\,pF$. The x-axis is frequency and the y-axis is the motional current. The motional current is determined by subtracting the background $i_{d,3}$ current from $i_{d,3}$. The total $i_{d,3}$ is a superposition of

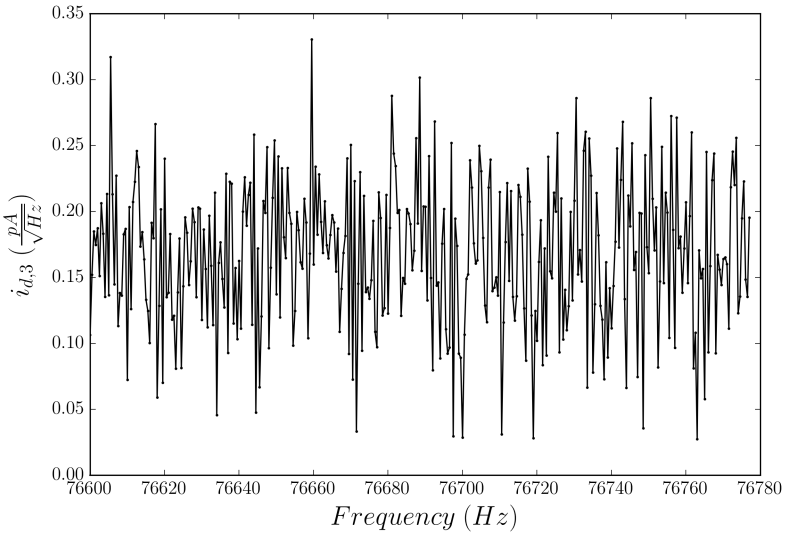


Figure 6.16: $i_{d,3}$ measured noise. The solid line is drawn as a guide to the eye

motional and background currents. This background $i_{d,3}$ current results from non-motional impedances. The background current is measured out of vacuum under the exact same incident DC and AC optical powers. As is seen from the figure the maximum resonance or motional current occurs for a load of 222 $pF$ . The variation in the motional current at resonance is attributed to thermal drifts.

### 6.4.8 Linear Response

Figure (6.19) is a plot of the normalized $i_{d,3}$ as $p_{opt}$ is increased. The x-axis is $p_{opt}$ and the y-axis is $i_{d,3}$ normalized to the $i_{d,3}$ measured for $p_{opt} = 2\,nW$. According to equation (2.67) $i_{d,3}$ should increase linearly with an increase in $i_{isc_1}$. $i_{isc_1}$ increases linearly with $p_{opt}$ therefore $i_{d,3}$ increases linearly with $p_{opt}$. This is demonstrated in the figure, i.e. as $p_{opt}$ is increased by an order of magnitude the normalized $i_{d,3}$ also increases by an order of magnitude. A theoretical prediction of the normalized $i_{d,3}$ is also plotted.

### 6.4.9 Opto-Electro-Mechanical Coupling

Figure (6.20) is a plot of $\frac{i_{d,3}(V_{DC})}{i_{d,3}(-0.5)}$ as the opto-piezo resonator is driven from reverse to forward bias, i.e. from the photoconductive to the photovoltaic quadrant. The measurement is made for an incident $P_{opt}$ and $p_{opt}$ of $304\,nW$ and $21\,nW$. The x-axis is DC bias, $V_{DC}$, which ranges from $-0.5$ to $0.5\,V$. $i_{d,3}\,(V_{DC})$ is the motional current measured at resonance as the bias is swept. The motional current is determined using the same methodology described in the impedance matching section. Figure (6.21) is a plot of the subtracted $i_{d,3}\,(V_{DC})$ for a $V_{DC}$ of $-0.5$, 0.0 and $0.5\,V$. Here the x-axis is frequency. As is seen from this plot and figure (6.20) as $V_{DC}$ increases from reverse to forward bias the normalized current decreases. This is the expected response as was discussed in the analytical section above. The solid line in

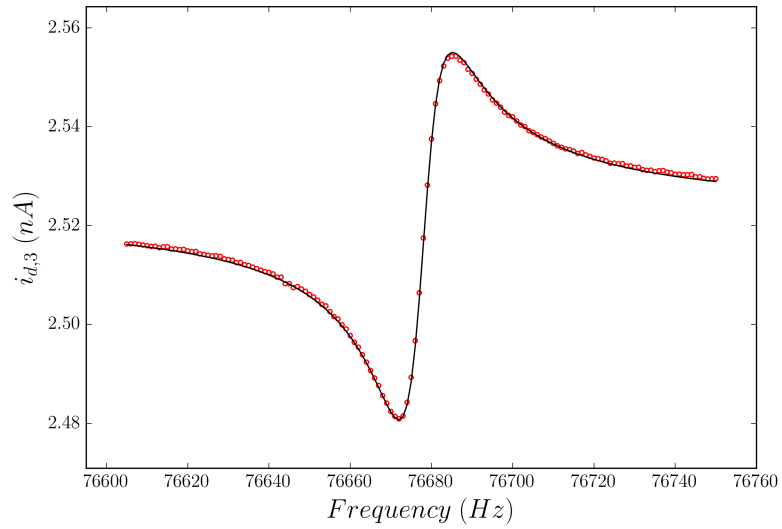


(a)

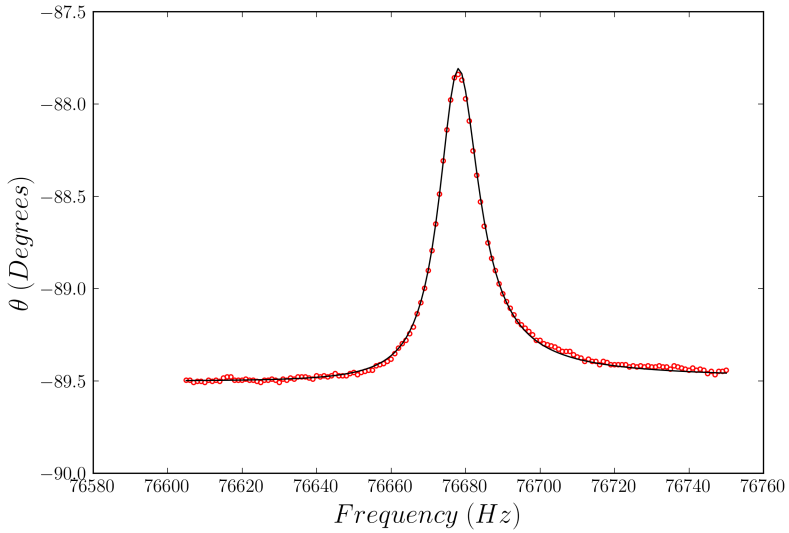


(b)

Figure 6.17: Optically driven torsional resonator for $P_{opt} = 304\,nW$ and $p_{opt} = 21\,nW$(a) $i_{d,3}\,vs\,Frequency$ The theoretical prediction is made using equation (2.67) and the circuit in figure (6.4) (b) $\vartheta\,vs\,frequency$ The theoretical prediction is made determined by calculating the arctan of the ratio of the imaginary and real part of $i_{d,3}$. In general for both good agreement is seen between the theoretical predictions and the measured response

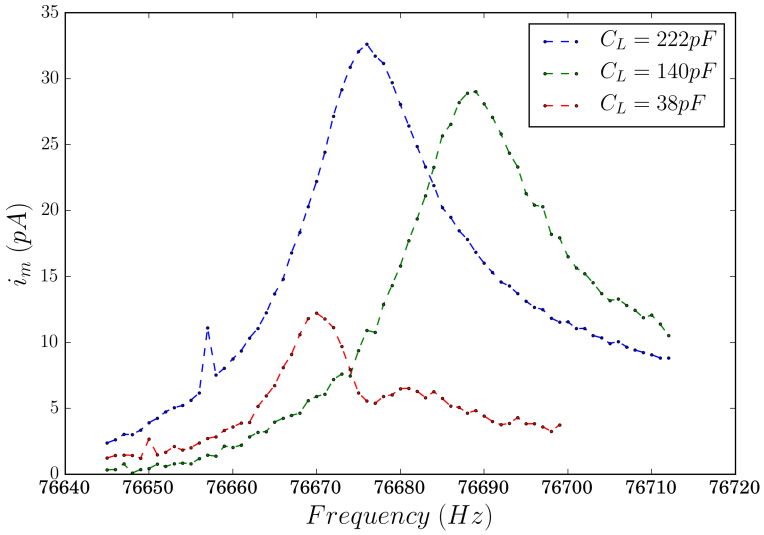


Figure 6.18: Optimal $C_L$ for impedance matching. The measured motional current is plotted for a $C_L$ of 222, 140 and 38 $pF$. As is seen from the figure the maximum resonance or motional current occurs for a load of 222 $pF$ . The motional current is determined by subtracting the background $i_{d,3}$ current from the total $i_{d,3}$. The total $i_{d,3}$ is a superposition of motional and background currents. The variation in the motional current at resonance is attributed to thermal drifts. The dotted line is drawn as a guide to the eye.

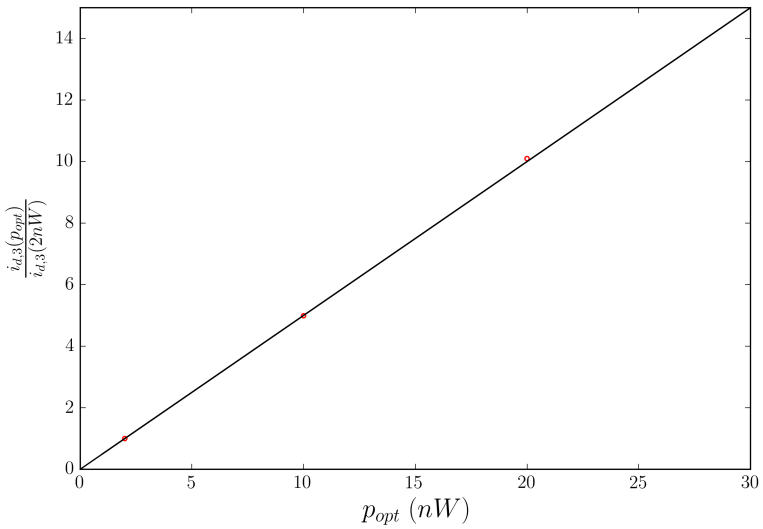


Figure 6.19: Normalized $i_{d,3}$ vs $p_{opt}$. Here $i_{d,3}$ is normalized to the value of $i_{d,3}$ at 2 $nW$. According to equation (2.67) $i_{d,3}$ should increase linearly with an increase in $i_{isc_1}$. $i_{isc_1}$ increases linearly with $p_{opt}$ therefore $i_{d,3}$ increases linearly with $p_{opt}$. This linear increase with $p_{opt}$ is seen. The theoretical predicted line is generated using equation (2.67)

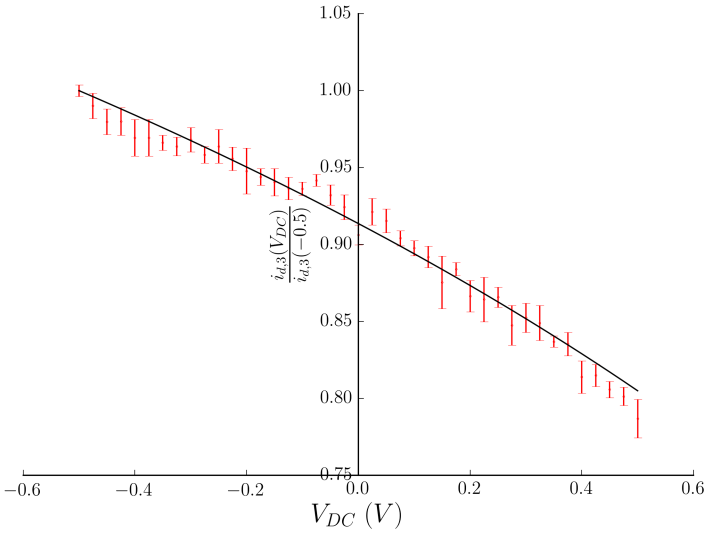


Figure 6.20: $\frac{i_{d,3}(V_{DC})}{i_{d,3}(-0.5)}$ vs $V_{DC}$ for $C_L = 222\,pF$. The measurement is made for an incident $P_{opt}$ and $p_{opt}$ of $304\,nW$ and $21\,nW$. $i_{d,3}$ is normalized to the value of $i_{d,3}$ for a $V_{DC} = -0.5\,V$. The theoretical line is also plotted. The prediction of $i_{d,3}$ using equation (2.67) is also normalized to the value of $i_{d,3}$ for a $V_{DC} = -0.5\,V$. Good agreement is seen between the experimental data and the predicted results. The variation in the data is attributed to thermal drifts. Each of the dots are an average of 5 measurement and the error bars are a result of this average.

this figure is the normalized theoretical prediction using the AC PV equation. The two are in agreement. To make the predictions: the motional and junction capacitance values chosen are the same as discussed in the chapter(5). The values for $R_{sh,4}$, $I_{isc}$ and $V_{oc}$ are taken from tables (6.2) and (6.3). The value for $R_{j,2}$ (hole-pile up resistance) is assumed to be $R_s$ (series resistance) from table (6.3). Two things are assumed in this assumption: (1) The calculated value of $R_s$, discussed in the photodiode DC response section, is the real experimental value and (2) $R_{sh,2}$ is approximately the same as $R_{sh,4}$. The latter assumption is justified because if the value of $R_{sh,2}$ was small then the piezoelectric contribution from the $In_{0.485}Ga_{0.515}P$ would not have to be taken into consideration. Using the same procedure discussed above figure (6.22) is $\frac{i_{d,3}(V_{DC})}{i_{d,3}(-0.5)}$ for $C_L = 144\,pF$ under same DC and AC incident optical powers and DC sweep. The variations in the experimental results are attributed to thermal drifts.

## 6.5 Opto-Mechanical Coupling Coefficient

The opto-mechanical coupling coefficient, $\kappa^2$, is defined as the ratio of mechanical energy or power to total energy or power. The inspiration for this definition follows from the Carnot cycle which provides an upper limit on the efficiency any engine can achieve during the conversion of heat into work. Below $\kappa^2$ is derived for the photothermal, radiation pressure and the opto-piezo effect. These coefficients are then compared. The geometry chosen for

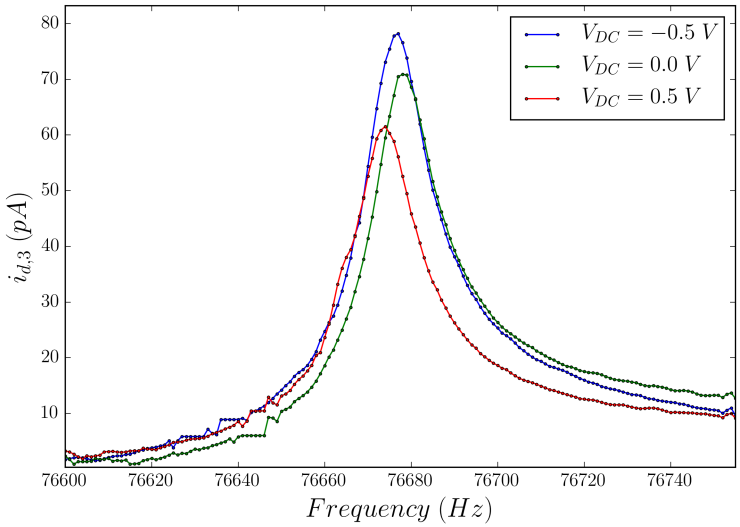


Figure 6.21: Background subtracted $i_{d,3}$ for a $V_{DC}$ of $-0.5$, 0.0 and $0.5\,V$. As is seen from the plot and figure (6.20) as $V_{DC}$ increases from reverse to forward bias the normalized current decreases. The dotted line is drawn as a guide to the eye

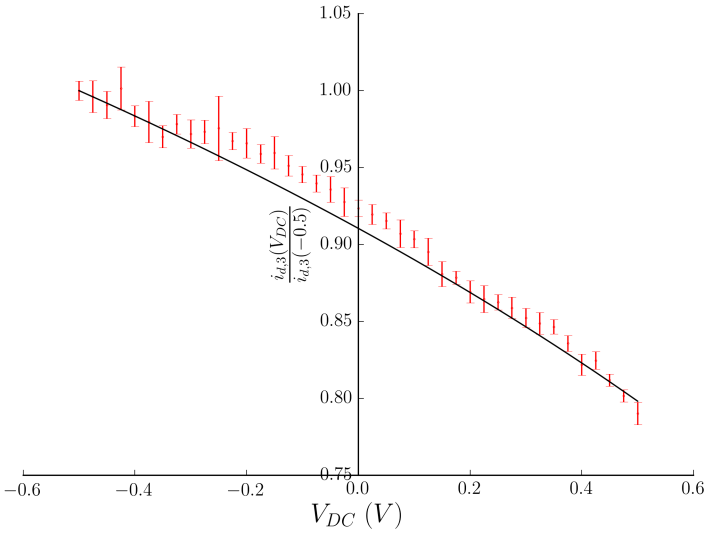


Figure 6.22: $\frac{i_{d,3}(V_{DC})}{i_{d,3}(-0.5)}$ vs $V_{DC}$ for $C_L = 144\,pF$. The measurement is made for an incident $P_{opt}$ and $p_{opt}$ of $304\,nW$ and $21\,nW$. $i_{d,3}$ is normalized to the value of $i_{d,3}$ for a $V_{DC} = -0.5\,V$. The theoretical line is also plotted. The prediction of $i_{d,3}$ using equation (2.67) is also normalized to the value of $i_{d,3}$ for a $V_{DC} = -0.5\,V$. Good agreement is seen between the experimental data and the predicted results. The variation in the data is attributed to thermal drifts. Each of the dots are an average of 5 measurement and the error bars are a result of this average.

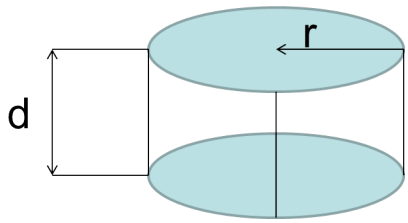


Figure 6.23: Circular disk with an radius $r$ and a thickness $d$. This resonator vibrates contracts and expands parallel to the thickness direction

the analysis, as illustrated in figure (6.23), is a circular disk having radius, $r$, and a thickness, $d$. The mode considered is the thickness mode of vibration. The resonance frequency for this mode is given in equation(6.2) where $v$ is the sound velocity of the material. The mode and geometrical structure are considered for ease of derivation and comparison.

$$f_r = \frac{v}{2d} \tag{6.2}$$

### 6.5.1 Photothermal

The photothermal opto-mechanical coupling coefficient, $\kappa_{pt}^2$, is mathematically defined as:

$$\kappa_{pt}^2 = \frac{E_{mech}}{E_{mech} + E_{heat}}$$

which is the ratio of the mechanical energy to the total energy stored in the disk. $E_{mech}$ is the mechanical work resulting from the deflection of the structure while $E_{heat}$ is the stored thermal energy. Conventionally $E_{heat}$ is written as $Q$ but $E_{heat}$ is adopted to avoid confusion with the quality factor, $Q$, of the mechanical resonator. The physics for the total energy stored is: absorption of light results in heating of the material and this heat is stored either as $E_{heat}$ or $E_{mech}$. This heating results in a temperature change, $\Delta T$. Therefore there is a relationship between $\Delta T$ and the incident optical power. Here an expression for $\Delta T$ is not derived. Instead $\Delta T$ is simulated using FEM software for various incident optical intensities. The details of the result will be presented in section (6.5.3). $\Delta T$ however can be written as:

$$\Delta T = P_0 f\left(k, c_p, \alpha_{abs}, \rho\right) exp\left(jwt\right)$$

where $\Delta T$ is linear with optical power, $P_0$, and is a function of the absorption coefficient, $\alpha_{abs}$, heat capacity $c_p$, thermal conductivity, $k$ and density of the material, $\rho$. The $exp\left(jwt\right)$ terms represents the modulation of optical power. $E_{heat}$ is mathematically defined as[62]:

$$E_{heat} = \rho\left(Ad\right) c_p \Delta T$$

where $A$ is the area of the resonator. The $exp\left(jwt\right)$ term corresponds to the frequency of modulation of the incident optical power. $E_{mech}$ is mathematically defined as:

$$E_{mech} = \frac{1}{2}kx^2 = \frac{1}{2\rho\left(Ad\right)}w_r^2\left[YA\alpha_{exp}\Delta T\frac{\left(w_r^2 - w^2 - 2j\gamma w\right)}{\left(w_r^2 - w^2\right)^2 + \left(2\gamma w\right)^2}\right]^2$$

where $k$ is the spring constant and defined as $k = w_r^2\rho\left(Ad\right)$. $x$ is the mechanical deformation of the resonator. For a harmonic oscillator it is defined as [38]:

$$x = \frac{F_{pt}}{\rho\left(Ad\right)}\frac{\left(w_r^2 - w^2 - 2j\gamma w\right)}{\left(w_r^2 - w^2\right)^2 + \left(2\gamma w\right)^2}$$

where $w_r$, $w$ and $F_{pt}$ are the resonance frequency, applied frequency and the photothermal force. $F_{pt}$ is [62]:

$$F_{pt} = \alpha_{exp}\Delta TYA$$

Here $\alpha_{exp}$ is the thermal expansion coefficient. Substituting the above the photothermal opto-mechanical coupling coefficient is:

$$\kappa_{pt}^2 = \frac{E_{mech}}{E_{mech} + E_{heat}} = \frac{\frac{1}{2(\rho Ad)}\left(YA\alpha_{exp}w_r\Delta T\right)^2\left[\frac{(\zeta - j\xi)}{\zeta^2+\xi^2}\right]^2 exp\left(2jwt\right)}{\frac{1}{2(\rho Ad)}\left(YA\alpha_{exp}w_r\Delta T\right)^2\left[\frac{(\zeta - j\xi)}{\zeta^2+\xi^2}\right]^2 exp\left(2jwt\right) + \left(\rho Ad\right)c_p\Delta T exp\left(jwt\right)}$$

where $\Gamma = \frac{1}{2(\rho Ad)}\left(YA\alpha_{exp}w_r\Delta T\right)^2$, $\zeta = w_r^2 - w^2$ and $\xi = 2\gamma w$. As is seen, $\kappa_{pt}^2$ has both real and complex parts. Therefore taking the complex conjugate and the root mean square $\kappa_{pt}^2$ is:

$$\kappa_{pt}^2 = \frac{\frac{1}{2(\rho Ad)}\left(YA\alpha_{exp}w_rP_0f\left(k, c_p, \alpha_{abs}, \rho\right)\right)^2}{\zeta^2 + \xi^2\sqrt{\frac{\left(\frac{1}{2(\rho Ad)}\left(YA\alpha_{exp}w_rP_0f(k,c_p,\alpha_{abs},\rho)\right)^2\right)^2}{\left(\zeta^2+\xi^2\right)^2} + \left[\left(\rho Ad\right)c_pP_0f\left(k, c_p, \alpha_{abs}, \rho\right)\right]^2}}$$

Simplifying this expression yields:

$$\kappa_{pt}^2 = \frac{P_0A\left(Y\alpha_{exp}w_rf\left(k, c_p, \alpha_{abs}, \rho\right)\right)^2}{2\left(\rho d\right)\left(\zeta^2 + \xi^2\right)\sqrt{\frac{P_0^2\left(\left(YA\alpha_{exp}w_rf(k,c_p,\alpha_{abs},\rho)\right)^2\right)^2}{4(\rho Ad)^2\left(\zeta^2+\xi^2\right)^2} + \left[\left(\rho Ad\right)c_pf\left(k, c_p, \alpha_{abs}, \rho\right)\right]^2}} \tag{6.3}$$

### 6.5.2 Radiation Pressure

The radiation pressure opto-mechanical coupling coefficient is mathematically defined as:

$$\kappa_{rp}^2 = \frac{P_{mech}}{P_{opt}}$$

which is the ratio of the mechanical power to the total power. $P_{mech}$ is the mechanical power resulting from the deflection of the structure while $P_{opt}$ is the optical power incident on the structure. $P_{opt}$ is:

$$P_{opt} = P_0 exp\left(jwt\right)$$

$P_{mech}$ is defined as:

$$P_{mech} = F_{rp}\dot{x} = \frac{w}{m}\left(\frac{P_0}{c}\right)^2 exp\left(j2wt\right)\left(\frac{j\left(w_r^2 - w^2\right) + 2\gamma w}{\left(w_r^2 - w^2\right)^2 + \left(2\gamma w\right)^2}\right)$$

where $F_{rp}$ is the radiation pressure force and $\dot{x}$ is the velocity of the mechanical structure. $F_{rp}$ for light reflected from a resonator is [67]:

$$F_{rp} = \frac{2P_{opt}}{c} = \frac{2P_0 exp\left(jwt\right)}{c}$$

The velocity of the mechanical resonator, $\dot{x}$, is the derivative of the position, $x$. $x$ is defined as:

$$x = \frac{F_{rp}}{\rho\left(Ad\right)}\frac{\left(w_r^2 - w^2 - 2j\gamma w\right)}{\left(w_r^2 - w^2\right)^2 + \left(2\gamma w\right)^2} = \frac{1}{\rho\left(Ad\right)}\left(\frac{2P_0 exp\left(jwt\right)}{c}\right)\frac{\left(w_r^2 - w^2 - 2j\gamma w\right)}{\left(w_r^2 - w^2\right)^2 + \left(2\gamma w\right)^2}$$

therefore $\dot{x}$ is:

$$\frac{dx}{dt} = \dot{x}\left(t\right) = jw\frac{F_0}{m}\frac{\left(w_r^2 - w^2 - 2j\gamma w\right)}{\left(w_r^2 - w^2\right)^2 + \left(2\gamma w\right)^2}exp\left(jwt\right) = jw\frac{2P_0}{mc}\frac{\left(w_r^2 - w^2 - 2j\gamma w\right)}{\left(w_r^2 - w^2\right)^2 + \left(2\gamma w\right)^2}exp\left(jwt\right)$$

After simplifying the radiation pressure opto-mechanical coupling coefficient is:

$$\kappa_{rp}^2 = \frac{P_{mech}}{P_{opt}} = \frac{2w}{\rho Ad}P_0\left(\frac{1}{c}\right)^2 exp\left(jwt\right)\left(\frac{j\left(w_r^2 - w^2\right) + 2\gamma w}{\left(w_r^2 - w^2\right)^2 + \left(2\gamma w\right)^2}\right)$$

Similar to the previous section $\kappa_{rp}^2$ has both real and imaginary parts. Therefore taking the complex conjugate and the root mean square $\kappa_{rp}^2$ is:

$$\kappa_{rp}^2 = \frac{2wP_0}{\left(\rho Ad\right)c^2\sqrt{\zeta^2 + \xi^2}} \tag{6.4}$$

#### 6.5.2.1 Opto-Piezo Effect

The opto-piezo opto-mechanical coupling coefficient is mathematically defined as:

$$\kappa_{opz}^2 = \frac{E_{mech}}{E_{mech} + E_{elec}}$$

where $E_{mech}$ and $E_{elec}$ are the stored mechanical and electrical energies. The physics for the total energy stored is: the incident optical power is converted into a voltage due to the photovoltaic effect. This voltage is dropped across the piezoelectric capacitance and the junction capacitance resulting in mechanical and electrical stored energies, i.e. $E_{mech}$ and $E_{elec}$. The equations for $E_{elec}$ and $E_{mech}$ are:

$$E_{elec} = \frac{1}{2} C_J V^2 = \frac{\epsilon_r \epsilon_0}{2} \frac{A}{d} V^2$$

$$E_{mech} = \frac{1}{2} k x^2 = \frac{1}{2} \frac{YA}{d} V^2 \left( w_r^2 d_{33} \frac{w_r^2 - w^2 - 2j\gamma w}{\left(w_r^2 - w^2\right)^2 + \left(2\gamma w\right)^2} \right)^2$$

where $V$ and $d_{33}$ are the photovoltage and piezoelectric coefficient. The photovoltage is given as $V = V_0 exp\left(jwt\right)$.

$x$ is defined as:

$$x = \frac{F_{opz}}{\rho\left(Ad\right)} \frac{\left(w_r^2 - w^2 - 2j\gamma w\right)}{\left(w_r^2 - w^2\right)^2 + \left(2\gamma w\right)^2}$$

and using the piezoelectric effect $F_{opz}$ is written as:

$$F_{opz} = k d_{33} V = \frac{YA}{d} d_{33} V$$

Therefore the opto-piezo opto-mechanical coupling coefficient is:

$$\kappa_{opz}^2 = \frac{E_{mech}}{E_{mech} + E_{elec}} = \frac{\frac{1}{2}\frac{YA}{d} V^2 \left( w_r^2 d_{33} \frac{w_r^2 - w^2 - 2j\gamma w}{\left(w_r^2 - w^2\right)^2 + \left(2\gamma w\right)^2} \right)^2}{\frac{1}{2}\frac{YA}{d} V^2 \left( w_r^2 d_{33} \frac{w_r^2 - w^2 - 2j\gamma w}{\left(w_r^2 - w^2\right)^2 + \left(2\gamma w\right)^2} \right)^2 + \frac{\epsilon_r \epsilon_0}{2} \frac{A}{d} V^2}$$

Taking the magnitude and simplifying, $\kappa_{opz}^2$ is:

$$\kappa_{opz}^2 = \frac{Y\left(w_r^2 d_{33}\right)^2}{\left(\zeta^2 + \xi^2\right) \sqrt{\left( \frac{Y\left(w_r^2 d_{33}\right)^2}{\left(\zeta^2 + \xi^2\right)} \right)^2 + \left(\epsilon_r \epsilon_0\right)^2}} \tag{6.5}$$

### 6.5.3 Comparison of the three opto-mechanical coefficients

The three opto-mechanical coefficients are summarized in table (6.4) where $\zeta = w_r^2 - w^2$ and $\xi = 2\gamma w$. As is seen from this table $\kappa_{opz}^2$ is independent of optical power while the three opto-mechanical coupling coefficients depend on the dimensions of the resonator. Figures (6.24) (a) and (b) are a plot of $\kappa_x^2 \, vs \, P_0$ at $f = 10\,Hz$ for a disk having the same area but with thicknesses, $d$, of $400\,\mu m$ and $400\,nm$ respectively. The subscript $x$ in $\kappa_x^2$ represents the three cases. Table (6.5) are the values of the constants used to generate the plots. These material constants are for $GaAs$. As mentioned above $\Delta T$ is generated from FEM simulations. In the simulations the back surface of the disk is held fixed at $0\,k$ while the incident power is absorbed at the front surface. The following are seen from the plots:

1. $\kappa_{opz}^2$ unlike $\kappa_{pt}^2$ and $\kappa_{rp}^2$ does not change with power
2. $\kappa_{rp}^2$ is the smallest of the three. In these figures the $\kappa_{rp}^2$ is restricted from going above $\frac{v}{c}$ where $v$ is the sound velocity of $GaAs$. As seen from equation (6.4) $\kappa_{rp}^2$ can increase beyond 1, which is not a physical result. Hence the $\frac{v}{c}$ restriction is chosen because physically the upper limit to the motion of the resonator is its sound velocity. For $GaAs$ $\kappa_{rp}^2$ is restricted to $1.6 \times 10^{-5}$

| Optical Actuation Type | Opto-Mechanical Coupling Coefficient Equation |
|---|---|
| Photothermal, $\kappa^2_{pt}$ | $\frac{P_0 A(Y\alpha_{exp} w_r f(k,c_p,\alpha_{abs},\rho))^2}{2(\rho d)(\zeta^2+\xi^2)\sqrt{\frac{P_0^2\left((YA\alpha_{exp} w_r f(k,c_p,\alpha_{abs},\rho))^2\right)^2}{4(\rho Ad)^2\left(\zeta^2+\xi^2\right)^2}+[(\rho Ad)c_p f(k,c_p,\alpha_{abs},\rho)]^2}}$ |
| Radiation Pressure, $\kappa^2_{rp}$ | $\frac{2wP_0}{(\rho Ad)c^2\sqrt{\zeta^2+\xi^2}}$ |
| Opto-Piezo, $\kappa^2_{opz}$ | $\frac{Y\left(w_r^2 d_{33}\right)^2}{(\zeta^2+\xi^2)\sqrt{\left(\frac{Y\left(w_r^2 d_{33}\right)^2}{\left(\zeta^2+\xi^2\right)}\right)^2+(\epsilon_r\epsilon_0)^2}}$ |

Table 6.4: Opto-Mechanical coupling coefficient for the photothermal, radiation pressure and the opto-piezo cases

3. $\kappa^2_{opz}$ has the same value for the two thickness of the resonator

4. $\kappa^2_{opz}$ generally is several orders of magnitude larger than $\kappa^2_{pt}$ and $\kappa^2_{rp}$. The power required for $\kappa^2_{pt}$ to become equivalent to $\kappa^2_{opz}$ is approximately $3\,MW$ for a disk having a thickness of $400\,nm$, figure (6.24)(b), while for a disk having a thickness of $400\,\mu m$, figure (6.24)(a), the power required is approximately $3\,KW$. This reduction in power with an increase in thickness is expected because thicker materials have a larger thermal gradient and hence a larger force. Unlike $\kappa^2_{pt}$ $\kappa^2_{rp}$ does not become equivalent to $\kappa^2_{opz}$. The powers required for $\kappa^2_{rp}$ to reach the $\frac{v}{c}$ condition are approximately $1\times10^{21}\,W$ and $1.0\times10^{24}\,W$ for the disk having thicknesses of $400\,\mu m$ and $400\,nm$ respectively. To compare the immenseness of the power required for parity with $\kappa^2_{opz}$ and to achieve $\frac{v}{c}$ the powers used for fiber optical telecommunications ranges between sub $mW$ to several 100s of $mW$ while the power required to ablate $1\,cm^2$ of material requires approximately $10.0\times10^{12}\,W$

Figures (6.25) (a), (b) and (c) are a plot of $\kappa^2_x\,vs\,f$ for $P_0 = 1\,mW$ and $Q = 1.0$ for a disk having the same area but with thicknesses, $d$, of $400\,\mu m$ and $400\,nm$ respectively. This plot shows a frequency roll off for the three cases. The following is observed:

1. As the thicknesses decrease the frequency roll off increases. This is expected because as the thickness decreases $w_r$ increases

2. Both $\kappa^2_{rd}$ and $\kappa^2_{opz}$ have similar frequency roll off while $\kappa^2_{pt}$ frequency roll off is approximately a thousand times lower. This earlier roll-off is due to the thermal time constant which can be approximated as $\tau \sim \frac{\rho V c_p}{k}$ where $V$ and $k$ are the volume and thermal conductivity of the material. Therefore as seen from this approximation and the plots the roll off frequency increases approximately linearly as the volume decreases.

3. $\kappa^2_{rd}$ increases linearly with $w$

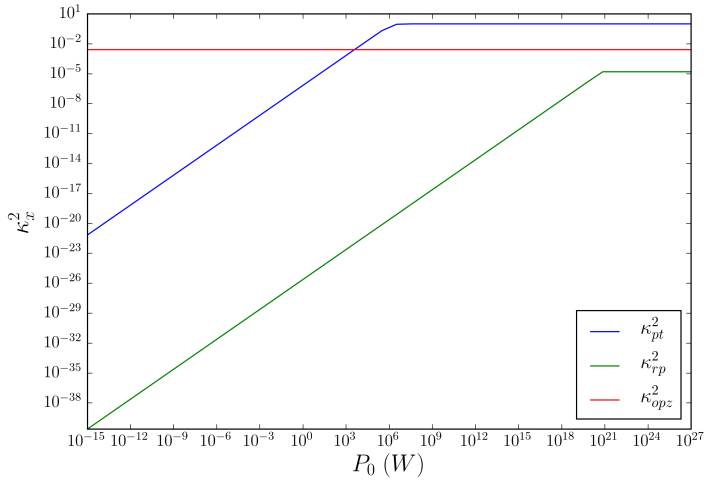


(a)

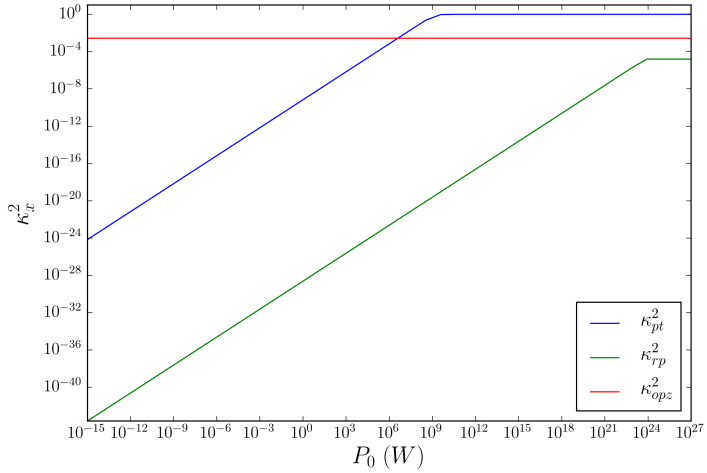


(b)

Figure 6.24: $\kappa_x^2 \, vs \, P_0$ at $f = 10\,Hz$ for a disk having the same area and thickness of (a) $d = 400\,\mu m$ and (b) $d = 400\,nm$. The subscript $x$ in $\kappa_x^2$ represents the three cases - photothermal, radiation pressure and opto-piezo. Equations (6.3), (6.4) and (6.5) are used for generating the three cases. In general, $\kappa_{opz}^2$ is several orders of magnitude larger than $\kappa_{pt}^2$ and $\kappa_{rp}^2$. The power required for $\kappa_{pt}^2$ to become equivalent to $\kappa_{opz}^2$ is approximately $3\,MW$ for a disk having a thickness of $400\,nm$, figure (6.24)(b), while for a disk having a thickness of $400\,\mu m$, figure (6.24)(a), the power required is approximately $3\,KW$. This reduction in power with an increase in thickness is expected because thicker materials have a larger thermal gradient and hence a larger force. $\kappa_{rp}^2$ does not become equivalent to $\kappa_{opz}^2$. At most $\kappa_{rp}^2$ can be equivalent to $\frac{v}{c}$. This is because because physically the upper limit to the motion of the resonator is its sound velocity. The powers required for $\kappa_{rp}^2$ to reach the $\frac{v}{c}$ condition are approximately $1 \times 10^{21}\,W$ and $1.0 \times 10^{24}\,W$ for the disk having thicknesses of $400\,\mu m$ and $400\,nm$ respectively

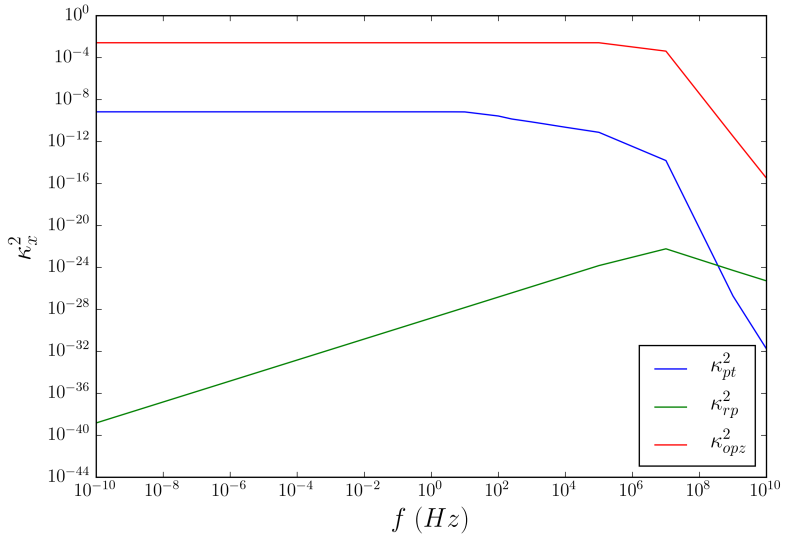


(a)

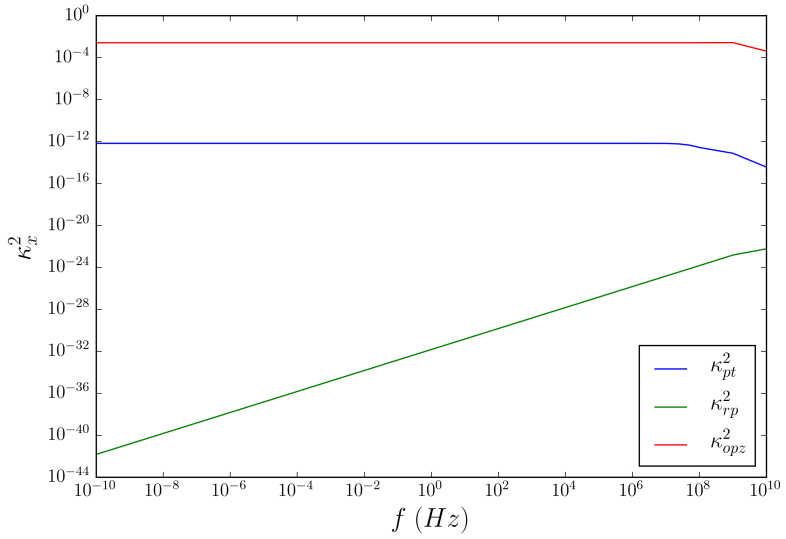


(b)

Figure 6.25: Plot of frequency roll-off, $\kappa_x^2\, vs\, f$, for $P_0 = 1\,mW$ and $Q = 1$ for a disk having the same area but with thicknesses, $d$, of (a) $400\,\mu m$ and (b) $400\,nm$ respectively. Equations (6.3), (6.4) and (6.5) are used for generating the three cases. As $d$ decreases the roll off frequency increases. This is expected because as the thickness decreases $w_r$ increases. Both $\kappa_{rd}^2$ and $\kappa_{opz}^2$ have similar frequency roll off while $\kappa_{pt}^2$ frequency roll off is approximately thousand times lower. This earlier roll-off is due to the thermal time constant and is approximated as $\tau = \frac{\rho V c_p}{k}$ where $V$ and $k$ are the volume and thermal conductivity of the material. Therefore as seen from this approximation and the plots the roll off frequency increases approximately linearly as the volume decreases

| Constant | Numerical Value |
|---|---|
| $Y$ | $80\,GPa$ |
| $\alpha_{exp}$ | $5.39e-6\frac{1}{K}$ |
| $\rho$ | $5320\frac{kg}{m^3}$ |
| $v$ | $4730\frac{m}{s}$ |
| $c_p$ | $350\frac{J}{kKg}$ |
| $r$ | $1.0\,mm$ |
| $A$ | $3.14\times10^{-6}m^2$ |
| $c$ | $2.99\times10^{8}\frac{m}{s}$ |
| $d_{33}$ | $1.345\frac{pm}{V}$ |
| $Q$ | 1 |

Table 6.5: Table of constants used for the calculations. The material parameters chosen are for $GaAs$

### 6.5.4 Opto-Piezo Devices

In this section the design and the operation of three devices using the opto-piezo effect are discussed. The three devices are an optical correlator (OC), optical clock signal generator (OCSG) and mechanical resonance enhanced photodetector (MREP). These opto-mechanical devices are possible because, as discussed above, of the conventional opto-actuation mechanisms the opto-piezo effect has the combination of highest $\kappa^2$ and bandwidth. Therefore allowing these devices to be used in situations of low intense light and large frequencies. Additionally, these devices are envisioned to be components in a photonic integrated circuit (PIC). Next, the photonic devices comprising a PIC and the advantages of PIC are stated followed by a short discussion motivating the processing of information with light. After this the design and operation of the three devices are discussed. The motivation for choosing the three devices will also be discussed in their respective sections.

#### 6.5.4.1 PIC

PIC is defined as the monolithic integration of multiple photonic devices on a single chip. This monolithic integration is similar to integrated circuits (IC) in electronics, i.e. IC integrates multiple electronic devices on a single chip. PIC similar to IC offers the following advantages:

1. Lower cost resulting from the reduction in the amount of material used for making photonic devices
2. Less energy consumption due to lower losses in the circuit
3. Easier packaging
4. Increase in complexity of optical signal processing by cascading many basic components on a single chip

A PIC is generally comprised of the following photonic devices: source, modulator, processor and detector. The functionalities of these devices are the source emits light, the modulator modulates this light thereby encoding information, the processor manipulates this information based on some logic and the detector is used for converting this optical information to current or voltage.

The materials used for the source are either $GaAs$ or $InP$. These III-V materials are used because LDs and LEDs can be made from them. Modulators and processors are made possible using the non-linear changes in the refractive index resulting from an applied field in $GaAs$, $InP$, $Si$ and $LiNbO_3$. These non-linear changes are due to the Pockel's effect in $GaAs$, $InP$ and $LiNbO_3$and Kerr effect in $Si$. The materials used for detectors are $GaAs$, $InP$ and $Si$. As is seen, both $GaAs$ and $InP$ satisfy the requirement for a PIC.

Processing of information using light is of interest because it offers the following advantages over electronics:

1. Larger bandwidth leading to higher data capacities
2. Ultimate speed for transferring and processing of information
3. Access to amplitude, phase and polarization properties of light leading to more methods to encode and transfer information
4. Wavelength multicasting i.e. transferring or copying data to selective predetermined wavelengths
5. The lack of interaction of light eliminates cross-talk

Next, the design and operation of the OC, OCSG and the MREP are discussed.

#### 6.5.4.2 Optical Correlator (OC)

The function of an OC device is to search for patterns in optical signals containing large amounts of data. The motivations for searching patterns optically is to speed up processing of information and to save electronic computation resources. The speed up in optical processing occurs because information is being processed at the speed of light and optical to electronic conversion does not have to occur. An example for the use of OC devices is in optical routers[86]. The role of a router is to direct data packets to the appropriate locations in the network. It does this by reading the header of the packets which contain the address of the location that the packet is destined for. The role of the OC device in the router will be to optically correlate the pattern of the header to the known patterns of addresses thereby reducing latency in the network. Another example for the use of OC devices is in processing big data and in artificial intelligence (AI). Both these fields require the correlation of an incoming signal to known patterns. For AI an additional requirement to processing patterns is learning new patterns. This learning of new patterns could be achieved using an OC that is free to deform. Details of a deformable OC is discussed after a brief introduction to the mathematics of the correlation function.

Mathematically the correlation function is[87]:

$$R(\tau) = \int_{-\infty}^{\infty} s(t) f(t-\tau) dt \tag{6.6}$$

where $s(t)$ is the incoming signal representing some code sequence, $f(t)$ represents the pattern and $R(\tau)$ is the output. If the two sequences $f(t)$and $s(t)$ are identical, then the output has maximum intensity which can be used for thresholding purposes. If the sequences are not matched the output is below threshold.

Figure (6.26) is an illustration of a possible architecture for a deformable optical correlator. This architecture is inspired by Hunter et al[88]. The important elements are the deformable Bragg gratings, photodiodes, photodetector and electronic processor. The electronic processor compares the output of the photodetector to a set threshold hence determining the existence of a pattern. The operation of the deformable OC, as illustrated in figure (6.27), is:

1. the incoming signal $s(t)$, consisting of a pattern, is incident into the arm containing the grating arrays
2. the pattern $f(t)$ is stored in the grating arrays. Each of the gratings are free to deform and the deformation of the gratings occurs via the opto-piezo effect. This gives the OC the ability to store new patterns. Gratings are used because of their wavelength selectivity. Deforming the gratings away from the designed wavelength results in a "0" signal corresponding to no reflection while the "1" signal corresponds to reflection resulting from the undeformed grating. For an $n$-grating array $2^n$ different codes can be processed by this correlator. In this figure, 4 gratings are used corresponding to 16 reconfigurable different codes. The number of the gratings in the array can be increased so that a large number of codes can be realized. The spacing between the gratings correspond to the delay between the bits
3. $R(\tau)$, generated based on the two patterns, is then converted to an electronic signal using the photodiode. The signature of a correlated signal is an intensity greater than the background
4. An amplitude threshold set by the electronic processor verifies if a pattern is found

#### 6.5.4.3 Optical Clock Signal Generator (OCSG)

The function of the OCSG is to generate clock pulses which can be used to synchronize the operation of different devices or systems on the PIC. Figure (6.28) is an illustration of a schematic of an OCSG using the opto-piezo effect to generate clock pulses. In this image, the optical gain medium, which is the source of light, is $GaAs$ and the resonator is a $GaAs$ mechanical structure. Both are connected by a waveguide. The waveguide is the depletion region of the PN junction. The idea for this design is the output of the gain is connected to its input in a feedback loop containing the resonator. The steps for the generation of the clock signals are:

1. DC Light form the source propagates through the resonator's waveguide
2. The resonator due to thermal fluctuations oscillate. The result of these oscillations is a cyclic deformation of the waveguide. As light propagates through this oscillating waveguide the intensity at the output terminal is modulated to the resonant frequency of the resonator

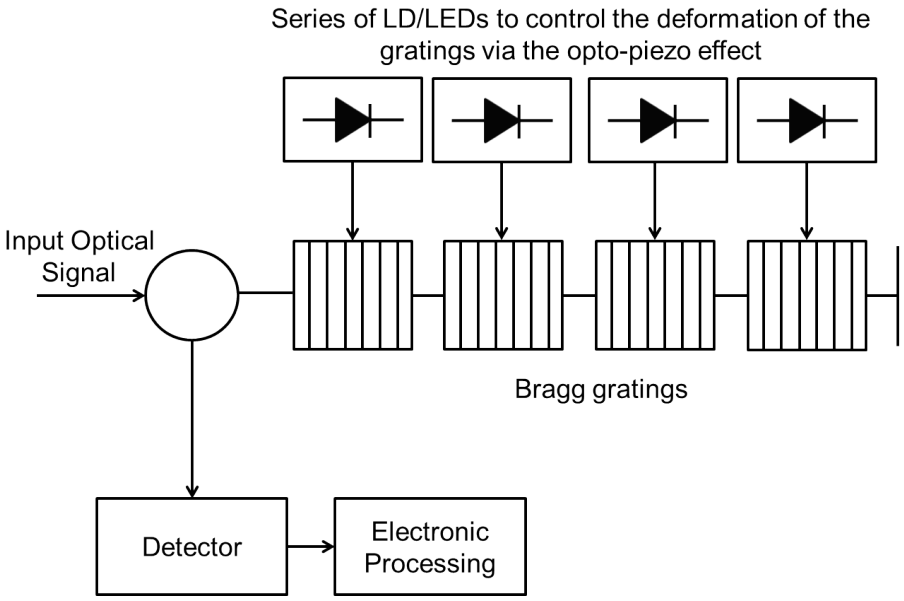


Figure 6.26: Illustration of the architecture of a deformable Optical Correlator (OC) on a PIC. The individual devices in this circuit are connected by waveguides. The circle in the figure is a bi-directional coupler. The structure containing the Bragg grating is released during fabrication thereby allowing for the gratings to deform. The opto-piezo effect is used to deform the gratings. Gratings are used because of their wavelength selectivity. Deforming the gratings away from the designed wavelength results in a "0" signal corresponding to no reflection while the "1" signal corresponds to reflection resulting from the undeformed grating. The electronic processing compares the output of the photodetector to a set threshold hence determining the existence of a pattern. An illustration of this is shown in figure (6.27).

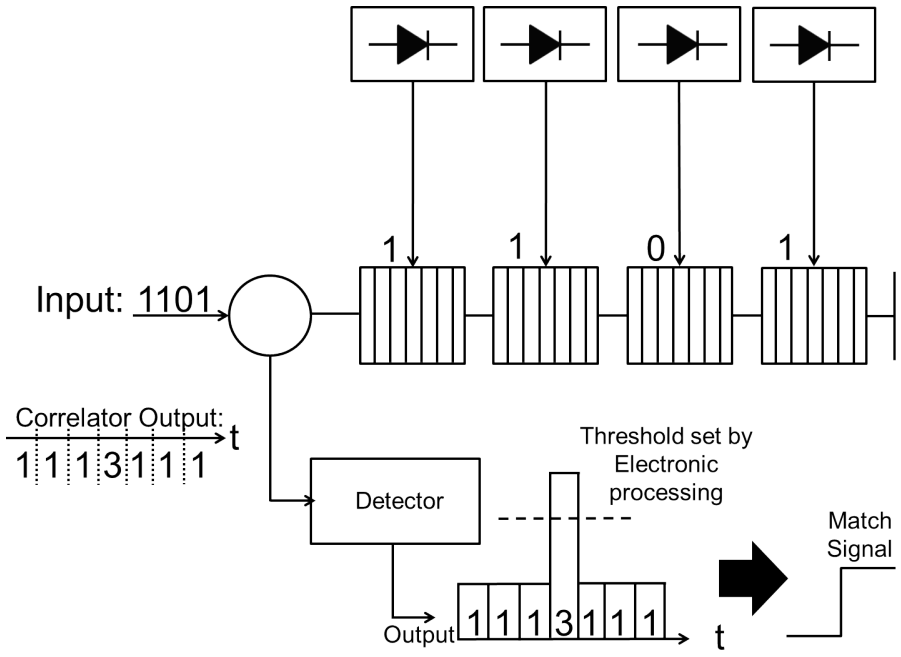


Figure 6.27: Operation of the deformable Optical Correlator (OC). The input signal, for example, consists of the 1101 pattern. To create this pattern on the Bragg gratings only the third grating from the left is deformed via the opto-piezo effect

3. This modulated light is then amplified by the gain medium
4. The amplified light then propagates through the lossy waveguide. As the light propagates some of this modulated light is absorbed causing a larger deformation and hence a larger modulation of light
5. This larger modulation of light is then amplified by the gain medium
6. Part of this modulated light is tapped between the source and the resonator so that it can provide a clock pulse to the PIC

#### 6.5.4.4 Mechanical Resonance Enhanced Photodetector (MREP)

The function of the MREP device is to enhance the responsivity of a photodetector by the Q of the resonator. The responsivity, $R$, is defined as

$$R(\lambda) = \frac{I}{p_{opt}(\lambda)} \tag{6.7}$$

where $I$ is the photogenerated current resulting from the incident optical power. The enhanced responsivity can be used to measure low power optical signals. Such a detector can be used in satellites or in remote terrestrial locations where limited power is only available. The responsivity enhancement is achieved using the opto-piezo effect. Here light modulated

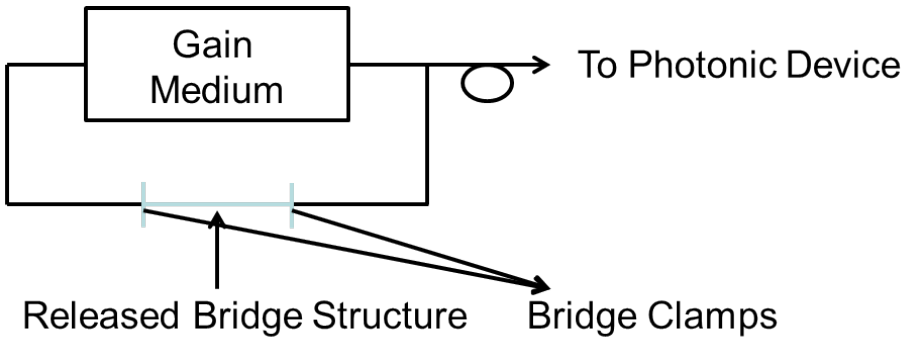


Figure 6.28: Illustration of an Optical Clock Signal Generator (OCSG). The gain medium is the source of light and the bridge structure is free to deform. The gain and the bridge structure are connected by a waveguide. The materials used for both are $GaAs$. The waveguide is the depletion region of the PN junction. The inspiration for this design is taken form the electrical Colpitt oscillator circuit which is used to generate clock pulses in an IC[9]

at the resonance frequency of the mechanical resonator is incident on the coupled photodiode mechanical resonator structure. Due to the opto-piezo effect the photocurrent or $I$ generated from the photodiode is increased by the Q of the resonator. The increased $I$ increases the responsivity as shown in equation (6.7). The advantage of using the MREP device is an amplifier for the modulated frequency may not be required or the reduction in gain requirement on the amplifier. This reduces the power requirement for operating a PIC or IC.

## 6.6 Conclusion

In this chapter, the opto-electro-mechanical coupling was investigated using the fabricated photodiode torsional resonator. This coupling was defined as the interaction between the optical, mechanical and electrical domains of $GaAs$. The interaction between the domains resulted in the opto-piezo actuation and tuning of the opto-piezo actuation using an applied DC bias. The former and the latter were verified by measuring the motional current resulting from the piezoelectric effect. Analytical predictions for the motional current were made using the AC PV circuit model. The circuit elements in this model were determined from the heterostructure of the photodiode. From this model it was found that impedance matching is required for an optimal signal to background ratio and the maximum measured current occurs at the anti-resonant frequency. Additionally, it was found and predicted that as the DC bias increased from reverse to forward bias the motional current decreased. This decrease is related to the change in depletion width of the $pn$ junction. Using the opto-mechanical coupling coefficient it was found that the opto-piezo actuation is several orders of magnitude larger than either photothermal or radiation pressure actuation and that the opto-piezo and radiation pressure actuation have bandwidths that are the same and both are larger than photothermal actuation. The former is an important result because in situations where low optical powers are only available the opto-piezo effect is the only method of actuation that

can be used. The coupling coefficient is mathematically defined to quantify the amount of incident optical energy or power converted to mechanical energy or power.

# Chapter 7

# Conclusion and Future Work

## 7.1 Conclusion

The objective of this thesis was to experimentally and theoretically validate the opto-electro-mechanical and electro-mechanical coupling in a $GaAs$ photodiode heterostructure. The results of these couplings are:

1. Optical and electrical actuation of a mechanical structure
2. Electrical measurements of the deformation of the structure
3. Ability to tune or vary the amount of mechanical deformation by varying the capacitance of the photodiode heterostructure

These couplings are possible because $GaAs$ is a direct band gap semiconductor material and is also a piezoelectric material. These material properties results in $GaAs$ having electrical, optical and mechanical degrees of freedom. Most III-V materials also exhibit these degrees of freedom. In this work $In_{0.485}Ga_{0.515}P$ was also shown to have electrical and mechanical degrees of freedom.

The objectives, mentioned above, were chosen because the coupling between the optical and mechanical domains, optical-electrical and mechanical domains and the non-linear coupling between the electrical and mechanical domains in a $GaAs$ heterostructure have not been explored. Additionally, designing, fabricating and testing of novel mechanical resonators using the orientation dependent piezoelectric properties of $GaAs$ have also not been explored. Thus, seizing the opportunity, this work is the first demonstration of designing, fabricating and using a torsional resonator to experimentally verify the aforementioned couplings. It is surprising, given the maturity of $GaAs$ technology, these couplings have not been previously explored. $GaAs$ technology is approximately 40 years old and has a market share of roughly 7 billion dollars[89]. The term $GaAs$ technology refers to the ability, on an industrial scale, to grow heterostructures, fabricate and package ICs and devices. The motivation for the maturity of this technology was to use $GaAs$ and the grown heterostructure layers' electrical degree of freedom to make monolithic microwave integrated circuits (MMIC), HEMTs etc and to use their electrical and optical degrees of freedom to make devices such as LEDs, LDs, solar cell etc.

The operation of the torsional resonator and the above mentioned couplings were experimentally validated using an MBE grown heterostructure. This heterostructure was optically and electrically designed as a $GaAs$ PV cell and mechanically as a bimorph. The PV cell consisted of a $GaAs$ pn junction where the n layers were grown at the front of the cell and the thickness of the $GaAs$ $p$ region dominated the thickness of the cell. The resulting depletion region, formed at the interface between the $p$ and $n$ regions, is close to the surface of the cell and is piezoelectric. Hence mechanically making the structure a bimorph

Using this bimorph structure and $GaAs$'s orientation dependent piezoelectric response a torsional resonator was designed. The geometry of the resonator consisted of a spine, two tines and a pad. The torsional modes were driven using the anti-symmetric flexural deformation of the two tines. The anti-symmetric deformation resulted from the orientation dependent piezoelectric response while the flexural deformation is a result of the bimorph structure.

The resonator was fabricated in a clean room and consisted of four masks, three metallization and a final release step. For the release step a critical point dryer had to be used in order to prevent stiction. To verify the design of the fabricated resonator the first three torsional modes were excited and measured electrically. Their frequencies are 77, 590 and $1,221\,KHz$ with Qs of $10,000$, $5,700$ and $9,000$. These resonant frequencies agreed well with FEM simulations.

The torsional resonator is one example of a novel structure that can be designed using a combination of the orientation dependent piezoelectric properties and a heterostructure design. This type of resonator was chosen because they have high Q and traditionally such resonators suffer from either having complicated non-planar fabrication processes or complicated drive and detection schemes. Such schemes involve either having complicated electrode designs or experimental setups that generally involve measurement apparatuses, that verify deflection, external to the resonator. As demonstrated in this work the fabrication, drive and detect issues are alleviated. Additionally, other novel resonators having high Q and resonant frequencies in the radio frequency (RF) regime can also be designed and fabricated. Some examples of these are discussed in the section on future work. High Q resonators are important for making sensors that are sensitive to tiny forces while High Q RF resonators can be used as a clock source or as electronic filters in smart devices. Such resonators can find use in for e.g. MMICs which are commonly found in smart devices.

Using the torsional resonator the non-linear electro-mechanical coupling was experimentally verified by operating the diode in its non-linear regime. The electro-mechanical coupling was defined as the interaction between the piezoelectric strain and the variation in the thickness of the depletion region of the diode. Operating the diode in its non-linear regime resulted in the generation of current at harmonic frequencies to the applied voltage. The current generated at twice the applied frequency was given the label $2f$. It was found that for generating a measurable resonant signal at $2f$ the drive voltage had to be roughly $300X$ greater than that used for the non-harmonic case. Additionally, it was found that the current at resonance, and hence piezoelectric strain, increased as the thickness of the depletion region decreased. This reduction in thickness occurred as a result of applying an increasing DC bias. The trend for increase in current was found to be proportional to the inverse $\frac{3}{2}$ of the depletion thickness. This experimental trend agreed with theoretical predictions. The demonstrated non-linear electro-mechanical coupling is important for a few

reasons:

1. In a simple 2 terminal setup, like this one, the drive signal can be separated from the detect signal improving the signal to background ratio. Additionally, this separation of drive and detect also eliminates contributions from feedthrough impedances thereby also improving the signal to background ratio

2. The resonator and the non-linearity of the diode can be used to make a parametric amplifier. Parametric amplifiers have low noise floors and take advantage of the Q of the resonator to amplify a signal. The low noise floor makes it easy to measure small or weak signals. Traditionally parametric amplifiers are made from discrete components involving a diode and a resonant circuit. Here, the two are integrated and thus making it a single device

Similar to above, the torsional resonator was used to experimentally verify the opto-mechanical and opto-electro-mechanical couplings. These couplings are defined as the interaction between the optical mechanical and optical-electro mechanical domains of $GaAs$. The interaction between the optical and mechanical domains results in actuation of the mechanical structure using light. This was called opto-piezo actuation. The voltage required for this actuation is a result of the photogenerated current and the total impedance of the photodiode. It was found that the piezoelectric current increased linearly with incident intensity and for commonly used optical powers this method of actuation is several orders of magnitude more efficient than thermal or radiation pressure methods of actuation. The latter is an important result because in situations where only low optical powers are available the opto-piezo effect is the only method of actuation that can be used.

The interaction between the optical-electrical and mechanical domains resulted in tuning of the optical actuation of the mechanical structure. Similar to the electro-mechanical case a DC bias was applied to change the thickness of the depletion region. It was found that the piezoelectric current decreased non-linearly with an increase in bias voltage. This result, although expected, is different from the electro-mechanical case. The decrease in the piezoelectric current was attributed to the fact that decreasing the depletion width results in decreasing the drive voltage. This result is important because using the opto-piezo effect photonic devices could be made.

To model the opto-piezo actuation and the resulting tuning an AC PV model was derived. This model predicts the behavior of a photodiode operated in its 3rd and 4th quadrant to resistive and reactive loads. From this model it was found that:

1. For a resistive load:

   (a) The AC maximum power point is at lower bias voltage, $V_D$, than for DC

   (b) From the DC IV curves the dimensionless AC current response $\frac{i_{d,1}}{i_{isc_1}}$ can be predicted using the $C$ parameter. The $C$ parameter is a function of two DC parameters - the open circuit voltage, $V_{oc}$ and $V_D$

2. For a reactive load zero power is extracted

3. Extracted AC electrical power decreases non-linearly with an increase of DC optical intensity and increases quadratically with an increase of incident AC optical intensity

4. For the opto-actuation case, impedance matching is required for an optimal signal to background ratio

This derived AC PV model can also find use in the PV industry for modeling arcing faults in solar farms.

## 7.2 Future Work

### 7.2.1 Heterostructure redesign

The inability to correctly predict the magnitude of the experimental results was attributed to the hole pile up region formed between the $p^{-}In_{0.485}Ga_{0.515}P$ and $pGaAs$ layers. A possible solution to this problem could be redesigning the heterostructure layer by removing the $p^{-}In_{0.485}Ga_{0.515}P$ layer. The motivation for growing this layer, initially, was for surface passivation and to create a back surface field. These two increase the chances of collecting photogenerated carriers. Both surface passivation and the back surface field could also be achieved by degenerately doping the bottom contact layer.

### 7.2.2 Mechanical structures

The unique piezoelectric property of $GaAs$ can be used to drive and detect other unique mechanical structures. Examples of these structure are given in figures (7.1) and (7.2)(a). Figure (7.1) is similar to the Y-structure except the tines are in the opposite direction. The mode shapes are similar to that shown in chapter 4. Figure (7.2)(a) is the driven mode shape of a square resonator As is seen from the picture:

1. the adjacent sides of the square flexurally deform in the opposite directions. Hence the opposite ends flexurally deform in the same direction

2. the mid point of the resonator does not deform

The advantage of this design is a three terminal measurement can be made. A three terminal measurement consist of a common ground, a drive and detect electrode. The advantage of this setup is lower package capacitance. This is understood as follows: the drive and detect electrodes can be physically separated to a larger distance. This separation reduces the package capacitance. A cartoon of this is shown in figure (7.2)(b). Here two of the anchors are the ground electrodes and are p doped while the drive and detect electrodes are n doped. The green section is the region that separates the drive and detect electrodes.

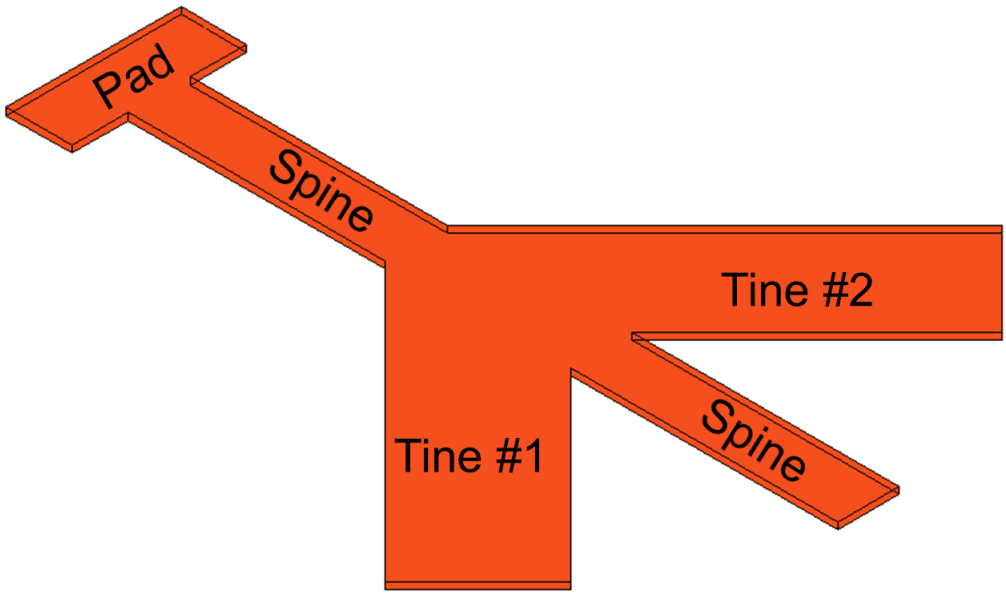


Figure 7.1: Arrow structure. This structure, called arrow, is similar to the Y-structure presented in chapter(4). In the arrow structure the tines are in the opposite direction to the Y tines

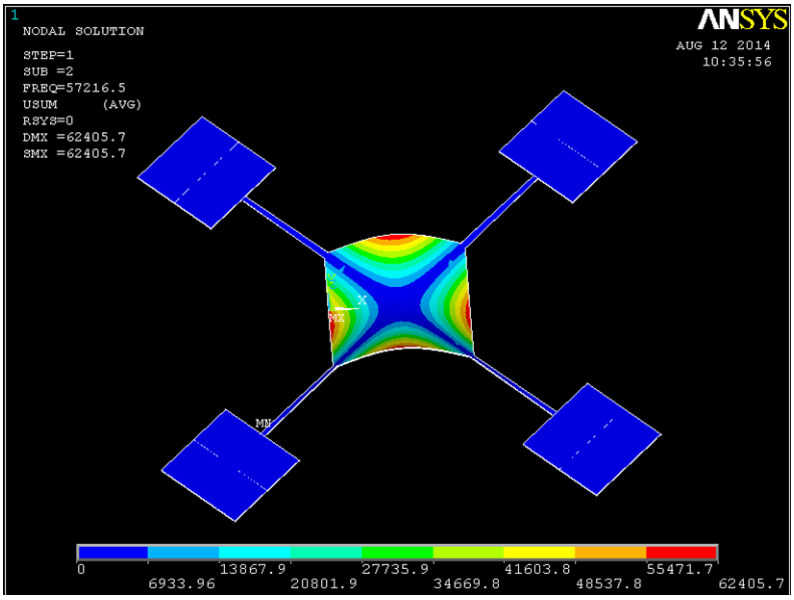


(a)

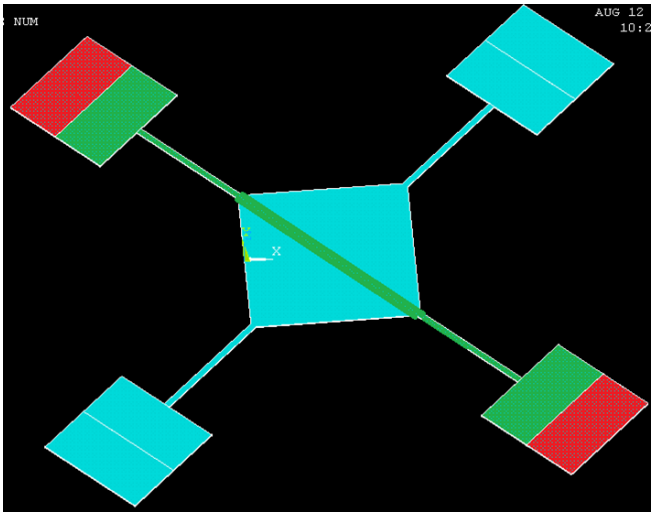


(b)

Figure 7.2: Square resonator. (a) Mode shape of the resonator. Adjacent sides of the resonator flexurally deform in the opposite direction. The middle of the resonator does not deform. (b) Three terminal setup for the square resonator. The green sections is $p$ doped and runs across the midpoint of the resonator. This separates the two $n^+$ regions. Hence one of the $n^+$ regions can be used to drive the device while the other can be used to detect. This results in lowering the package capacitance

# Bibliography


[1] J Soderkvist and K Hjort. The piezoelectric effect of GaAs used for resonators and resonant sensors. *Journal of Micromechanics and Microengineering*, 4(1):28–34, mar 1994.

[2] Ferdinand Beer, Jr., E. Russell Johnston, and John DeWolf. *Mechanics of Materials*. McGraw-Hill Science/Engineering/Math, 2005.

[3] R.G. Ballas. *Piezoelectric Multilayer Beam-Bending Actuators (Microtechnology and MEMS)*. Springer, 2007.

[4] The IET. Standard Definitions and Methods of Measurement for Piezoelectric Vibrators, 1966.

[5] Simon M. Sze. *Physics of Semiconductor Devices*. Wiley-Interscience, 1981.

[6] Jenny Nelson. *The Phisics of Solar Cells*. Imperial College Press, 2003.

[7] G. E. Jellison. Optical functions of GaAs, GaP, and Ge determined by two-channel polarization modulation ellipsometry. *Optical Materials*, 1(3):151–160, 1992.

[8] Mathias Schubert, V. Gottschalch, Craig M. Herzinger, Huade Yao, Paul G. Snyder, and John A. Woollam. Optical constants of GaxIn1-xP lattice matched to GaAs. *Journal of Applied Physics*, 77(7):3416–3419, 1995.

[9] Irving M. Gottlieb. *Practical oscillator handbook*. Newnes, 1997.

[10] K. K. Wong. *Properties of lithium niobate*. INSPEC/Institution of Engineering and Technology, 2002.

[11] M.G. Lippman. Principe de la conservation de l'electricite. *Annales de Chime et de Physique*, 5:159, 1881.

[12] Qing Guo, G Z Cao, and I Y Shen. Measurements of Piezoelectric Coefficient d33 of Lead Zirconate Titanate Thin Films Using a Mini Force Hammer . *Journal of Vibration and Acoustics*, 135(1):11003, feb 2013.

[13] H. C. (Horace Craig) Casey and M. B. Panish. *Heterostructure lasers*. Academic Press, 1978.

[14] William R. Einspruch, Norman G. Wisseman. *GaAs Microelectronics: VLSI Electronics Microstructure Science, Vol. 11 (Volume 11).* Academic Press, 2014.

[15] A. G. Baca and Carol Iris Hill Ashby. *Fabrication of GaAs devices.* Institution of Electrical Engineers, 2005.

[16] H. Welker. Über neue halbleitende Verbindungen II. *Zeitschrift für Naturforschung A*, 8(4):248–251, jan 1953.

[17] P. Aigrain. , as reported in. *Proc. Conf. Quantum Electron.*, page 1762, 1963.

[18] M.B. Basov, G.N. Vul and M. Yu. Popov. *Sov. Phys. JETP*, 10:416, 1960.

[19] Sladek R.J. Boyle W.F. Piezoelectric constant and conductivity relaxation in n-type InP from ultrasonic attenuation measurements. *Solid State Communications*, 16(3):323–326, 1975.

[20] M.B. Basov, G.N. Vul and M. Yu. Popov. *Sov. Phys. JETP*, 13:1320, 1961.

[21] E. M. Jones and C. E. Wurst Jr. *IRE Conv. Rec.*, 9:26, 1961.

[22] Nick Holonyak and S. F. Bevacqua. COHERENT (VISIBLE) LIGHT EMISSION FROM Ga(As1-xPx) JUNCTIONS. *Applied Physics Letters*, 1(4):82, 1962.

[23] T. Gremmelmeier. *Z. Naturforsch*, 11a:511, 1956.

[24] J.B. Mullin, B.W. Straughan, and W.S. Brickell. Liquid encapsulation techniques: The use of an inert liquid in suppressing dissociation during the melt-growth of InAs and GaAs crystals. *Journal of Physics and Chemistry of Solids*, 26(4):782–784, apr 1965.

[25] J. R. Arthur. Interaction of Ga and As2 Molecular Beams with GaAs Surfaces. *Journal of Applied Physics*, 39(8):4032, 1968.

[26] A.Y. Cho. Epitaxy by periodic annealing. *Surface Science*, 17(2):494–503, 1969.

[27] A. Y. Cho and H. C. Casey Jr. GaAs[Single Bond]Alx Ga1x As double-heterostructure lasers prepared by molecular-beam epitaxy. *Applied Physics Letters*, 25(5):288, 1974.

[28] J. Curie, P., Curie. Contractions et dilations produits par des tensions electriques dans les cristeaux hemieedres a faces inclinees. *Comptes Rendus de l'Academie des Sciences*, 93:1137–1140, 1881.

[29] Virgil E Bottom. *Introduction to quartz crystal unit design (Van Nostrand Reinhold electrical/computer science and engineering series).* Van Nostrand Reinhold, 1982.

[30] W.G. Cady. *Piezoelectricity: An Introduction to the Theory and Application of Electromechanical Phenomena in Crystals.* International series in pure and applied physics. McGraw-Hill, 1946.

[31] D. L. White. Depletion layer transducer - a new high-frequency ultrasonic transducer. *I.R.E International Convention Record Part 6*, page 304, 1961.

[32] G. Arlt and P. Quadflieg. Piezoelectricity in iii-v compounds with a phenomenological analysis of the piezoelectric effect. *Physica Status Solidi (b)*, 25(1):323–330, 1968.

[33] K Hjort, J Soderkvist, and J A Schweitz. Gallium arsenide as a mechanical material. *Journal of Micromechanics and Microengineering*, 4(1):1–13, mar 1994.

[34] Sotiris C Masmanidis, Rassul B Karabalin, Iwijn De Vlaminck, Gustaaf Borghs, Mark R Freeman, and Michael L Roukes. Multifunctional nanomechanical systems via tunably coupled piezoelectric actuation. *Science (New York, N.Y.)*, 317(5839):780–3, 2007.

[35] Antonio Nuñez. A survey of GaAs computer designs. *Microprocessing and Microprogramming*, 21(1-5):665–670, aug 1987.

[36] Lawrence M. Fisher. Cold War's End Hits Cray Computer - NYTimes.com, feb 1992.

[37] F Rosenblatt. The perceptron: a probabilistic model for information storage and organization in the brain. *Psychological review*, 65(6):386–408, 1958.

[38] Fowles. *Analytical Mechanics*, volume 68. 2000.

[39] X.M. Huang, M.K. Prakash, C.A. Zorman, M. Mehregany, and M.L. Roukes. *TRANSDUCERS '03 Proceedings 12th International Conference on Solid State Sensors, Actuators and Microsystems, Boston*, 2003.

[40] W. Weaver Jr., S. P. Timoshenko, and D. H. Young. *Vibration Problems in Engineering*. Wiley-Interscience, 1990.

[41] W. P. Robins. *Phase Noise in Signal Sources(Theory and Application) - IEE Telecommunications Series*. Institution of Engineering and Technology, 1984.

[42] K. L. Ekinci. Ultimate limits to inertial mass sensing based upon nanoelectromechanical systems. *Journal of Applied Physics*, 95(5):2682, 2004.

[43] K. Wang and C.T.-C. Nguyen. High-order micromechanical electronic filters. *Proceedings IEEE The Tenth Annual International Workshop on Micro Electro Mechanical Systems. An Investigation of Micro Structures, Sensors, Actuators, Machines and Robots*, pages 25–30, 1997.

[44] T D Stowe, K Yasumura, T W Kenny, D Botkin, K Wago, and D Rugar. Attonewton force detection using ultrathin silicon cantilevers. *Nanotechnology*, 71(July):288–290, 1997.

[45] M. M. Midzor, P. E. Wigen, D. Pelekhov, W. Chen, P. C. Hammel, and M. L. Roukes. Imaging mechanisms of force detected FMR microscopy. *Journal of Applied Physics*, 87(9):6493, 2000.

[46] V. B. Braginsky and V. P. Mitrofanov. *Systems with Small Dissipation*. University Of Chicago Press, 1986.

[47] Stephen O Saltsman. *The Silicon Solar Cell as an Optical Detector*. PhD thesis, University of Central Florida, 1977.

[48] Leo A. Mallette and Ronald L. Phillips. Modeling solar cells for use as optical detectors: background illumination effects. *Applied Optics*, 17(11):1786, jun 1978.

[49] Martin A. Green. Solar cell fill factors: General graph and empirical expressions. *Solid State Electronics*, 24(8):788–789, 1981.

[50] Newport 818-SL. Newport 818-SL Photodetector Specification Sheet.

[51] Newport 818-BB. Newport 818-BB Photodetector Specification Sheet.

[52] D. Chenvidhya, K. Kirtikara, and C. Jivacate. PV module dynamic impedance and its voltage and frequency dependencies. *Solar Energy Materials and Solar Cells*, 86(2):243–251, 2005.

[53] Philip Raymond Bevington and D. Keith Robinson. *Data Reduction and Error Analysis for the Physical Sciences, 2nd edn.*, volume 7. 1992.

[54] Henry Ott. *Noise Reduction Techniques in Electronic Systems, 2nd Edition.* Wiley-Interscience, 1988.

[55] R. Knobel and A. N. Cleland. Piezoelectric displacement sensing with a single-electron transistor. *Applied Physics Letters*, 81(12):2258, 2002.

[56] H B Chan, V A Aksyuk, R N Kleiman, D J Bishop, and F Capasso. Quantum mechanical actuation of microelectromechanical systems by the Casimir force. *Science (New York, N.Y.)*, 291(5510):1941–4, mar 2001.

[57] Guiti Zolfagharkhani, Alexei Gaidarzhy, Pascal Degiovanni, Stefan Kettemann, Peter Fulde, and Pritiraj Mohanty. Nanomechanical detection of itinerant electron spin flip. *Nature nanotechnology*, 3(12):720–3, dec 2008.

[58] R. N. Kleiman, G. K. Kaminsky, J. D. Reppy, R. Pindak, and D. J. Bishop. Single-crystal silicon high-Q torsional oscillators. *Review of Scientific Instruments*, 56(11):2088, nov 1985.

[59] Sadao Adachi. *Physical properties of III-V semiconductor compounds: InP, InAs, GaAs, GaP, InGaAs, and InGaAsP.* John Wiley & Sons Inc., 2005.

[60] Sadao Adachi. GaAs, AlAs, and AlxGa1xAs Material parameters for use in research and device applications. *Journal of Applied Physics*, 58(3):R1, aug 1985.

[61] Abhishaik Rampal. *Experimental and theoretical study of Quartz and InP Piezoelectric MEMS Resonators.* 2004.

[62] V Kaajakari. *Practical MEMS:Analysis and design of microsystems, MEMS sensors, electronics, actuators, rf mems, optical mems, and microfluidic systems.* Small Gear Publishing, 2009.

[63] D. Leenov and A. Uhlir. Generation of Harmonics and Subharmonics at Microwave Frequencies with P-N Junction Diodes. *Proceedings of the IRE*, 47(10):1724–1729, oct 1959.

[64] H. Barth. A Wideband, Backshort-Tunable Second Harmonic W-Band Gunn-Oscillator. In *MTT-S International Microwave Symposium Digest*, volume 81, pages 334–337. MTT005.

[65] W.H. Haydl. Fundamental and Harmonic Operation of Millimeter-Wave Gunn Diodes. *IEEE Transactions on Microwave Theory and Techniques*, 31(11):879–889, nov 1983.

[66] Yiming Liu, Yun Sun, and Angus Rockett. A new simulation software of solar cells—wx-AMPS. *Solar Energy Materials and Solar Cells*, 98:124–128, mar 2012.

[67] David J. Griffiths. *Introduction to Electrodynamics (3rd Edition)*. Benjamin Cummings, 1999.

[68] Mani Hossein-Zadeh, Hossein Rokhsari, Ali Hajimiri, and Kerry J. Vahala. Characterization of a radiation-pressure-driven micromechanical oscillator. *Physical Review A*, 74(2):023813, aug 2006.

[69] Maxim Zalalutdinov, Keith L. Aubin, Robert B. Reichenbach, Alan T. Zehnder, Brian Houston, Jeevak M. Parpia, and Harold G. Craighead. Shell-type micromechanical actuator and resonator. *Applied Physics Letters*, 83(18):3815–3817, 2003.

[70] B. Kundys. Photostrictive materials. *Applied Physics Reviews*, 2(1):011301, mar 2015.

[71] B. Kundys, V. Iurchuk, C. Meny, H. Majjad, and B. Doudin. Sub-coercive and multi-level ferroelastic remnant states with resistive readout. *Applied Physics Letters*, 104(23):232905, jun 2014.

[72] R. W. Keyes. The Electronic Contribution to the Elastic Properties of Germanium. *IBM Journal of Research and Development*, 5(4):266–278, oct 1961.

[73] Claus D. Eisenbach. Isomerization of aromatic azo chromophores in poly(ethyl acrylate) networks and photomechanical effect. *Polymer*, 21(10):1175–1179, 1980.

[74] I. Tatsuzaki, K. Itoh, S. Ueda, and Y. Shindo. Strain Along c Axis of SbSI Caused by Illumination in dc Electric Field. *Physical Review Letters*, 17(4):198–200, jul 1966.

[75] B Kundys, M Viret, C Meny, V Da Costa, D Colson, and B Doudin. Wavelength dependence of photoinduced deformation in BiFeO 3. *PHYSICAL REVIEW B*, 85, 2012.

[76] Dan Daranciang, Matthew J. Highland, Haidan Wen, Steve M. Young, Nathaniel C. Brandt, Harold Y. Hwang, Michael Vattilana, Matthieu Nicoul, Florian Quirin, John Goodfellow, Tingting Qi, Ilya Grinberg, David M. Fritz, Marco Cammarata, Diling Zhu, Henrik T. Lemke, Donald A. Walko, Eric M. Dufresne, Yuelin Li, Jörgen Larsson, David A. Reis, Klaus Sokolowski-Tinten, Keith A. Nelson, Andrew M. Rappe, Paul H. Fuoss, G. Brian Stephenson, and Aaron M. Lindenberg. Ultrafast Photovoltaic Response in Ferroelectric Nanolayers. *Physical Review Letters*, 108(8):087601, feb 2012.

[77] J. Lagowski and H. C. Gatos. Photomechanical Effect in Noncentrosymmetric Semiconductors-CdS. *Applied Physics Letters*, 20(1):14, 1972.

[78] Jacek Łagowski and Harry C. Gatos. Photomechanical vibration of thin crystals of polar semiconductors. *Surface Science*, 45(2):353–370, oct 1974.

[79] T. Figielski. Photostriction Effect in Germanium. *physica status solidi (b)*, 1(4):306–316, 1961.

[80] John R. Buschert and R. Colella. Photostriction effect in silicon observed by time-resolved x-ray diffraction. *Solid State Communications*, 80(6):419–422, 1991.

[81] G. VAN DER VEEN and W. PRINS. Photomechanical Energy Conversion in a Polymer Membrane. *Nature*, 230(11):70, 1971.

[82] H. Finkelmann, E. Nishikawa, G. G. Pereira, and M. Warner. A New Opto-Mechanical Effect in Solids. *Physical Review Letters*, 87(1):015501, jun 2001.

[83] Frank L Pedrotti and Leno S Pedrotti. Introduction to optics 2nd edition. *Introduction to Optics 2nd Edition by Frank L. Pedrotti, SJ, Leno S. Pedrotti New Jersey: Prentice Hall, 1993*, 1, 1993.

[84] M. Suzuki, H. Tanaka, and S. Akiba. Effect of hole pile-up at heterointerface on modulation voltage in GaInAsP electroabsorption modulators. *Electronics Letters*, 25(2):88, 1989.

[85] Jasprit. Singh. *Semiconductor optoelectronics : physics and technology*. McGraw-Hill, 1995.

[86] Alan E. Willner, Salman Khaleghi, Mohammad Reza Chitgarha, and Omer Faruk Yilmaz. All-optical signal processing. *Journal of Lightwave Technology*, 32(4):660–680, 2014.

[87] R N Bracewell. *The Fourier Transform and its Applications*, volume 42. 1986.

[88] D. B. Hunter and R. A. Minasian. Programmable high-speed optical code recognition using fibre bragg grating arrays. *Electronics Letters*, 35(5):412–414, Mar 1999.

[89] Technavio.com. Global Gallium Arsenide Devices Market 2016-2020 | Technavio - Discover Market Opportunities. Technical report, Chicago, 2015.